

488324

IN-02
DATE OVERRIDE
132855
P.222

Two- and Three-Dimensional Blade Vortex Interactions

F. Davoudzadeh, N. -S Liu, W. R. Briley, R. C. Buggeln, and S. J. Shamroth

CONTRACT NAS2-12635
August 1990



(NASA-CR-177567) TWO- AND
THREE-DIMENSIONAL BLADE VORTEX
INTERACTIONS (Scientific Research
Associates) 222 p

N93-16942

Unclas

G3/02 0132855

Two- and Three-Dimensional Blade Vortex Interactions

F. Davoudzadeh
N. -S Liu
W. R. Briley
R. C. Buggeln
S. J. Shamroth
Scientific Research Associates Inc.
Glastonbury, Connecticut

Prepared for
Ames Research Center
CONTRACT NAS2-12635
August 1990



National Aeronautics and
Space Administration

Ames Research Center
Moffett Field, California 94035-1000

Table of Contents

SUMMARY.....	1
INTRODUCTION.....	1
ANALYSIS.....	4
Governing Equations and Solution Algorithm.....	4
Artificial Dissipation and Turbulence Model.....	5
Grid Construction.....	8
Boundary Conditions.....	10
ISOLATED VORTEX STUDY.....	10
Computational Grids.....	12
Initial Conditions.....	12
Central Difference Scheme.....	14
Case #1.....	14
Second-Order in Time and Iteratively Implicit Scheme.....	15
(A) Pseudo Time-Step Parameter.....	15
(B) Physical Time-Step DT.....	16
(C) Number of Pseudo Time Iterations.....	16
Case #2.....	17
Case #3.....	17
Case #4.....	17
Case #5.....	19
Case #6.....	19
Initial Vortex Strength.....	20
Cases 7-8.....	20
Cases 9.....	21
Solving Navier-Stokes Equations (Case 12).	22
Summary.....	22
Table 1.....	23
TWO-DIMENSIONAL BLADE VORTEX INTERACTION.....	24
Grid.....	24
Flow Parameters.....	25
Results and Discussion.....	25

THREE-DIMENSIONAL BLADE VORTEX INTERACTION.....	29
CONCLUDING REMARKS.....	36
SYMBOLS.....	37
References.....	39
Figures 1 - 107	41

SUMMARY

A three-dimensional time dependent Navier-Stokes analysis was applied to the rotor blade vortex interaction problem. The numerical procedure is an iterative implicit procedure using three point central differences to represent spatial derivatives. A series of calculations were made to determine the time steps, pseudo-time steps, iterations, artificial dissipation level, etc. required to maintain a nondissipative vortex. Results show the chosen method to have excellent non-dissipative properties provided the correct parameters are chosen. This study was used to set parameters for both two- and three-dimensional blade vortex interaction studies. The two-dimensional study considered the interaction between a vortex and a NACA0012 airfoil. The results showed the detailed physics during the interaction including the pressure pulse propagating from the blade. The simulated flow physics was qualitatively similar to that experimentally observed. The 2-D BVI phenomena is the result of the buildup and violent collapse of the shock waves and local supersonic pockets on the blade surfaces. The resulting pressure pulse build-up appears to be centered at the blade leading edge. The three-dimensional interaction study considered the case of a vortex at 20° incidence to the blade leading edge. Although the qualitative results were similar to that of the two-dimensional interaction, details clearly showed the three-dimensional nature of the interaction process.

I. INTRODUCTION

The interaction of concentrated vortices with blades induces unsteady aerodynamic loading responsible for blade vibrations, aeroelastic instabilities, and impulsive noise. The effects of blade-vortex interaction (BVI) are especially significant in the transonic flow regime, in which the strength and position of the shock waves are sensitive to small changes in the flow parameters. Due to its common occurrence in many aerodynamic applications, BVI has been a subject of many experimental, analytic and computational investigations. Recent examples of experimental investigations include the work of Caradonna and his colleagues (1984, 1988) and Booth and Yu (1986). Analytical studies include those of Panares (1987), Lee and Smith (1987) and Poling, Dadone and Telionis (1989). Investigations based upon numerical simulations include the two-dimensional full

Navier-Stokes simulations of Sankar and Tang (1985), the two-dimensional thin layer Navier-Stokes simulations of Srinivasan and McCroskey (1987), Srinivasan, McCroskey and Baeder (1986) and Rai (1987), and the three-dimensional thin layer Navier-Stokes simulation of Srinivasan and McCroskey (1989).

The BVI problem can be viewed as an unsteady, three-dimensional close encounter of curved vortex filaments, at arbitrary intersection angles, with a blade that is in combined translational and rotational motion. Under certain operating conditions, the blade can encounter a vortex that is almost parallel to itself. Such an encounter is essentially two-dimensional but unsteady, and has been the focus of many BVI investigations. However, in general the blade vortex interaction is a three-dimensional phenomenon. Both two-dimensional and three-dimensional interactions are considered here.

At the present time, a key problem in computing flows containing concentrated vortices is the ability to preserve and convect these vortices in a finite-difference or finite-volume grid without false numerical diffusion due to truncation error, artificial dissipation and turbulence modelling. Various investigators have dealt with the vortex preservation problem in different ways. One approach, the prescribed vortex approach (e.g. Srinivasan and McCroskey, 1987 and 1989) assumes a background flow field consisting of a specified vortex and solves the governing partial differential equations for the difference between the full dependent variable field and that of the specified vortex. Under this approach the numerical diffusion is applied only to that part of the flow field which represents the perturbation from the isolated vortex flow field. A conceptually similar approach is taken by Sankar and Tang (1985) who solve the Navier-Stokes equations for the usual dependent variables; i.e., do not use a perturbation approach but modify the numerical dissipative operator to act on the difference between the instantaneous total field values and some presumed vortex field values, thereby removing a large part of the spurious dissipation of the vortex structure. More recently, strong BVI problems were solved by using a fifth-order accurate upwind-biased scheme without employing any vortex preservation techniques (Rai, 1987).

In the present work, the ensemble-averaged, time-dependent Navier-Stokes equations are solved on a body-fitted grid around a NACA0012 airfoil in two and three dimensions to study strong interaction of a vortex with a stationary blade. The Navier-Stokes equations are solved by using an iterative implicit finite-difference scheme with second order spatial and temporal accuracies. Furthermore,

simple vortex preservation techniques are used to minimize the amount of spurious numerical dissipation and eddy viscosity caused by the presence of the vortex during its convective motion towards the leading edge of the blade. In terms of spatial differencing, the present study employs three-point central differences with adjustable dissipation terms. An alternative approach is to use various upwind differencing schemes in transformed coordinates. For example, Rai (1987) has used first- and second-order upwind differences and also fifth-order upwind-biased differences to study blade vortex interactions. Although higher-order centered and upwind schemes can be more accurate, the order of accuracy refers to transformed coordinate variables. The high order schemes are usually first-order accurate in physical space variables for general non-uniform grids. Centered schemes can be made equivalent to upwind schemes by using special forms of dissipation with particular choices of dissipation parameters, as discussed in Pulliam (1985), Yoon and Kwak (1988) and Briley, Govindan and McDonald (1990).

One attraction of the upwind schemes is that they propagate waves according to local characteristic behavior (in a one-dimensional sense). This is offset somewhat by complexity and the use of expanded grid molecules for higher order upwind schemes, which complicates their use near boundaries. An upwind approach can also be used to advantage in constructing special schemes for capturing strong shocks. Central-difference schemes also approximate local physics correctly for smooth flows, but require special treatment of (extraneous) boundary conditions to avoid error due to boundary conditions which conflict with characteristic behavior at boundaries.

In our experience, the present scheme is more accurate than a first-order upwind scheme, and has accuracy comparable to the higher-order upwind schemes for general non-uniform grids. The present scheme also has a three-point bandwidth and is simple and economical. The simple artificial dissipation approach used here does not require assumptions regarding the velocity field associated with the prescribed vortex approach used by some other investigators, e.g. Srinivasan et al. (1989). Finally, the main focus of the present effort is a three-dimensional simulation based upon the full Navier-Stokes equations whereas the previous three-dimensional simulations, Srinivasan et al. (1989), are based upon a solution of the thin layer equations.

The present effort proceeds in three separate steps. First consideration is given to the isolated vortex to develop a run protocol which has suitable vortex

preservation properties. Vortex preservation is necessary for viable two- and/or three-dimensional simulations. Secondly, a two-dimensional, transonic blade vortex interaction simulation is made. This allows a qualitative assessment prior to the three-dimensional interaction. The third portion of the program is the three-dimensional blade vortex interaction simulation .

II. ANALYSIS

Governing Equations and Solution Algorithm

Prior to discussing the results a discussion of the governing equations and numerical approach is appropriate. As previously stated, the present approach solves the full ensemble-averaged Navier-Stokes equations without any shear layer assumption. The approach uses second-order spatial differencing and a second-order artificial dissipation model which does not require any assumption regarding the velocity field associated with the vortex. The equations are:

Continuity

$$\frac{\partial \rho}{\partial t} + \nabla \cdot \rho \mathbf{U} = 0 \quad (1)$$

Momentum

$$\frac{\partial \rho \mathbf{U}}{\partial t} + \nabla \cdot (\rho \mathbf{U} \mathbf{U}) = -\nabla P + \nabla \cdot (\vec{\pi} + \vec{\pi}^T) \quad (2)$$

Energy

$$\frac{\partial \rho h}{\partial t} + \nabla \cdot (\rho \mathbf{U} h) = -\nabla \cdot (\mathbf{Q} + \mathbf{Q}^T) + \frac{DP}{Dt} + \Phi + \rho \epsilon \quad (3)$$

where ρ is density, \mathbf{U} is velocity, P is pressure, π is the molecular stress tensor, $\vec{\pi}^T$ is the turbulent stress tensor, h is enthalpy, \mathbf{Q} is the mean heat flux vector, \mathbf{Q}^T is the turbulent heat flux vector, Φ is the mean flow dissipation rate and ϵ is the turbulence energy dissipation rate.

In regard to the numerical method, the basic scheme used is a Linearized Block Implicit (LBI) ADI procedure of Briley and McDonald (1977, 1980). The splitting error and the linearization error associated with this basic scheme are removed by introducing an inner ADI iterative procedure at each time step. In brief, the procedure adds terms $\partial \rho / \partial \tau$, $\partial \rho U / \partial \tau$ and $\partial \rho h / \partial \tau$ to the continuity, momentum and energy equations, Eqs. (1) - (3), respectively. Three point central differences are used to represent spatial derivatives and, unless specified otherwise, three point backward time differencing is used to represent temporal differences leading to a second order temporal technique. The spatial accuracy is second order except for the use of numerical dissipation which is discussed later. The equations, including the $\partial () / \partial \tau$ terms are solved by the LBI technique in a manner analogous to that used by Rai (1987). On convergence of the inner iteration the scheme becomes a fully implicit nonlinear backward time difference scheme. Extensive tests have been made on the most effective choice of inner iterations and physical time steps and these tests are discussed subsequently.

Artificial Dissipation and Turbulence Model

When calculating high Reynolds number flows using centered spatial differencing, some artificial dissipation is needed to maintain numerical stability and to suppress spurious oscillations in the numerical results. Such "artificial dissipation" could be added via the spatial differencing formulation (e.g., one-sided difference approximations for first derivatives) or by explicitly adding an additional dissipative term. The present effort utilizes the latter approach. When an additional term is explicitly added, the physical approximation being made is usually clearer than when dissipative mechanisms are contained within numerical truncation errors, and further, explicit addition of an artificial dissipation term allows greater control over the amount of nonphysical dissipation being added. Obviously, the most desirable technique would add only enough dissipation to suppress oscillations without deteriorating solution accuracy. Various methods of adding artificial dissipation were investigated by Shamroth et al. (1982), and these were evaluated in the context of a model one-dimensional problem containing a shock with a known analytic solution (one-dimensional flow with heat transfer). The methods considered included second-order dissipation, fourth-order dissipation and pressure dissipation techniques.

As a result of this investigation, it was concluded that for nearly normal shocks such as that expected in this study a second-order anisotropic artificial dissipation formulation suppressed spatial oscillations while maintaining solution accuracy, and could be used to capture shocks successfully. In this formulation, the terms

$$\frac{\partial}{\partial x_i} \left(\rho^{n-1} d_{x_i} \frac{\partial \phi}{\partial x_i} \right)$$

are added to the governing equations where $\phi = u_i$ for the x_i -momentum equation and $\phi = \rho$ for the continuity equation, respectively. The exponent, n , is zero for the continuity equation and unity for the momentum equations. The dissipation coefficient, d_{x_i} , is determined as follows: the general equation without addition of any artificial dissipation has an x_i -direction convective term of the form $a \partial \phi / \partial x_i$ and an x_i -direction diffusion term of the form $\partial (b \partial \phi / \partial x_i) / \partial x_i$. The diffusive term is expanded

$$\partial \left(\frac{b \partial \phi}{\partial x_i} \right) / \partial x_i = \frac{b \partial^2 \phi}{\partial x_i^2} + \frac{\partial b}{\partial x_i} \frac{\partial \phi}{\partial x_i} \quad (4)$$

and then a local cell Reynolds number, $Re_{\Delta x_i}$, is defined for the x_i -direction by

$$Re_{\Delta x_i} = \left| a - \frac{\partial b}{\partial x_i} \right| \Delta x_i / b \quad (5)$$

where b is the total effective viscosity, including both laminar and turbulent contributions, and Δx_i is the grid spacing. The numerical dissipation coefficient, d_{x_i} , is nonnegative and is chosen as the larger of zero and the local quantity

$$\mu_e (\sigma_{x_i} Re_{\Delta x_i}^{-1}) \quad (6)$$

The dissipation parameter σ_{x_i} , is a specified constant and represents the inverse of the cell Reynolds number below which no artificial dissipation is added. The maximum value of the dissipation, $\sigma_{x_i} = 0.5$, corresponds approximately to that obtained by using one-sided differencing throughout. A term of the form $\partial (\rho^{n-1} d_{x_i} \partial \phi / \partial x_i) / \partial x_i$ is added to each equation.

The present results have been obtained with a mixing length turbulence model, and an isotropic eddy viscosity. This model assumes the existence of a mixing

length, ℓ , and then relates an eddy viscosity, μ_T , to the mixing length by

$$\mu_T = \rho \ell^2 \left[\left[\frac{\partial u_i}{\partial x_j} + \frac{\partial u_j}{\partial x_i} \right] \frac{\partial u_i}{\partial x_j} \right]^{\frac{1}{2}} \quad (7)$$

For flow regions upstream of the trailing edge where the flow is attached, the mixing length is determined by the usual boundary layer formulation

$$\ell = \kappa y D \quad \ell < \ell_{\max} \quad (8)$$

where κ is the von-Karman constant, D is a sublayer damping factor and ℓ_{\max} is taken as 0.09δ , where δ is the boundary layer thickness. The van Driest damping factor is defined as

$$D = (1 - e^{-y^+/26}) \quad (9)$$

where $y^+ = y u_\tau / \nu$ is the dimensionless coordinate normal to the wall.

When the mixing length formulation is used in a boundary layer environment, δ is usually taken as the location where $u/u_e = 0.99$. However, this definition assumes the existence of an outer portion of the flow where u_e is independent of distance from the wall, and assumes that the location where u_e becomes independent of distance from the wall marks the end of the viscous region. In an airfoil Navier-Stokes calculation, no such clear flow division occurs as even in the nominally inviscid region there are velocity gradients due to potential flow effects. Therefore, the boundary layer thickness, δ , is set by first determining u_{\max} , the maximum velocity at each given streamwise station, and then setting δ using

$$\delta = 2.0y (u/u_{\max} = k_1) \quad (10)$$

i.e., δ is taken empirically as twice the distance from the wall to the location where $u/u_{\max} = k_1$. In the present calculations, k_1 was set to 0.90.

This boundary layer thickness specification is not suitable in the airfoil leading edge stagnation regions or near the rounded trailing edges where two small separation regions form, hence special treatment is required in these areas. The points 1 and 2 shown in region I of Fig. 1 are at a specified arc-length (Δs_1 and Δs_2) from the nominal stagnation point, and in the present calculation Δs_1 and

Δs_2 were approximately 5% of axial chord. In region I, a value of δ is defined using a quadratic fit between the computed values δ_1 and δ_2 and a specified minimum value δ_{\min} assumed at the stagnation point. The points 3 and 4 shown in region II of Fig. 1 are at a specified arc-length (Δs_3 and Δs_4) from the trailing edge point, and in the present calculations Δs_3 and Δs_4 were approximately 6% of axial chord. Downstream of points 3 and 4, the value of δ is set to δ_3 and δ_4 , respectively. In the wake region an assumed spreading rate is used.

Obviously, both artificial dissipation and turbulence viscosity are sources of false diffusion and distortion of a vortex convected in a finite-difference grid. In the present work, the effects of artificial dissipation on the vortex structure is minimized by specifying a proper value of the adjustable parameter (σ_{xi}) which controls the amount of added dissipation, and for the present BVI study this value was determined from a separate set of calculations in which the effects of this parameter's magnitude on the preservation of a free vortex convected over a long distance are examined. To minimize the spurious diffusion of vortex structure due to the turbulence model, the turbulent viscosity is set to be zero in a region ranging between the inflow section to a section which is approximately one chord length upstream of the leading edge of the blade. The turbulent viscosity then gradually blends into the values provided by the employed mixing length model. The numerical results obtained show these simple techniques to be effective in preserving the vortex during its convection towards the blade.

Grid Construction

During the course of this effort calculations were run with several types of grids. The BVI calculations require a grid which extends far upstream (perhaps five chords) to a station where the vortex is placed initially. Furthermore, it is important that the vortex be convected to the blade with minimum distortion or dissipation due to numerical effects. This demand argues strongly for an orthogonal grid upstream of the blade since significant non-orthogonality leads to a higher degree of numerical error and is expected to distort and dissipate the vortex in a physically unrealistic manner. With these considerations in mind, SRA has developed a "four corner" grid, a sketch of which is shown in Fig. 2. This grid was generated using the EAGLE code of Thompson (1987). This grid can be easily extended to far upstream without introducing excessive grid non-orthogonality in the upstream region. On the other hand, if a "C"-grid is

used such an extension to the far upstream would present considerable grid non-orthogonality in the far upstream region. Therefore a "four corner" grid is the grid of choice for the desired simulation, and is used here.

As can be seen in Fig. 2, the points A, B, C, and D are points with singular metric information. However, they are on the boundary and the change in coordinate line direction at these points can be kept to 45° as compared to a change of 90° for a standard "H"-grid. This decrease in coordinate direction rate of change should make the four corner grid less susceptible to numerical error in the vicinity of the singular boundary points.

Figure 3 presents a computer generated plot of the overall grid for a NACA0012 airfoil. Detailed grid distributions in the leading edge and trailing edge regions are shown in Figs. 4 and 5. A total of 12,000 grid points are used with high resolution both near the blade and in the vicinity of the blade leading and trailing edges. Typical resolution at the blade surface is 3.0×10^{-4} chords. As previously discussed, the major disadvantage with the conventional "H"-type grid is the presence of the singular points in the leading edge and the trailing edge, where the branch cut lines meet the airfoil body and the grid lines change their slopes at very sharp (almost ninety degrees) angles. The severity of this problem is reduced for the "four corner" grid by changing the location of the points at which branch cut lines meet the airfoil body to positions away from the center line so that these lines can connect to airfoil with a 45° angle, as shown in Fig. 4.

A calculation was performed for the isolated airfoil given in Fig. 3 at zero incidence. The free stream Mach number and the Reynolds number used for this calculation were 0.3 and 1.0×10^4 , respectively. The calculation was continued until an asymptotic steady solution was obtained. The surface pressure distribution at such a steady state is shown in Fig. 6 which qualitatively demonstrates the typical behavior of the NACA 0012 airfoil. The pressure distribution, for the same type of airfoil, reported by Mehta (1977) also is given in Fig. 6 for comparison. The results are in reasonable agreement with some moderate difference in the suction peak which may be attributable to the four corner grid. The contours of streamwise velocity, u , and transverse velocity, v , are given in Figs. 7-10. The major item to be noted in Figs. 7-10 are the smooth dependent variable fields which occur even in the presence of the coordinate singularities. This computation is a demonstration case for an isolated airfoil with a four corner grid. Comparisons against data for a variety of cases with an

earlier version of the code using a C-grid are given by Shamroth (1979 and 1985). In general, the comparisons both for pressure distribution and velocity distribution in the boundary layer showed good agreement with data.

Boundary Conditions

The authors' experience in solving Navier-Stokes equations has indicated the important role which correctly modeled boundary conditions play in determining accurate solutions and rapid numerical convergence. The present approach follows that of Briley, Buggeln and McDonald (1985). In brief, this approach sets total pressure and flow angle at the upstream inflow boundary, boundary EH of Fig. 2 and static pressure at the downstream outflow boundary, boundary HILE of Fig. 2. These represent the physical boundary conditions for the governing set of differential equations. In addition, the second derivative of pressure is set to zero at the upstream boundary, and second derivatives of all velocity components are set to zero at the downstream boundary. On the airfoil surface, no-slip conditions are applied. These are applied with sublayer resolution; wall functions are not used, as the first grid point off the wall is within the sublayer. In addition, the wall normal pressure gradient is set to zero. These conditions suffice for two-dimensional flow. For three-dimensional flow, as will be discussed later, symmetry conditions were set on the spanwise boundaries.

III. ISOLATED VORTEX STUDY

The first study of the present effort is an isolated vortex study aimed at developing a computational protocol which would preserve the vortex strength and shape as it is convected downstream. The present study uses three-point centered spatial differences as opposed to five-point upwind differences which is potentially more efficient and uses a numerical dissipation scheme which does not require any assumptions on the location or distribution of the velocity field associated with the vortex. However, prior to performing either two-dimensional or three-dimensional blade vortex interaction studies it is necessary to determine a run protocol which will preserve the vortex. If a numerical procedure does not preserve an isolated vortex, this same procedure can not be used for the blade vortex interaction study since non-physical dissipation will occur prior to the

interaction process and the process will be based upon a vortex of artificially low strength and large extent.

The vortex preservation test for an isolated vortex was used by Rai (1987) as a measure to assess the time accuracy of different numerical schemes. In this test, the flow associated with a Lamb-type vortex convecting in a freestream is calculated. The pressure field associated with such a vortex is a minimum at the vortex center and increases asymptotically to the freestream value with distance from the vortex center. A dissipative scheme is incapable of maintaining the minimum value of the pressure at the core of the vortex at its original value; instead, the pressure at the center increases continually as the vortex convects with the flow. In the absence of any physical viscosity (Euler equations) this change in pressure at the center of the vortex represents numerically induced vortex decay. Therefore, a good measure of the vortex preserving capability is the core pressure. Rai reported the results of a series of calculations using a conventional second-order-accurate, central-difference scheme (the Beam-Warming scheme) and an upwind biased, fifth-order scheme. Variation of vortex core pressure as a function of the number of core radii traveled by a vortex, as reported by Rai, is given in Fig. 11. Although the grid spacing in the vortex path was given, the overall number of grid points and the value of CFL used for these calculations are not reported. Under the present program a similar approach of monitoring the vortex core pressure as the vortex convects downstream was adopted to measure the time accuracy of the SRA Navier-Stokes code. A series of calculations were performed to assess the vortex preservation capabilities of the current numerical procedure and to indicate areas where refinement would be required. Based on the results of these calculations, the code was further developed to enhance the features required for the blade vortex interaction (BVI) study. The BVI investigation may require considerable computer resources. This is due to the large physical domain needed to avoid boundary effects and to the very fine mesh required to resolve flow details. Calculations were performed to study the effects of the physical boundary distances, grid spacing, artificial viscosity, initial vortex strength, boundary conditions and time iterations to optimize the use of the computer resources as a prelude to the actual BVI simulations.

Computational Grids

Three major different types of grids were used for the free vortex calculations:

- 1) Type "A" grid - is a rectangular grid that is 52.5 x 7.5 radii in a length to width with equal spacing in the x- and y-directions. The physical domain and the trajectory of the vortex path from its initiation to 45 radii of travel are shown in Fig. 12a. The grid spacing for this grid is $\Delta x = \Delta y = 1/4$, the core radius of vortex being 1.0. A portion of the grid is shown in Fig. 12b.
- 2) Type "B" grid - is identical to the type "A" grid except for spacing. The spacing used for this grid is $\Delta x = \Delta y = 1/8$. The "A" and "B" grids will be used to demonstrate the effect of the grid density on the vortex preservation characteristics of the scheme.
- 3) Type "C" Grid - is shown in Fig. 13. Equal spacing ($\Delta x = y = 1/4$) is used in the central region containing the vortex path and a stretched grid is used to extend the physical domain to the far field. The boundaries of the grid are 245 x 200 radii in length to width, the core radius of the vortex being 1.0. The boundaries of the equally spaced grid region, the overall boundaries and the vortex path are shown in Fig. 14. In contrast to grid types "A" and "B", the boundaries of the type "C" grid are considerably farther from the vortex path than the type "A" or "B" grid; calculations performed on this grid are intended to demonstrate the effect of the boundary extents.

Initial Conditions, Calculation Procedures

Initializations used for all the calculations are the same. With respect to a coordinate system fixed at the vortex center, the cylindrical velocity component of the vortex used is given by:

$$V_{\theta} = \frac{\Gamma}{2\pi r} \cdot \frac{r^2}{r^2 + a^2} \quad (11)$$

The pressure and density for the vortex flow are obtained as below:

The r momentum equation gives

$$\frac{dp}{dr} = \frac{\rho v_{\theta}^2}{r} \quad (12)$$

The energy equation yields

$$p = \left[\frac{p_{\infty}}{\rho_{\infty}} - \frac{\gamma-1}{\gamma} \cdot \frac{v_{\theta}^2}{2} \right] \rho \quad (13)$$

From Eq. (12) and Eq. (13)

$$\frac{dp}{dr} - \frac{v_{\theta}^2}{\rho} \frac{1}{\left[\frac{p_{\infty}}{\rho_{\infty}} - \frac{\gamma-1}{\gamma} \frac{v_{\theta}^2}{2} \right]} p = 0 \quad (14)$$

Eq. (14) is a first order ordinary differential equation. From Eqs. (11) and (14), the analytical solution of p is

$$p = p_{\infty} \exp(f) \quad (15)$$

where f is

$$f = \frac{2D}{\sqrt{4a^2 - B^2}} \left[\tan^{-1} \left(\frac{2r^2 + B}{\sqrt{4a^2 - B^2}} \right) - \frac{\pi}{2} \right] \quad (16)$$

where

$$D = \frac{1}{2} \left[\frac{\Gamma}{2\pi} \right]^2 \cdot \frac{\rho_{\infty} U_{\infty}^2}{p_{\infty}} \quad (17)$$

and

$$B = 2a - \frac{\gamma-1}{\gamma} D \quad (18)$$

The temperature is then given by the equation of state. It is noted here that the exact solution of the Lamb-type vortex satisfies the Euler equations. Options

were added to the code to solve the Euler equations rather than the Navier-Stokes equations.

Having an analytical solution for v_θ , p , ρ and T , the initial flow field is established by adding a uniform flow to the above exact solution. Pressure, vorticity and velocity contours for the initial conditions are given in Figs. 15-19. The flow is then allowed to develop in physical time. Since the vortex is translated with the freestream velocity, u_∞ , the location of the vortex is known at all times and the boundary condition is accordingly updated to the exact solution at each time step. Non-exact boundary conditions were also utilized in some of the calculations to assess the appropriate choice of boundary conditions for BVI problems. In these runs, the total temperature/total pressure/flow direction inflow boundary conditions and static pressure outflow boundary conditions were utilized. Most cases were run with three inner iterations per time step. However, tests were also conducted with two iterations per time step which, for the same conditions, gave identical results as those having three iterations. The number of iterations at each time step and the value for the physical time step were chosen based on the analysis performed to establish criteria for choosing these values. The criteria is described in later sections. The vortex was allowed to travel 45 radii downstream and the variation of the vortex core pressure was registered during the travel. At the end of vortex travel, plot files were written to produce contour plots.

Central Difference Scheme, First-Order in Time

Case #1

A calculation was performed to determine the flow characteristics associated with a Lamb-type vortex convecting in a freestream, using the SRA first-order-in-time, central difference scheme without any inner iteration at each time step. The purpose of these free vortex calculations is to assess the vortex preservation capability of the code when applied to blade-vortex interaction problems. A type "B" grid was used for this case. As described before, the exact solution was used to set up the initial condition and the subsequent unsteady boundary conditions. Figure 20 shows the variation of the vortex core pressure with the travelled distance of the vortex. From this result it is evident that the first-order-time-accurate scheme is very dissipative; an improvement is needed

for vortex preservation. This is achieved via the second-order unsteady iterative implicit scheme described in the next section. However, the results of the Case 1 calculation are qualitatively consistent with those obtained by Rai using the first-order temporal accuracy Beam and Warming procedure, although the present results show somewhat less dissipation. It is interesting to note that although the vortex has lost a significant amount of its strength, the vortex structure is very well preserved after 45 radii of travel. This is evident from the contour plots of Figs. 21-24, which are taken at the final point of the vortex travel; i.e. after 45 core radii of travel.

Second-Order in Time and Iteratively Implicit Scheme

This procedure utilizes second-order accurate time-differencing, together with inner iterations at each physical time step. The iteration at each time-step decreases numerical errors resulting from ADI splitting, time linearization and implementation of the intermediate boundary conditions. A series of calculations were performed to determine the most appropriate choices for the parameters controlling the inner iteration pseudo-time step, the physical time step and the number of inner iterations. All the calculations were performed on an equally spaced grid distribution. The problem chosen for these tests was the two-dimensional vortex in a uniform flow. This is a very relevant case for the current overall effort and results obtained for this case are expected to have strong relevance for the blade vortex interaction problem. The effects of these new parameters on the solution behavior have been studied and are described in the following.

(A) Pseudo Time-Step Parameter, DTAU

The effect of this parameter upon the convergence behavior is shown in Fig. 25. In this figure, the maximum residual of the streamwise momentum equation is chosen to assess the degree of iteration convergence. The residual of each equation is obtained by summing all the terms in the equation with the exception of the pseudo time-derivative term; i.e., the $\partial(\)/\partial\tau$ term. Obviously, when the residual is zero, a converged solution including unsteady effects is attained. Since the rate of convergence depends upon the magnitude of the iteration-step, termed here as the pseudo time-step DTAU, it is necessary to study this dependency

so as to develop an efficient running, time accurate code for application to complex two-dimensional or three-dimensional flow cases.

Figure 25 shows the dependence of convergence rate for the iteration at each time-step upon the pseudo time parameter DTAU. The calculations were initiated from an analytic solution and the results of Fig. 25 pertain to the first time-step. As can be seen, once a value of $DTAU = 2.0$ is reached, further increase does not significantly improve the rate of convergence.

(B) Physical Time-Step DT

After the determination of an appropriate iteration pseudo time-step DTAU, a physical time-step needs to be chosen to minimize the temporal error. The preservation of the vortex core pressure against different values of physical time-step (or in terms of CFL number) was chosen to determine the time accuracy associated with the size of the time-step. It is noted here that a time accurate solution should preserve the magnitude of the vortex core pressure as it is convected toward downstream. Obviously, numerical error will lead to some dissipative effects; however, it is expected that these effects can be made small. A series of calculations using different values of CFL were performed to determine this relationship. The calculations were run for the same total physical time interval. These runs were made with the three time-level procedure. Figure 26 demonstrates this relationship and can be used to give guidance in choosing an appropriate value for the time-step for a given grid geometry.

(C) Number of Pseudo Time Iterations

For a specified pseudo time-step and a specified value for physical time-step, it is necessary to determine the number of iterations required at each physical time-step to achieve the desired degree of convergence. This relationship is shown in Fig. 27. Convergence is defined here as a state at which the per cent change of each and every dependent variable does not vary, at least for six significant digits, and the maximum residual of each and every equation reduces by at least four orders of magnitude during the iteration. It is noted that larger values of DT, the time step, not only require more iterations to achieve convergence (Fig. 27), they also introduce larger time truncation error (Fig. 26), as is expected. Using the iteratively implicit scheme, various calculations were

performed to assess the vortex preservation capabilities of the newly improved code and to study the effects of grid spacing, artificial dissipation, initial vortex strength and the boundary condition.

Spatial Spacing - Two calculations were performed on grids with different spacing to study the effects of grid spacing on the vortex preservation. A calculation was also performed to investigate the effect of the physical time step.

Case #2

The type "A" grid was used for this calculation. Variation of vortex core pressure versus number of core radii travelled is shown in Fig. 28. It can be seen that the numerical solution is oscillating, particularly toward the later parts of the vortex travel. Contour plots of pressure after 45 radii of vortex travel are given in Fig. 29, which is a picture of a badly deformed vortex. As mentioned before, spacing used for the grid is $\Delta x = \Delta y = 1/4$.

Case #3

A type "B" grid was used for this calculation. The type "B" grid is identical to the type "A" grid except its spacing is $\Delta x = \Delta y = 1/8$. All the other conditions of the calculation were identical to Case #2. The variation of vortex core pressure with number of core radii is shown in Fig. 28, which indicates a very stable and accurate solution. It should be noted that there is almost no perceptible rise in core pressure after 45 radii of travel in this case. Contour plots of pressure, vorticity magnitude, streamwise velocity and transverse velocity for this case after 45 radii of travel are shown in Figs. 30-34. In contrast to the previous case, $\Delta x = \Delta y = 1/4$, this case shows no significant distortion of the vortex during this travel.

Case #4

Conditions for this case are identical to Case 3 but physical time-step Δt was doubled, i.e., it was increased from $\Delta t = 0.02$ to $\Delta t = 0.04$. This will correspond to increasing CFL from $CFL = 0.16$ to $CFL = 0.32$. The calculation was performed as an additional confirmation of the results presented in Fig. 26, which

demonstrates preservation of the vortex core pressure for different values of CFL. Figure 26 indicates that for CFL = 0.32 the vortex core pressure is still well preserved. A comparison of the variation of the vortex core pressure with number of core radii travelled for Case 3 and Case 4 is given in Fig. 35. Contour plots of pressure, etc. for Case 4 were nearly identical to those of Case 3.

Boundary Conditions: Calculations were performed to investigate the effect of the boundary conditions and the influence of the extents (i.e. the physical distance between the boundary and the vortex) of the boundaries on the vortex behavior. In most cases function boundary conditions were applied, i.e. the exact solution corresponding to the vortex moving in a freestream was imposed on the boundaries. This is possible since the vortex is translated with the freestream velocity, u_∞ , therefore location of the vortex is known at all times and the boundary condition is accordingly applied and updated to the exact solution at each time step.

The function boundary condition discussed in the preceding section could only be applied to free vortex calculations. These boundary conditions cannot be applied to the flow calculations involving a blade. "Non-function" boundary conditions were used in some of the free vortex calculations as an attempt to find appropriate boundary conditions for the flow situations containing vortex and a blade. The "non-function" boundary conditions used for free vortex calculations are such that the total pressure, total enthalpy and flow angle are specified, and second derivative of pressure set to zero. It should be noted that these are time dependent unsteady boundary conditions and their values are changed and updated at each time step. Total pressure is obtained from

$$P_0 = P(T_0/T)^{\gamma/(\gamma-1)} \quad (19)$$

where

P_0 = total pressure

P = static pressure

T_0 = total temperature

and H_0 , the total enthalpy, is obtained from

$$H_0 = h + \frac{1}{2} [u^2 + v^2] \quad (20)$$

where

$$h = C_p T \quad (21)$$

The specifications of the above boundary conditions require the values of pressure p , density ρ , streamwise velocity u and transverse velocity v . These values are supplied from the exact solution. It should be pointed out here that the specifications of total enthalpy, total pressure and flow angle amount to requiring the dependent variables (i.e., u , v , ρ and T) to satisfy a system of algebraic equations; this is different from directly imposing functional values of these variables, as in the case of function boundary condition.

The boundary conditions used on the downstream boundary are such that the time-dependent static pressure is specified, the second derivative of streamwise velocity u , transverse velocity v and the total enthalpy H_0 set to zero. Again downstream static pressure is supplied from the exact solution. The "non-function" boundary conditions used on the upper and lower boundaries of the rectangular grid are identical to those applied on the downstream boundary.

Case #5

This calculation is identical to Case 2 except the type "C" grid is used instead of the type "A" grid. The boundaries of the type "C" grid are much further away from the vortex path than those of the type "A" grid (see Figs. 12a and 14). The results were identical to those of Case 2, indicating that when function boundary conditions are used, the physical locations of the boundaries from the vortex have little bearing on the calculated solutions.

Case #6

All the conditions of this calculation were identical to Case 3 with the exception that the alternative boundary conditions were used. Variations of vortex core pressure versus number of core radii is almost identical to the Case 3 calculation (Fig. 36). Contours of pressure, vorticity magnitude, streamwise velocity and transverse velocity for Case 6 are shown in Figs. 37-40, respectively. Pressure contours of this case (Fig. 37) are identical to those of Case 3. However, an examination of the vorticity magnitude contours (Fig. 38) and

velocity component contours (Figs. 39-40) reveals the influence of the boundary condition on the unsteady vortex flow behavior. Compare these figures with those of Case 3 calculations (i.e., Figs. 31-34) where the exact function boundary conditions were used. It is clear that use of the alternate boundary conditions do distort the vorticity and velocity field in those regions where the field is relatively weak. For example, as shown in Fig. 39, the vorticity distortion occurs primarily in the region where $\omega/\omega_{\max} < 0.15$. The region where the major vortex strength occurs stays relatively undistorted. The influence of the boundary conditions on the vortex flow behavior can be definitely minimized by extending the boundaries further away from the vortex center, as they would be with the stretched grids contemplated for the BVI study. It should be noted that the upper and lower boundaries of the domain for Case 6 were only 3.75 radii away from the vortex center during the entire calculation, where the vortex core radius is 1.0.

Initial Vortex Strength

Two cases were conducted to assess the effect of the initial vortex strength upon the decay rate.

Cases 7-8:

The type "C" grid was used for these calculations. The initial core pressure of the vortex was 0.95. In all the previous cases the initial core pressure was 0.84. In Case 7 calculations, a central difference scheme with first-order accuracy in time was used, whereas a second-order accurate in time and iteratively implicit scheme was used for Case 8 calculations. The variation of the vortex core pressure with number of radii travelled by vortex for Cases 7 and 8 is shown in Fig. 41 and for stronger vortex, having a core pressure of 0.84, in Fig. 42. It is clear from these figures that the weaker vortex loses less of its initial strength, i.e., the weaker vortex numerically preserves itself better. This is consistent with the fact that the degree of preservation depends upon the truncation error associated with difference schemes, and these errors are proportional to the flow gradients, which have larger values for stronger vortex. Pressure contours for Cases 7 and 8 after 45 radii of vortex travel are shown in Figs. 43-44, respectively.

Artificial Dissipation - Since all the calculations are at high Reynolds numbers, it is generally necessary to add "artificial dissipation" terms to suppress central difference spatial oscillations. Such "artificial dissipation" could be added via the spatial differencing formulation (e.g., one-sided difference approximations for first derivatives) or by explicitly adding an additional dissipative term. In the numerical scheme used in this study, the latter approach was adopted. When an additional term is explicitly added, the physical approximation being made is usually clearer than when dissipative mechanisms are contained within numerical truncation errors. Further, explicit addition of an artificial dissipation term allows greater control over the amount of non-physical dissipation being added. Obviously, the most desirable technique would add only enough dissipation to suppress oscillations without deteriorating solution accuracy. Four cases were run to assess the effect of the "artificial dissipation" on the unsteady vortex flow. In all cases the item AVISC is equal to σ_{xi} (See Eq. 6) which is approximately an inverse for all Reynolds numbers.

Cases 9, 10, 11:

All the conditions for these cases were identical to Case 3 with the exception of the amount of "artificial dissipation" added. The parameter "AVISC" is a measure of the amount of artificial dissipation added. The larger the AVISC value, the larger the added artificial dissipation. The values used in Cases 9-11 are 0.0, 0.005 and 0.05. The value used in the Case 3 calculation was 0.001. Variation of the vortex core pressure versus number of core radii travelled by the vortex for different values of the "artificial dissipation" calculations is given in Fig. 45. It is clear from these curves that the higher the value of the "artificial dissipation" the more dissipative the calculation. As discussed before, there should be only enough dissipation to suppress oscillations without deteriorating solution accuracy. It should be noted that in the present calculation the solution remains stable without any added artificial dissipation throughout this calculation. Contours of pressure and vorticity magnitudes after 45 radii of travel for calculations each having a different value of "artificial dissipation" are given in Figs. 31-32 (AVISC = 0.001) and Figs 46-51. These contour plots indicate that the vortex shape is very well preserved after 45 radii of travel, despite the fact that for higher values of "artificial dissipation" the vortex has lost more of its strength.

Solving Navier-Stokes Equations (Case 12):

In all the cases discussed before, since a Lamb-type vortex was used, the Euler equations were solved. A calculation with an identical condition to Case 3 was performed, except instead of Euler equations, Navier-Stokes equations were solved. The results were identical to Case 3. This is expected since, in free vortex calculations, in the absence of walls the contributions of the viscous terms are very small.

Summary

The original form of the SRA Navier-Stokes code which was used for this study was a central difference scheme, first-order accurate in time. It was shown to be very dissipative. The code was further developed to be second-order accurate in time and to do multiple iterations at each time step. These improvements proved to increase the time accuracy of the code significantly. Free vortex calculations demonstrating this aspect of the improvements were presented. Fig. 52 demonstrates vortex preservation capabilities of the original SRA central difference scheme code and the improved second-order accurate in time and iteratively implicit scheme code. Results of Rai's fifth-order-accurate upwind-biased scheme are also presented in this figure for comparison. Numerous test cases were performed to assess the effects of grid size, initial vortex strength, boundary conditions and artificial dissipation on the unsteady free vortex flow calculations. The calculation conditions and the results are summarized in Table 1. It can be noted from Fig. 52 that the inclusion of the second order accurate scheme, together with the use of iteratively implicit techniques greatly increase the time accuracy of the solution and the numerical simulation and preserve the vortex strength and structure for the duration needed for the blade vortex interaction study.

	1	2	3	4	5	6	7	OBSERVATIONS
	NX · NY	AVISC	Pcore	KITER	$\Delta X = \Delta Y$	Δt	BC USED	
CASE 1	421 · 61	0.001	0.84	1	1/8	0.02	FUNCTION	STABLE SOLUTION, FAST DISSIPATION, VORTEX STRUCTURE PRESERVED AFTER 45 RADII OF TRAVEL
CASE 2	211 · 31	0.001	0.84	3	1/4	0.04	FUNCTION	SOLUTION OSCILLATES, LESS DISSIPATIVE THAN CASE 1, VORTEX SEVERELY DEFORMED AFTER 48 RADII OF TRAVEL
CASE 3	421 · 61	0.001	0.84	3	1/8	0.02	FUNCTION	VORTEX STRENGTH AND STRUCTURE PRESERVED
CASE 4	421 · 61	0.001	0.84	3	1/8	0.04	FUNCTION	VORTEX STRENGTH AND STRUCTURE PRESERVED, ALMOST IDENTICAL TO CASE 3
CASE 5	333 · 153	0.001	0.84	3	1/4	0.04	FUNCTION	SOLUTION OSCILLATES, VORTEX STRUCTURE SEVERELY DEFORMED, IDENTICAL TO CASE 2
CASE 6	421 · 61	0.001	0.84	3	1/8	0.02	NON-FUNCTION	STABLE SOLUTION, VORTEX STRENGTH AND STRUCTURE WELL PRESERVED, SOME EFFECTS OF BC NOTICED ON CONTOUR PLOTS OF VORTICITY, U AND V
CASE 7	333 · 153	0.001	0.95	1	1/4	0.04	FUNCTION	STABLE SOLUTION, VORTEX LOSES SOME OF ITS STRENGTH, VORTEX SHAPE, OVAL
CASE 8	333 · 153	0.001	0.95	2	1/4	0.04	FUNCTION	STABLE SOLUTION, VORTEX STRUCTURE SOMEHOW PRESERVED BUT IT IS SHEDDING AFTER 45 RADII
CASE 9	421 · 61	0.000	0.84	3	1/8	0.02	FUNCTION	STABLE SOLUTION, VORTEX STRENGTH AND SHAPE PRESERVED, EXTREMELY WELL
CASE 10	421 · 61	0.005	0.84	3	1/8	0.02	FUNCTION	STABLE SOLUTION, VORTEX STRENGTH AND SHAPE PRESERVED
CASE 11	421 · 61	0.05	0.84	3	1/8	0.02	FUNCTION	STABLE SOLUTION, FAST DISSIPATION, VORTEX STRUCTURE PRESERVED
CASE 12	421 · 61	0.001	0.84	3	1/8	0.02	FUNCTION	VORTEX STRENGTH AND STRUCTURE PRESERVED VERY WELL, ALMOST IDENTICAL TO CASE 4, NAVIER-STOKES EQUATIONS SOLVED

COLUMN 1	NUMBER OF GRID POINTS
COLUMN 2	ARTIFICIAL DISSIPATION
COLUMN 3	VORTEX CORE PRESSURE AT INITIALIZATION
COLUMN 4	NUMBER OF ITERATIONS PER TIME STEP
COLUMN 5	GRID SPACING
COLUMN 6	PHYSICAL TIME STEP
COLUMN 7	TYPE OF BOUNDARY CONDITION USED

Table 1. Summary of the Vortex Preservation Test Calculations.

IV. TWO-DIMENSIONAL BLADE VORTEX INTERACTION

The second case considered is that of a two-dimensional blade vortex interaction. The isolated vortex study showed the proper choice of time step, iteration step, iteration number, etc. required to preserve the vortex strength and radius. However, this study does not address resolution and artificial dissipation issues for the BVI problem. These issues were addressed in a two-dimensional BVI simulation.

Grid, Boundary Conditions and Artificial Dissipation

Fig. 53 illustrates the grid distribution used for the BVI simulation. The total number of grid points is 144 x 118. The inflow boundary is located at 7 chords from the blade leading edge while the outflow boundary is located at 5 chords from the blade trailing edge. Based upon the isolated vortex study the distance between the top boundary and the chord line of the NACA0012 airfoil was set at 5 chord lengths. The geometric configuration is symmetric about the chord line. Along the inflow boundary, the total pressure, the total temperature and the inflow angle are specified. The pressure is obtained by extrapolation. Along the outflow, top and bottom boundaries, the static pressure is specified, the velocity and the total temperature are obtained by extrapolation. On the blade surface, non-slip conditions are imposed. The density is obtained by solving the continuity equation and the surface temperature is specified as the constant, free stream total temperature. When the vortex is introduced into the transonic flow field at a point upstream of the blade, the boundary values must take into account the existence of this vortex, e.g., the inflow angle will not be zero and generally is not uniform along the inflow boundary. In addition, as the vortex is convecting towards the blade, these boundary values are changing with time. For the present simulation, they are taken from the composite "vortex in a free-stream" solution.

A spatially varying artificial dissipation was used in the BVI calculation presented here. Upstream of the blade AVISC was set to 0.005. Based upon the vortex preservation studies this should keep the vortex decay within allowable levels prior to the interaction. However, it should be recognized that the vortex preservation studies were done on a uniform grid whereas the present calculation is done on a non-uniform grid. Downstream of the airfoil leading edge station the

value of AVISC was set at 0.05 except in the immediate vicinity of the leading and trailing edge locations where it was set to 0.5. The relatively high value of 0.5 was required due to the highly stretched, highly skewed grids and the marginal resolution of the flow in these regions. The regions of different AVISC values were blended at boundaries to avoid discontinuous changes in the artificial dissipation.

Although this procedure for specifying numerical dissipation does put a higher than desired level in the immediate vicinity of the leading and trailing edge regions, it is necessary to suppress oscillations in these regions. This same procedure has been used in a variety of airfoil and cascade studies and has given good agreement with experimental data for a wide variety of cases, e.g. Shamroth (1985), Weinberg et al. (1986) and Shamroth et al. (1988).

Flow Parameters

The reference length is the chord length of the blade and the reference flow conditions are the free stream condition with $M_\infty = 0.8$ and $Re = 1.0 \times 10^6$. The background flow is a steady transonic flow with shock waves standing in the middle of the blade. Furthermore, the flow is symmetric about the chord line; hence, the lift coefficient (C_L) is zero. The surface pressure distribution of this background flow is shown in Fig. 54.

The dimensionless strength and core radius of the vortex are -1.6 and 0.2 , respectively, where the minus sign indicates that the vortex has a clockwise sense. The initial location of the vortex center is at a point 5 chords upstream of the airfoil leading edge ($x_v = -5.0$) and 0.26 chords below ($y_v = -0.26$). The calculation is carried out from $t = 0$ to $t = 8$ with constant time step $\Delta t = 0.005$. It is noted here that the vortex core arrives at the blade leading edge when $t = 4.95$, which indicates an average core velocity of $0.99 v_\infty$.

Results and Discussion

The time histories of the aerodynamic coefficients during the blade-vortex-shock interactions are described in Figs. 55-57. It should be noted that the small amplitude variations occurring for t up to 1.0 are due to the impulsive introduction of the vortex into the background flow, and these small amplitude oscillations have been damped out long before the onset of significant blade

vortex interactions. Furthermore, these coefficients are evaluated in terms of static pressure; they do not include the contribution of viscous stresses. The lift coefficient (C_L) and the quarter-chord pitching moment coefficient (C_M) are shown in Figs. 55 and 56, respectively. It should be noted that the background flow is a nonlifting case and that any lift generated during the interaction is induced by the vortex. Since the vortex flow is revolving in the clockwise direction, when the vortex is approaching the blade, it induces nonuniform and unsteady velocities that result in negative angles of attack at the blade. This influence changes to increasing angles of attack after the vortex has reached the blade. Severe load variations occur during the time period from $t = 4.0$ to $t = 6.0$; i.e., when the vortex is within one chord length of the blade leading edge. During this period of time, C_L and C_M change their signs, while C_D undergoes rapid variation exhibiting two distinct temporal maxima (Fig. 57). The coefficients have not yet returned to their undisturbed value at $t = 8.0$ indicating that the interaction is still affecting the flow. This is consistent with the results of Srinivasan et al. (1986).

The interaction between the vortex and the blade with a shock are further elucidated in terms of the instantaneous static pressure distribution at several selected time stations. Fig. 58(a) gives the pressure contours over the entire computational domain at $t = 0$, while Fig. 58(b) gives the distribution of static pressure coefficient on the blade surface at $t = 0$. This is the starting flow field. As the vortex convects towards the blade, the upper surface shock moves in the upstream direction, its strength is decreasing and the extent of the associated supersonic pocket also is reducing. On the other hand, the lower surface shock moves in the downstream direction with increased strength. In addition to the motion of the shock waves, pressure difference between the upper and lower surfaces start to build up. These generic features are illustrated in Fig. 59(a) and (b), which are obtained at $t = 2.0$. The outer pressure contours on the aft region of the blade shows some "wiggles"; however, this is in a region of nearly uniform pressure and, therefore, the presence of these "wiggles" is not significant, but represents small changes in a nearly uniform field. The flow field at $t = 4.0$, i.e., when the vortex core is about one chord length upstream of the blade, is shown in Fig. 60(a) and (b). The upper surface supersonic pocket practically has disappeared. The lower surface shock wave becomes stronger and is located in a further downstream position; at the shock's root the flow shows signs of separation. In addition, a significant transverse pressure gradient exists in

the leading edge region. At $t = 4.5$, this leading edge transverse pressure gradient becomes the dominant feature of the interaction. In addition, the lower surface shock stops moving towards the trailing edge, in spite of the fact that its strength is still increasing. These features are depicted in Figs. 61(a) and (b). When $t = 5.0$, the vortex core 'hits' the blade, the averaged Mach number inside the lower surface supersonic pocket increases to approximately 2. Most of the disturbances on this surface will propagate downstream until reaching the shock. Part of the disturbance is able to leave the supersonic pocket near the outer region of the shock. However, the remainder seems to build up at the root of the shock, as indicated by Fig. 62(a). At the same time, high pressure disturbance starts to be released from the upper surface of the leading edge, as indicated by Fig. 62(a). The state of the flow at this moment is very volatile, within a short period of time, this process of disturbance build-up has collapsed, as illustrated by Fig. 63 at $t = 5.5$. The shock is no longer an approximately normal shock but has an oblique leg which intersects the blade wall upstream of the intersection location at $t = 5.0$ (Fig. 62(a)). The emission of a high pressure pulse from the upper surface of the leading edge is evident from Fig. 63(a); this high pressure pulse then propagates upstream in a domain including the frontal region of the entire leading edge (see Fig. 64(a)). Between this frontal high pressure region and the lower surface shock wave, a low pressure pulse is propagating towards the lower outer boundary. Figs. 62(b), 63(b) and 64(b) illustrate the collapse of the disturbance building up process and the subsequent relaxation of the strength and the location of the shock wave on the lower surface. The general features of the flow at $t = 6.0$ are: the existence of a supersonic pocket on the lower surface, significant flow separation originating at the root of the shock, the appearance of vortex remnants near the blade trailing edge, and the development of supersonic flow on the upper surface. Subsequently, the lower surface supersonic pocket continually reduces its extent and eventually disappears by $t = 8.0$. The lower surface shock moves towards the leading edge with continually diminished strength and then vanishes. At $t = 8.0$, the vortex remnants have been further convected downstream. The flow on the lower surface does not exhibit any appreciable separation and is entirely transonic. Furthermore, about 70% of the upper surface is covered by a supersonic pocket, with compression waves appearing near the trailing edge of the blade. It is clear that the interaction is a strong one and the vortex path particularly, when the vortex is near the blade is influenced by the blade and the interaction. The

local velocity changes significantly during the interaction. This makes techniques based upon assumed vortex position or shape unlikely to provide an accurate simulation.

The radiation of pressure pulses from the leading edge region as a result of the blade-vortex interaction is further investigated in terms of the scaled pressure disturbance. In the two-dimensional linear far field, the amplitude of propagating waves should be proportional to $1/r^{1/2}$, where r is the distance to the origin of the disturbance. The scaled pressure disturbance is obtained by subtracting the steady-state pressure background value from the instantaneous BVI solution and then dividing the difference by the far upstream value of pressure. The result is then multiplied by $r^{1/2}$, where r is the distance to the leading edge. Fig. 66 defines the points at which the time histories of the scaled disturbances are recorded and presented in Figs. 67 (a), (b) and (c). These points are taken as grid points leading to some variation in θ . The first peak, I, is due to the interaction between the incoming vortex and the leading edge, when the vortex center is within one chord length of the blade. The valley, II, is associated with the passage of the vortex core through these points, and the peak, III, originates from the upper surface of the leading edge, after the vortex case 'hits' the blade, as described before. The results of Fig. 67 shows the simulation to give $1/r^{1/2}$ scaling only approximately. Points #1 and #2 satisfy the scaling reasonably well. The results for point #3 show the same shape but the level of the maximum and minimum distributions are significantly more negative than points 1 and 2.

The lift coefficient time history of the present effort showed the same qualitative features as that obtained by Srinivasan, McCroskey and Baeder (1986) and Sanker and Tang (1985) and the moment coefficient showed qualitative similarity with that of Srinivasan et al. (1986). Surface pressure distributions also showed qualitative agreement with the results of Srinivasan et al. (1986) and Rai (1987) as the shock strength on the upper surface decreased and that on the lower surface increased during the interaction. Finally, the details of the acoustic wave leaving the blade during the interaction show considerable similarity with those of Rai (1987).

V. THREE-DIMENSIONAL BLADE VORTEX INTERACTION

The final case considered is that of a three-dimensional blade vortex interaction. The two-dimensional isolated vortex study clearly indicates the need for appropriate grid resolution to avoid unacceptable levels of numerical dissipation in the vortex. This need to maintain high grid resolution even in the three-dimensional case influenced the choice of case to be studied. Although numerical simulation of a blade with a tip is the eventual goal, inclusion of a tip would require resolution of an entire new set of length scales associated with the tip geometry and the local tip flow; this would increase the number of grid points required beyond what is practical for this effort. Therefore a simpler problem which contains the basic three-dimensional flow field physics was chosen for the present investigation.

A sketch of the case to be considered is shown in Fig. 68, which shows a periodic vortex initially consisting of straight line segments in a plane parallel to the airfoil midline. Since there is a natural symmetry, the computational domain is reduced to the region between spaced spanwise symmetry planes and, further, since no tip is included an equally spaced spanwise grid can be used. This allows use of a computational grid consisting of 21 equally spanwise planes with each plane containing 144×118 points for a total of 356,832 grid points in the computational domain. The specific configuration chosen had an angle ϕ of 20 degrees, a distance d of 2.0 chords and points a and b were 5.0 and 4.27 chords upstream of the blade, respectively.

The equations solved are the three-dimensional Navier-Stokes equations as given in Section II. These solve the equations in an inertial frame. Extension to a rotating frame can be made either by having the wing move in this inertial frame as was done in the dynamic stall study of Shamroth (1985) or by adding centrifugal and Coriolis terms. This latter approach was used at SRA in a three-dimensional rotor-stator interaction study using the same computer code as used here by Gibeling et al. (1990). It is this latter approach which would be recommended if the rotational effects were to be included. Although this additional capability was not available at the initiation of the present study, it is now available and adds little complexity to the numerical solution. Obviously boundary conditions must be written in the rotating frame but this should be straightforward.

Having specified the initial vortex geometry, it is necessary to create compatible velocity, density and pressure fields. Considering a vortex line segment, as shown in Fig. 69, the induced velocity at a point P due to this line segment is given by:

$$\vec{\Delta V}' = \left[\frac{\Gamma}{4\eta} \frac{1}{s^2 r_m^2} \left(r_1 + r_2 \right) \left(1 - \frac{\vec{r}_1 \cdot \vec{r}_2}{r_1 r_2} \right) \right] \left(\vec{r}_1 \times \vec{r}_2 \right) \quad (22)$$

where

- \vec{r}_1 & \vec{r}_2 : "relative" position vector of P defined from the end points to P.
- r_m : minimum distance of P from the vortex line.
- s : distance between the end points "1" and "2" of the line element.
- Γ : a constant and its sense is consistent with a vorticity vector directed from "1" to "2".

The influence of the core is accounted for by multiplying $\vec{\Delta V}$ by a factor

$$f_{\text{core}} = r_m^2 / \left(r_m^2 + r_c^2 \right)$$

where r_c is the core radius and it is the location at which the tangential velocity has its maximum. Induced velocity due to the overall geometry consisting of many line segments is given by:

$$\vec{V}' = \sum \vec{\Delta V}' \quad (23)$$

The number of filaments is chosen such that the induced velocity field satisfies the symmetric condition for the flow in the computational domain. Experience indicates that, by placing approximately 30 or more vortices on each side of the representative vortex, an excellent approximation to the spanwise periodicity required by an infinite number of vortices can be achieved. Fig. 70 shows the overall geometry and the relative position of the vortex and the blade. It should be noted here that the induced flow field associated with the filament present in the computational domain contains not only the dominant contribution of this

vortex but also the contributions of all the other vortices in the same array. The vortex model constructed according to Eq. (22) and illustrated in Fig. 70 is to be used only in setting the initial flow condition of the simulation. The subsequent flow development is governed by the solution of the Navier-Stokes equations.

The composite flow will consist of the background flow and the variation from that background flow due to the initiation of the vortex filament. The presence of the blade wall is incorporated into this initial flow specification by multiplying the induced velocity field \vec{v}' by $\tanh(\kappa d/\delta)$ where:

d is the distance to the wall

κ is the von Karman constant

and

δ is the boundary layer thickness

thus

$$\vec{u}' = \vec{u}' \tanh(\kappa d/\delta) \quad (24)$$

and \vec{u}' satisfies the no-slip condition.

The composite velocity field is:

$$u = u_b + u' \quad (25)$$

$$v = v_b + v' \quad (26)$$

$$w = w_b + w' \quad (27)$$

where u_b , v_b and w_b are streamwise velocity, spanwise velocity and transverse velocity of the background flow; i.e., the flow without a vortex.

The initial pressure field of the composite flow must be evaluated in such a way that it is consistent with the prescribed composite velocity field. Two approaches were attempted. Under the first approach the temperature was assumed to be that of the background flow.

$$T = T_b \quad (28)$$

The strategy was to find the density (ρ) and pressure (P) of the composite field such that they are consistent with the velocity field given by Eqs. (25) - (26)

and the temperature field given by Eq. (28). This was done by initially assuming

$$\rho = \rho_b$$

where ρ_b is the background density, and then integrating the suitable component of the momentum equation in its steady form

$$\left[\text{i.e. } \frac{\partial}{\partial t} = 0 \right]$$

to obtain the pressure field. Utilizing this pressure, temperature (T) and the equation of state, ρ can be updated. Using the updated ρ and integrating the same component of the momentum equation, a new pressure (P) is obtained. Convergence of this iteration process implies that a consistent P, ρ field is achieved. Although a convergent solution could be obtained the numerical truncation error of the integration process was excessive and an alternative numerical specification was sought.

Under this alternative the flow field was constructed on a spanwise plane by spanwise plane basis. At each spanwise plane the vortex was assumed to be a Lamb vortex and the pressure, density and temperature found via Eqs. (11) - (18). Although this does represent an approximation, it did provide an initial starting flow field from which the computation was able to proceed without any significant discontinuity.

The initial pressure field is shown in Fig. 71. A top view of the pressure contours is shown in the upper portion of the figure with the pressure contours due to the vortex being on the left hand side of the figure and that of the blade on the right hand side of the figure. The inclination of the vortex relative to the blade is evident. The lower portion of the figure shows a perspective plot with contours plotted in three spanwise planes. It should be noted for future reference that the vortex is initially closest to the blade at $LY = 21$, and furthest upstream from the blade at $LY = 1$. The initial pressure and Mach number fields through the center spanwise plane, $LY = 11$, are shown in Fig. 72 and Fig. 73. There is no spanwise pressure variation for this initial condition.

The remaining figures present either pressure contours or Mach number contours at a specific time in three spanwise planes or surface pressure distributions on the blade. When figures showing contours are vertical, the

LY = 1 plane which initially has the vortex at its furthest upstream location is at the top of the figure, LY = 11 is in the middle and LY = 21 is at the bottom. When presented horizontally, LY = 1 is on the left.

Figure 74 shows pressure contours at $t = 1.23$, $\Delta t = 1$ is the time a particle at undisturbed freestream velocity traverses a distance of one chord. At all spanwise locations the movement of the upper shock forward and the lower surface shock backwards is evident. The vortex centerline which was initially in a plane parallel to that of the blade midspan has migrated out of that plane, with the vortex core location being at progressively higher locations as the spanwise location proceeds from plane LY = 1 to plane LY = 21; i.e., the portion of the vortex for that downstream rises due to the self-induced motion as is expected (e.g. Hama and Nutant, 1963). The result is an interaction where the vortex is at angle to the blade and is no longer parallel to the blade centerline which changes vortex location relative to the blade as a function of span.

Figures 75 and 76 present pressure and Mach number contours at $t = 2.838$. At this time the upper surface shock has nearly disappeared at all spanwise locations. The height of the vortex core clearly varies with spanwise location and a strong shock remains on the lower surface with the shock appearing to be significantly stronger than that shown at $t = 0.0$, Fig. 72. In all cases the contours are quite clear and free of oscillations. A composite surface pressure plot consisting of surface pressure plots at 7 different spanwise locations is shown in Fig. 77; no significant spanwise pressure variation is observed at this time. Pressure and Mach number fields at $t = 4.139$ are presented in Figs. 78 and 79. At this time the interaction is very strong at all streamwise locations. The interaction at LY = 21 has proceeded the furthest. A composite surface pressure plot is shown in Fig. 80; at this time significant surface pressure differences are evident with the highest suction peaks occurring at the LY = 21 location. This is the spanwise location at which the vortex is closest to the blade and at which the vortex is highest. The shock location varies mildly with span; however, the shock strength is approximately constant with span. The vortex center at the LY = 21 plane has nearly reached the blade leading edge at this time. The fields at $t = 4.56$ are presented in Figs. 81 and 82. At $t = 4.56$ the three-dimensionality of the interaction is very clear from both pressure and Mach number plots. By $t = 4.56$, the shock on the lower surface at the LY = 21 plane has moved forward whereas that on the LY = 1 plane remains aft on the blade. The surface pressure distributions indicate shock bifurcation

at some spanwise locations. As in the two-dimensional case, high pressure pulses are being released from the upper surface of the leading edge at all spanwise locations at this time. The pulses are most apparent at the $LY = 21$ plane; however, they are apparent even at the $LY = 1$ plane. A composite pressure plot is shown in Fig. 83.

At time, $t = 4.7$, the interaction is very strong over the entire spanwise extent of the domain. The pressure contours are shown in Fig. 84 and the Mach number contours in Fig. 85. Based upon these figures the lower surface shock system on the $LY = 21$ plane has moved considerably forward from its most aft position and continues to sharpen in the freestream. The $LY = 1$ system is a single shock on the aft portion of the blade. Figs. 86-88 show details of the contours. These plots were created from a culled plot file hence the somewhat discontinuous appearance of the contours. Of particular interest is the vortex interaction induced shock bifurcation shown in Fig. 88. This represents the spanwise plane where the interaction has proceeded furthest. The contours at $LY = 11$ in Fig. 87 show bifurcation starting, whereas those in Fig. 86 show no significant sign of bifurcation. Pressure and Mach number fields at $t = 5.157$ are given in Figs. 89 and 90. At this location the effects of three dimensionality are significant, as can be seen by comparing Figs. 81 and 89. Figure 81 presents results at $t = 4.56$, at which time the vortex at spanwise plane $LY = 21$ has just passed the airfoil leading edge. Figure 89 presents results at $t = 5.15$, at which time the vortex at $LY = 1$ has just passed the leading edge. At $LY = 1$, $t = 5.15$, (Fig. 89) the shock shows a clear bifurcation which is not present at $LY = 21$, $t = 4.56$ (Fig. 81). This is likely to be an effect associated with the three dimensionality. Details of the lower surface pressure contours at $t = 5.157$ are presented in Figs. 91-93, where the different shock locations and strengths at the various spanwise locations are apparent. A composite surface pressure plot is given in Fig. 94 and lower surface contour plots are shown in Fig. 95.

Plots of blade lift, drag and moment coefficient as a function of time are given in Figs. 96-98. Although these are qualitatively similar to their two-dimensional counterparts, they are affected by the variation of vortex height with spanwise location. Surface pressure contours on both the upper and lower surfaces are shown in Figs. 99-107.

The general qualitative picture obtained for the three-dimensional interaction is similar to that previously obtained for the two-dimensional interaction as modified by the inclination of the vortex relative to the blade leading edge and

the migration of the vortex core line so that it does not lie on a plane parallel to the blade midplane. As the vortex approaches the blade, the core location at one spanwise boundary rises and that at the other spanwise boundary falls. At all spanwise locations the upper surface shock moves forward, its strength reduces and the associated supersonic pocket reduces. The extent of the interaction at any specified time is a definite function of the spanwise location. However, although at any spanwise location the general flow development is similar to that of the two-dimensional case; three-dimensional effects influence the flow details. The lower surface shock moves aft with increasing strength. As the vortex core moves closer to the airfoil the upper surface shock system disappears. All these interactions, as well as the ones discussed subsequently, occur first in the $LY = 21$ plane, which is the plane in which the vortex is initially closest to the blade. During the interaction the lower surface shock system reaches a maximum downstream position and then moves forward and sharpens. High pressure disturbances appear at the leading edge and propagate upstream. As the interaction continues, the shock shows a bifurcation with the appearance of an oblique leg, which produces a diffuse pressure rise at the blade surface; however, the shock remains very sharp in the outer flow removed from the blade. The pressure pulse continues to propagate in the upstream direction.

The present BVI simulation is based upon a solution of the full Navier-Stokes equations. The only previously published viscous solution to this problem to the present authors' knowledge is that of Srinivasan and McCroskey (1989) based upon the thin shear layer approximation to the Navier-Stokes equations. The Srinivasan and McCroskey effort considered unsteady interaction of a rotor with a vortex with the equations solved in an inertial frame with the rotor being represented as a moving no-slip/no through flow boundary. A prescribed vortex formulation was used. The present approach uses the full three-dimensional Navier-Stokes equations without any thin shear layer assumption and does not split the velocity field into a prescribed vortex portion and a background flow. However, the present effort considers a simpler problem, that of a vortex encountering a blade section of finite spanwise extent in an inertial frame. Therefore, no direct comparisons of the results of the two efforts can be made.

Based upon the three-dimensional simulation of the present effort certain conclusions can be made. For vortices of modest angle to the blade, the present case was 20° , the three-dimensional interaction is qualitatively similar to the two-dimensional interaction on a section by section basis. However, differences

do exist as details of the flow field at any spanwise locations for which the interaction had occurred at any earlier time. This effects the details of the shock shape, shock location, surface pressure distribution and field pressure distribution. Therefore, although qualitative conclusions can be drawn from two-dimensional simulations, a need for detail or quantitative conclusions require a three-dimensional simulation. This conclusion is in basic agreement with that of Srinivasan and McCroskey (1989).

CONCLUDING REMARKS

A Navier-Stokes analysis has been applied to the problem of two- and three-dimensional blade vortex interactions. The two-dimensional interaction studies have shown the ability of an iterative implicit procedure using three point central differences to provide a highly non-dissipative solution procedure. Results were obtained which showed details of the flow including the propagating pressure disturbances resulting from the interaction. The results showed many of the known physical features and gave good qualitative correspondence with other analyses. The three-dimensional study considered a blade vortex interaction with the vortex initially at 20° incidence to the blade. A solution was obtained showing general features of the two-dimensional interaction with modifications due to the angle between the vortex and the blade. As in the two-dimensional case, pressure disturbances were observed leaving the blade leading edge. Details of the simulated flow physics are presented in the appropriate sections of this report.

SYMBOLS

a	Vortex core radius
C_D	Drag coefficient
C_L	Lift coefficient
C_M	Moment coefficient
C_p	Specific heat
D	Damping coefficient
d	Distance from wall
DT	Time step
$D \text{ TAU}$	Pseudo time step parameter
dx_i	Artificial dissipation coefficient
f_{core}	Velocity damping factor in vortex core
h	Enthalpy
H_0	Stagnation enthalpy
l	Mixing length
LY	Spanwise plane number
p	Pressure
Q	Heat flux vector
r	Radial distance
T	Temperature
t	Time
u_i	Velocity component in i^{th} direction
u, v	Cartesian velocity component
u_b, v_b, w_b	Background flow velocity components excluding contribution of vortices
V	Velocity
V_θ	Tangential Velocity
x_i	Cartesian Coordinate
y^+	Dimensionless coordinate normal to wall
Γ	Circulation
δ	Boundary layer thickness
$\Delta x, \Delta y$	Grid spacing
Δx_i	Grid spacing in i^{th} direction
ϵ	Turbulence dissipation
κ	Von-Karman constant

μ	Viscosity
π	Stress tensor
ρ	Density
τ	Relaxation time step coordinate
Φ	Mean flow dissipation
ϕ	Dependent variable

Subscripts

b	Background value
o	Stagnation value
∞	Far upstream value

REFERENCES

- Booth, E.R. and Yu, J.C., "Two-dimensional Blade-Vortex Flow Visualization Investigation," AIAA Journal, Vol. 24, No. 9, 1986, pp. 1468-1473.
- Briley, W.R., Govindan, T.R. and McDonald, H., "Efficient Navier-Stokes Flow Predication Algorithms," SRA Report R90-900068-F, 1990.
- Briley, W.R., Buggeln, R.C. and McDonald, H.: Solution of the Three-Dimensional Navier-Stokes Equations for a Steady Laminar Horseshoe Vortex Flow, AIAA Paper No. 85-1520, 1985.
- Briley, W.R. and McDonald, H., "On the Structure and Use of Linearized Block Implicit Schemes," Journal of Comp. Physics, Vol. 34, No. 1, 1980, pp. 54-72.
- Briley, W.R. and McDonald, H.: Solution of the Multidimensional Compressible Navier-Stokes Equations by a Generalized Implicit Method, Journal of Comp. Physics, Vol. 24, pp. 372-397, August 1977.
- Caradonna, F.X., Liatenschlage, J.L., and Silva, M.J., "An Experimental Study of Rotor-Vortex Interactions," AIAA paper 88-0045, Reno, Nevada, January 1988.
- Caradonna, F.X., Laub, G.H., and Tung, C., "An Experimental Investigation of the Parallel Blade Vortex Interaction," The 10th European Rotorcraft Forum, The Hague, Holland, August 1984.
- Gibeling, H.J., Bugglen, R.C., Rosco, D.V. and Shamroth, S.J.: Application of Stator-Rotor Stage Navier-Stokes Analysis, SRA Final Report R89-900070-F, NASA Contract NAS8-37198, October 1989.
- Hama, F.R. and Nutant, J., "Detailed flow-field observations in the transition process in a thick boundary layer," Proc. 1963 Heat Transfer & Fluid Mech. Inst., pp. 77-94, Stanford, Univ. Press, 1963.
- Lee, D.J. and Smith, C.A., "Distortion of the Vortex Core During Blade/Vortex Interaction," AIAA paper 87-1243, Honolulu, Hawaii, June 1987.
- Panaras, A.G., "Numerical Modeling of the Vortex/Airfoil Interaction," AIAA Journal, Vol. 25, No. 1, 1987, pp. 5-11.
- Poling, D.R., Dadone, L. and Telionis, D.P., "Blade-Vortex Interaction," AIAA Journal, Vol. 27, No. 6, 1989, pp. 694-699.
- Pulliam, T.H., "Artificial Dissipation Models for Euler Equations," AIAA Paper 85-0438, 1985.
- Rai, M.M., "Navier-Stokes Simulations of Blade-Vortex Interaction Using High-Order Accurate Upwind Schemes," AIAA paper 87-0543, Reno, Nevada, Jan. 1987.
- Sankar, L.N. and Tang, W., "Numerical Solution of Unsteady Viscous Flow Past Rotor Sections," AIAA paper 85-0129, Reno, Nevada, Jan. 1985.

Shamroth, S.J., Choi, S.K. and Buggeln, R.C., "Comparison of the Results of a Navier-Stokes Simulation with Two-Dimensional Cascade Data," SRA Report R88-920025-F, 1988.

Shamroth, S.J., "Calculation of Steady and Unsteady Flow Fields via the Navier-Stokes Equations, NASA CR 3899, 1985.

Shamroth, S.J., McDonald, H. and Briley, W.R.: A Navier-Stokes Solution for Transonic Flow Through a Cascade, SRA Report R82-92007-F, 1982.

Shamroth, S.J. and Gibeling, H.J.: "The Prediction of Turbulent Flow about an Isolated Airfoil," AIAA Paper 79-1543, Williamsburg, VA, 1979.

Srinivasan, G.R. and McCroskey, W.J., "Unsteady Interaction of a Rotor with a Vortex," AIAA 20th Fluid Dynamics, Plasma Dynamics and Lasers Conference, Buffalo, New York, June 12-14, 1989.

Srinivasan, G.R. and McCroskey, W.J., "Numerical Simulations of Unsteady Airfoil-Vortex Interactions," Vertica, Vol. 11, No. 112, 1987, pp. 3-28.

Srinivasan, G.R., McCroskey, W.J. and Baeder, J.D, "Aerodynamics of Two-Dimensional Blade-Vortex Interaction," AIAA Journal Vol. 24, No. 10, October 1986.

Thompson, J.F., "Program EAGLE Numerical Grid Generation System User's Manual," AFATL-TR-87-15, Vol. I-III, March 1987.

Weinberg, B.C., Yang, R.-J., McDonald, H. and Shamroth, S.J.: Calculation of Two- and Three-Dimensional Transonic Cascade Flow Fields Using the Navier-Stokes Equations, Journal of Eng. for Gas Turbines and Power, Vol. 108, pp. 93-102, 1986.

Yoon, S. and Kwak, D., "Artificial Dissipation Models for Hypersonic Internal Flow," AIAA Paper 88-3277, 1988.

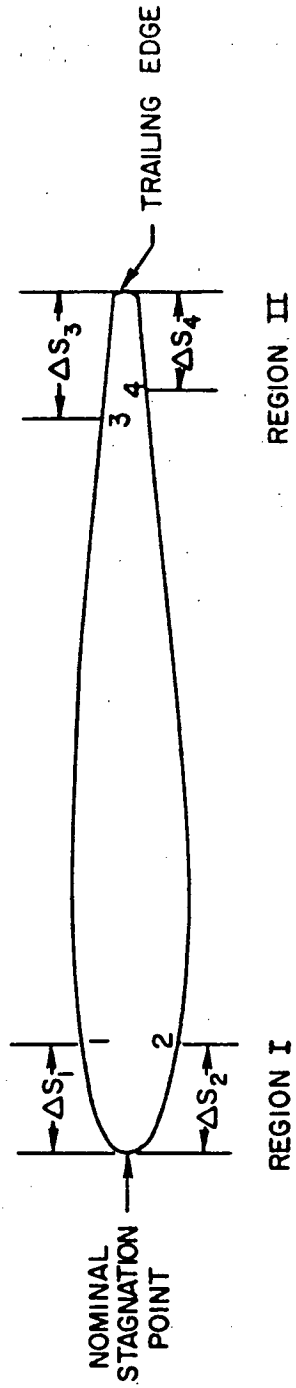


Fig. 1 Nomenclature for Leading and Trailing Edge Turbulence Length Scale Specification

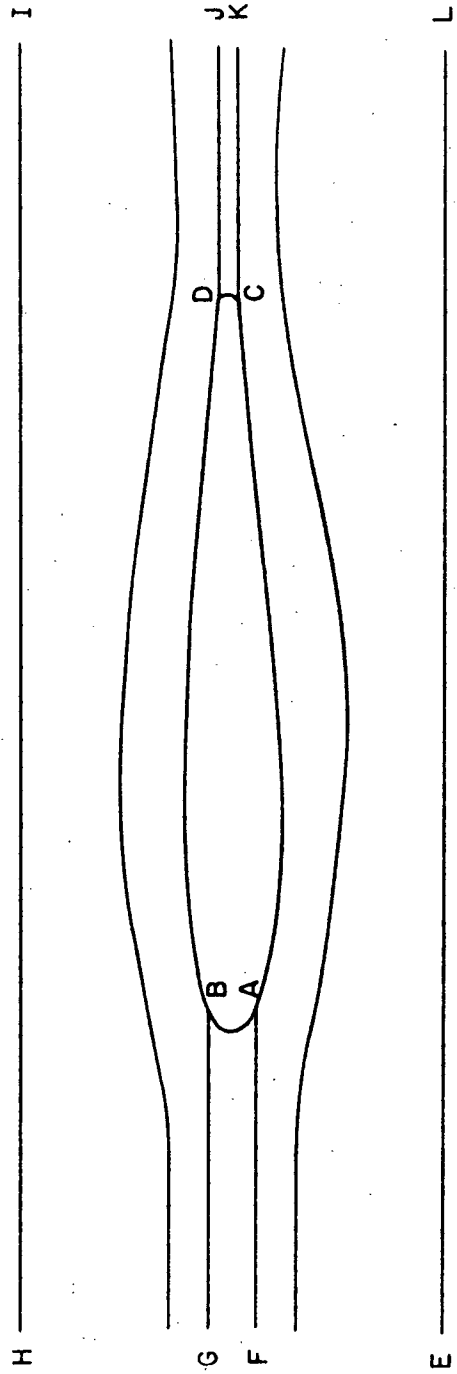


Fig. 2 Schematic of Grid

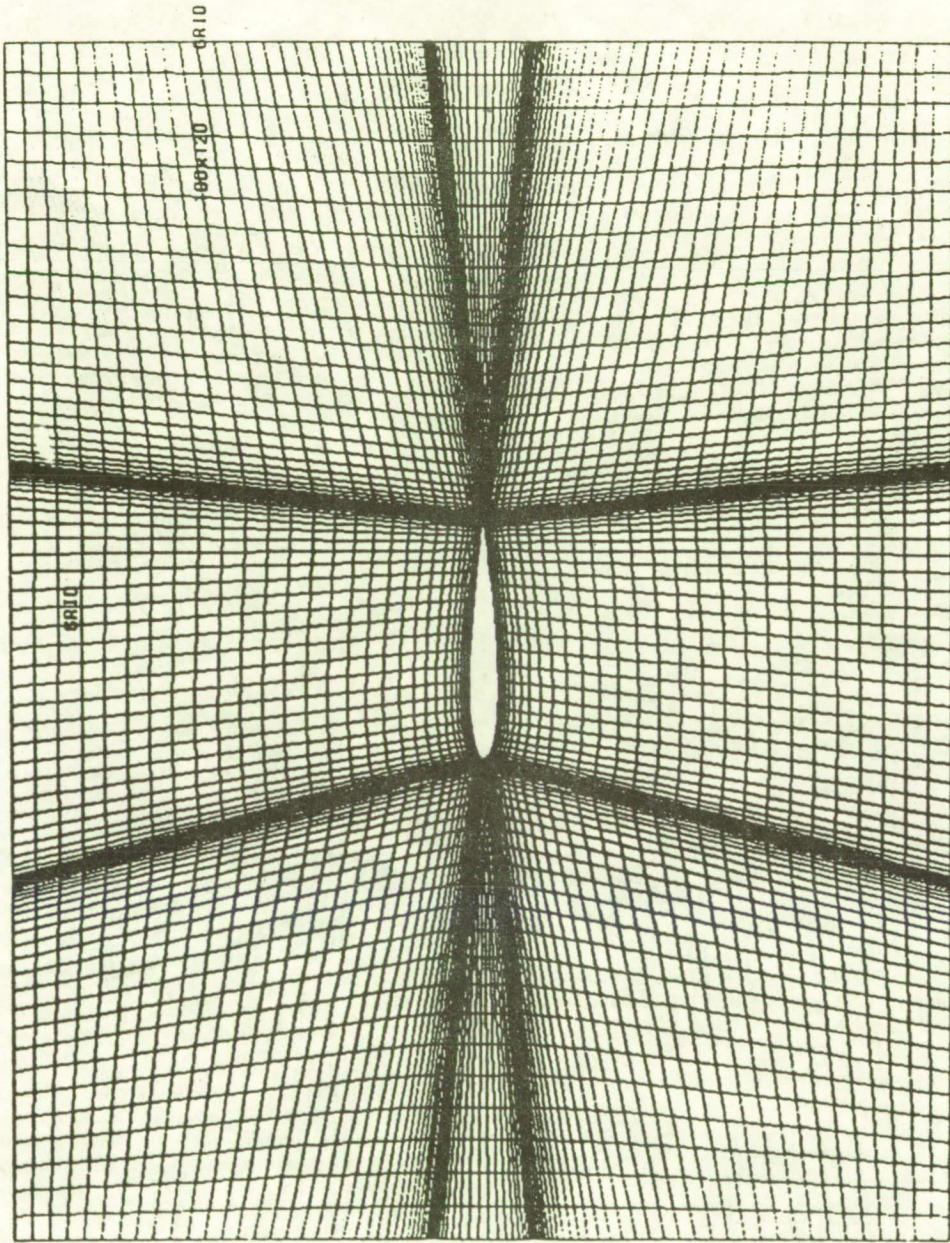


Fig. 3 Grid Distribution for NACA 0012 Airfoil

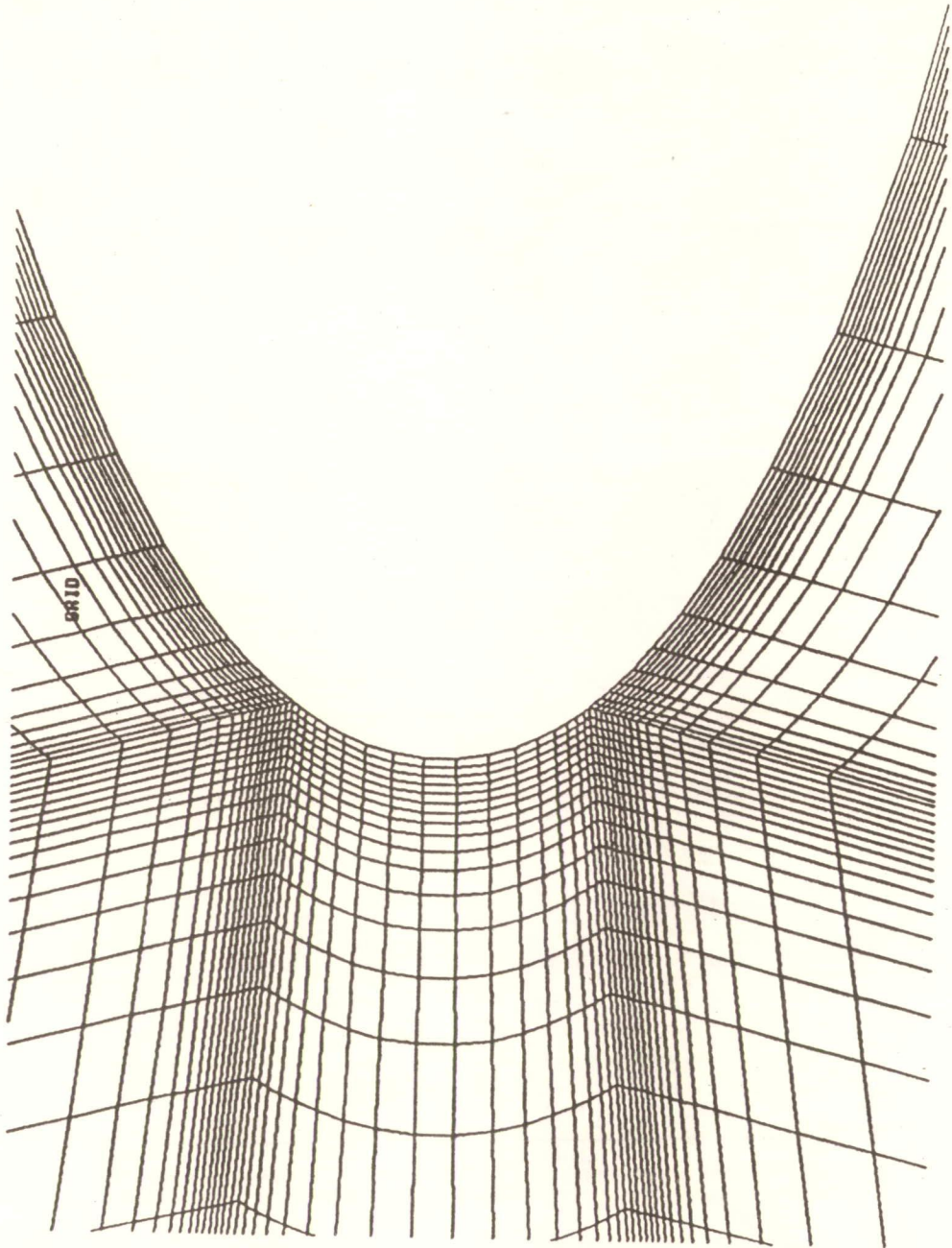


Fig. 4 Leading Edge Grid Distribution

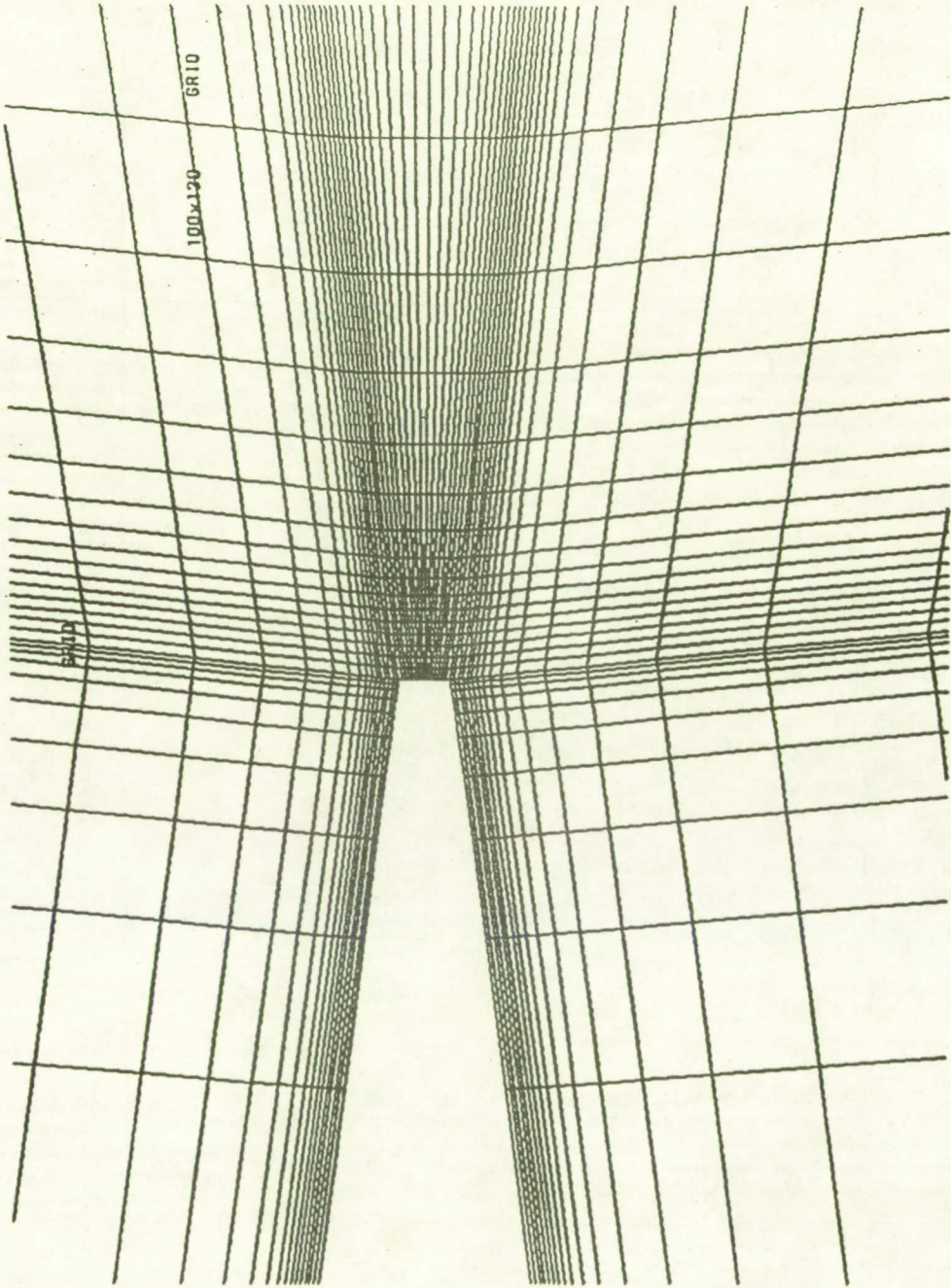
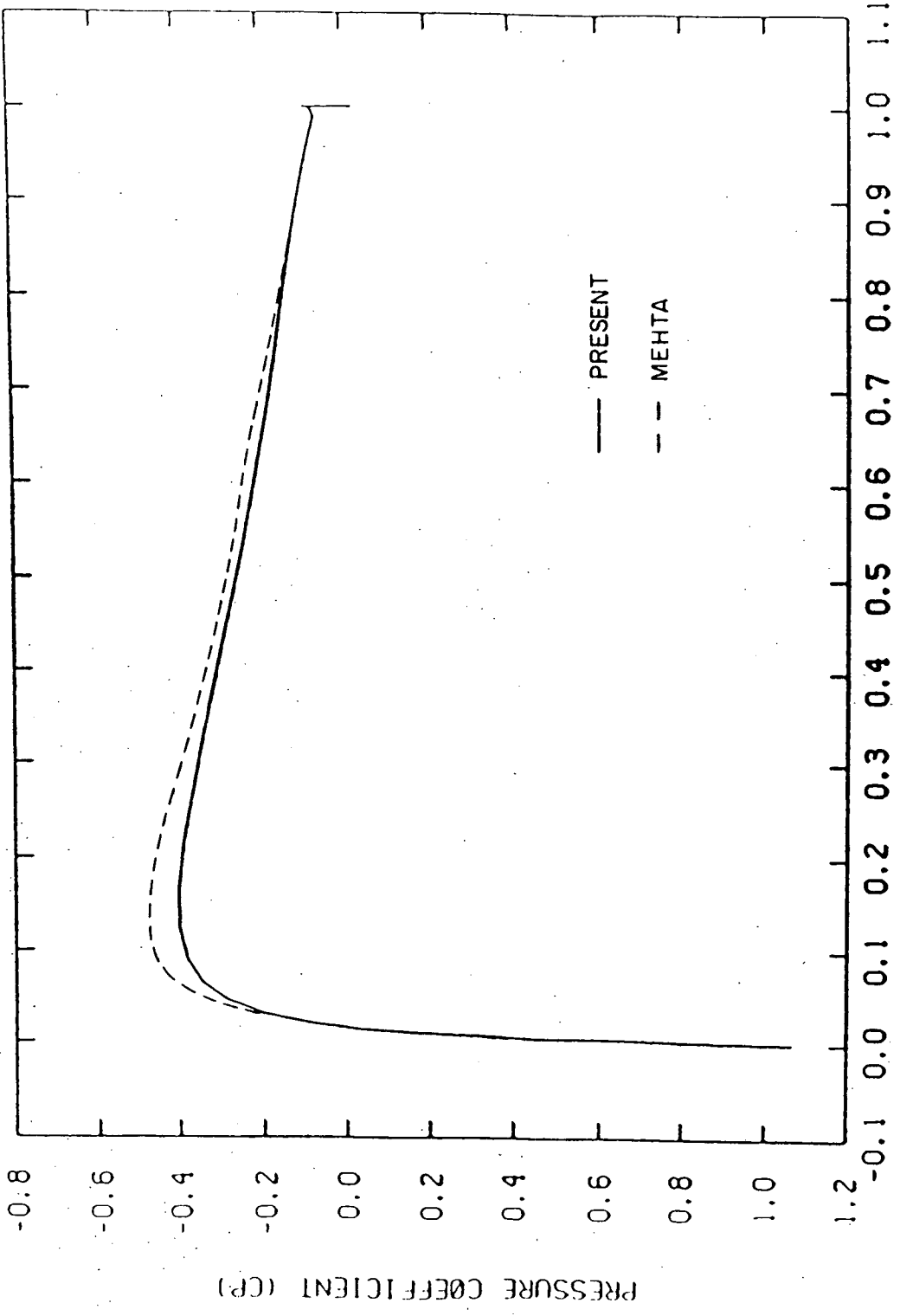


Fig. 5 Trailing Edge Grid Distribution



AXIAL DISTANCE FROM LEADING EDGE (X)

Fig. 6. Surface Pressure Distribution for NACA 0012 Airfoil, Re = 10000

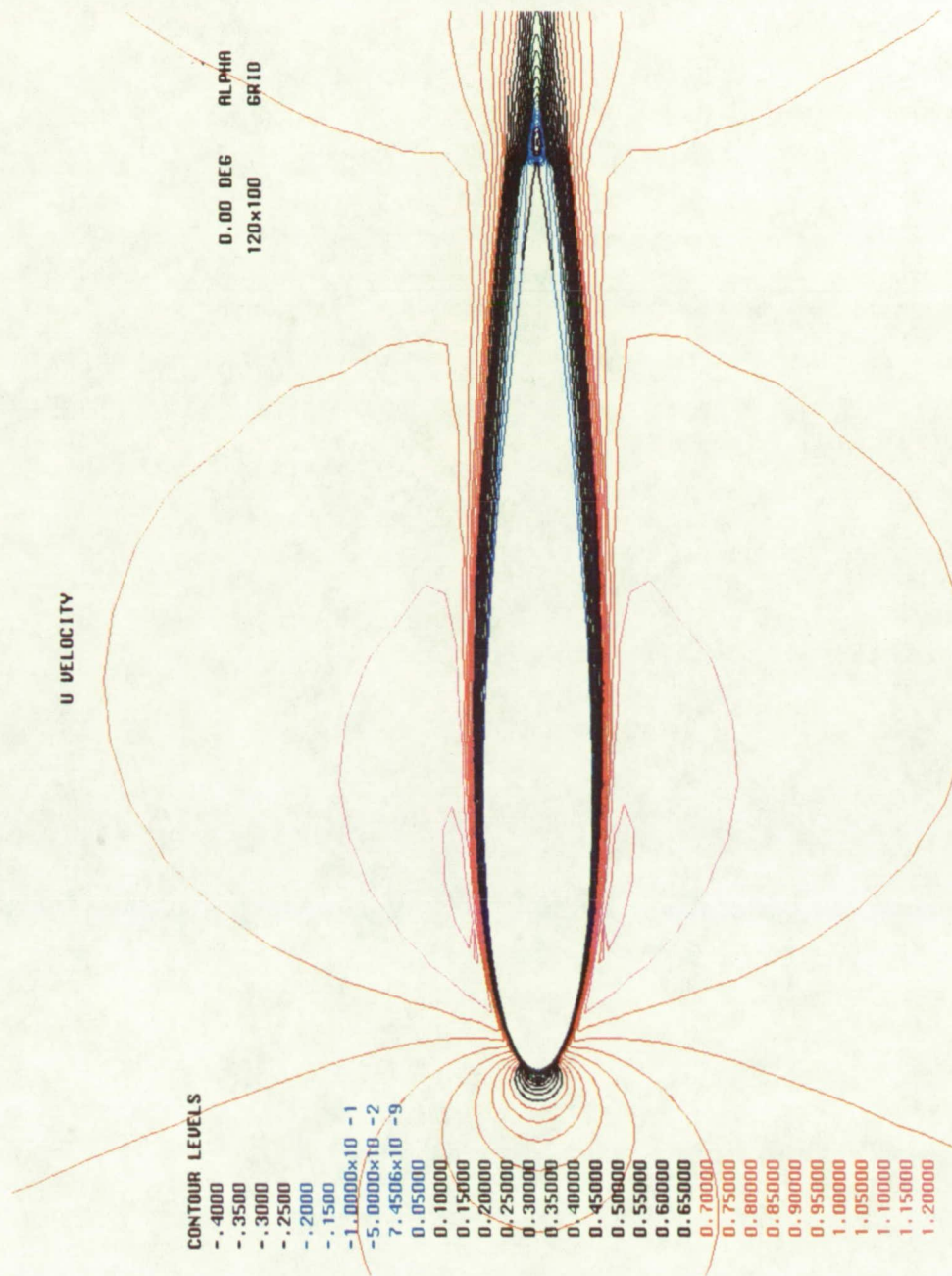


Fig. 7 Streamwise Velocity Contours

U VELOCITY

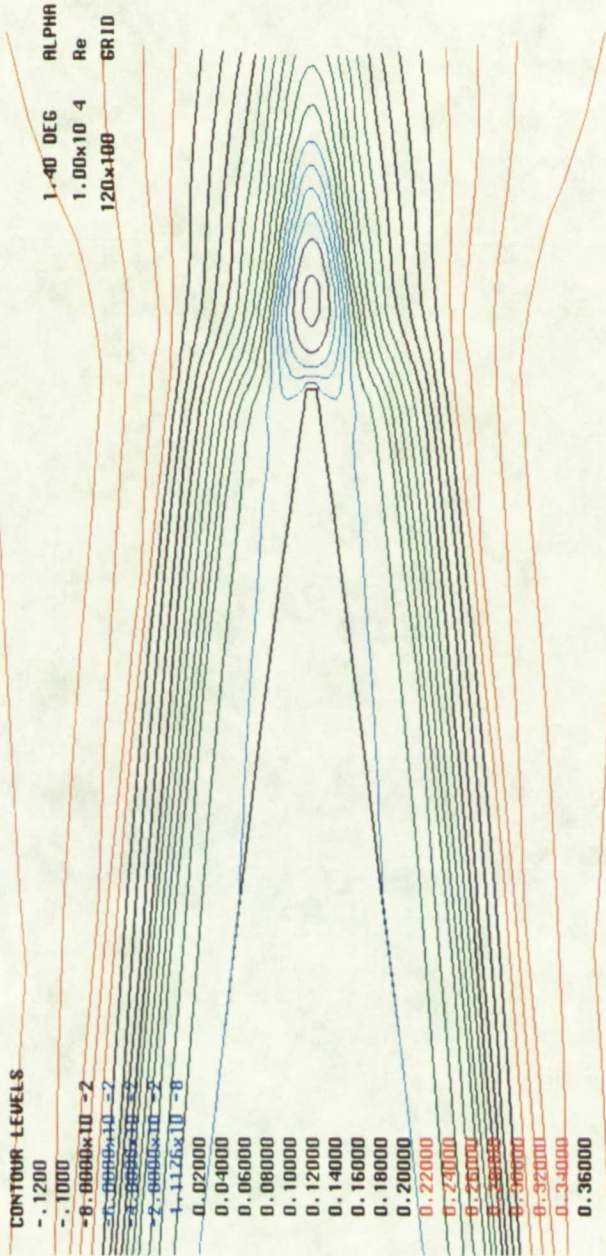


Fig. 8 Streamwise Velocity at Trailing Edge

ORIGINAL PAGE
COLOR PHOTOGRAPH

48

INTENTIONALLY BLANK

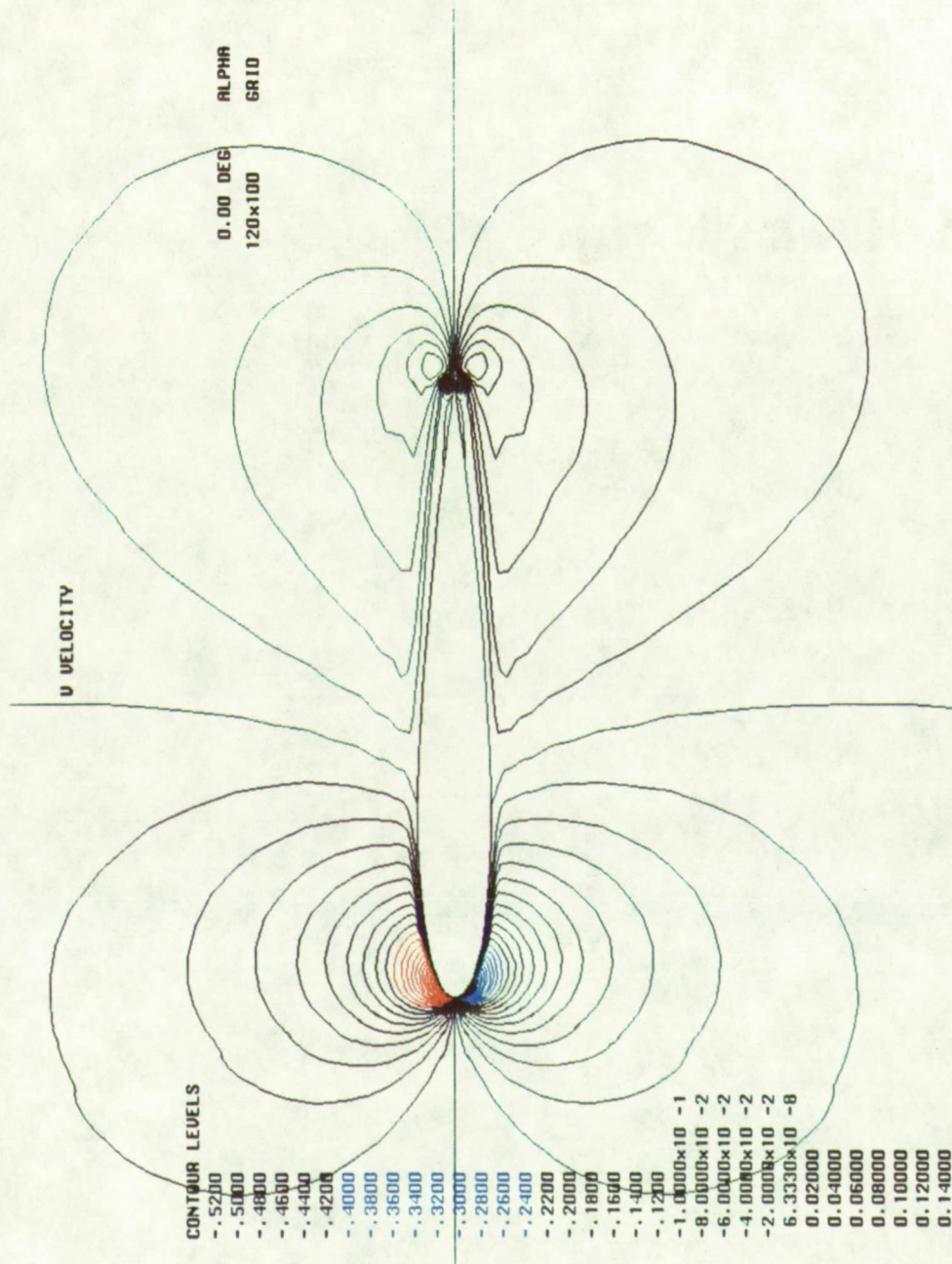


Fig. 9 Transverse Velocity Contours

ORIGINAL PAGE
COLOR PHOTOGRAPH

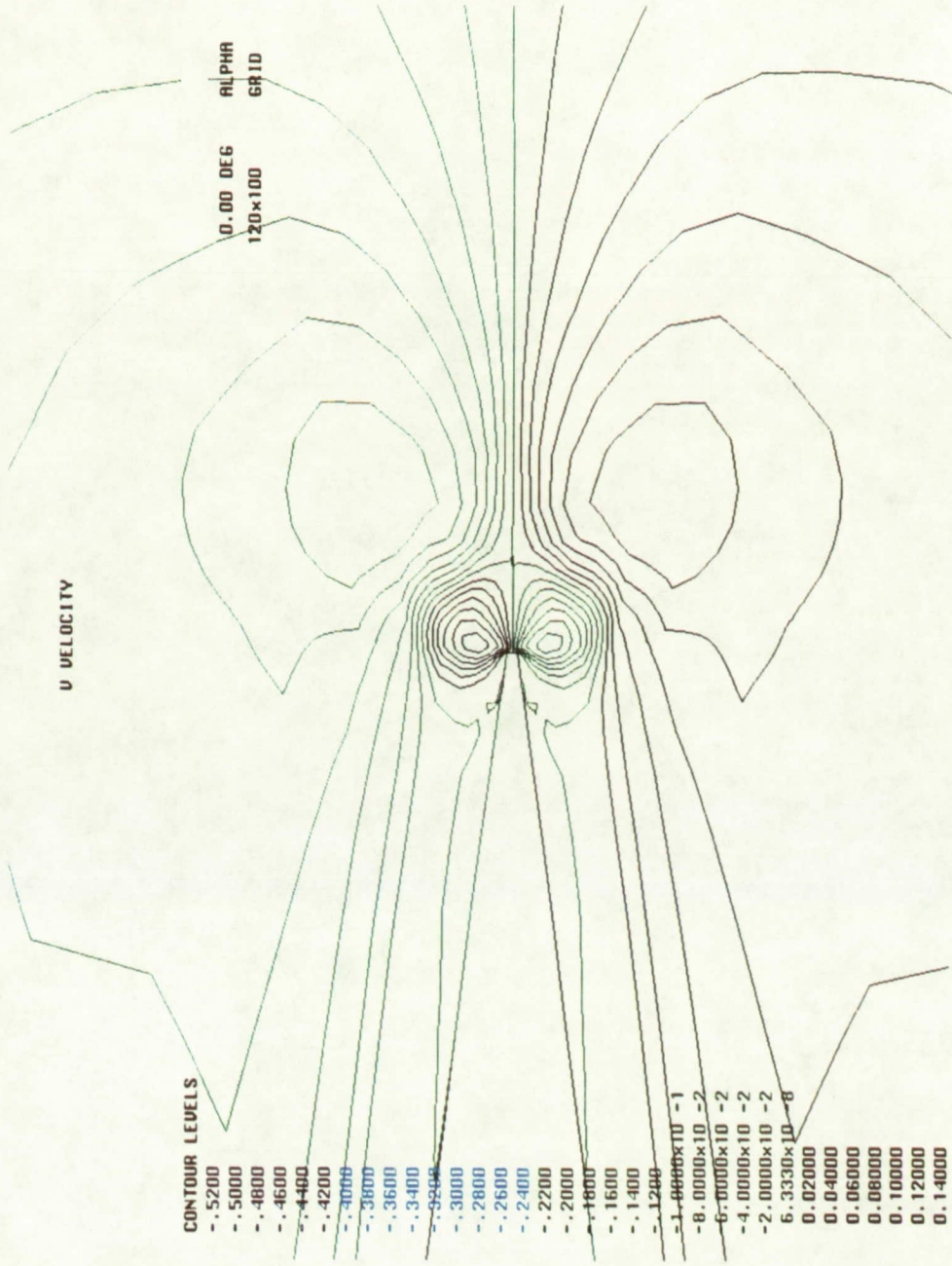


Fig. 10 Transverse Velocity Contours at Trailing Edge

ORIGINAL PAGE
COLOR PHOTOGRAPH

PRECEDING PAGE BLANK NOT FILMED

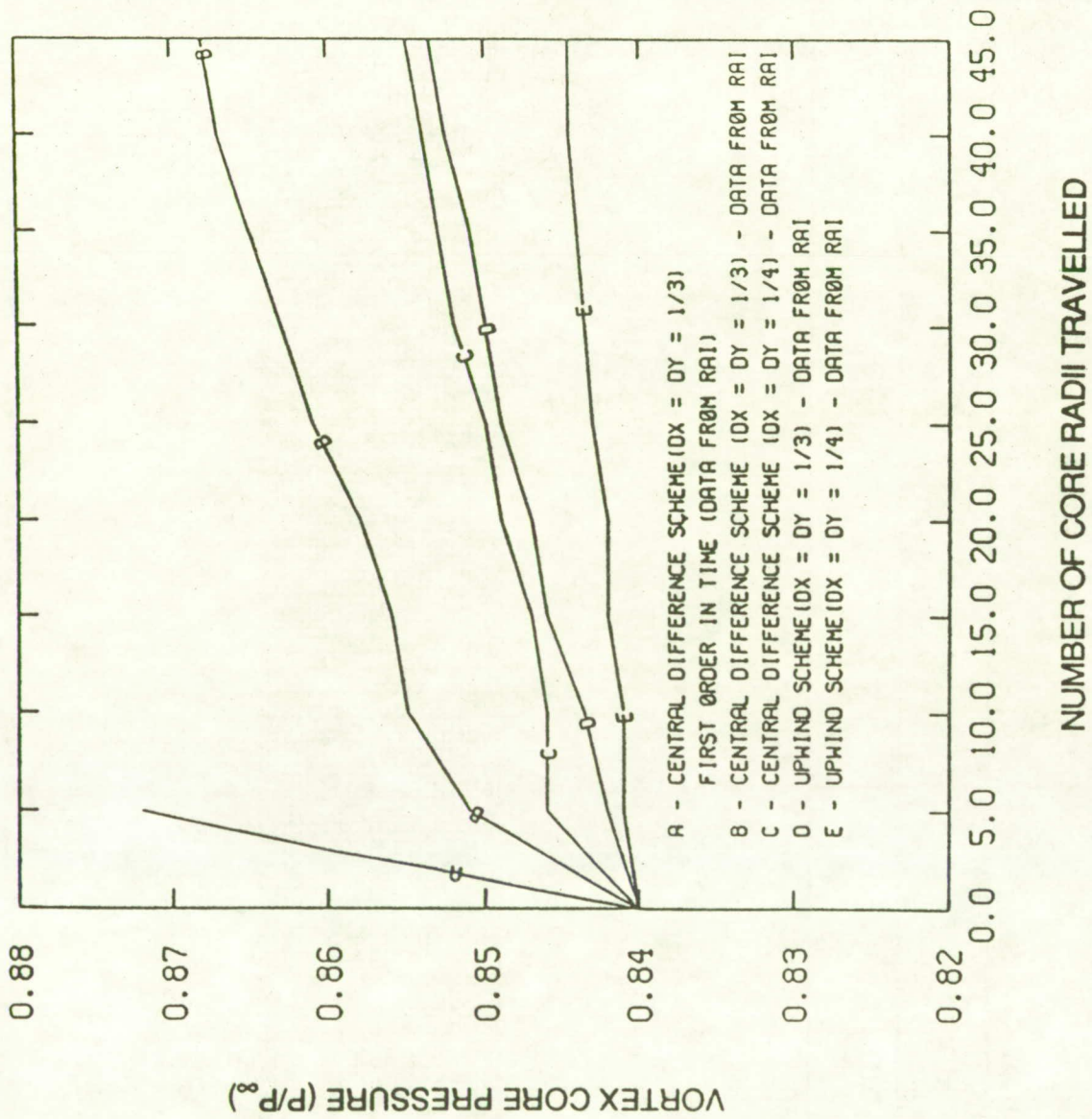
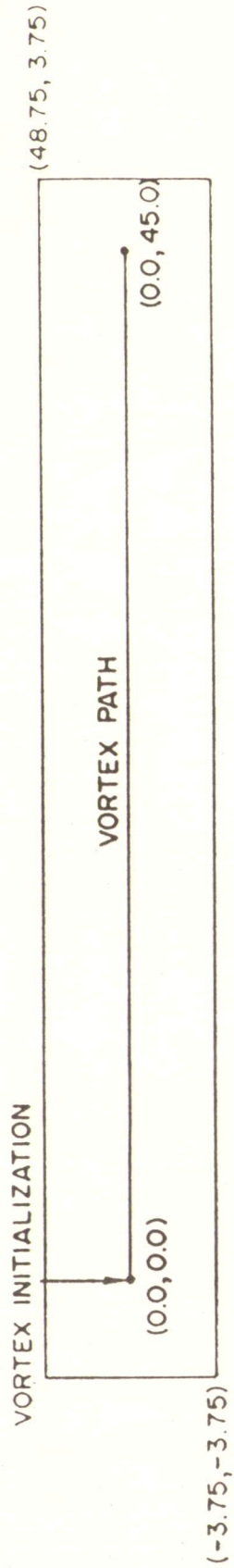
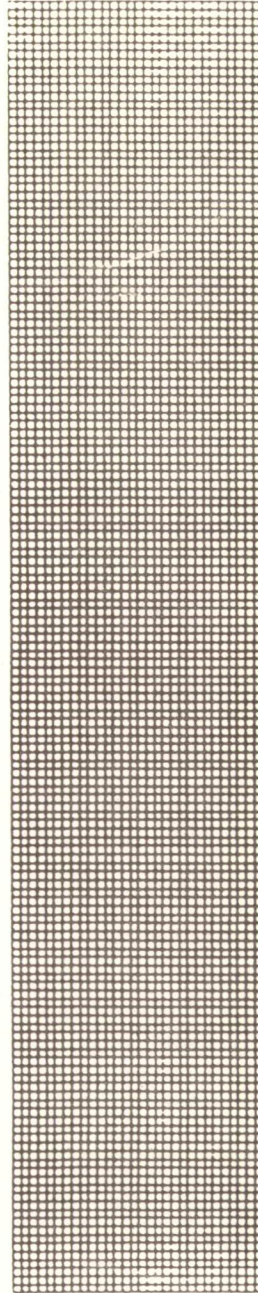


Fig. 11 Vortex Decay Rates for Various Schemes



(a)



(b)

Fig. 12 Physical Domain and the Vortex Path for the "A" Type Grid.

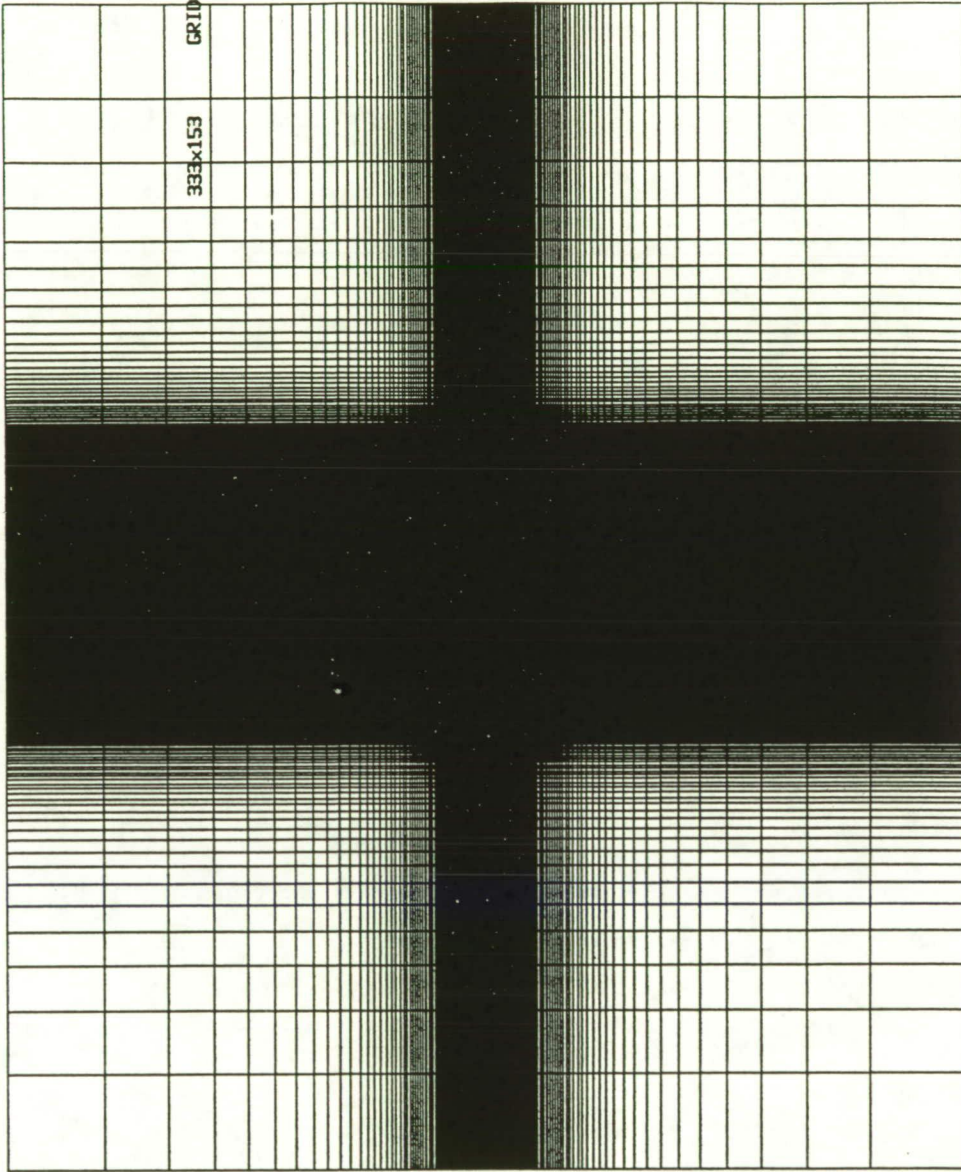
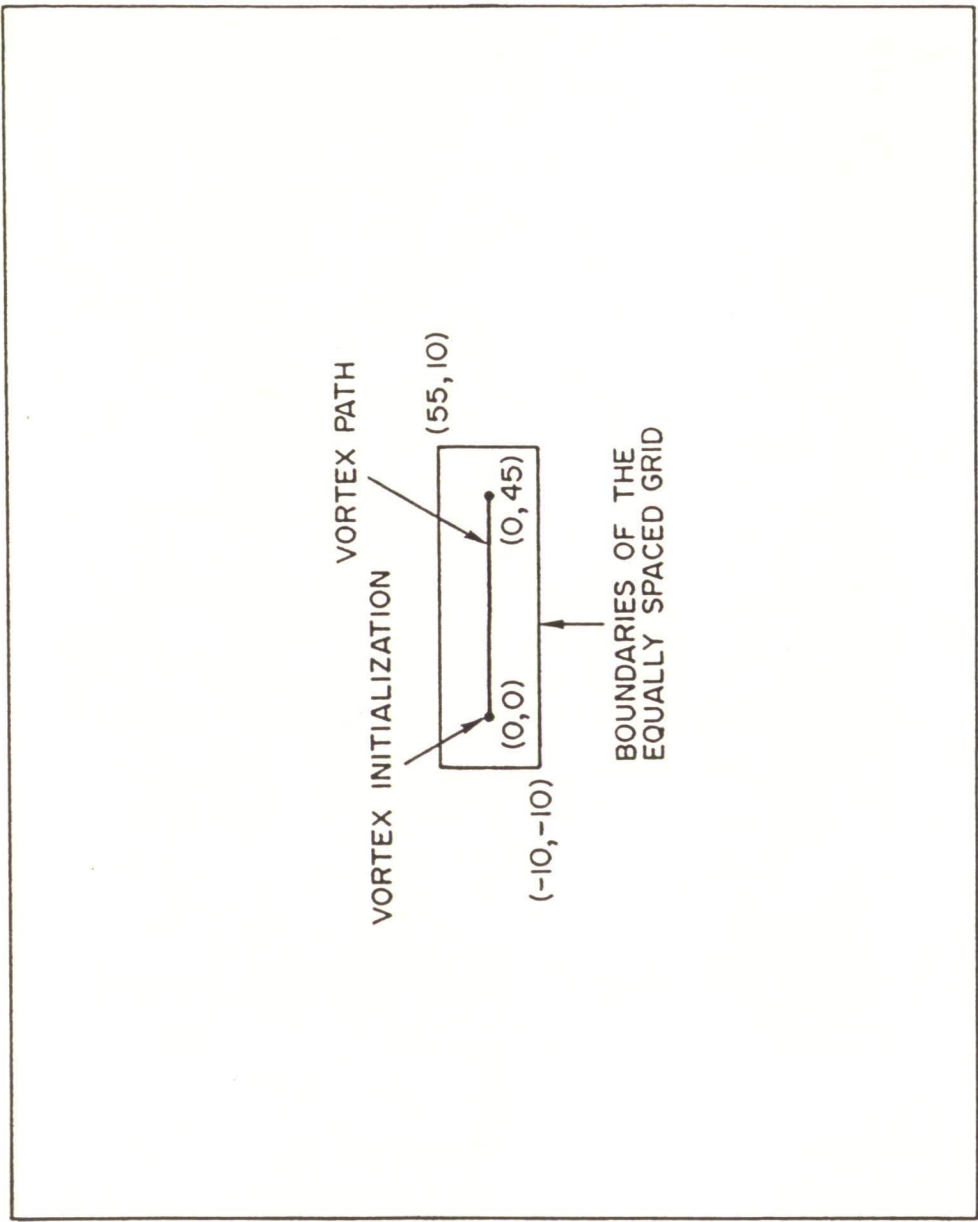


Fig. 13 Grid Spacing for Type "C" Grid

(145, 100)



(-100, -100)

Fig. 14 Physical Domain and the Vortex Path for Type "C" Grid.

PRESSURE

CONTOUR LEVELS

0.835000
0.840000
0.845000
0.850000
0.855000
0.860000
0.865000
0.870000
0.875000
0.880000
0.885000
0.890000
0.895000
0.900000
0.905000
0.910000
0.915000
0.920000
0.925000
0.930000
0.935000
0.940000
0.945000
0.950000
0.955000
0.960000
0.965000
0.970000
0.975000
0.980000
0.985000
0.990000
0.995000
1.000000

0.00 DEG ALPHA
421x61 GRID

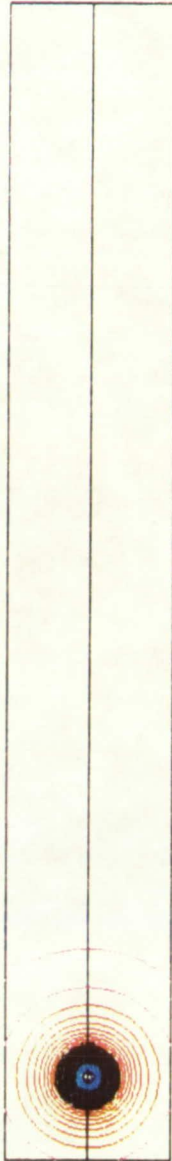


Fig. 15 Contours of Pressure at Initialization

ORIGINAL PAGE
COLOR PHOTOGRAPH

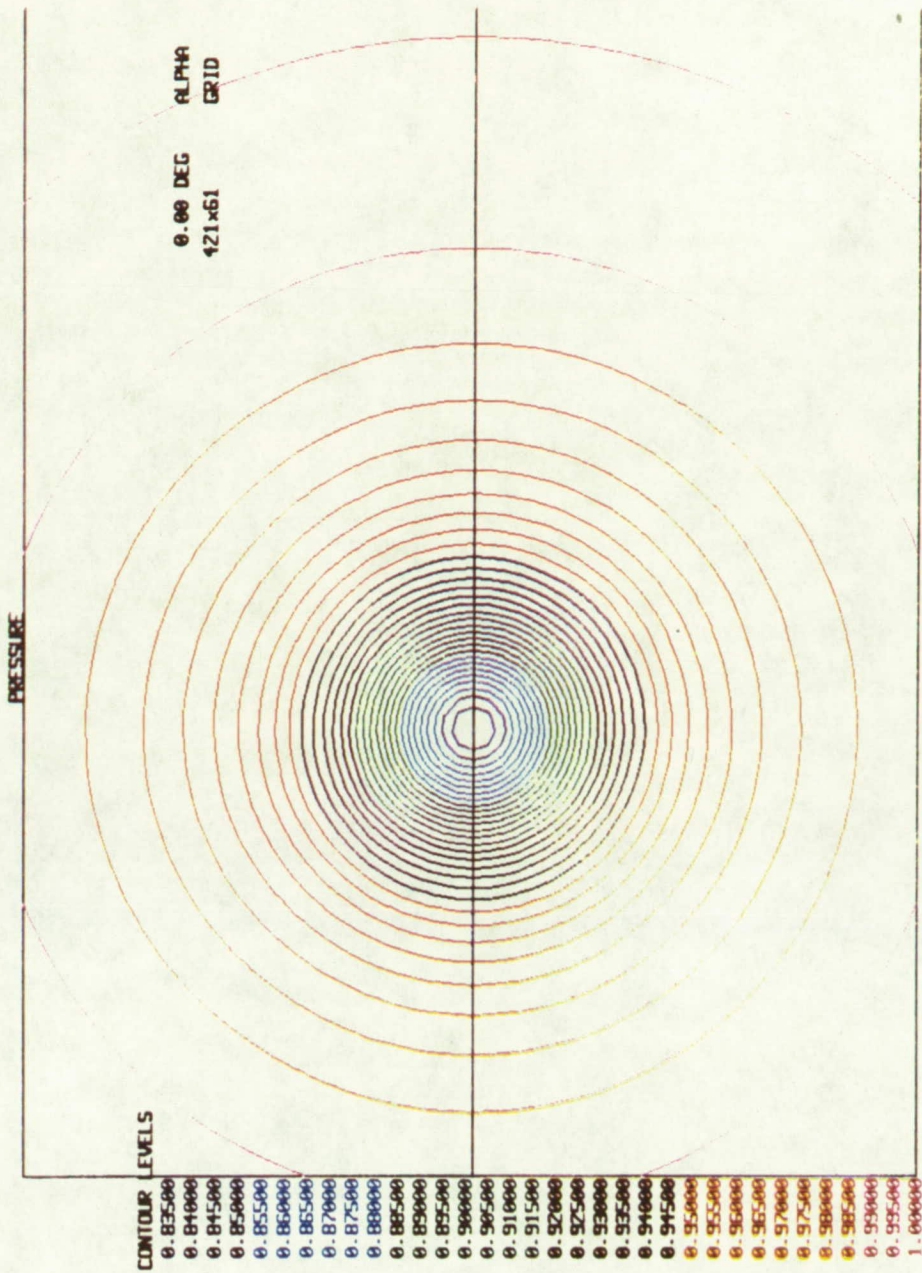


Fig. 16 Contours of Pressure at Initialization

VORTICITY MAGNITUDE

CONTOUR LEVELS

0.00000E+00
0.05000E+00
0.10000E+00
0.15000E+00
0.20000E+00
0.25000E+00
0.30000E+00
0.35000E+00
0.40000E+00
0.45000E+00
0.50000E+00
0.55000E+00
0.60000E+00
0.65000E+00
0.70000E+00
0.75000E+00
0.80000E+00
0.85000E+00
0.90000E+00
0.95000E+00
1.00000E+00
1.05000E+00
1.10000E+00
1.15000E+00
1.20000E+00
1.25000E+00
1.30000E+00
1.35000E+00
1.40000E+00
1.45000E+00
1.50000E+00
1.55000E+00
1.60000E+00
1.65000E+00

0.00 DEG ALPHA
421x61 GRID

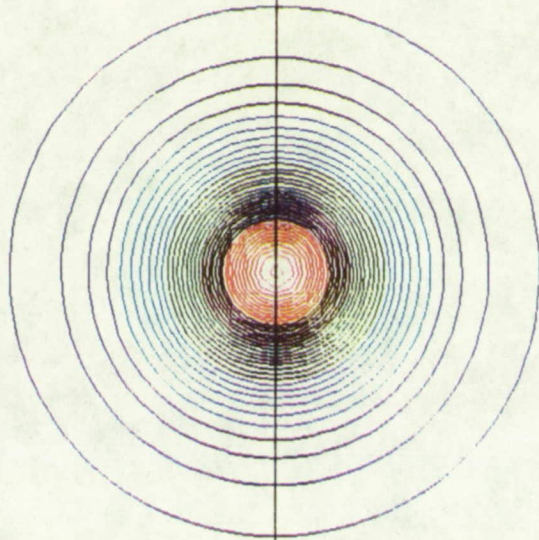


Fig. 17 Contours of Vorticity Magnitude at Initialization

ORIGINAL PAGE
COLOR PHOTOGRAPH

62 INTENTIONALLY BLANK

U VELOCITY

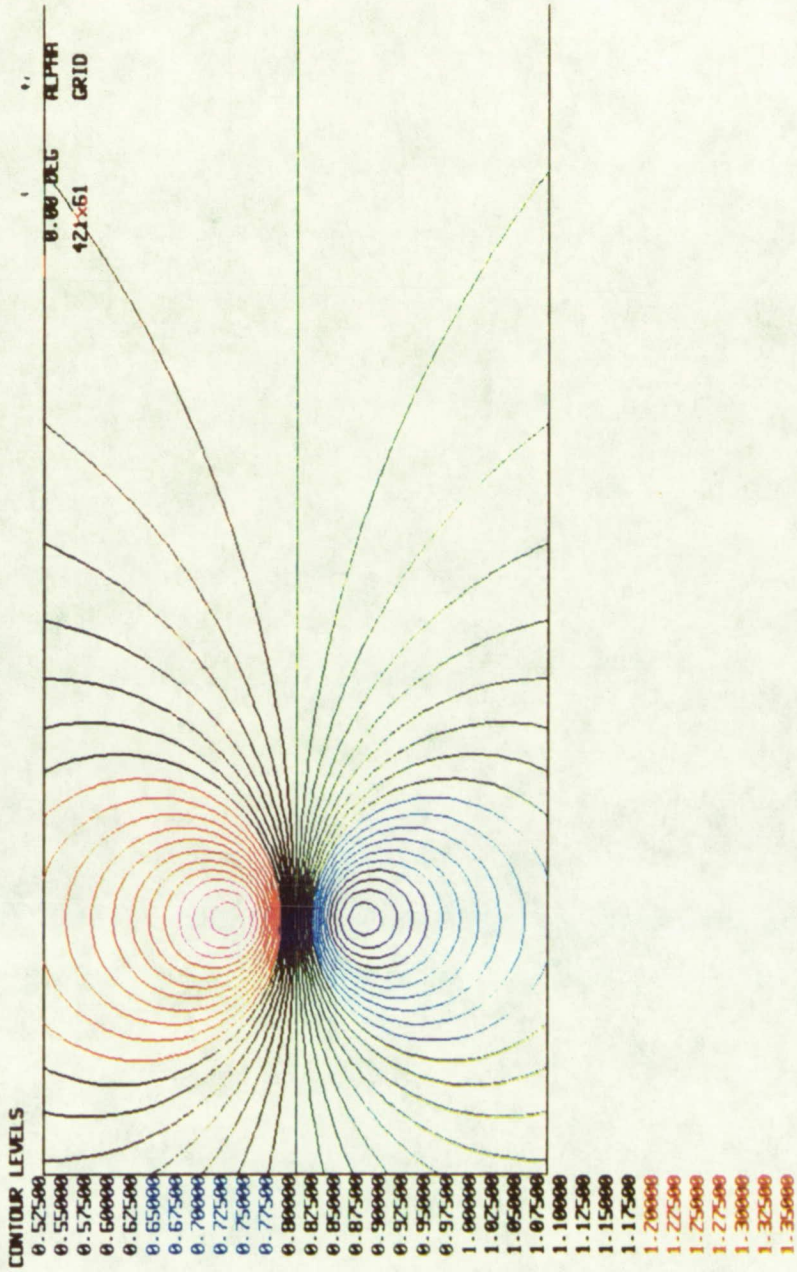


Fig. 18 Contours of Streamwise Velocity at Initialization

ORIGINAL PAGE
COLOR PHOTOGRAPH

V VELOCITY

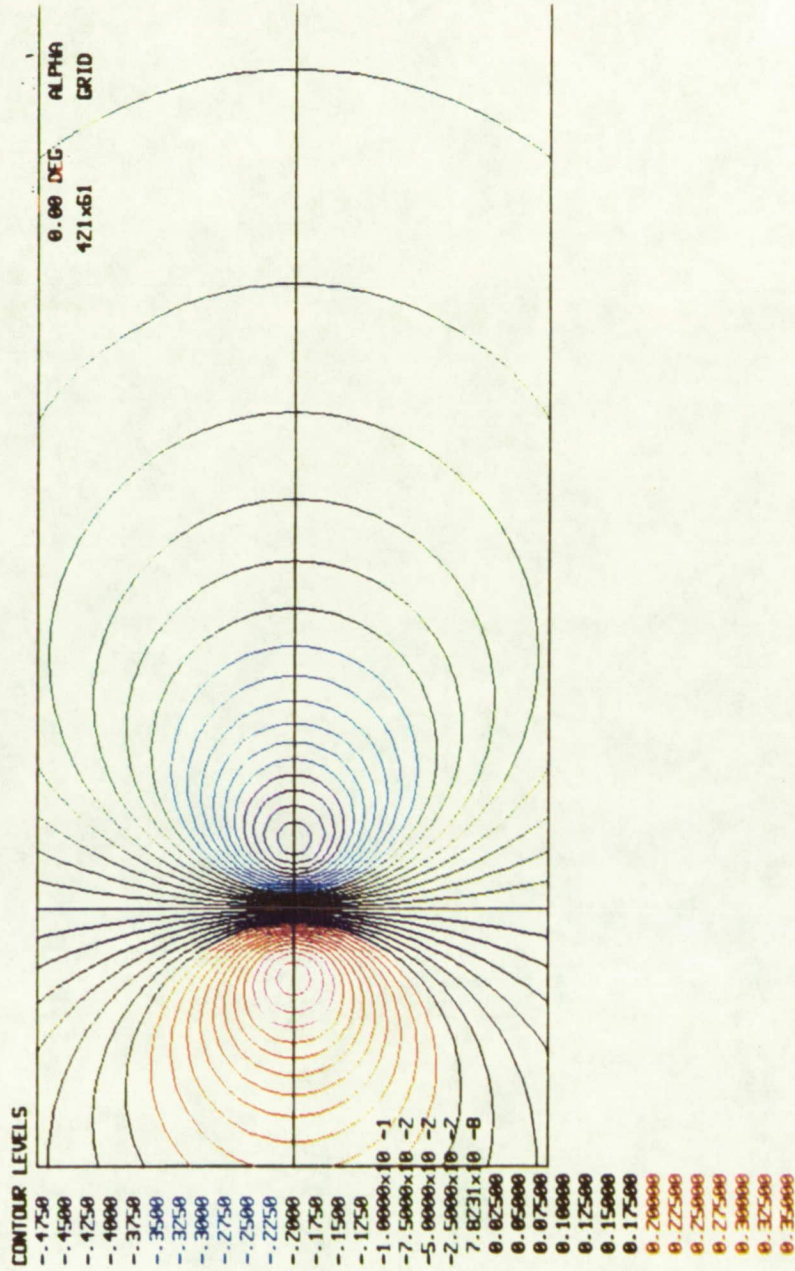
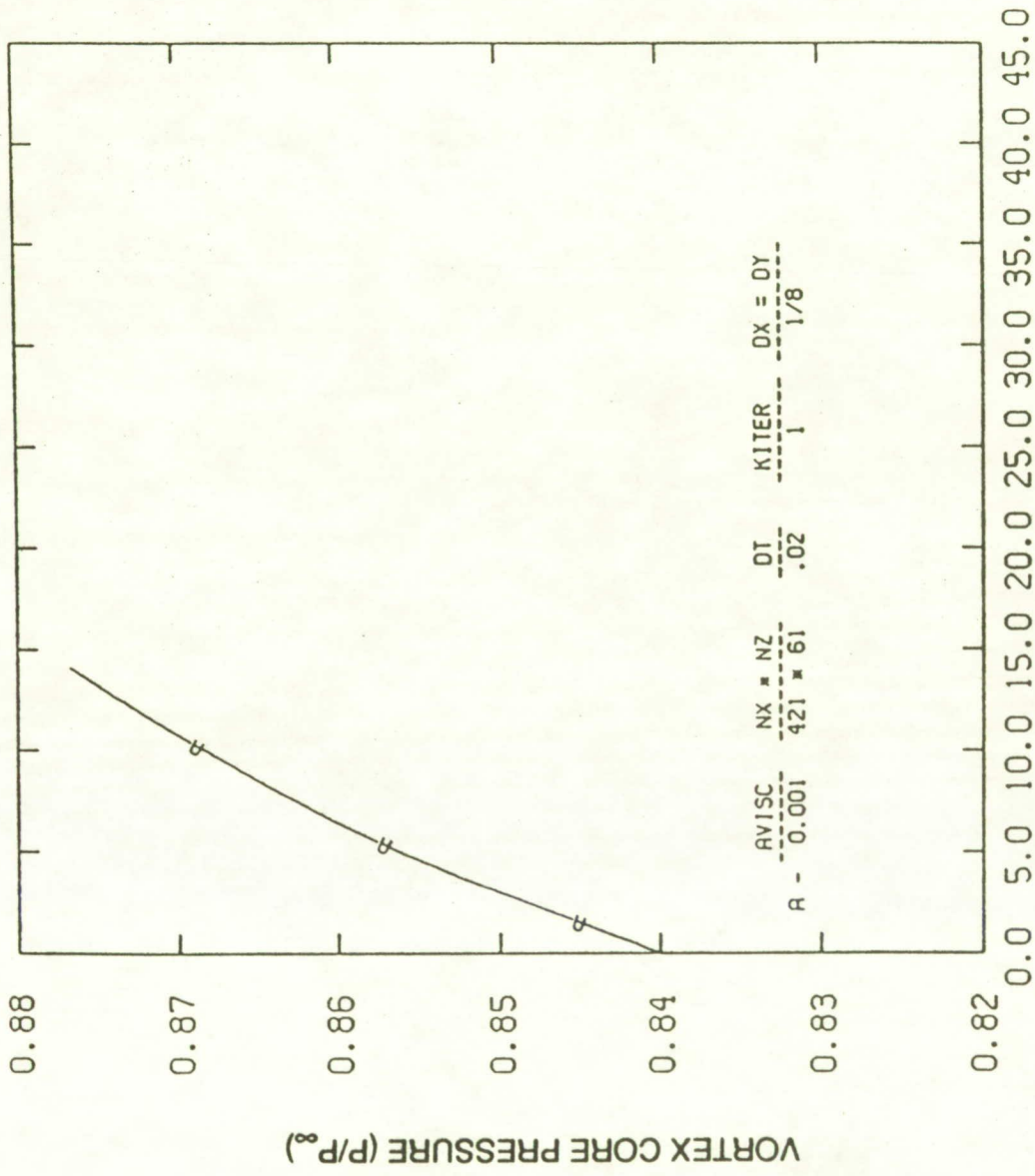


Fig. 19 Contours of Transverse Velocity at Initialization

ORIGINAL PAGE
COLOR PHOTOGRAPH

66 ~~XXXXXXXXXXXX~~ BEARR



NUMBER OF CORE RADII TRAVELLED

Fig. 20 Vortex Decay Rates for Central Difference Scheme
First Order in Time

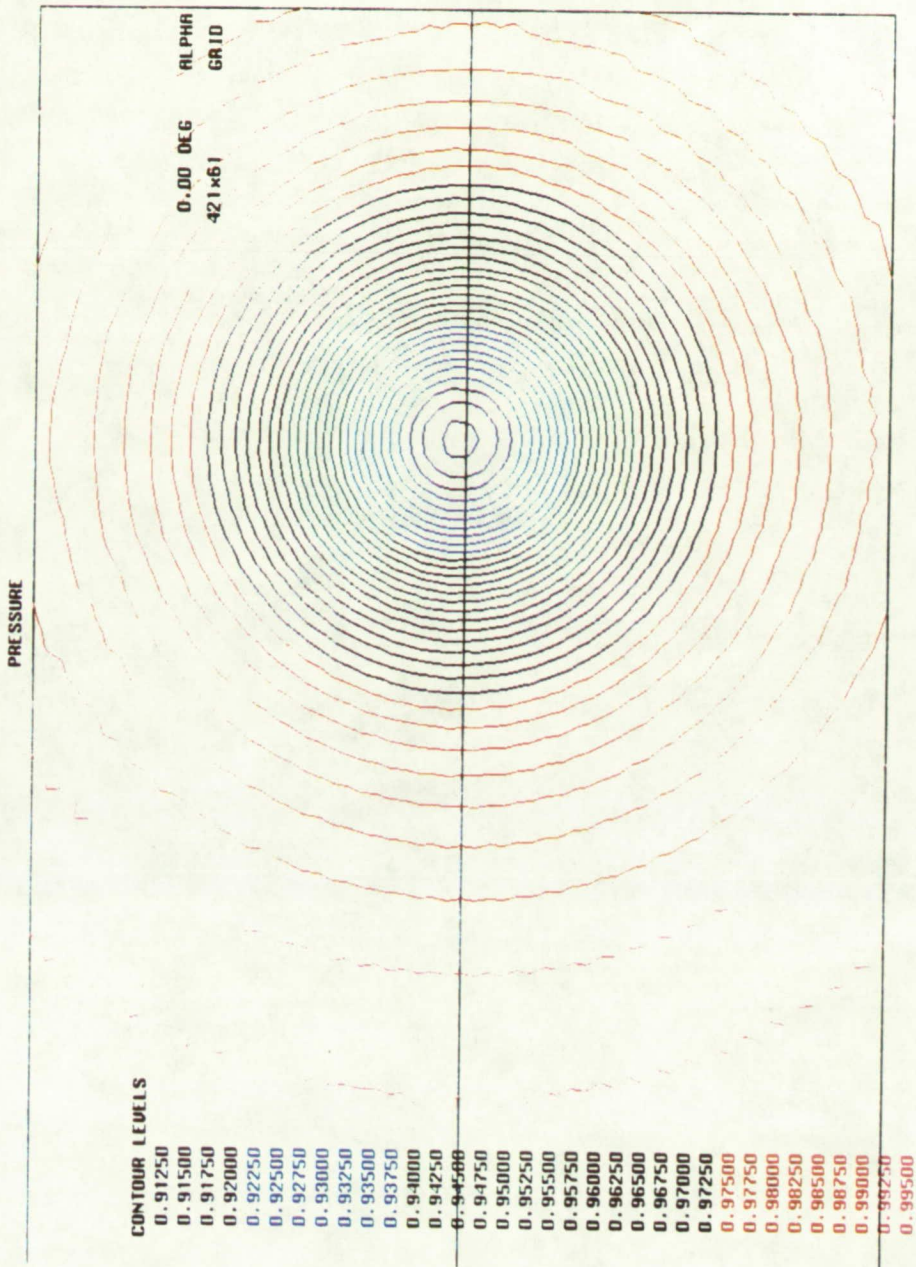


Fig. 21 Contours of Pressure after 45 Core Radii of Travel
(first-order-time-accurate central-difference scheme)

ORIGINAL PAGE
COLOR PHOTOGRAPH

VORTICITY MAGNITUDE

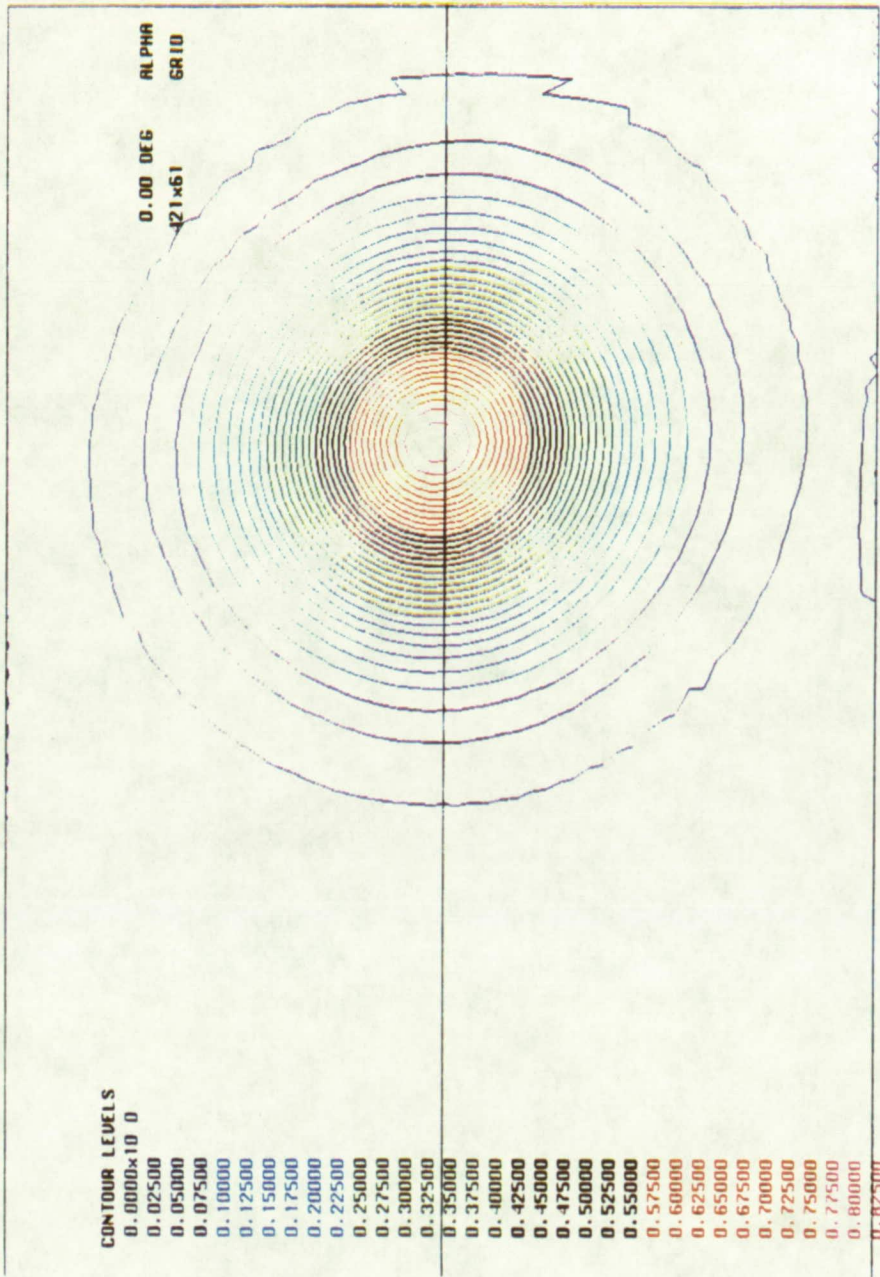


Fig. 22 Contours of Vorticity Magnitude after 45 Core Radii of Travel

U VELOCITY

CONTOUR LEVELS

- 0.640000
- 0.660000
- 0.680000
- 0.700000
- 0.720000
- 0.740000
- 0.760000
- 0.780000
- 0.800000
- 0.820000
- 0.840000
- 0.860000
- 0.880000
- 0.900000
- 0.920000
- 0.940000
- 0.960000
- 0.980000
- 1.000000
- 1.020000
- 1.040000
- 1.060000
- 1.080000
- 1.100000
- 1.120000
- 1.140000
- 1.160000
- 1.180000
- 1.200000
- 1.220000
- 1.240000
- 1.260000
- 1.280000
- 1.300000

0.00 DEG ALPHA
-21x61 GRID

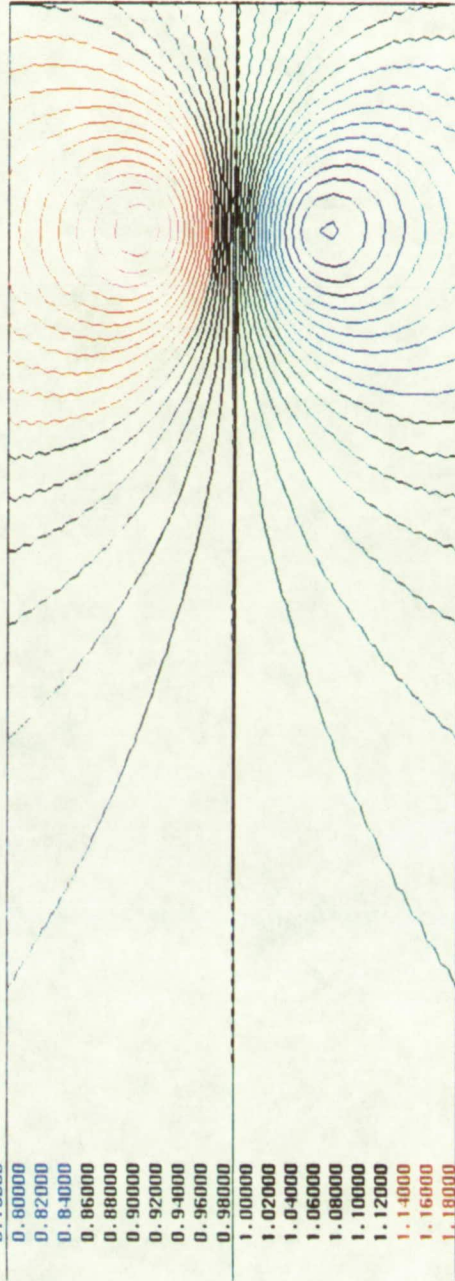


Fig. 23 Contours of Streamwise Velocity after 45 Core Radii of Travel

ORIGINAL PAGE
COLOR PHOTOGRAPH

U VELOCITY

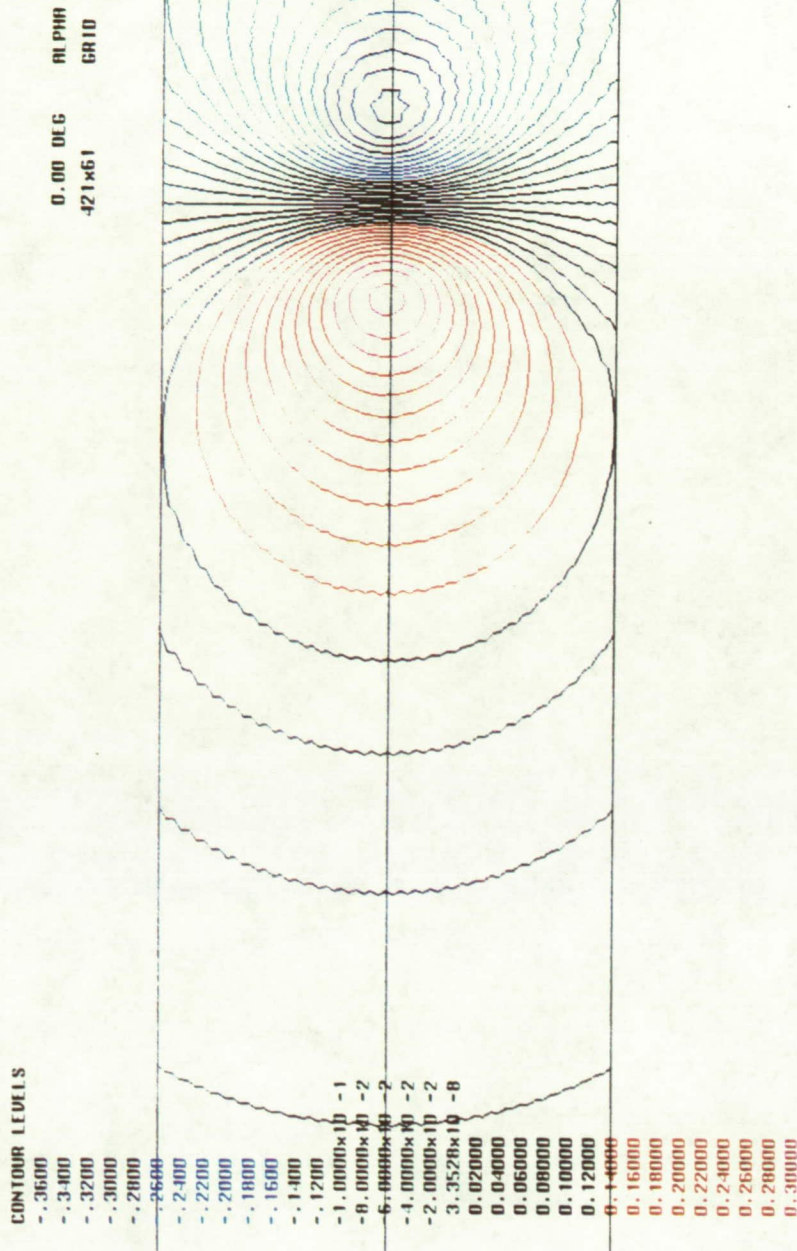


Fig. 24 Contours of Transverse Velocity after 45 Core Radii of Travel

ORIGINAL PAGE
COLOR PHOTOGRAPH

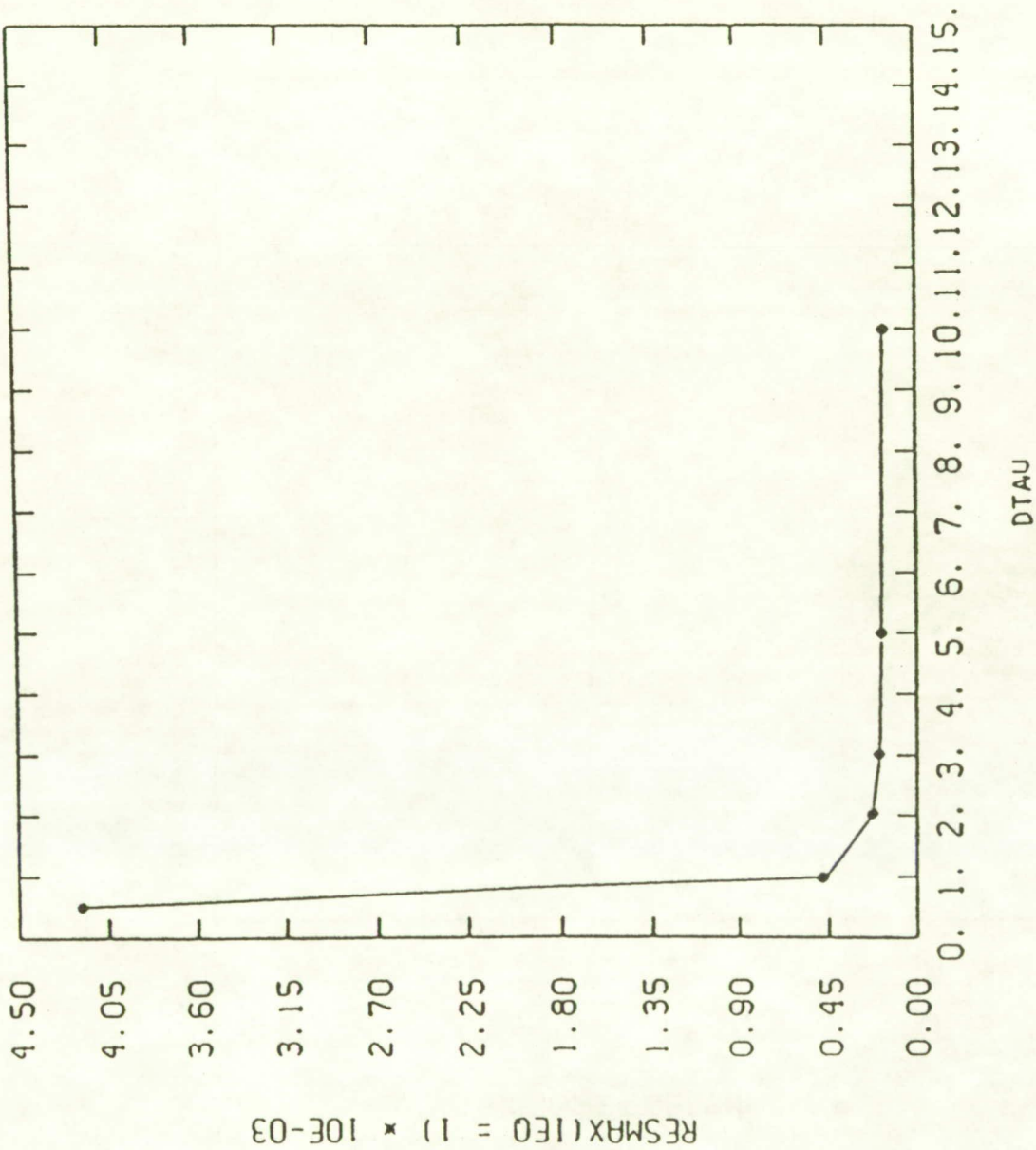


Fig. 25 Effects of Iteration Step on the Convergence Rate
Resmax Versus DTAU After 4 Iteration for DT = .08

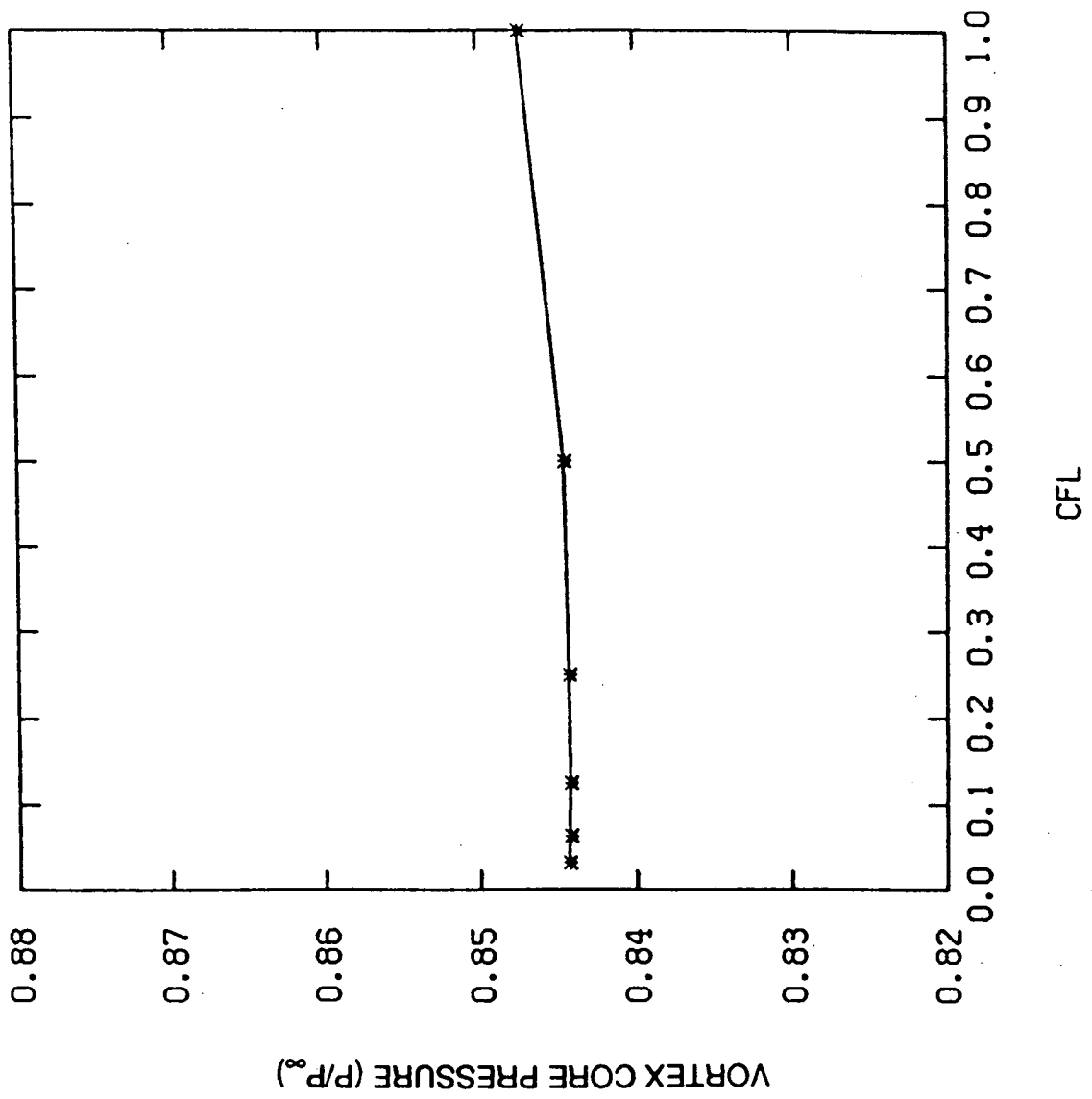


Fig. 26 Effects of Time Step on Core Pressure

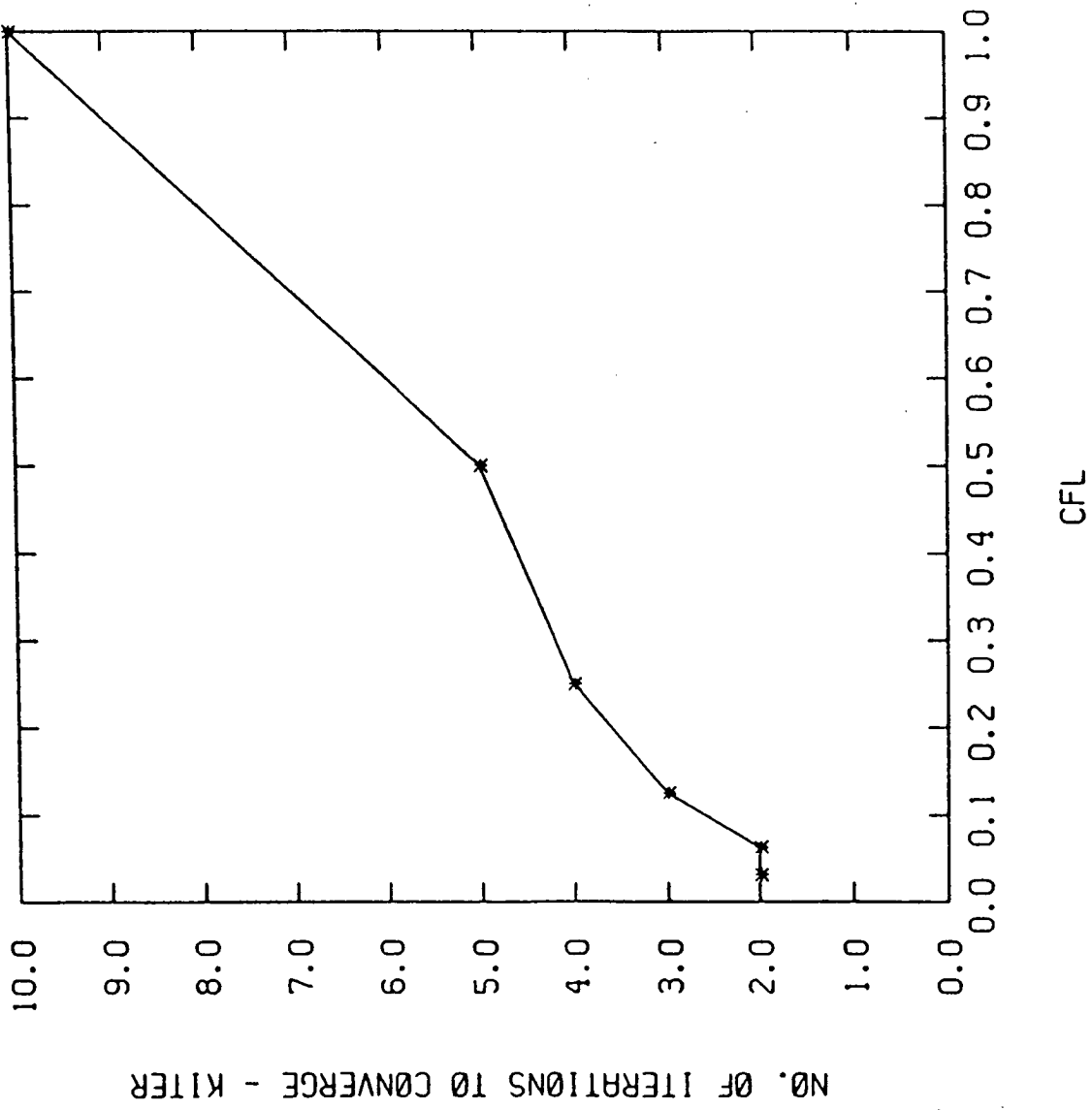


Fig. 27 No. of Iterations to Convergence Versus CFL

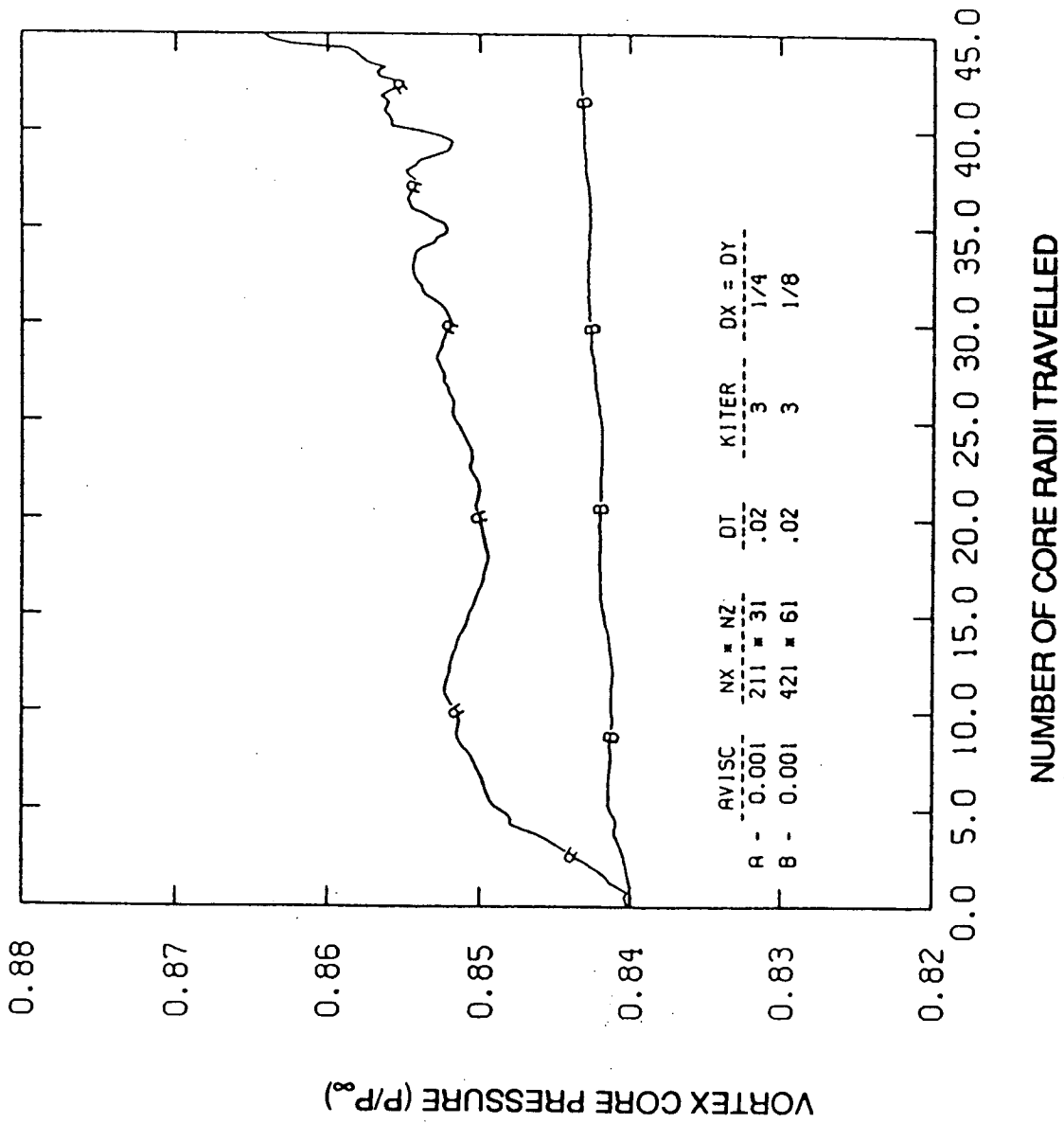


Fig. 28 Effects of Grid Spacing on Vortex Decay

PRESSURE

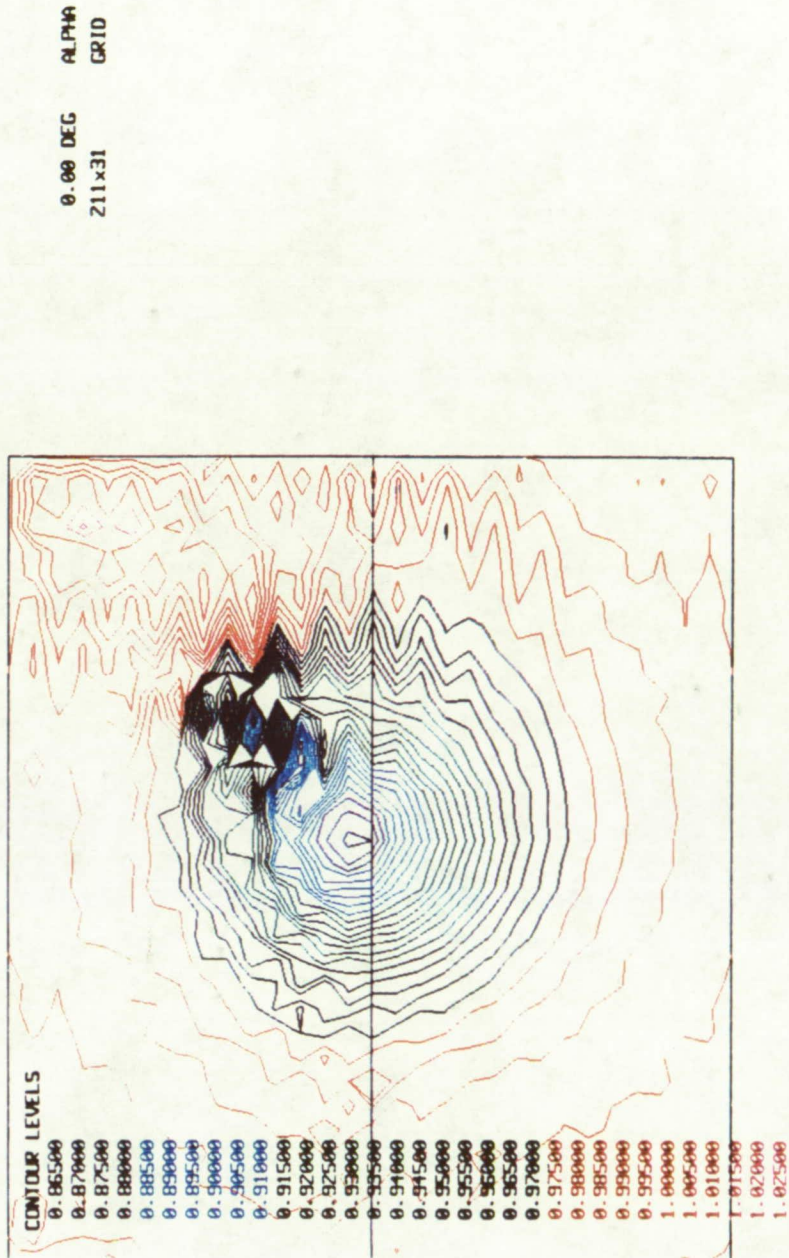


Fig. 29 Contours of Pressure after 45 Core Radii at Travel
($\Delta x = \Delta y = 1/4$)

ORIGINAL PAGE
COLOR PHOTOGRAPH

PRESSURE

CONTOUR LEVELS

0.81000
0.84500
0.85000
0.85500
0.86000
0.86500
0.87000
0.88000
0.88500
0.89000
0.89500
0.90000
0.90500
0.91000
0.91500
0.92000
0.92500
0.93000
0.93500
0.94000
0.94500
0.95000
0.95500
0.96000
0.96500
0.97000
0.97500
0.98000
0.98500
0.99000
0.99500
1.00000
1.00500

0.00 DEG ALPHA
421x61 GRID CRID

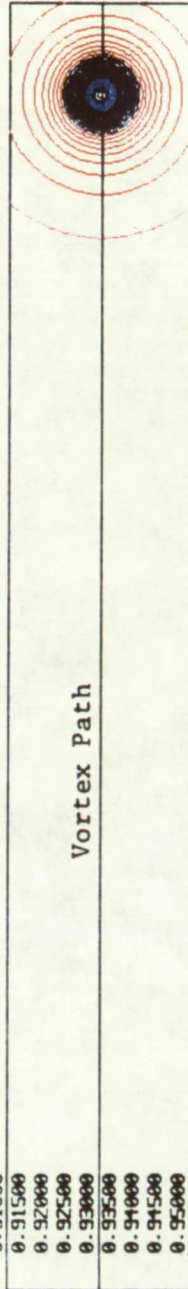


Fig. 30 Contours of Pressure after 45 Core Radii of Travel
($\Delta x = \Delta y = 1/8$)

ORIGINAL PAGE
COLOR PHOTOGRAPH

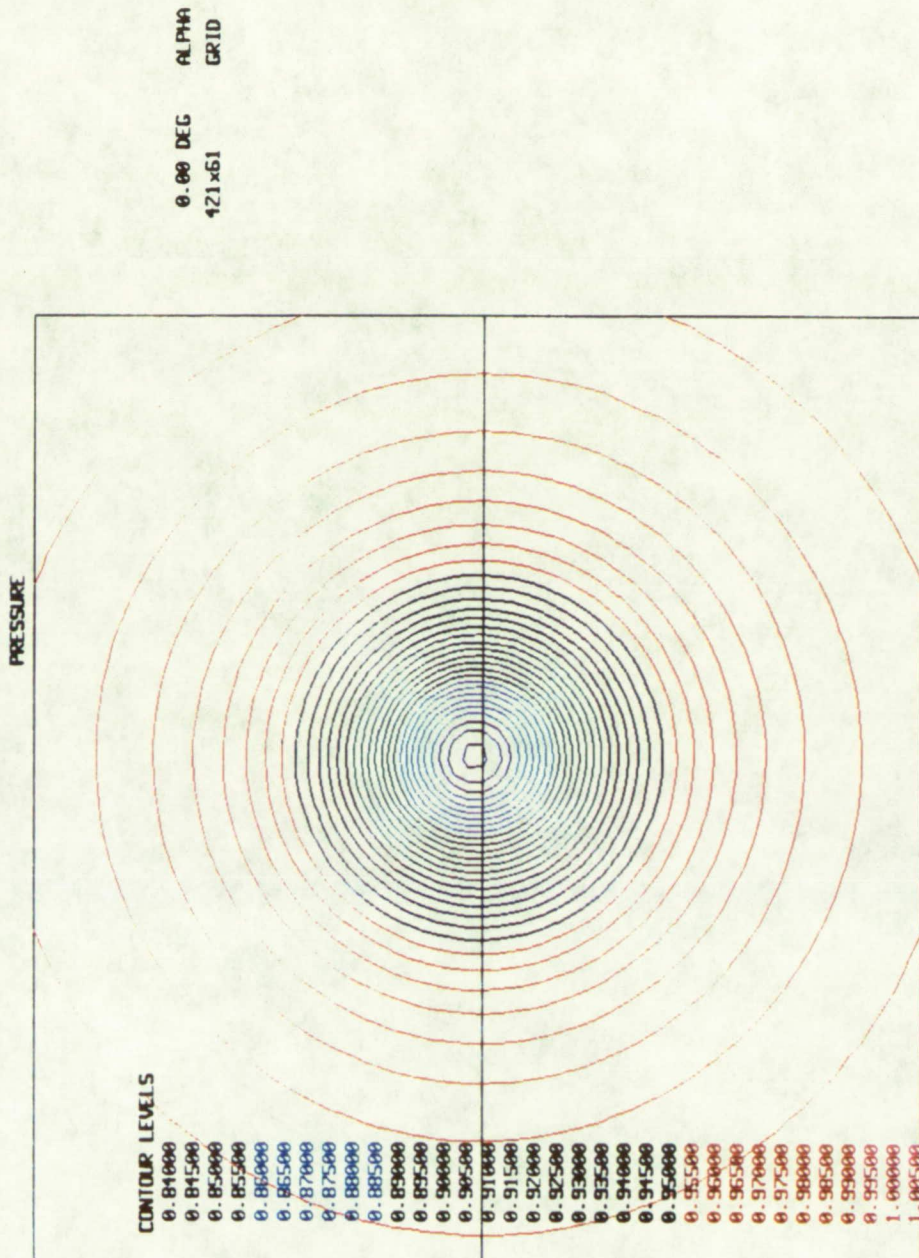


Fig. 31 Blow up of Contours of Pressure after 45 Radii of Travel
($\Delta x = \Delta y = 1/8$)

ORIGINAL PAGE
COLOR PHOTOGRAPH

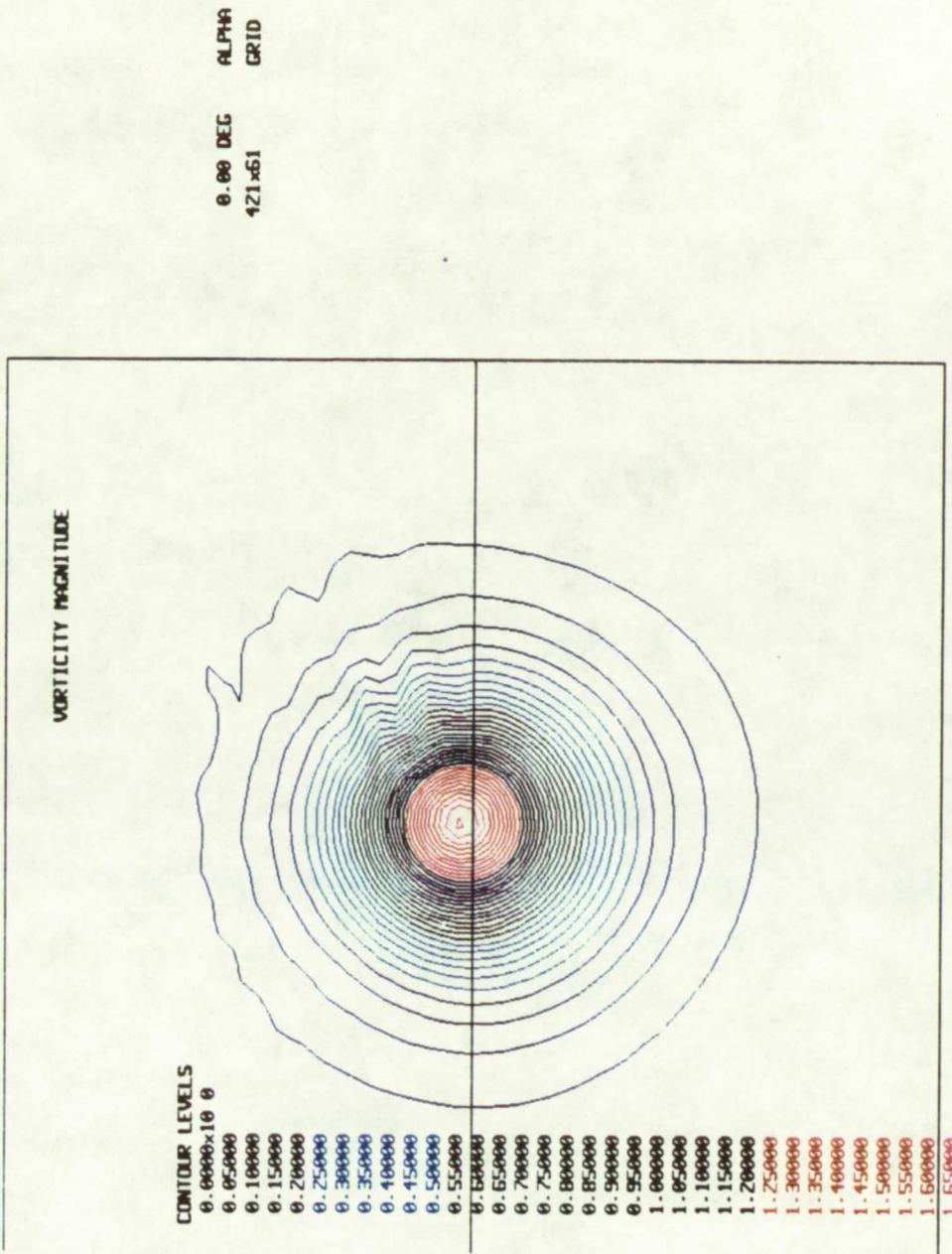


Fig. 32 Contours of Vorticity Magnitude after 45 Core Radii of Travel

ORIGINAL PAGE
 COLOR PHOTOGRAPH

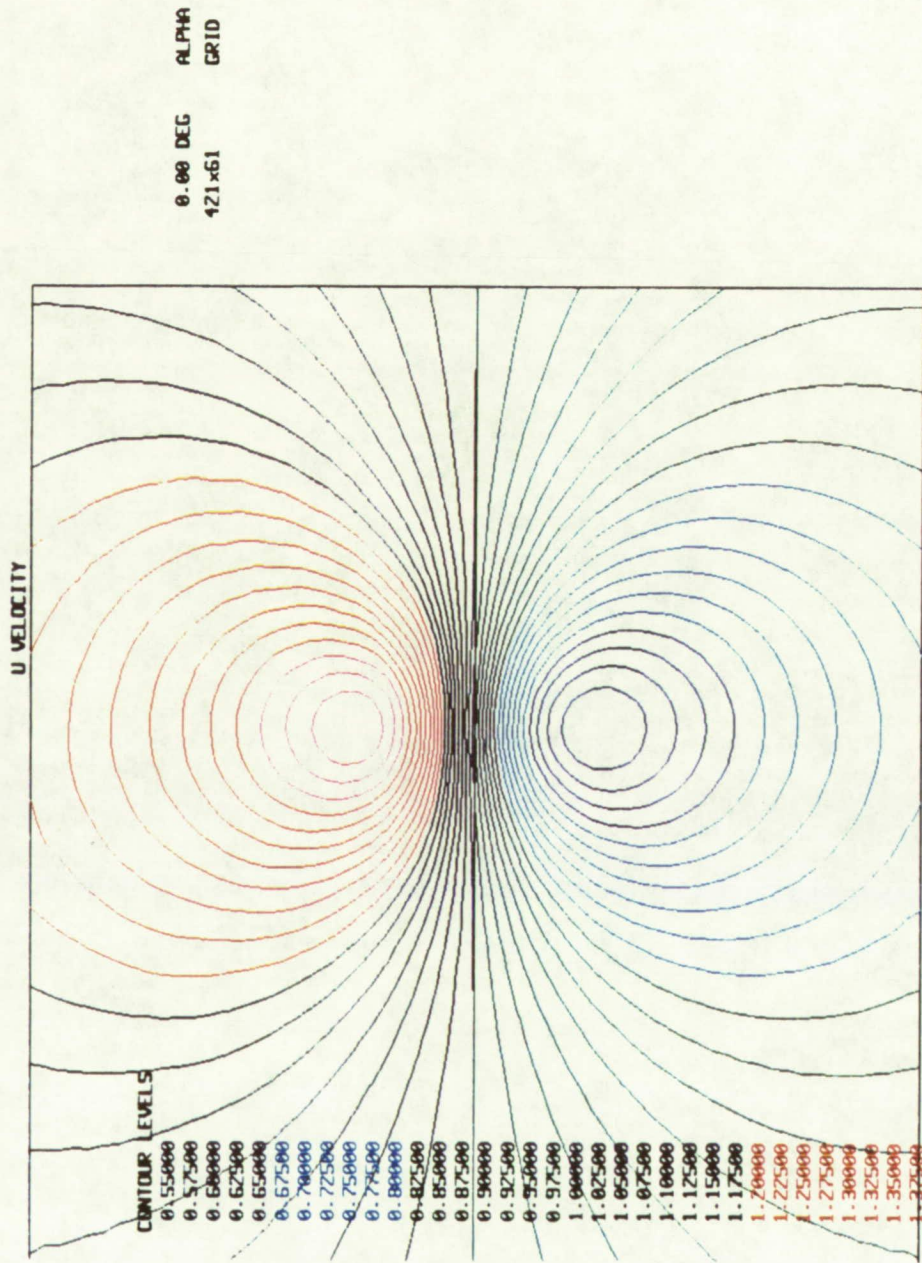


Fig. 33 Contours of Streamwise Velocity after 45 Core Radii of Travel

ORIGINAL PAGE
COLOR PHOTOGRAPH

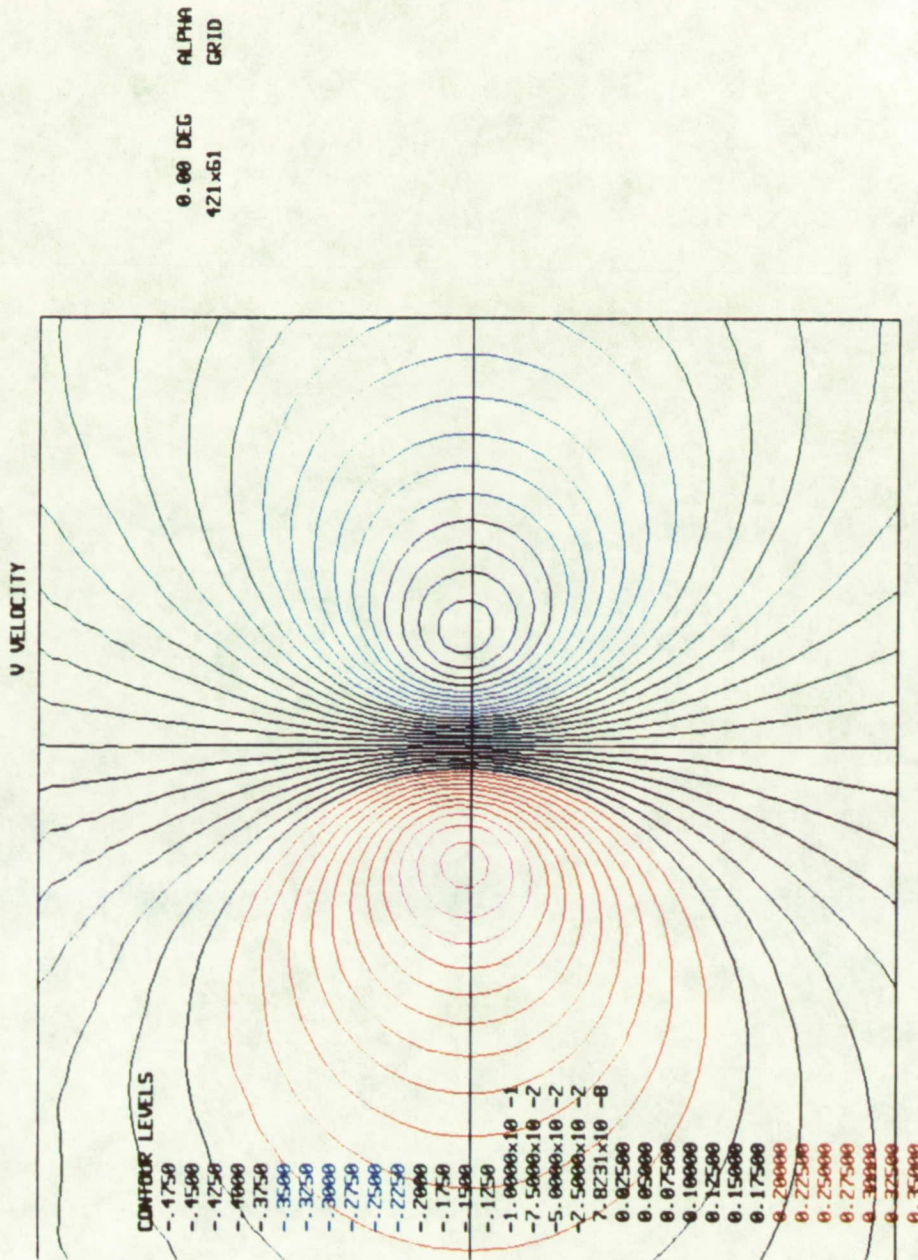


Fig. 34 Contours of Transverse Velocity after 45 Core Radii of Travel

ORIGINAL PAGE
COLOR PHOTOGRAPH

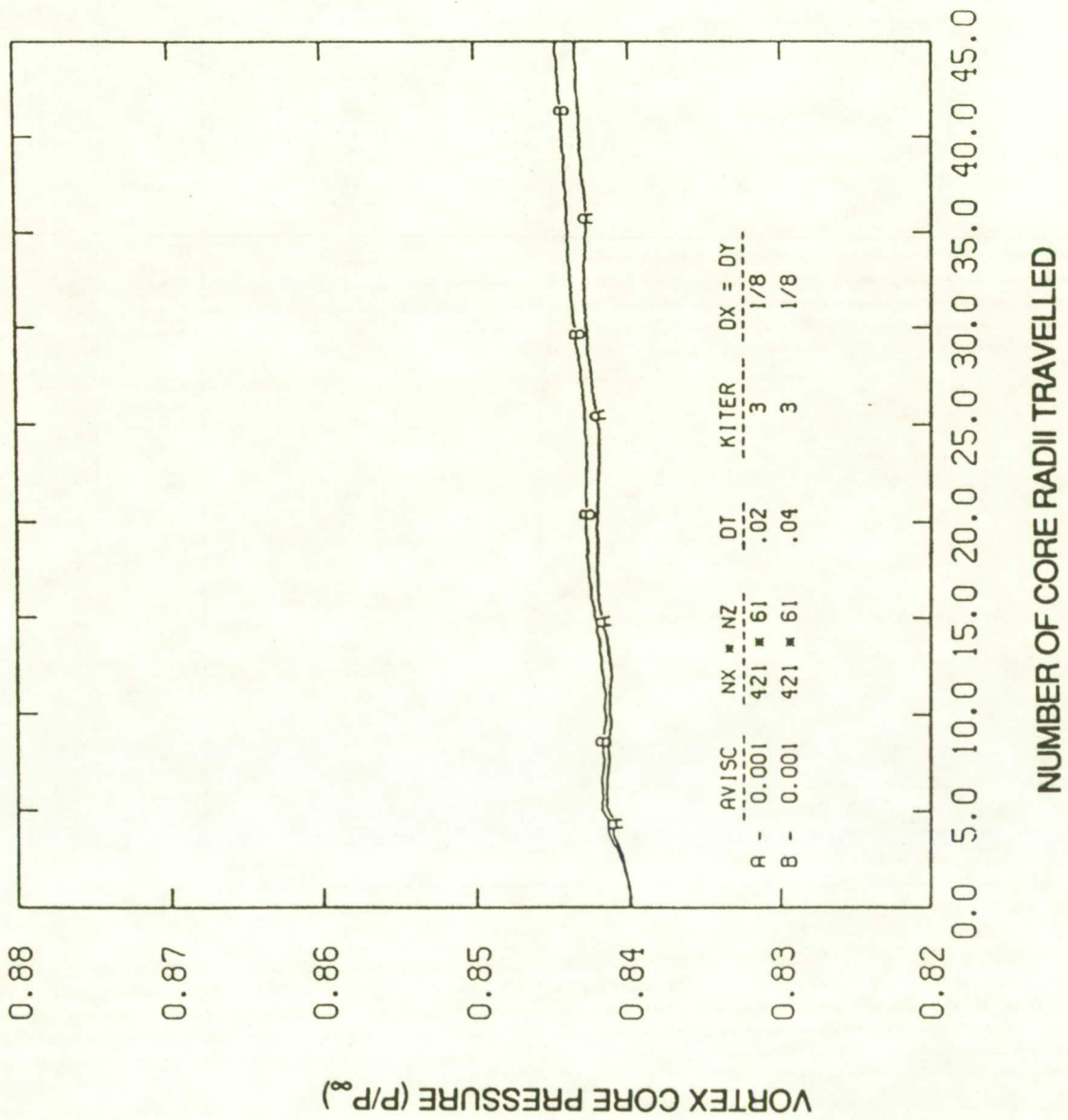


Fig. 35 Effects of Time Step on Vortex Decay

94 KODENKINKELF REAR

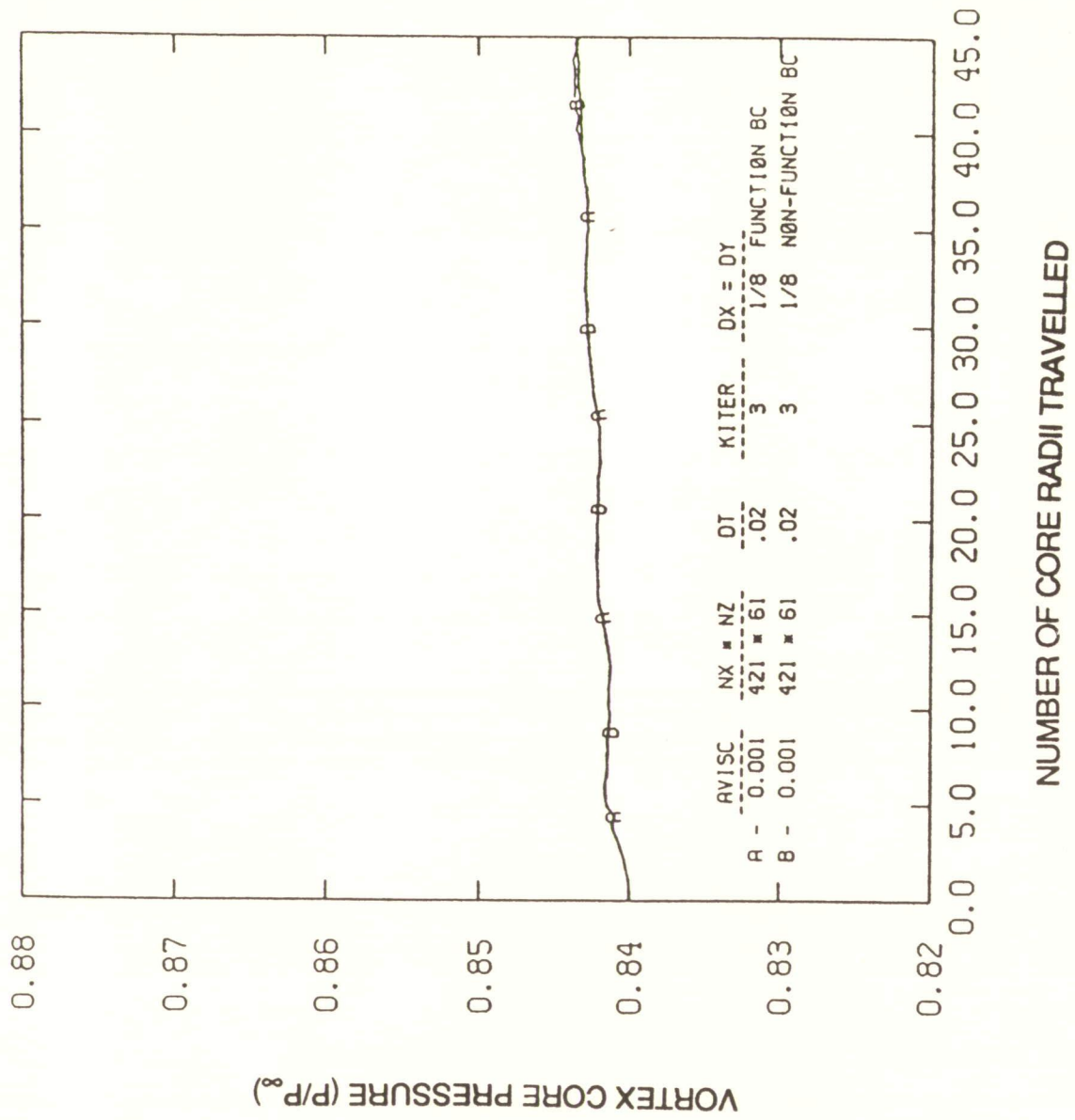


Fig. 36 Boundary Condition Effects on Vortex Decay

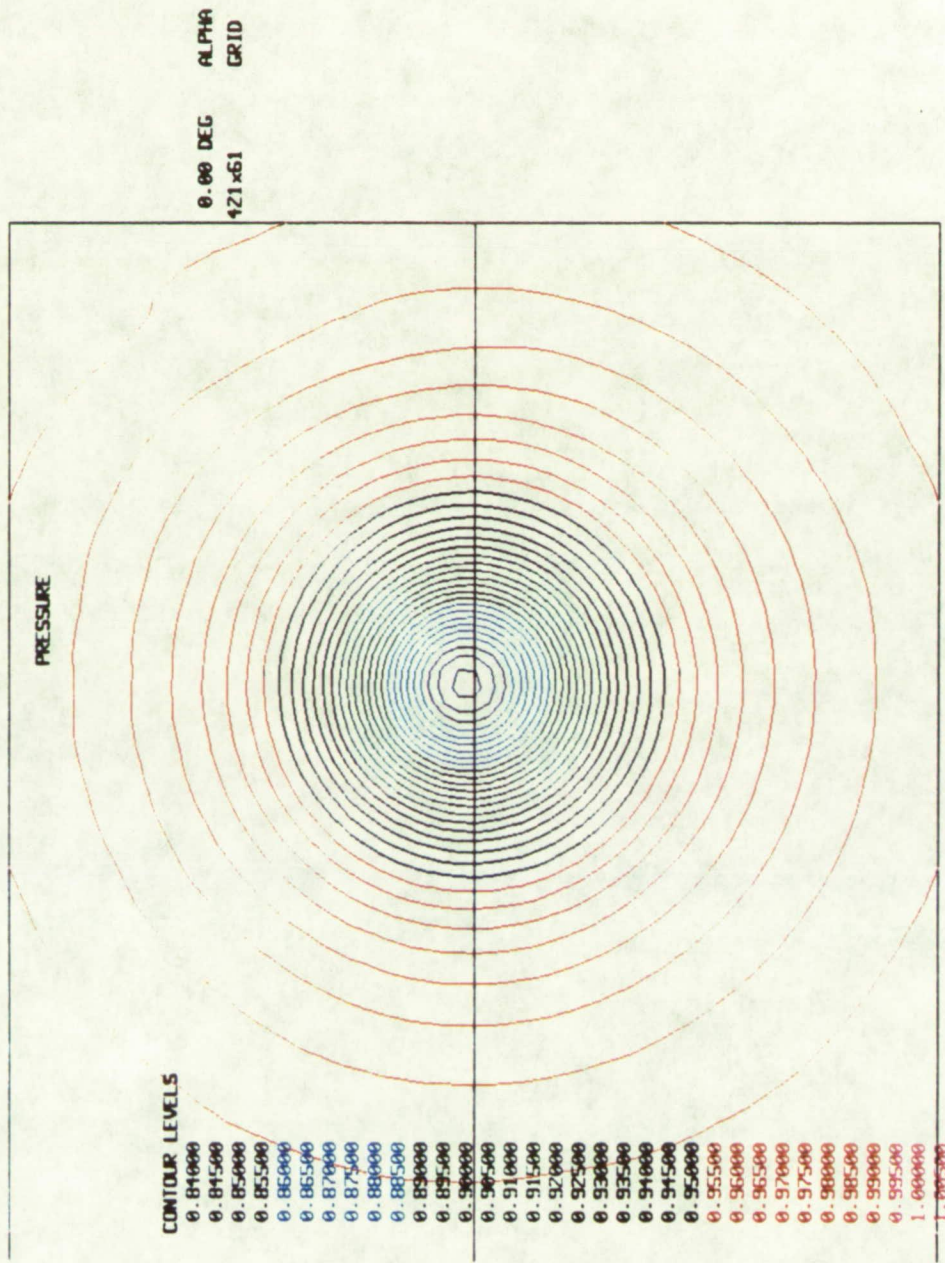
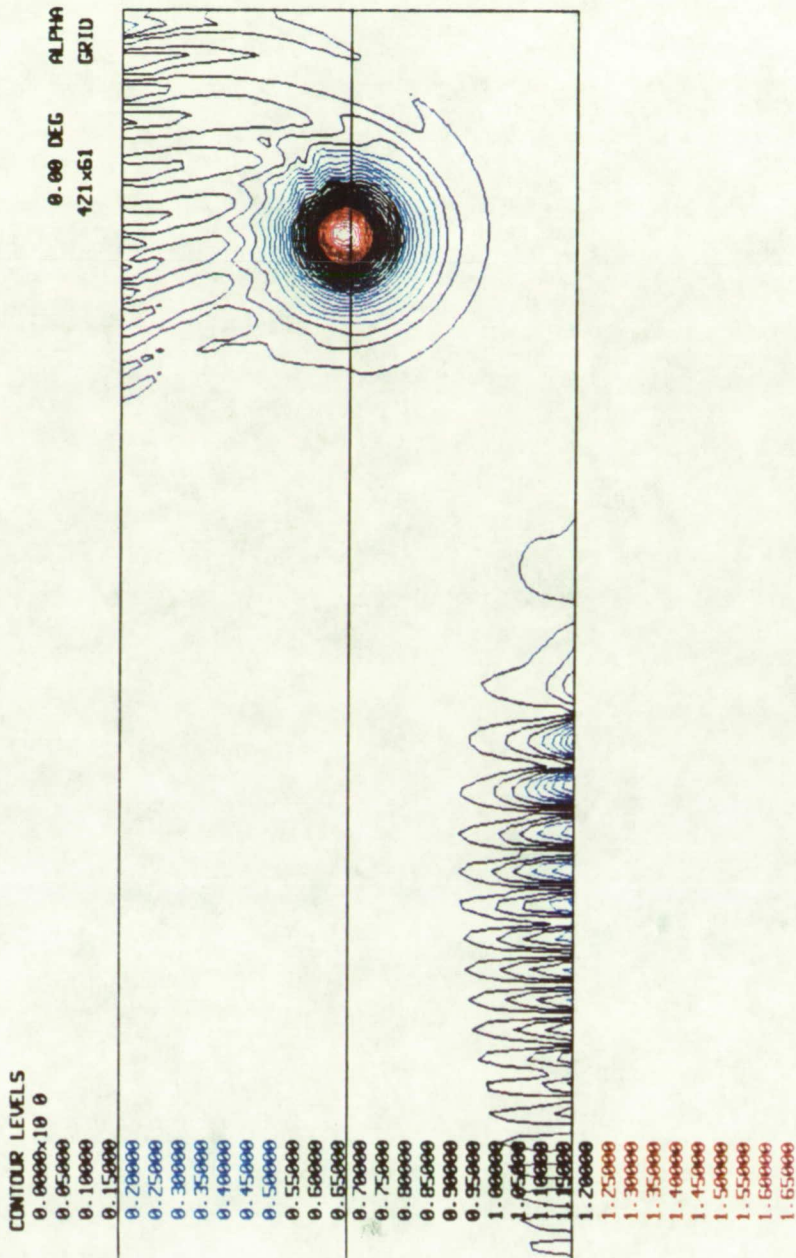


Fig. 37 Contours of Pressure after 45 Radii of Travel - Alternate Boundary Conditions Used

VORTICITY MAGNITUDE



ORIGINAL PAGE
COLOR PHOTOGRAPH

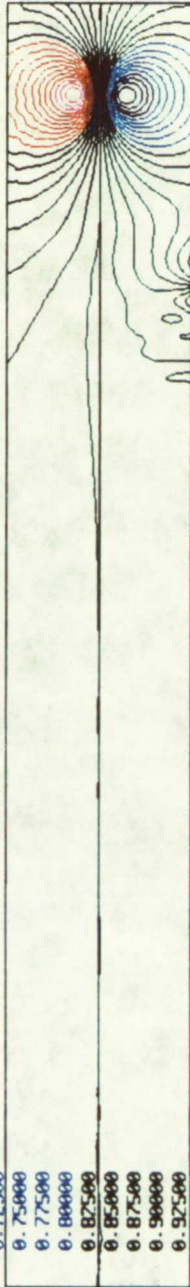
Fig. 38 Contours of Vorticity Magnitude after 45 Core Radii of Travel - Alternate Boundary Conditions Used

U VELOCITY

CONTOUR LEVELS

- 0.55000
- 0.57500
- 0.60000
- 0.62500
- 0.65000
- 0.67500
- 0.70000
- 0.72500
- 0.75000
- 0.77500
- 0.80000
- 0.82500
- 0.85000
- 0.87500
- 0.90000
- 0.92500
- 0.95000
- 0.97500
- 1.00000
- 1.02500
- 1.05000
- 1.07500
- 1.10000
- 1.12500
- 1.15000
- 1.17500
- 1.20000
- 1.22500
- 1.25000
- 1.27500
- 1.30000
- 1.32500
- 1.35000
- 1.37500

0.00 DEG ALPHA
421x61 GRID



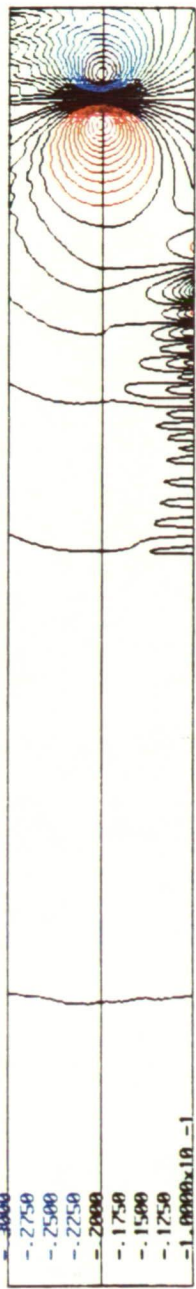
ORIGINAL PAGE
COLOR PHOTOGRAPH

Fig. 39 Contours of Streamwise Velocity after 45 Core Radii of Travel - Alternate Boundary Conditions Used

V VELOCITY

0.00 DEG ALPHA
421x61 GRID

- CONTOUR LEVELS
- 1.750
 - 1.500
 - 1.250
 - 1.000
 - 0.750
 - 0.500
 - 0.250
 - 0.000
 - 0.250
 - 0.500
 - 0.750
 - 1.000
 - 1.250
 - 1.500
 - 1.750
 - 2.000
 - 2.250
 - 2.500
 - 2.750
 - 3.000
 - 3.250
 - 3.500
 - 3.750
 - 4.000
 - 4.250
 - 4.500
 - 4.750
 - 5.000
 - 5.250
 - 5.500
 - 5.750
 - 6.000
 - 6.250
 - 6.500
 - 6.750
 - 7.000
 - 7.250
 - 7.500
 - 7.750
 - 8.000
 - 8.250
 - 8.500
 - 8.750
 - 9.000
 - 9.250
 - 9.500
 - 9.750
 - 10.000
 - 10.250
 - 10.500
 - 10.750
 - 11.000
 - 11.250
 - 11.500
 - 11.750
 - 12.000
 - 12.250
 - 12.500
 - 12.750
 - 13.000
 - 13.250
 - 13.500
 - 13.750
 - 14.000
 - 14.250
 - 14.500
 - 14.750
 - 15.000
 - 15.250
 - 15.500
 - 15.750
 - 16.000
 - 16.250
 - 16.500
 - 16.750
 - 17.000
 - 17.250
 - 17.500
 - 17.750
 - 18.000
 - 18.250
 - 18.500
 - 18.750
 - 19.000
 - 19.250
 - 19.500
 - 19.750
 - 20.000
 - 20.250
 - 20.500
 - 20.750
 - 21.000
 - 21.250
 - 21.500
 - 21.750
 - 22.000
 - 22.250
 - 22.500
 - 22.750
 - 23.000
 - 23.250
 - 23.500
 - 23.750
 - 24.000
 - 24.250
 - 24.500
 - 24.750
 - 25.000
 - 25.250
 - 25.500
 - 25.750
 - 26.000
 - 26.250
 - 26.500
 - 26.750
 - 27.000
 - 27.250
 - 27.500
 - 27.750
 - 28.000
 - 28.250
 - 28.500
 - 28.750
 - 29.000
 - 29.250
 - 29.500
 - 29.750
 - 30.000
 - 30.250
 - 30.500
 - 30.750
 - 31.000
 - 31.250
 - 31.500
 - 31.750
 - 32.000
 - 32.250
 - 32.500
 - 32.750
 - 33.000
 - 33.250
 - 33.500
 - 33.750
 - 34.000
 - 34.250
 - 34.500
 - 34.750
 - 35.000
 - 35.250
 - 35.500
 - 35.750
 - 36.000
 - 36.250
 - 36.500
 - 36.750
 - 37.000
 - 37.250
 - 37.500
 - 37.750
 - 38.000
 - 38.250
 - 38.500
 - 38.750
 - 39.000
 - 39.250
 - 39.500
 - 39.750
 - 40.000
 - 40.250
 - 40.500
 - 40.750
 - 41.000
 - 41.250
 - 41.500
 - 41.750
 - 42.000
 - 42.250
 - 42.500
 - 42.750
 - 43.000
 - 43.250
 - 43.500
 - 43.750
 - 44.000
 - 44.250
 - 44.500
 - 44.750
 - 45.000
 - 45.250
 - 45.500
 - 45.750
 - 46.000
 - 46.250
 - 46.500
 - 46.750
 - 47.000
 - 47.250
 - 47.500
 - 47.750
 - 48.000
 - 48.250
 - 48.500
 - 48.750
 - 49.000
 - 49.250
 - 49.500
 - 49.750
 - 50.000
 - 50.250
 - 50.500
 - 50.750
 - 51.000
 - 51.250
 - 51.500
 - 51.750
 - 52.000
 - 52.250
 - 52.500
 - 52.750
 - 53.000
 - 53.250
 - 53.500
 - 53.750
 - 54.000
 - 54.250
 - 54.500
 - 54.750
 - 55.000
 - 55.250
 - 55.500
 - 55.750
 - 56.000
 - 56.250
 - 56.500
 - 56.750
 - 57.000
 - 57.250
 - 57.500
 - 57.750
 - 58.000
 - 58.250
 - 58.500
 - 58.750
 - 59.000
 - 59.250
 - 59.500
 - 59.750
 - 60.000
 - 60.250
 - 60.500
 - 60.750
 - 61.000
 - 61.250
 - 61.500
 - 61.750
 - 62.000
 - 62.250
 - 62.500
 - 62.750
 - 63.000
 - 63.250
 - 63.500
 - 63.750
 - 64.000
 - 64.250
 - 64.500
 - 64.750
 - 65.000
 - 65.250
 - 65.500
 - 65.750
 - 66.000
 - 66.250
 - 66.500
 - 66.750
 - 67.000
 - 67.250
 - 67.500
 - 67.750
 - 68.000
 - 68.250
 - 68.500
 - 68.750
 - 69.000
 - 69.250
 - 69.500
 - 69.750
 - 70.000
 - 70.250
 - 70.500
 - 70.750
 - 71.000
 - 71.250
 - 71.500
 - 71.750
 - 72.000
 - 72.250
 - 72.500
 - 72.750
 - 73.000
 - 73.250
 - 73.500
 - 73.750
 - 74.000
 - 74.250
 - 74.500
 - 74.750
 - 75.000
 - 75.250
 - 75.500
 - 75.750
 - 76.000
 - 76.250
 - 76.500
 - 76.750
 - 77.000
 - 77.250
 - 77.500
 - 77.750
 - 78.000
 - 78.250
 - 78.500
 - 78.750
 - 79.000
 - 79.250
 - 79.500
 - 79.750
 - 80.000
 - 80.250
 - 80.500
 - 80.750
 - 81.000
 - 81.250
 - 81.500
 - 81.750
 - 82.000
 - 82.250
 - 82.500
 - 82.750
 - 83.000
 - 83.250
 - 83.500
 - 83.750
 - 84.000
 - 84.250
 - 84.500
 - 84.750
 - 85.000
 - 85.250
 - 85.500
 - 85.750
 - 86.000
 - 86.250
 - 86.500
 - 86.750
 - 87.000
 - 87.250
 - 87.500
 - 87.750
 - 88.000
 - 88.250
 - 88.500
 - 88.750
 - 89.000
 - 89.250
 - 89.500
 - 89.750
 - 90.000
 - 90.250
 - 90.500
 - 90.750
 - 91.000
 - 91.250
 - 91.500
 - 91.750
 - 92.000
 - 92.250
 - 92.500
 - 92.750
 - 93.000
 - 93.250
 - 93.500
 - 93.750
 - 94.000
 - 94.250
 - 94.500
 - 94.750
 - 95.000
 - 95.250
 - 95.500
 - 95.750
 - 96.000
 - 96.250
 - 96.500
 - 96.750
 - 97.000
 - 97.250
 - 97.500
 - 97.750
 - 98.000
 - 98.250
 - 98.500
 - 98.750
 - 99.000
 - 99.250
 - 99.500
 - 99.750
 - 100.000



ORIGINAL PAGE
COLOR PHOTOGRAPH

Fig. 40 Contours of Transverse Velocity after 45 Core Radii of Travel - Alternate Boundary Conditions Used

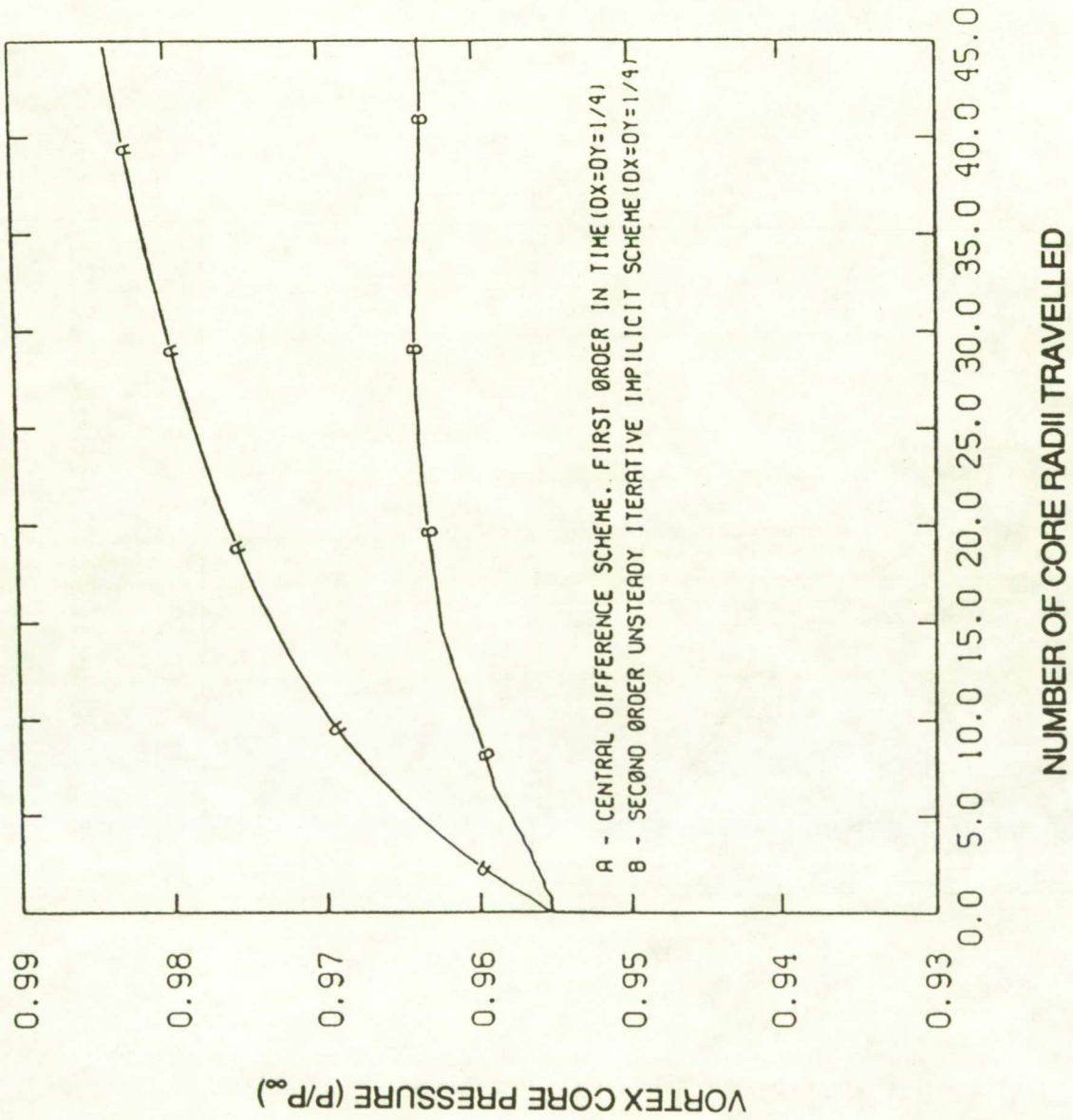


Fig. 41 Vortex Decay Rate for the Weaker Vortex

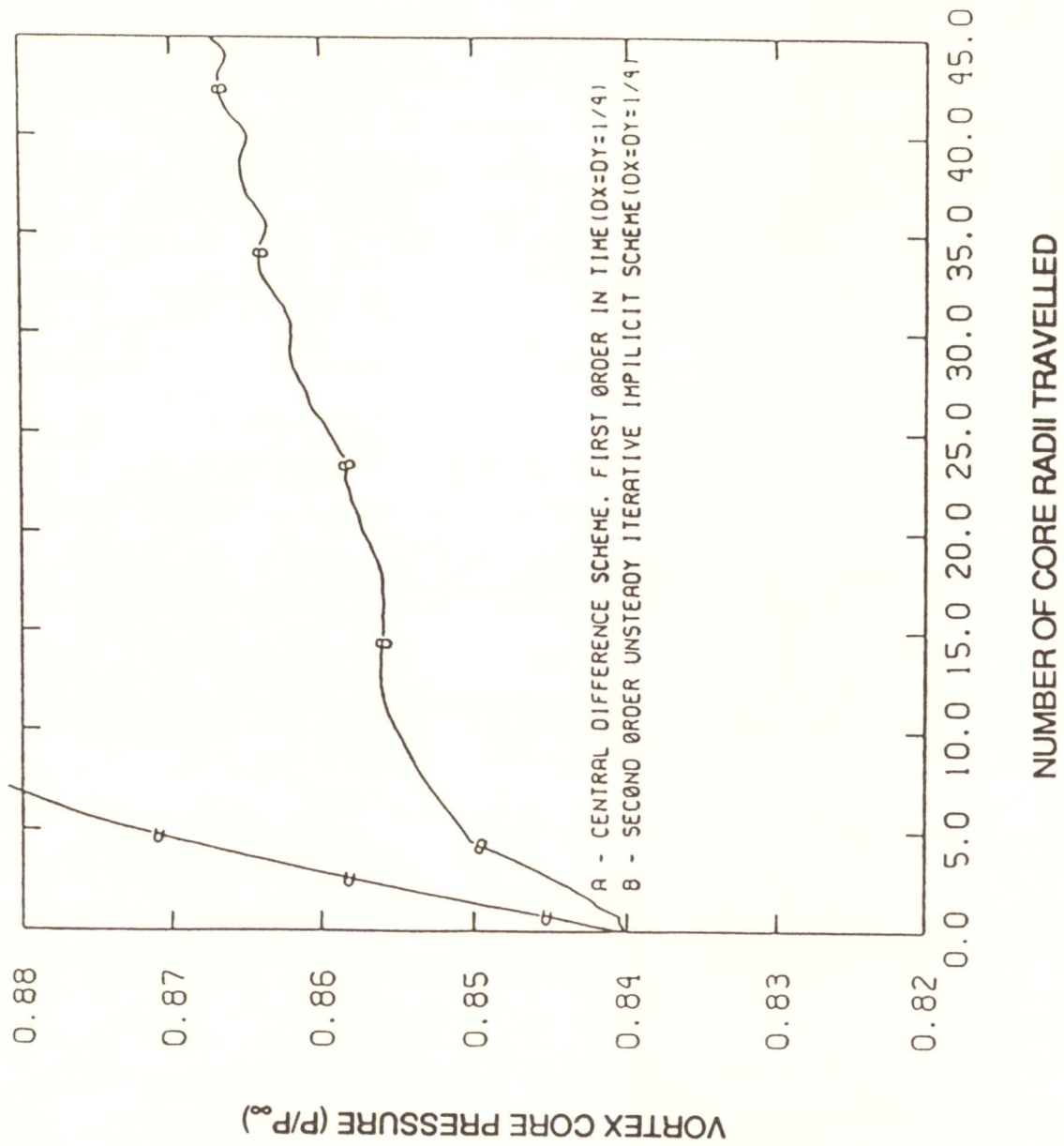


Fig. 42 Vortex Decay Rate for the Stronger Vortex

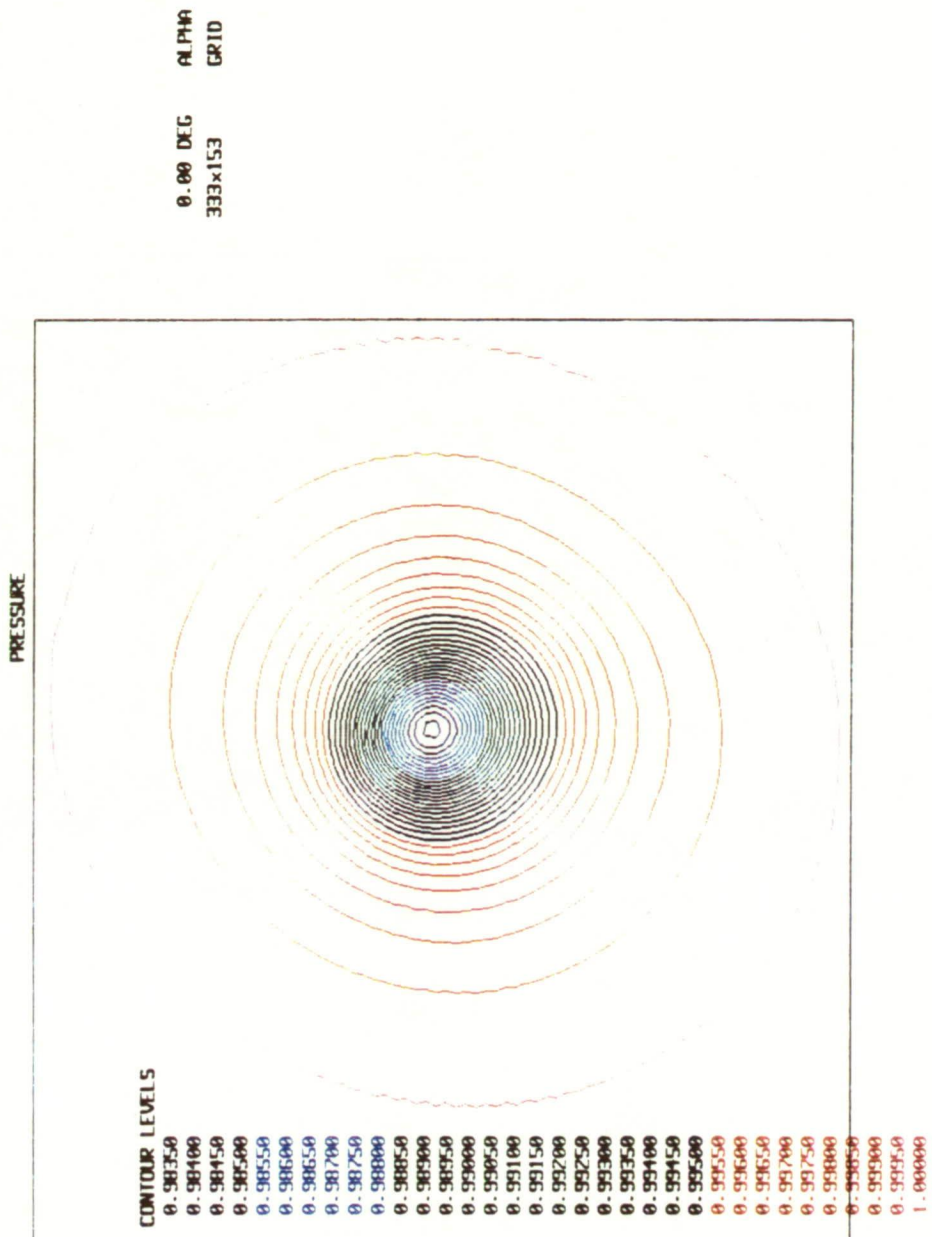


Fig. 43 Pressure Contours after 45 Radii of Vortex Travel for Weaker Vortex. Central Difference Scheme - First Order Accurate in Time.

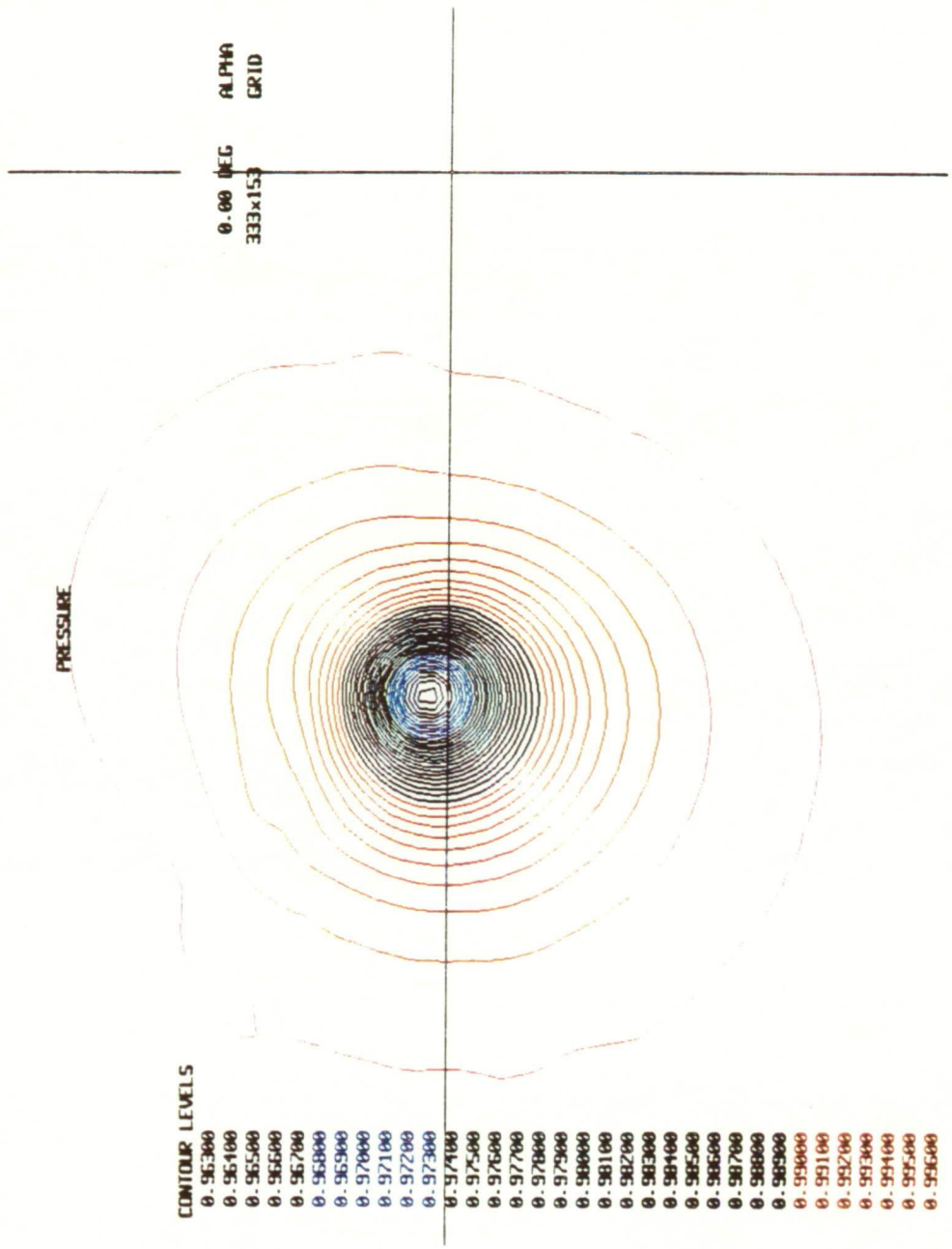


Fig. 44 Pressure Contours after 45 Core Radii of Vortex Travel for Weaker Vortex. Second Order Unsteady Iterative Implicit Scheme.

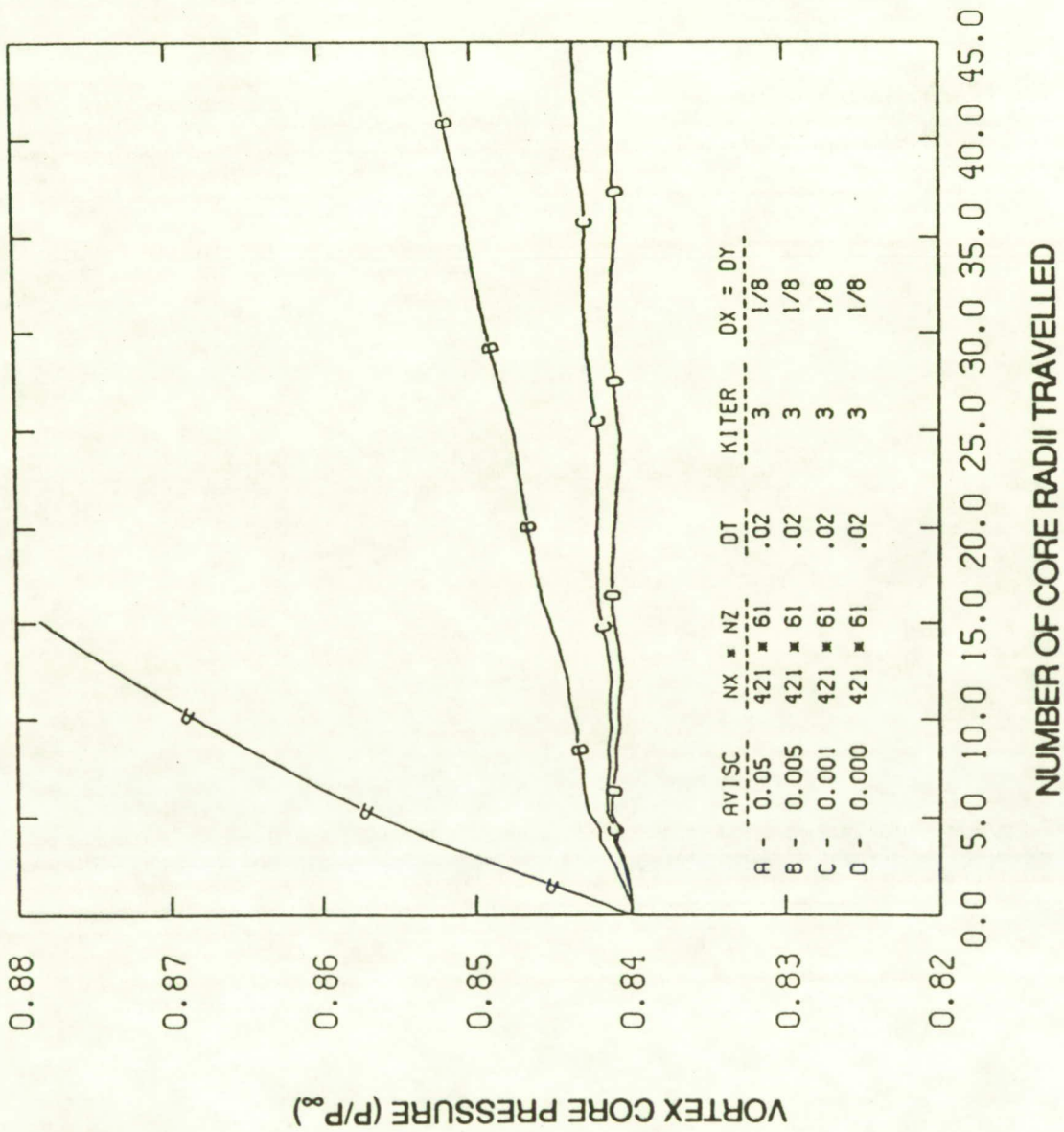


Fig. 45 Effects of Artificial Dissipation on Vortex Decay

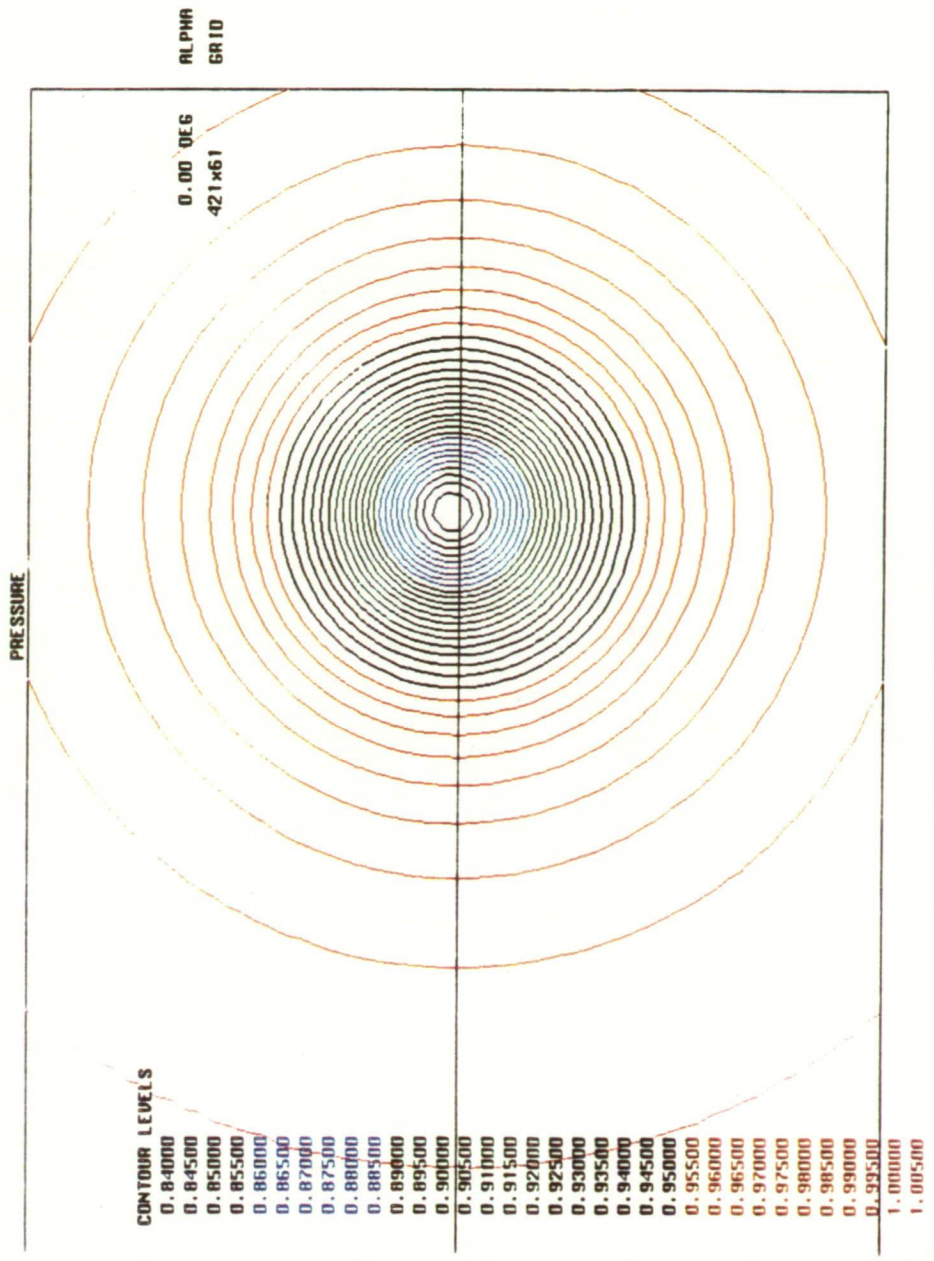


Fig. 46 Pressure Contours after 45 Core Radii of Travel, AVISC=0.00

112 INTENTIONALLY BLANK

ORIGINAL PAGE
COLOR PHOTOGRAPH

PRECEDING PAGE BLANK NOT FILMED

VORTICITY MAGNITUDE

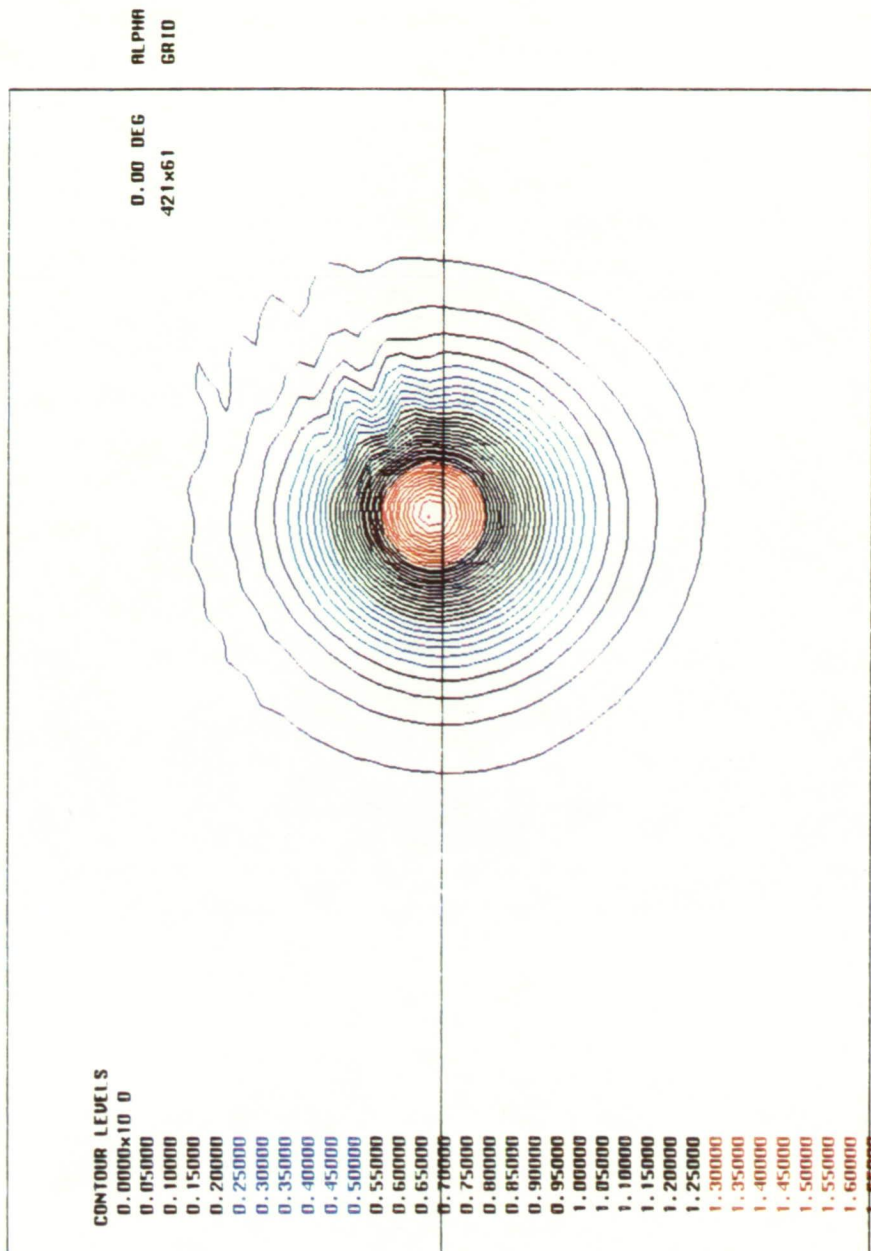


Fig. 47 Vorticity Magnitude Contours after 45 Radii of Travel, AVISC=0.00

ORIGINAL PAGE
COLOR PHOTOGRAPH

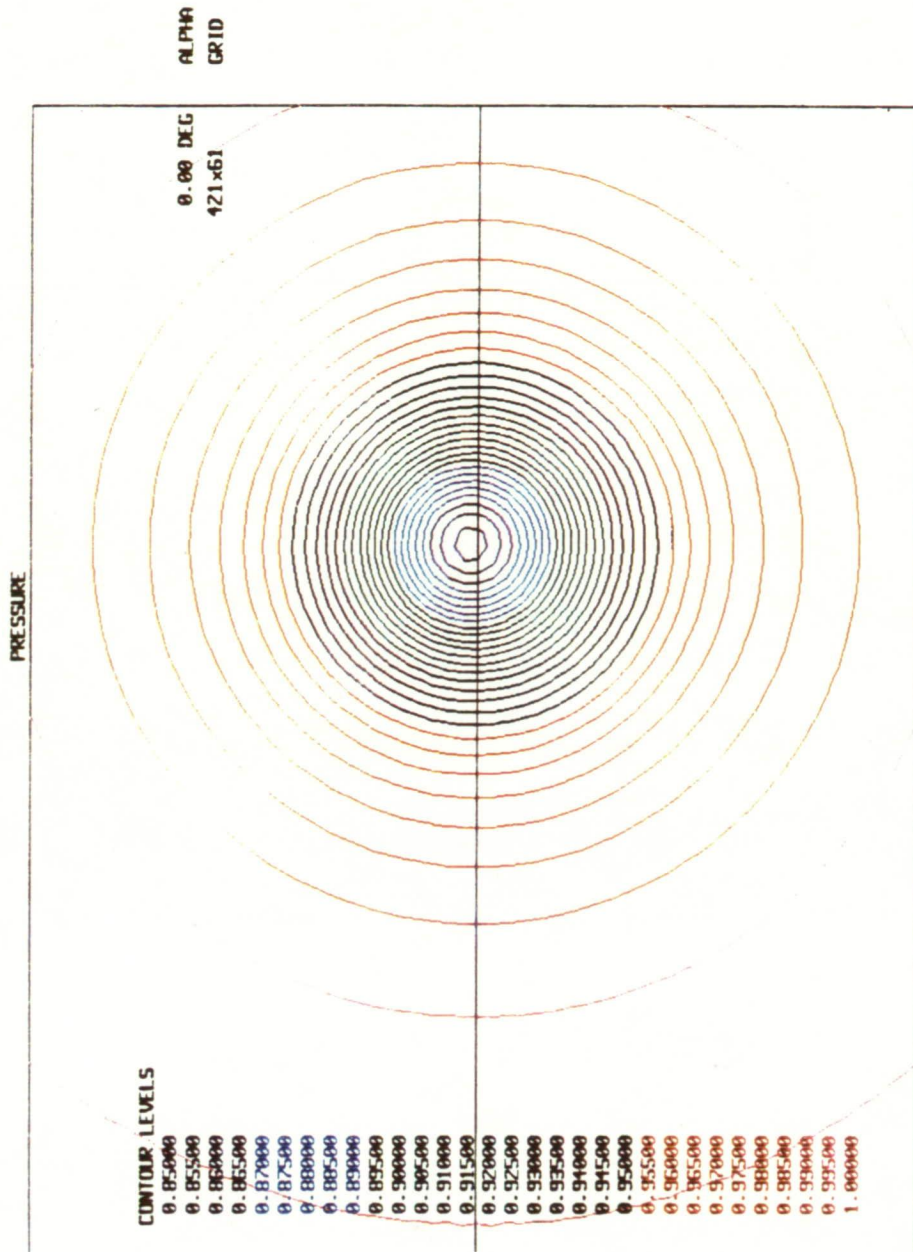


Fig. 48 Pressure Contours after 45 Radii of Travel, AVISC=0.005

ORIGINAL PAGE
 COLOR PHOTOGRAPH

116 INTENTIONALLY BLANK

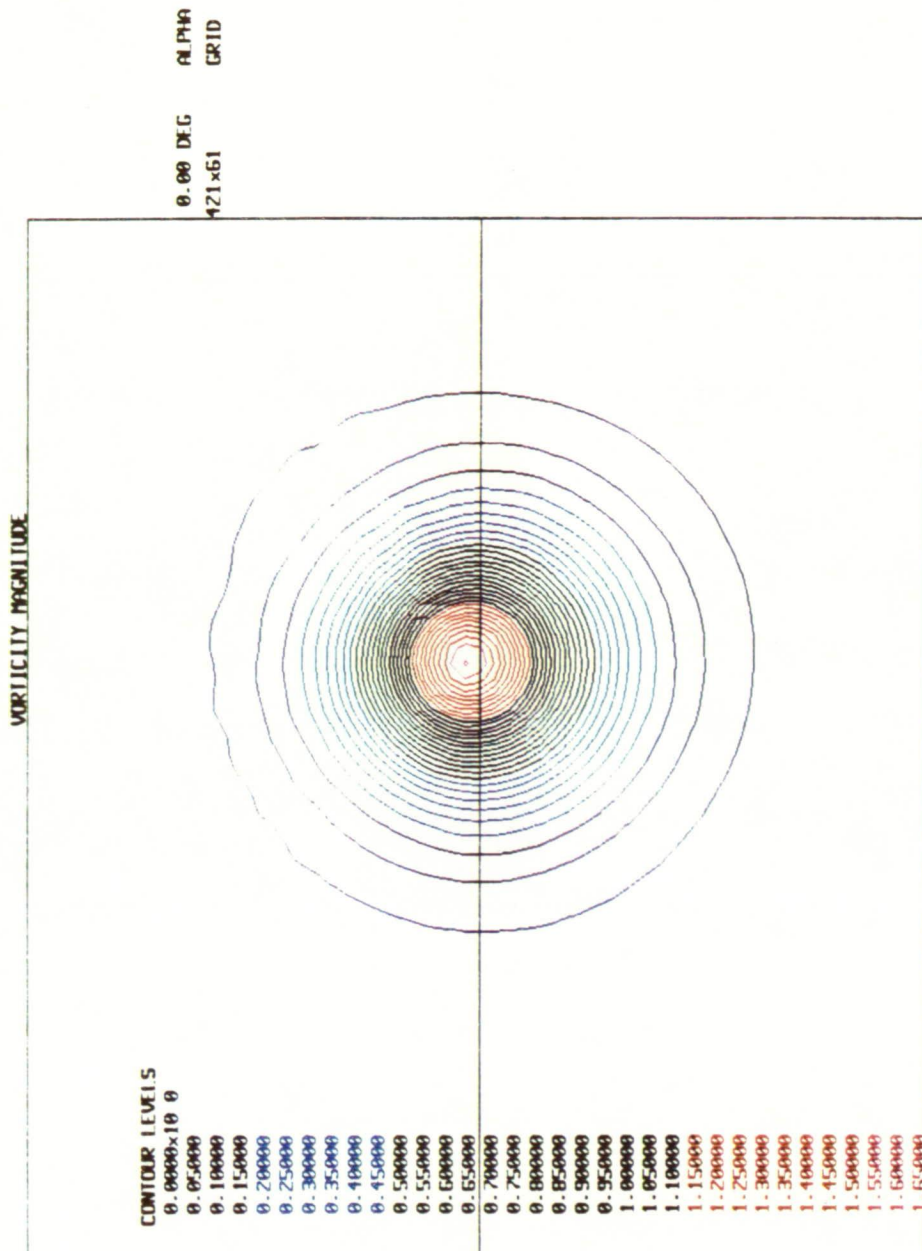


Fig. 49 Vorticity Magnitude Contours after 45 Radii of Travel, AVISC=0.005

ORIGINAL PAGE
COLOR PHOTOGRAPH

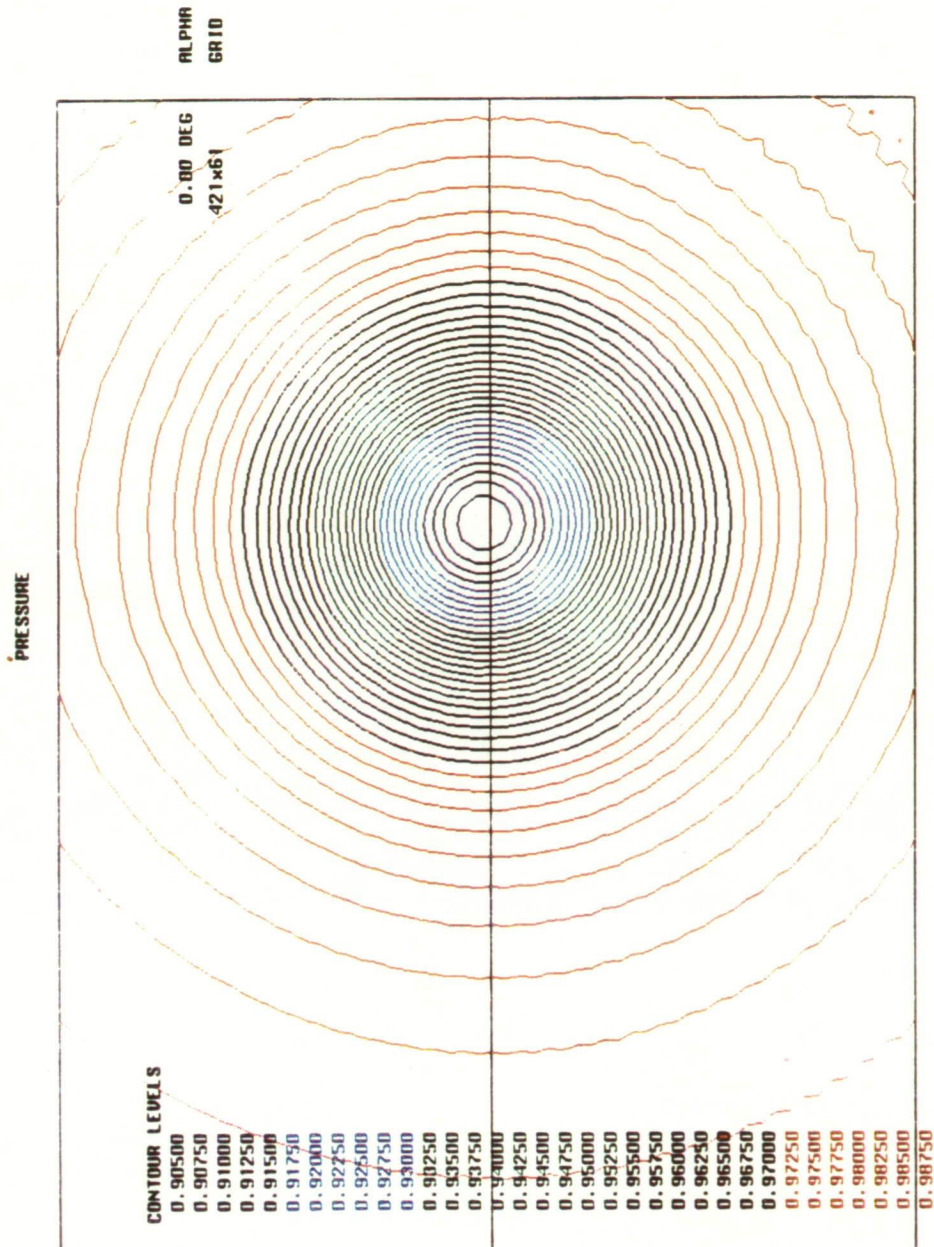


Fig. 50 Pressure Contours after 45 Radii of Travel, AVISC=0.05

ORIGINAL PAGE
COLOR PHOTOGRAPH

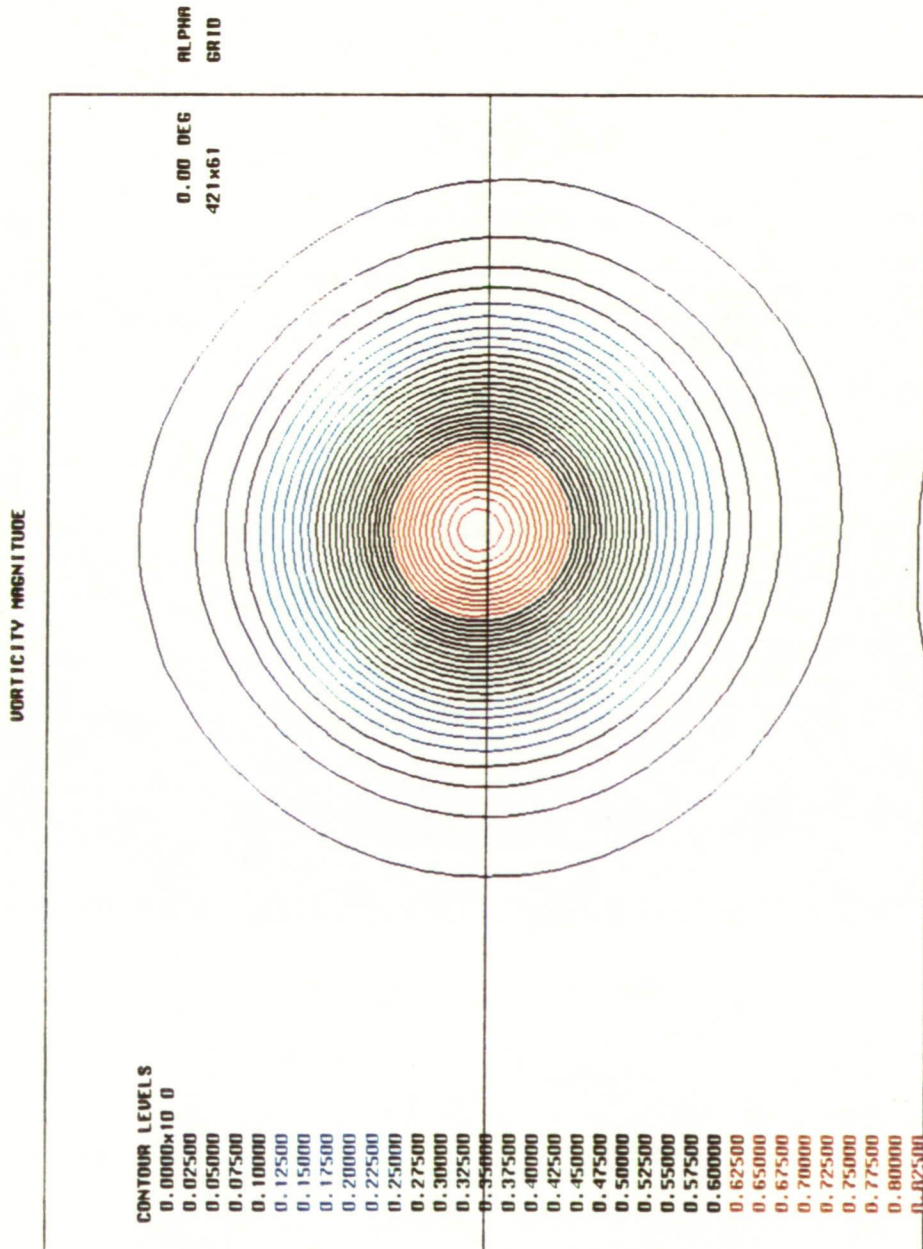


Fig. 51 Vorticity Magnitude Contours after 45 Radii of Travel, AVISC=0.05

ORIGINAL PAGE
COLOR PHOTOGRAPH

122 INTENTIONALLY BLANK

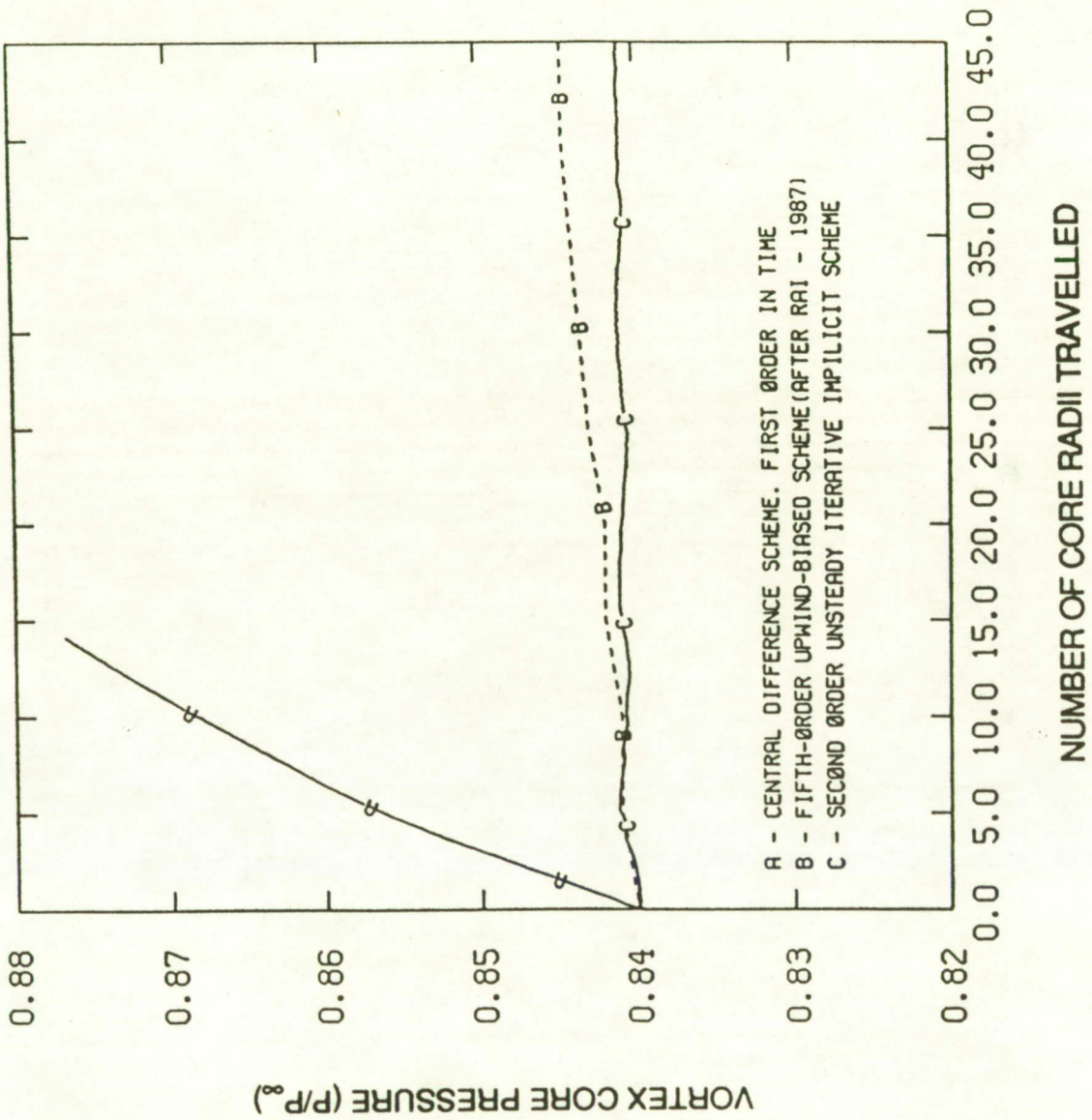


Fig. 52 Vortex Decay Rates for Different Schemes

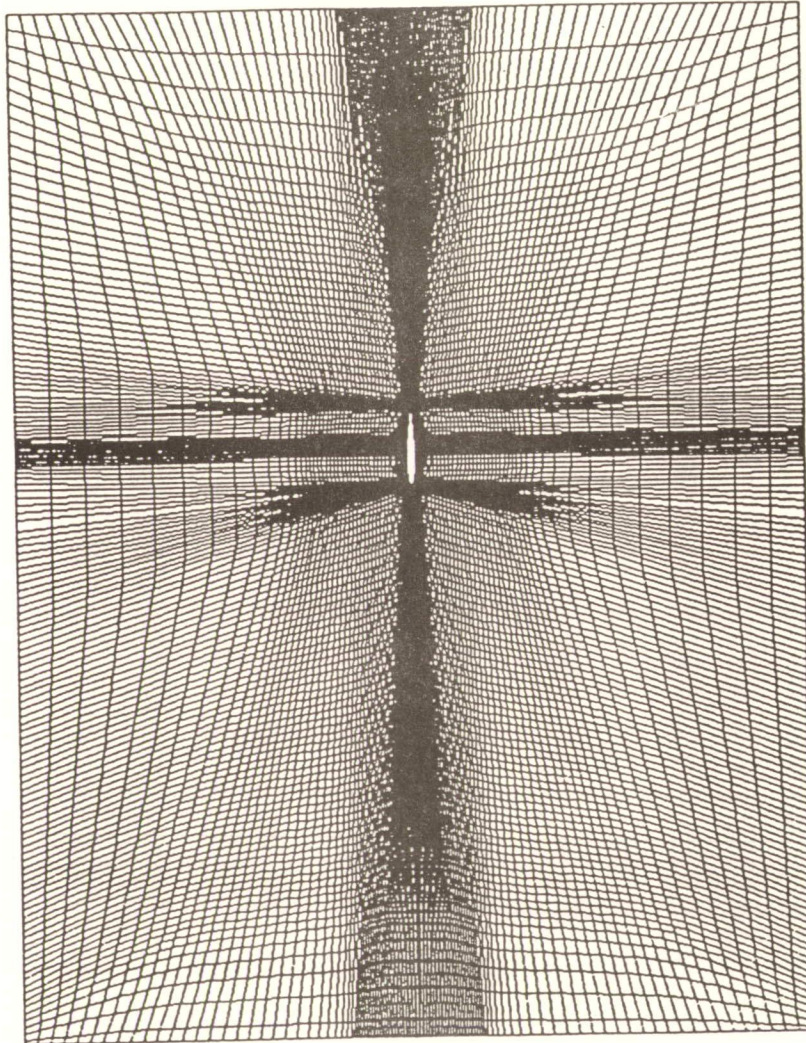
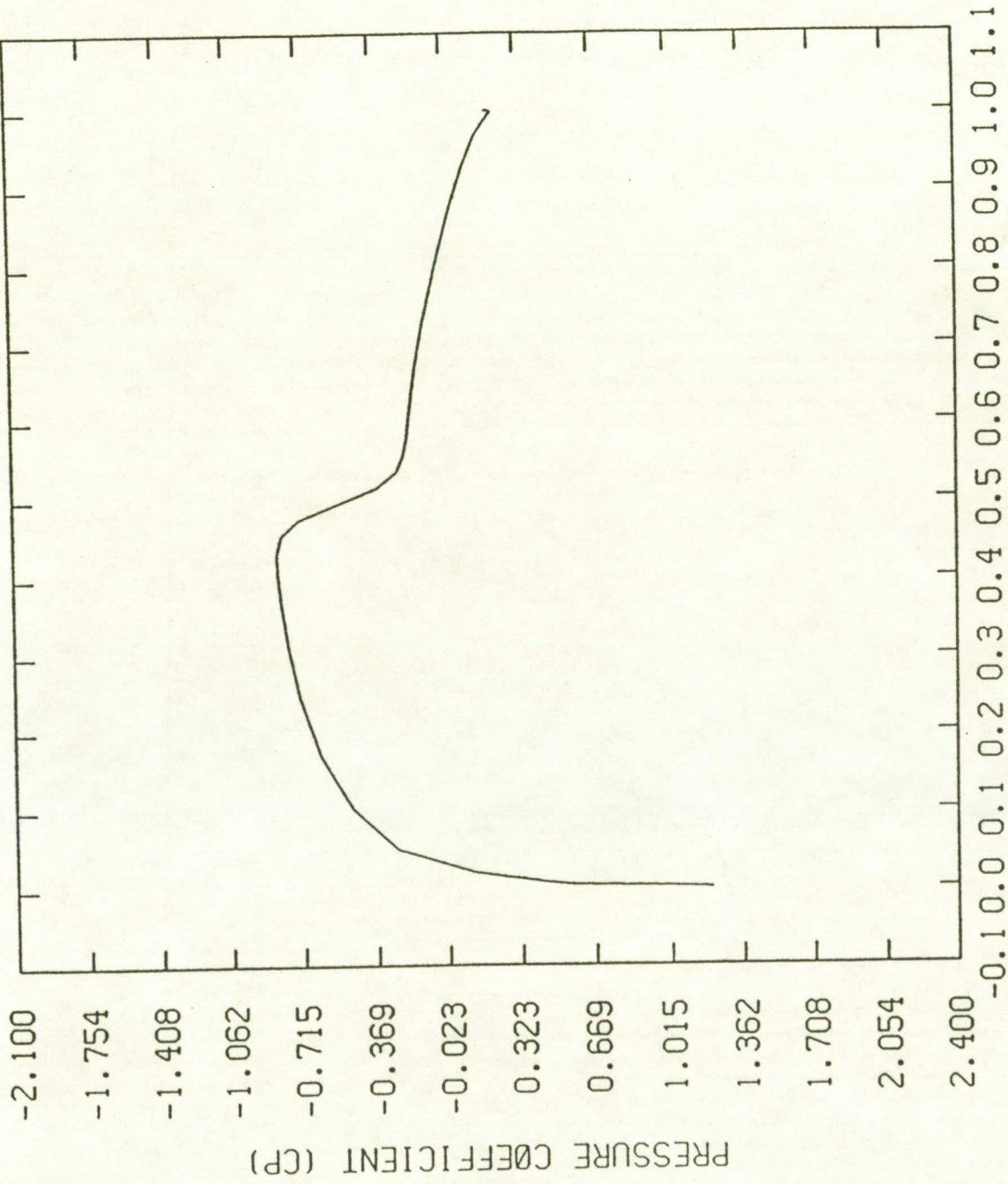


Fig. 53 Grid Distribution for BVI Simulation.



AXIAL DISTANCE FROM LEADING EDGE (X)

Fig. 54 Blade Surface Pressure Distribution (Background Flow).

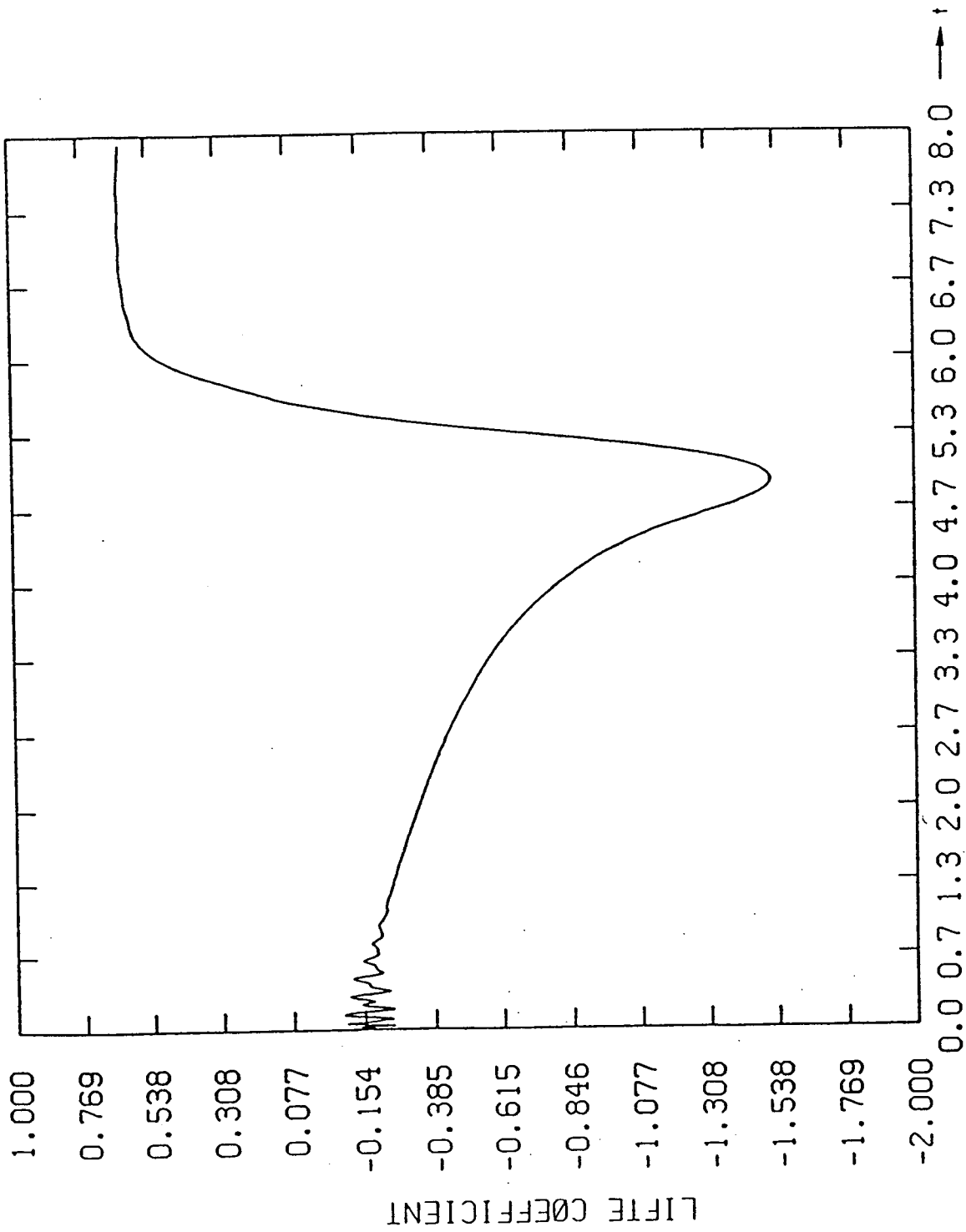


Fig. 55 Time History of the Lift Coefficient, C_L .

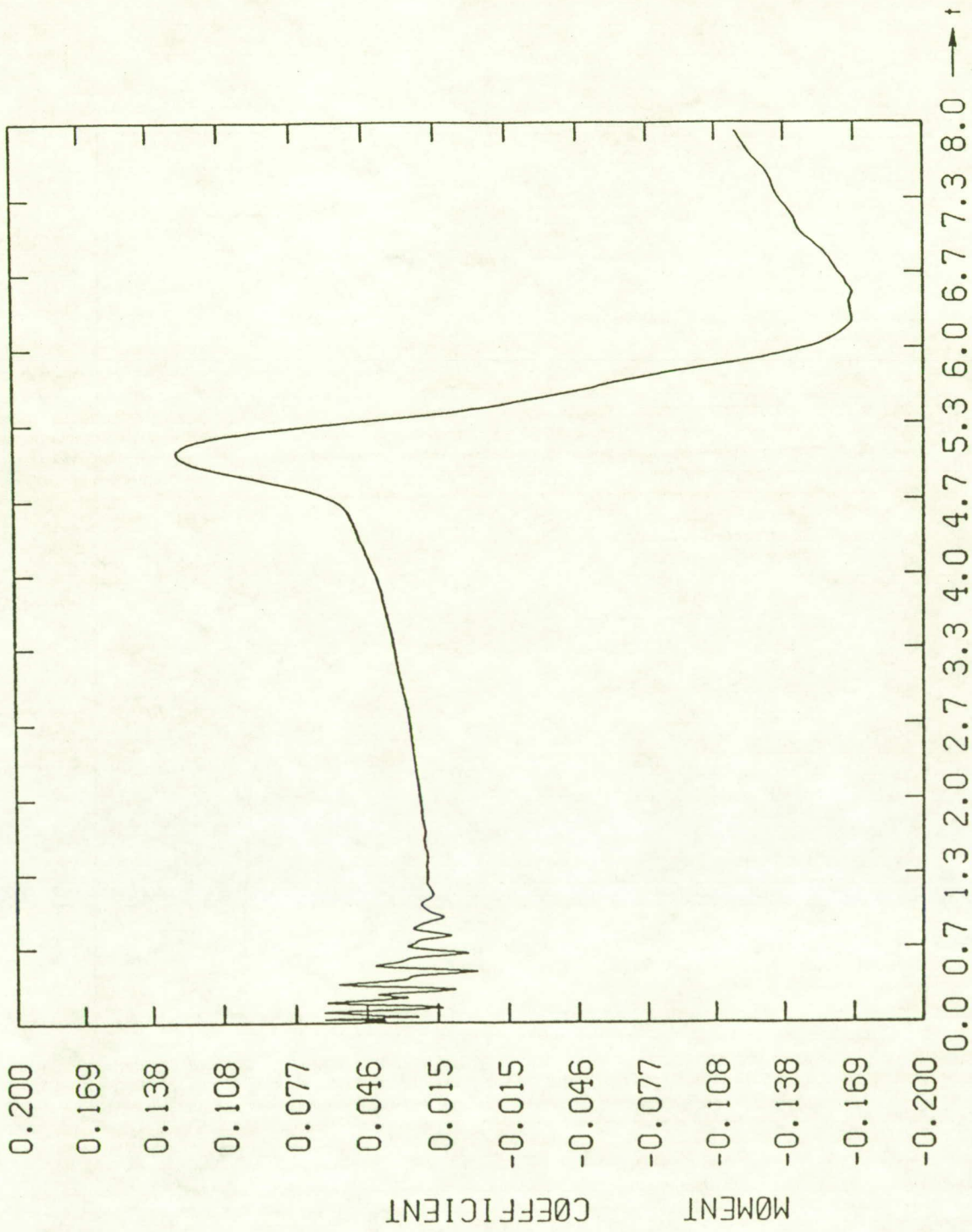


Fig. 56 Time History of the Quarter-Chord Pitching Moment Coefficient, C_M .

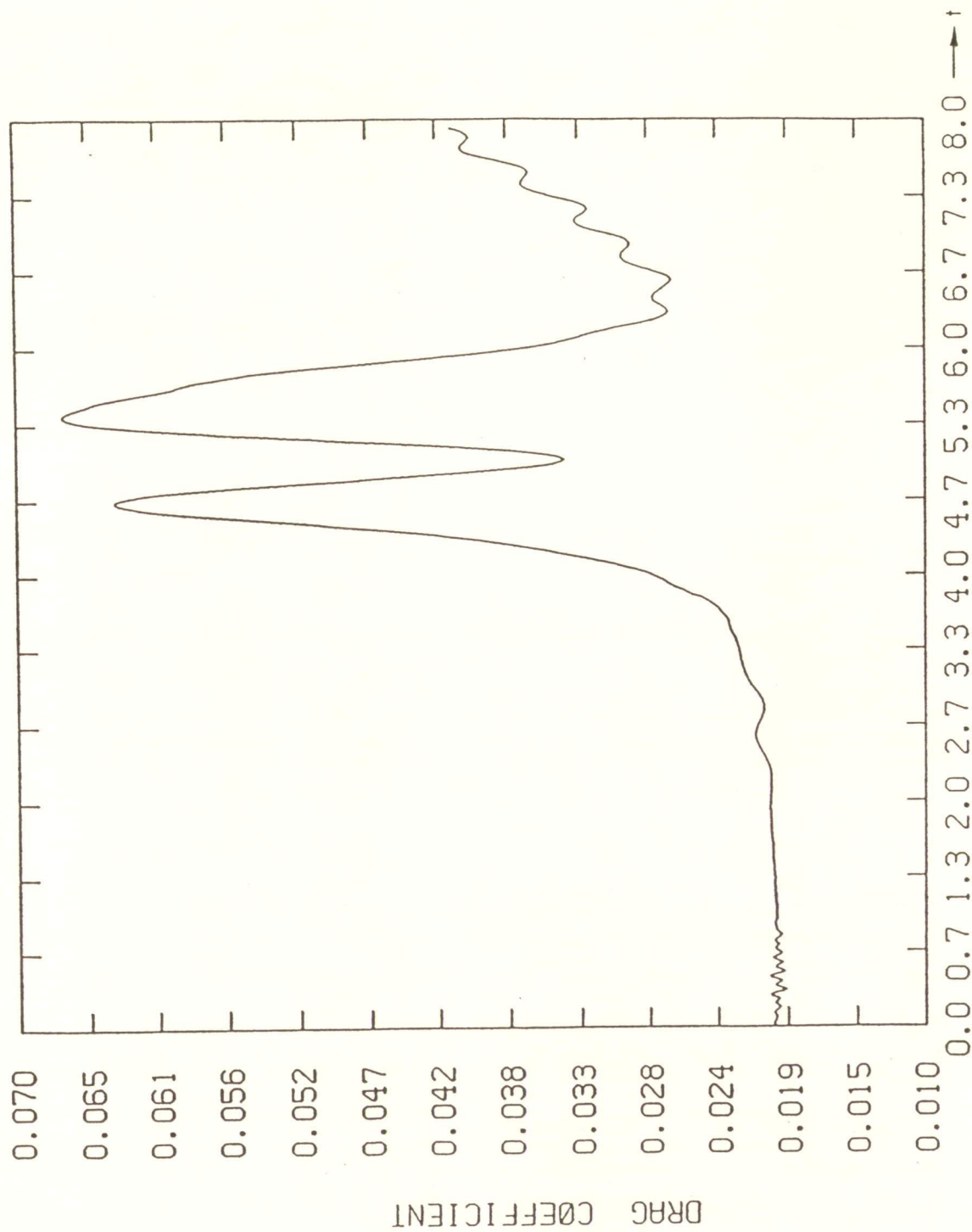


Fig. 57 Time History of the Drag Coefficient, C_D .

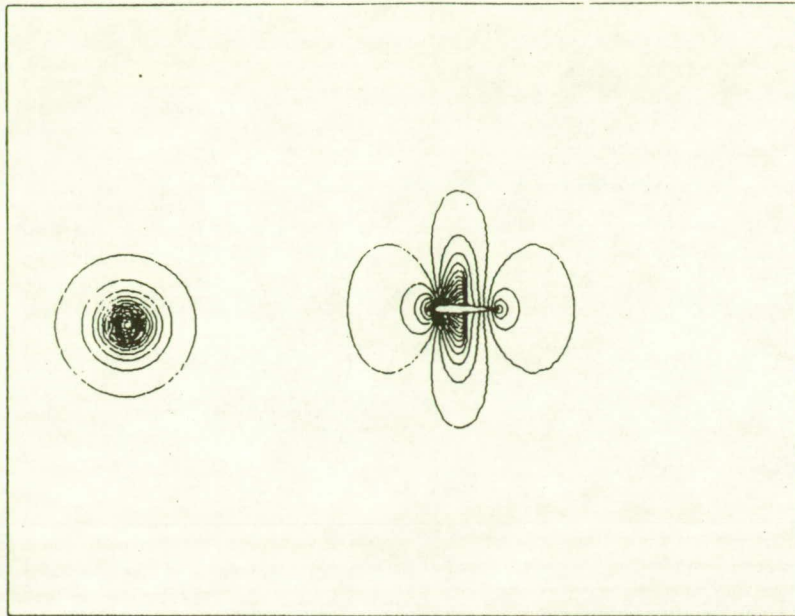


Fig. 58a Static Pressure Contours (t=0)

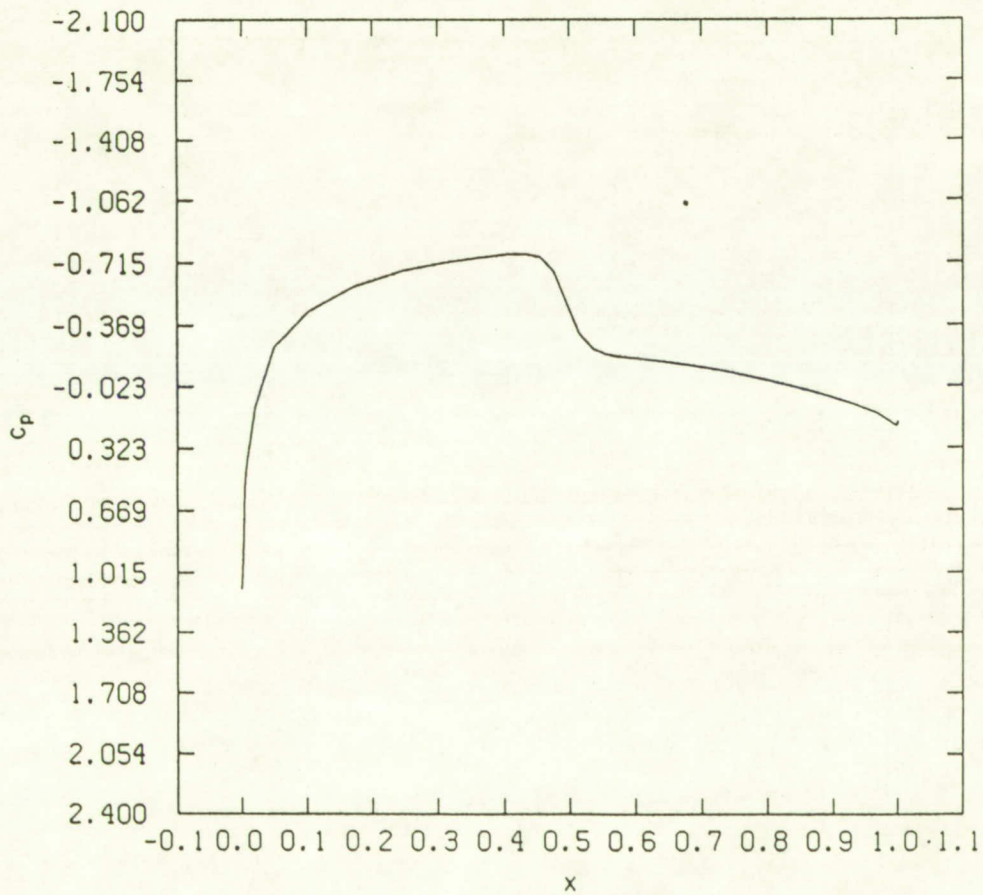


Fig. 58b Surface C_p (t=0)

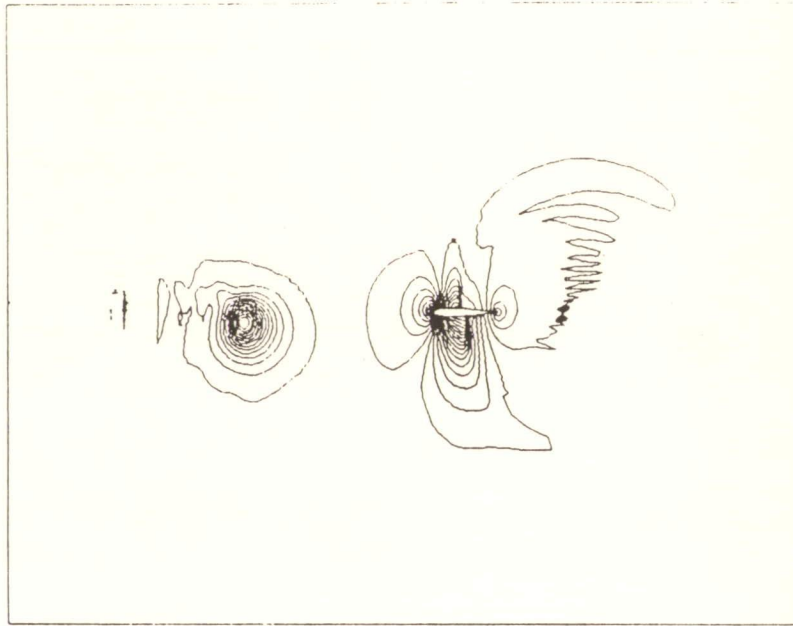


Fig. 59a Static Pressure Contours (t=2.0)

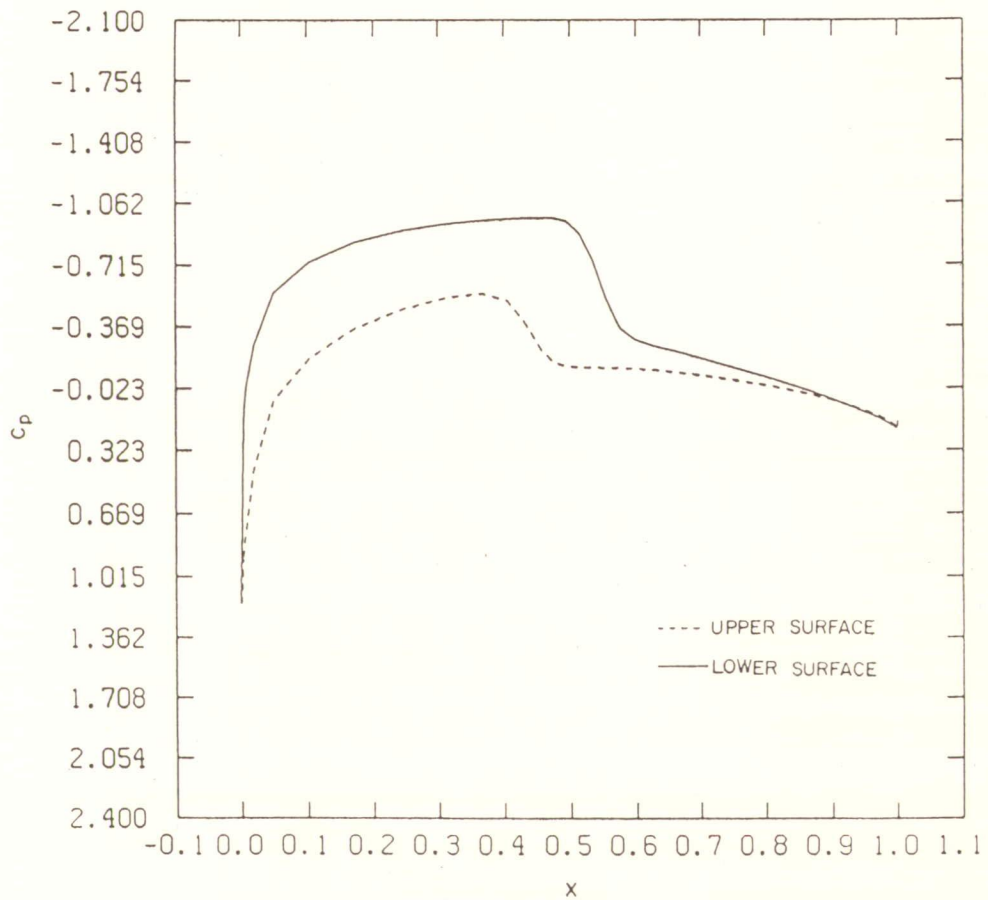


Fig. 59b Surface C_p (t=2.0)

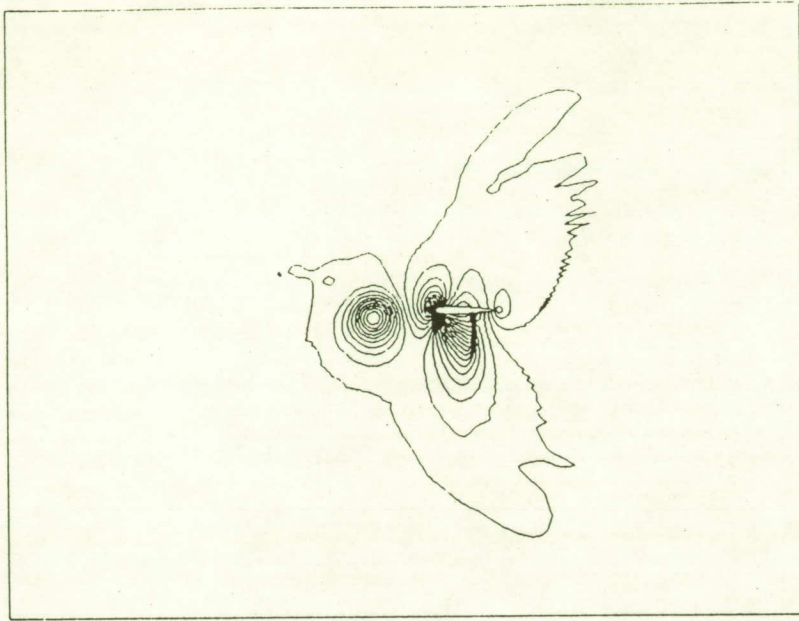


Fig. 60a Pressure Contours (t=4.0)

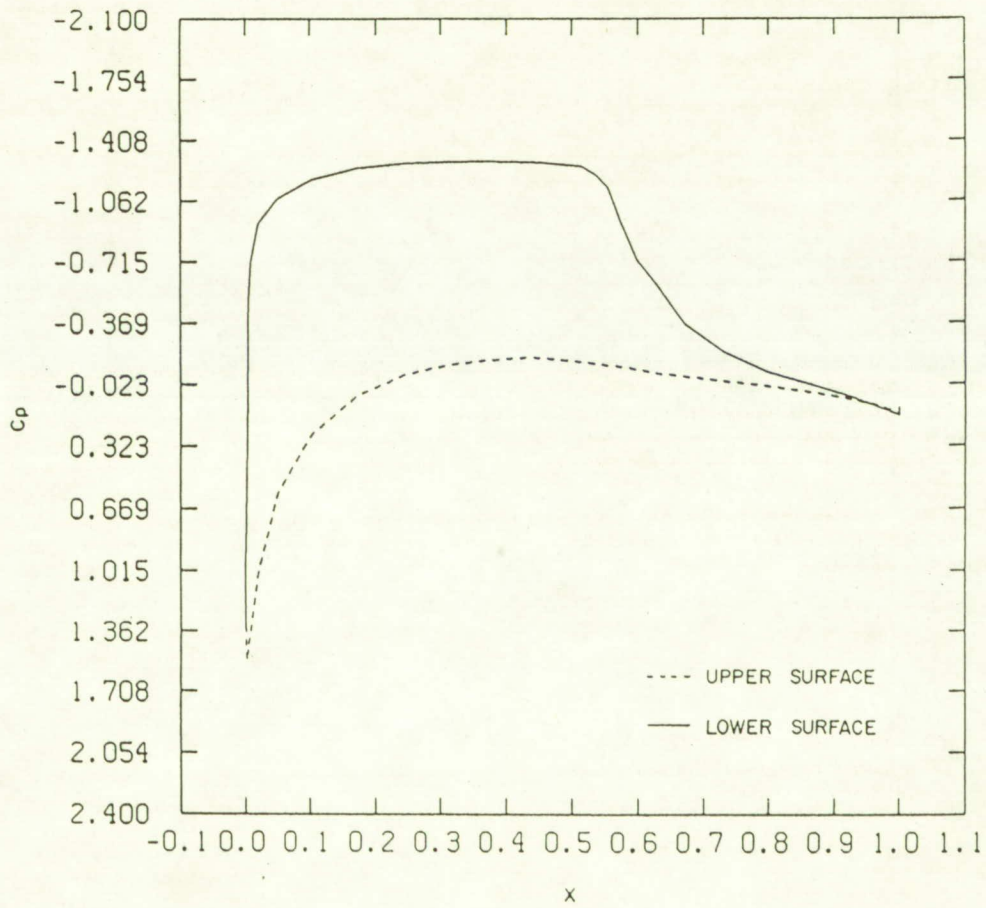


Fig. 60b Surface C_p (t=4.0)

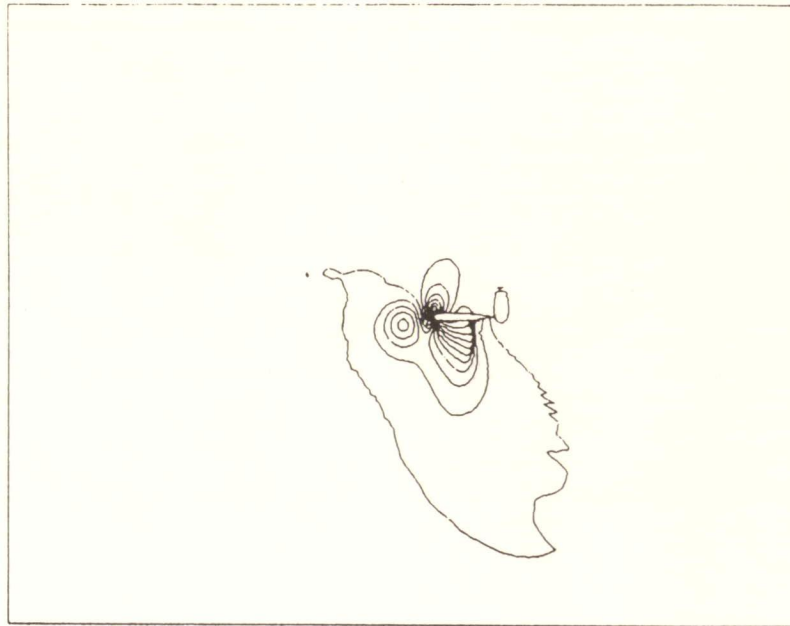


Fig. 61a Pressure Contours ($t=4.5$)

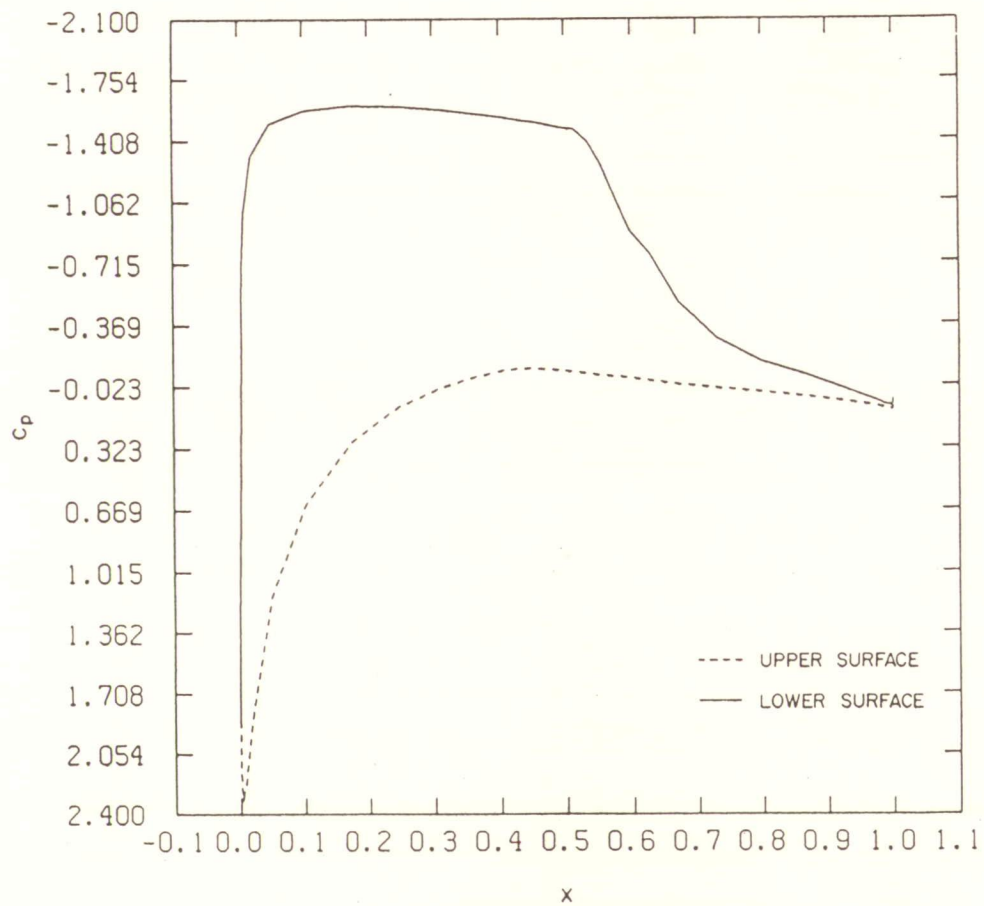


Fig. 61b Surface C_p ($t=4.5$)

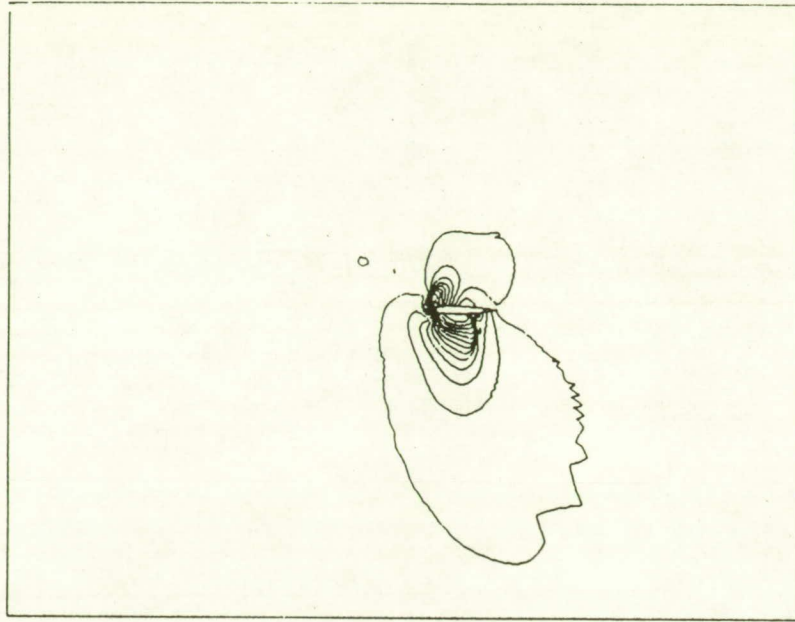


Fig. 62a Pressure Contours ($t=5.0$)

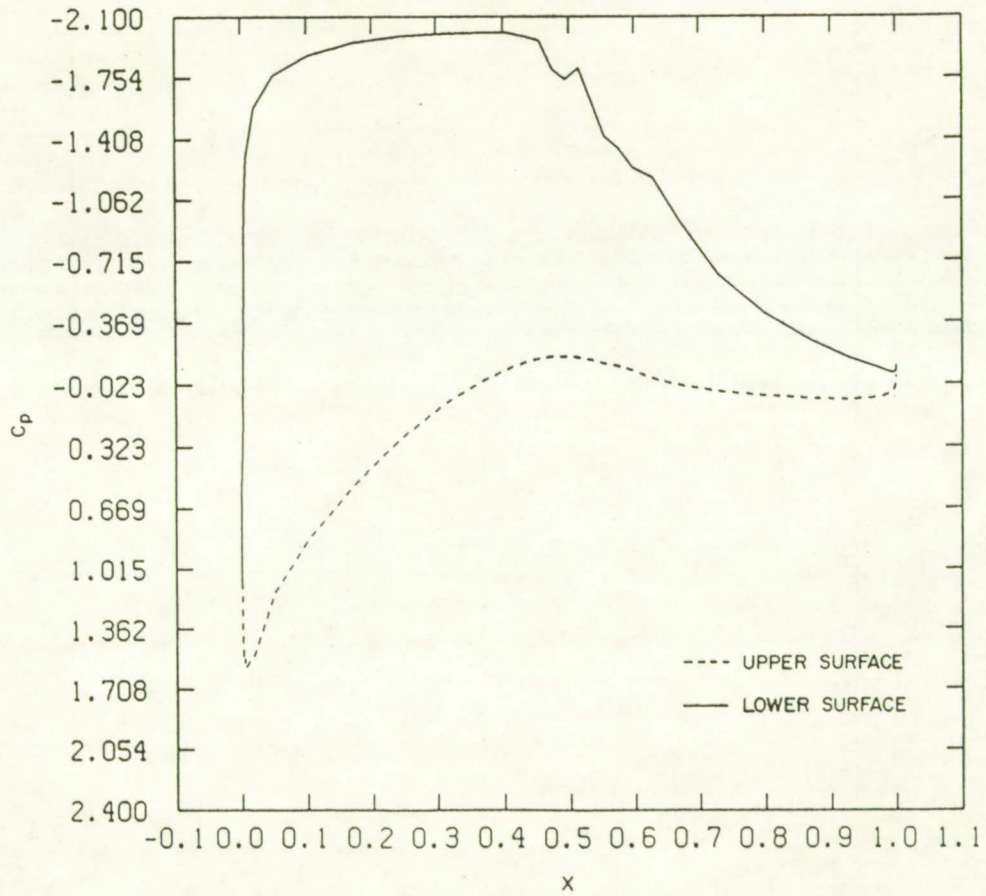


Fig. 62b Surface C_p ($t=5.0$)

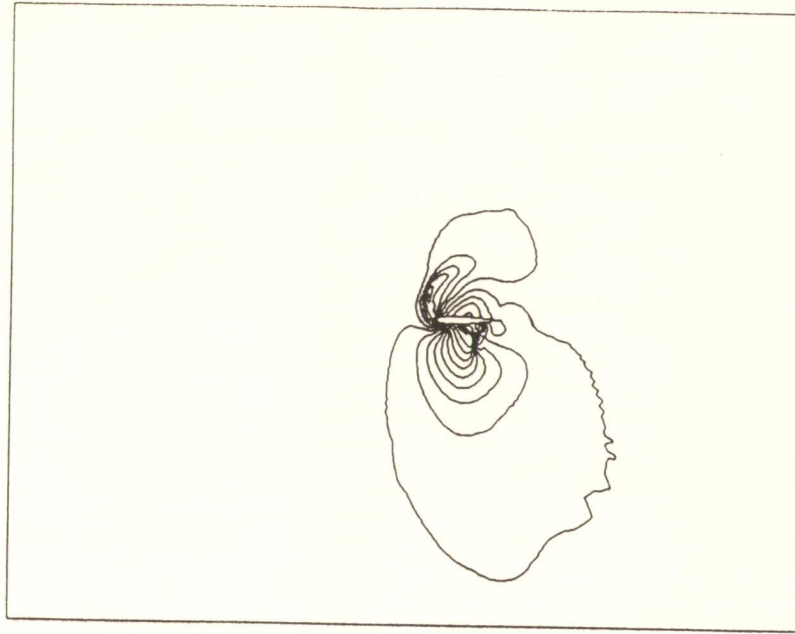


Fig. 63a Pressure Contours ($t=5.5$)

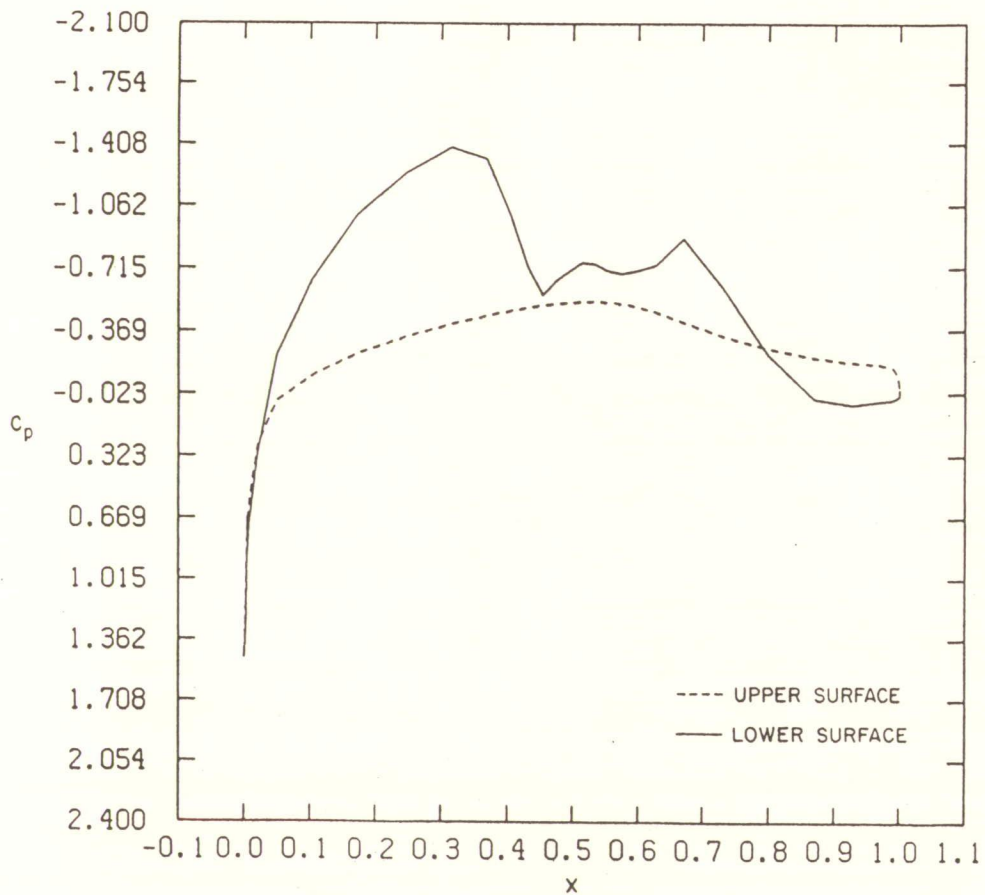


Fig. 63b Surface C_p ($t=5.5$)

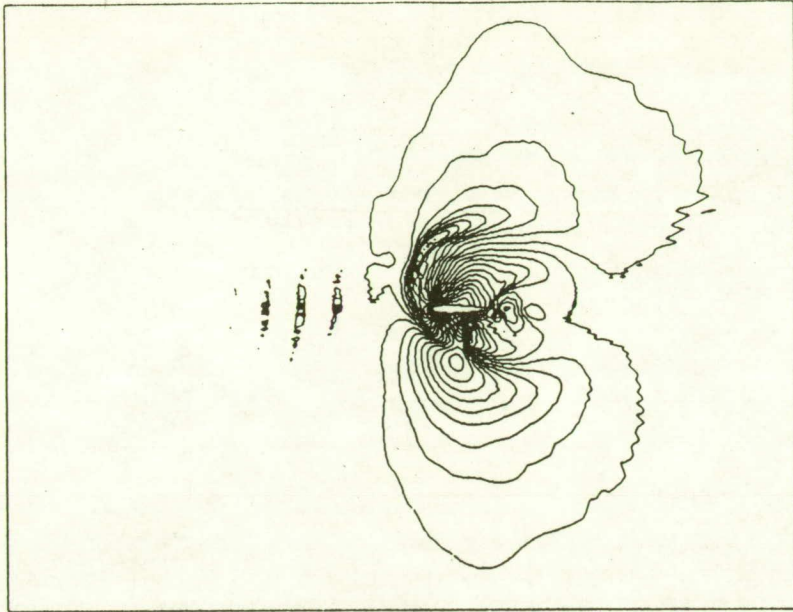


Fig. 64a Pressure Contours ($t=6.0$)

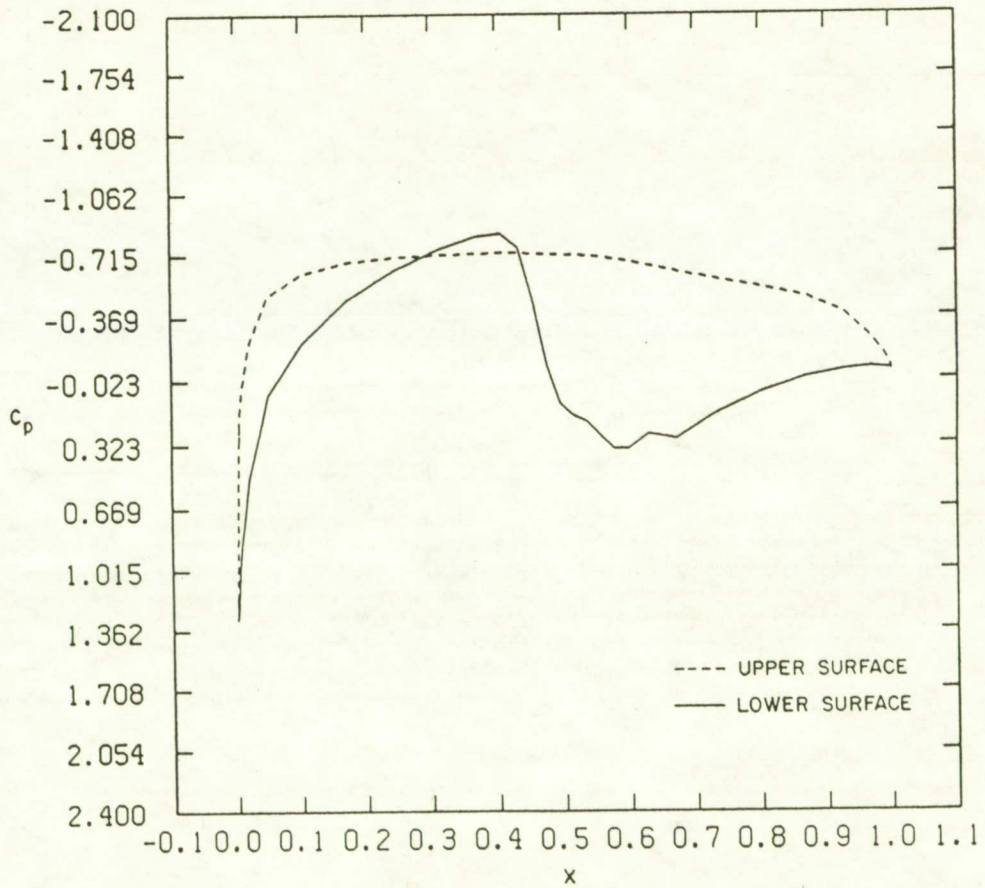


Fig. 64b Surface C_p ($t=6.0$)

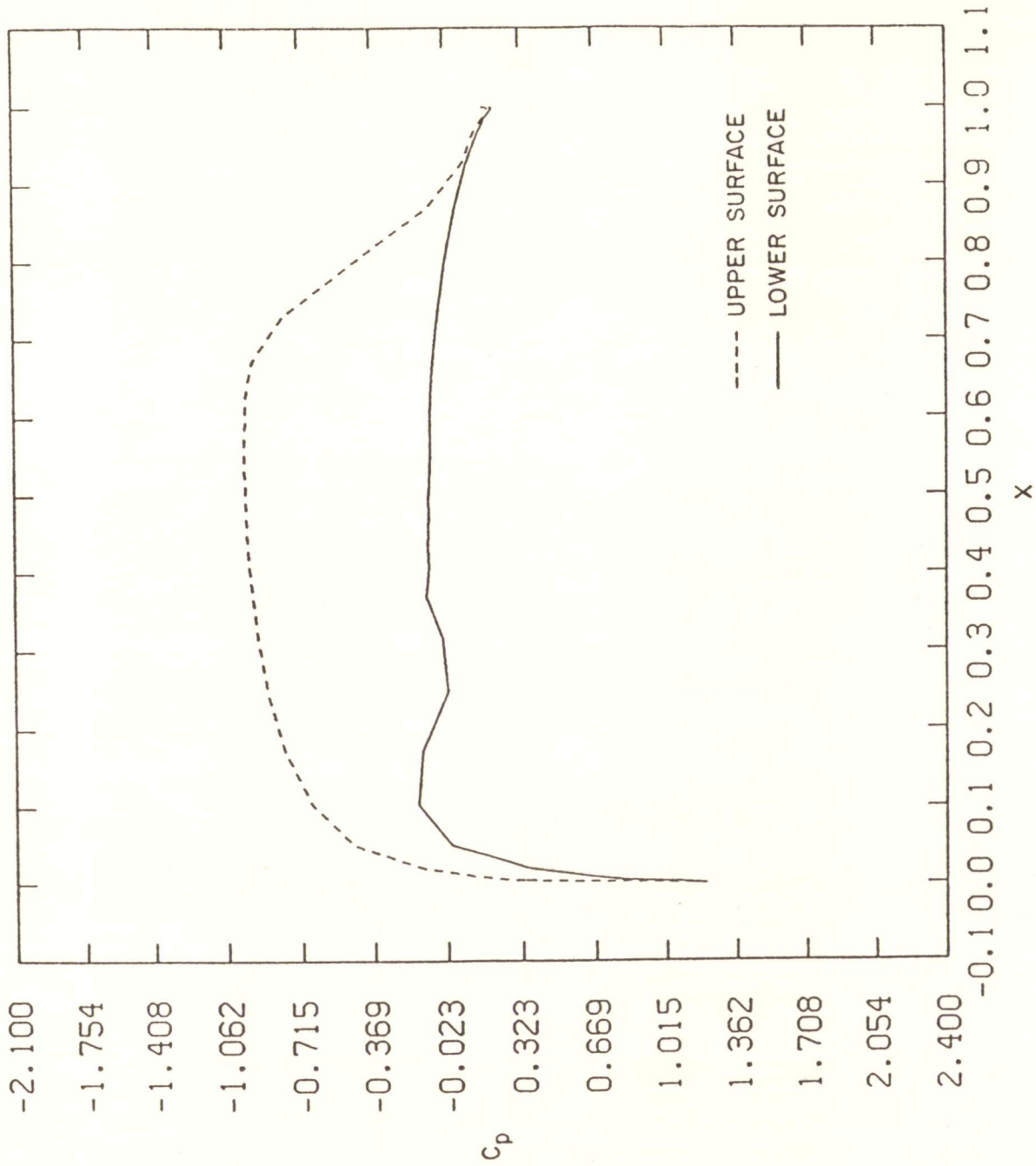
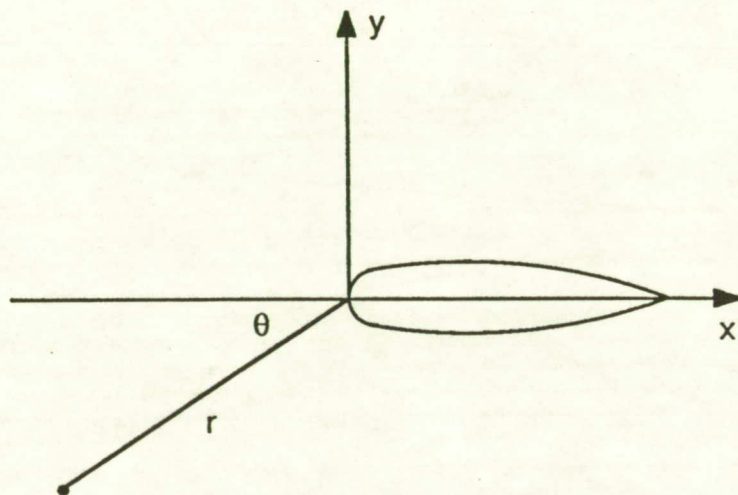


Fig. 65 Surface Cp (t=8.0).



POINT #	r	θ
1	2.31×10^{-2}	28.76°
2	5.40×10^{-2}	25.71°
3	10.73×10^{-2}	26.01°

Fig. 66 Points where Scaled Pressure Disturbance are Calculated.

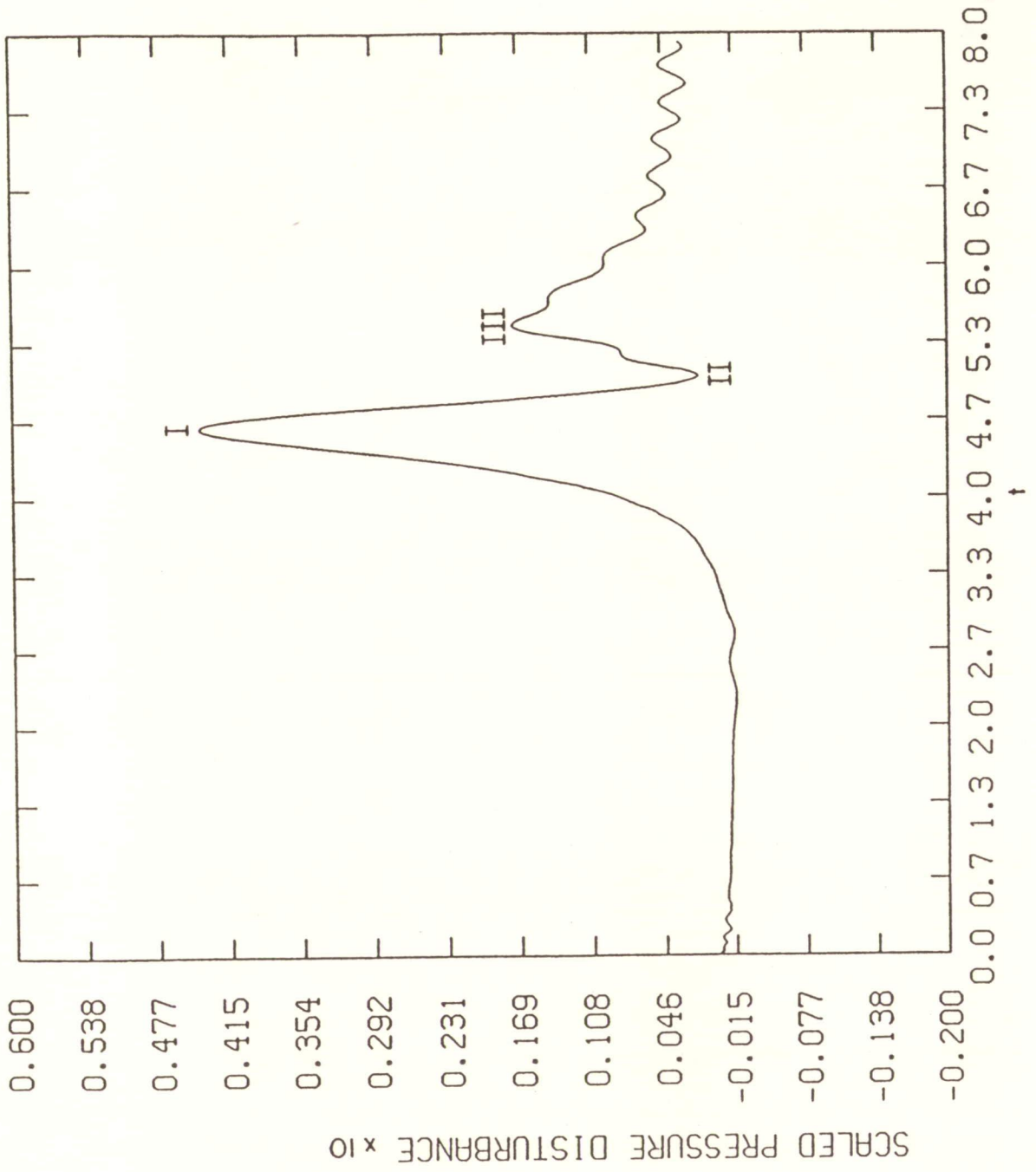


Fig. 67a Scaled p' at Point #1.

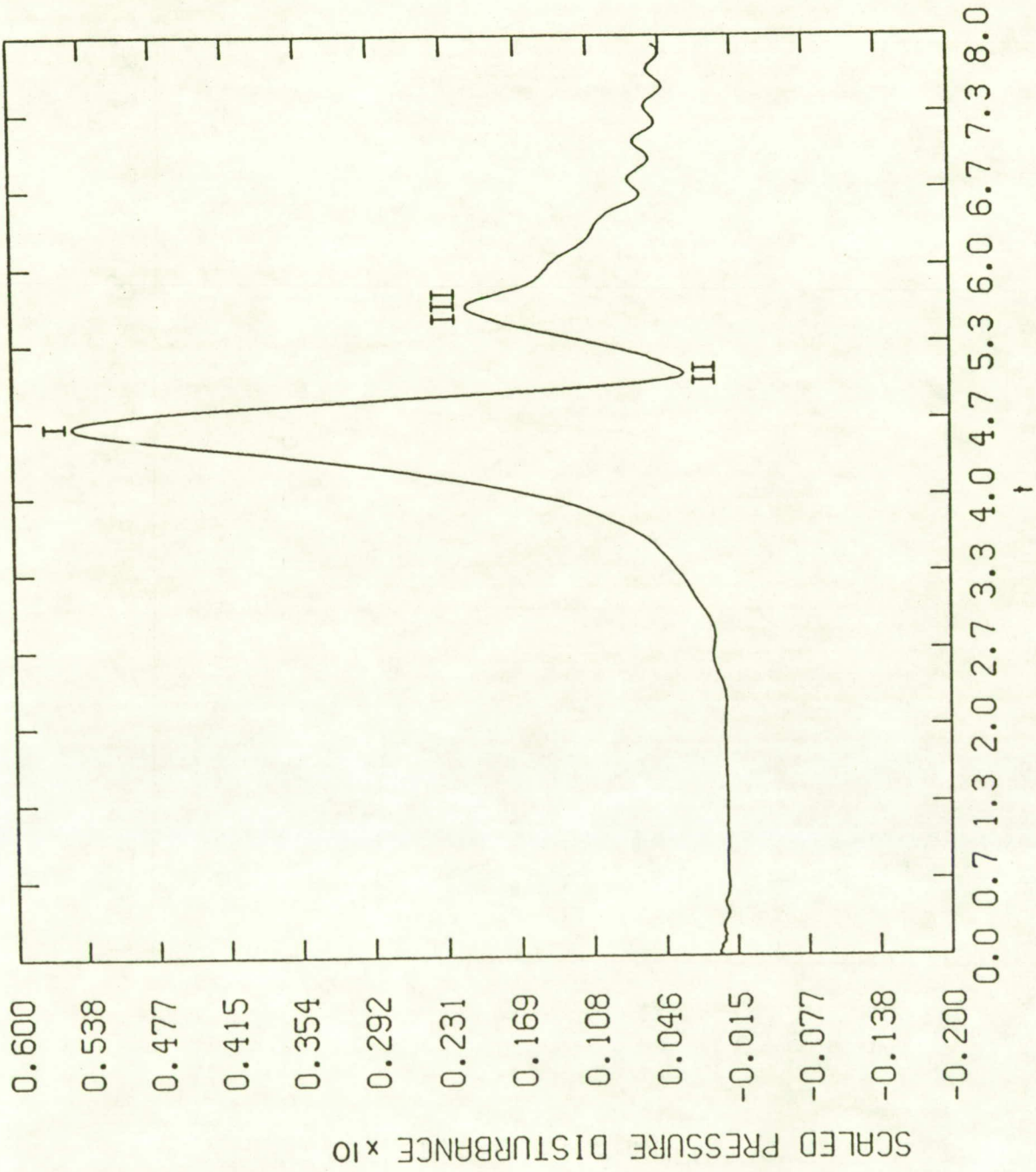


Fig. 67b Scaled p' at Point #2.

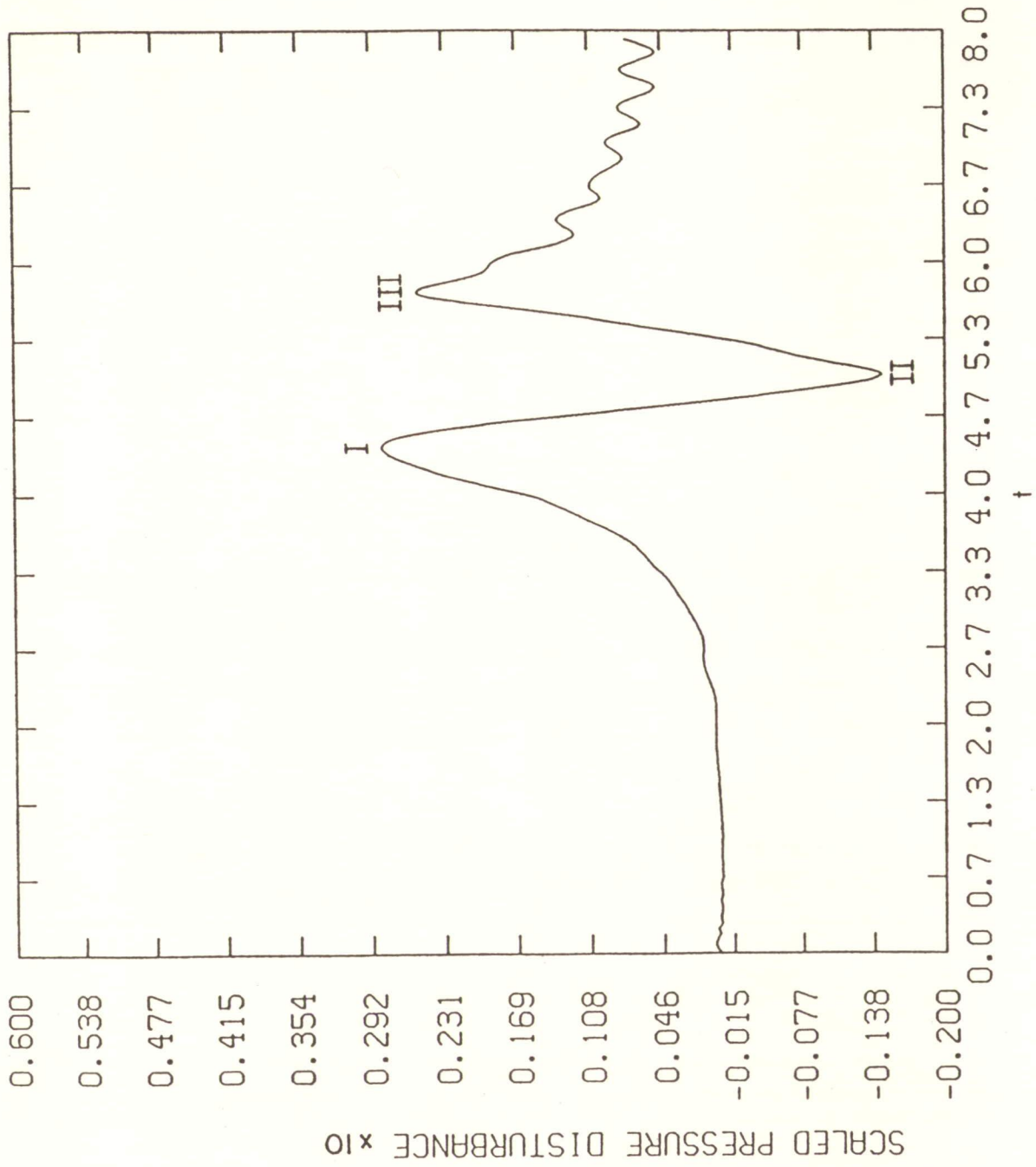


Fig. 67c Scaled p' at Point #3.

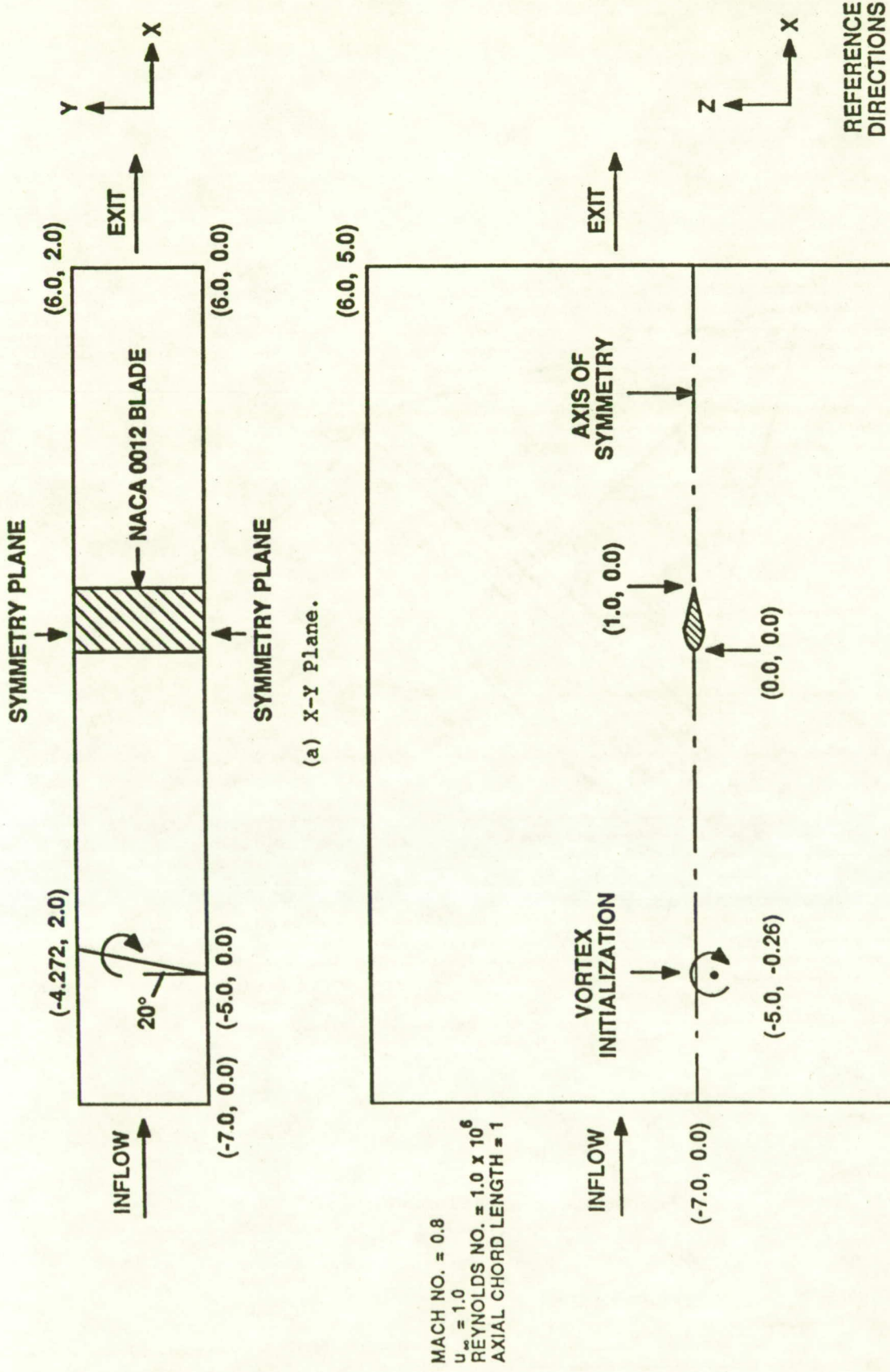


Fig. 68 Physical Domain for 3D BVI Simulation.

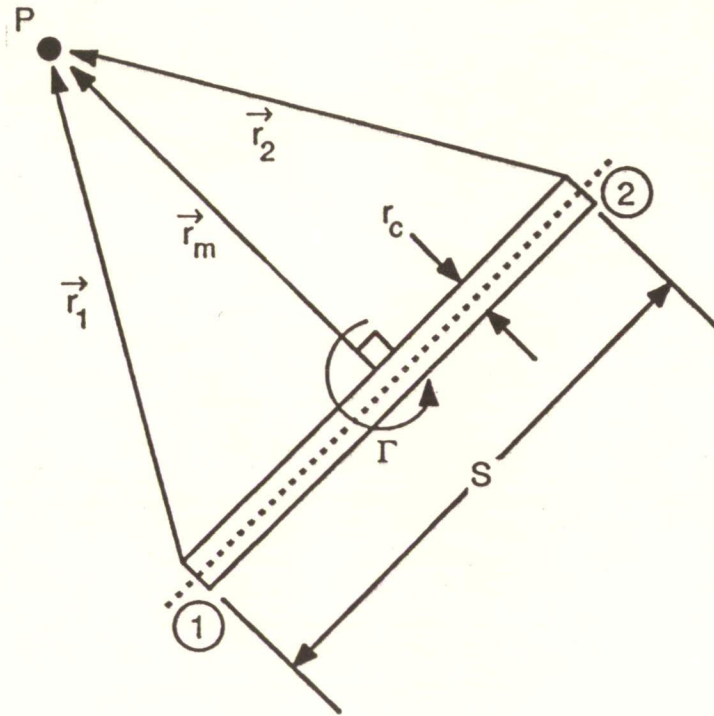


Figure 69 Vortex Filament.

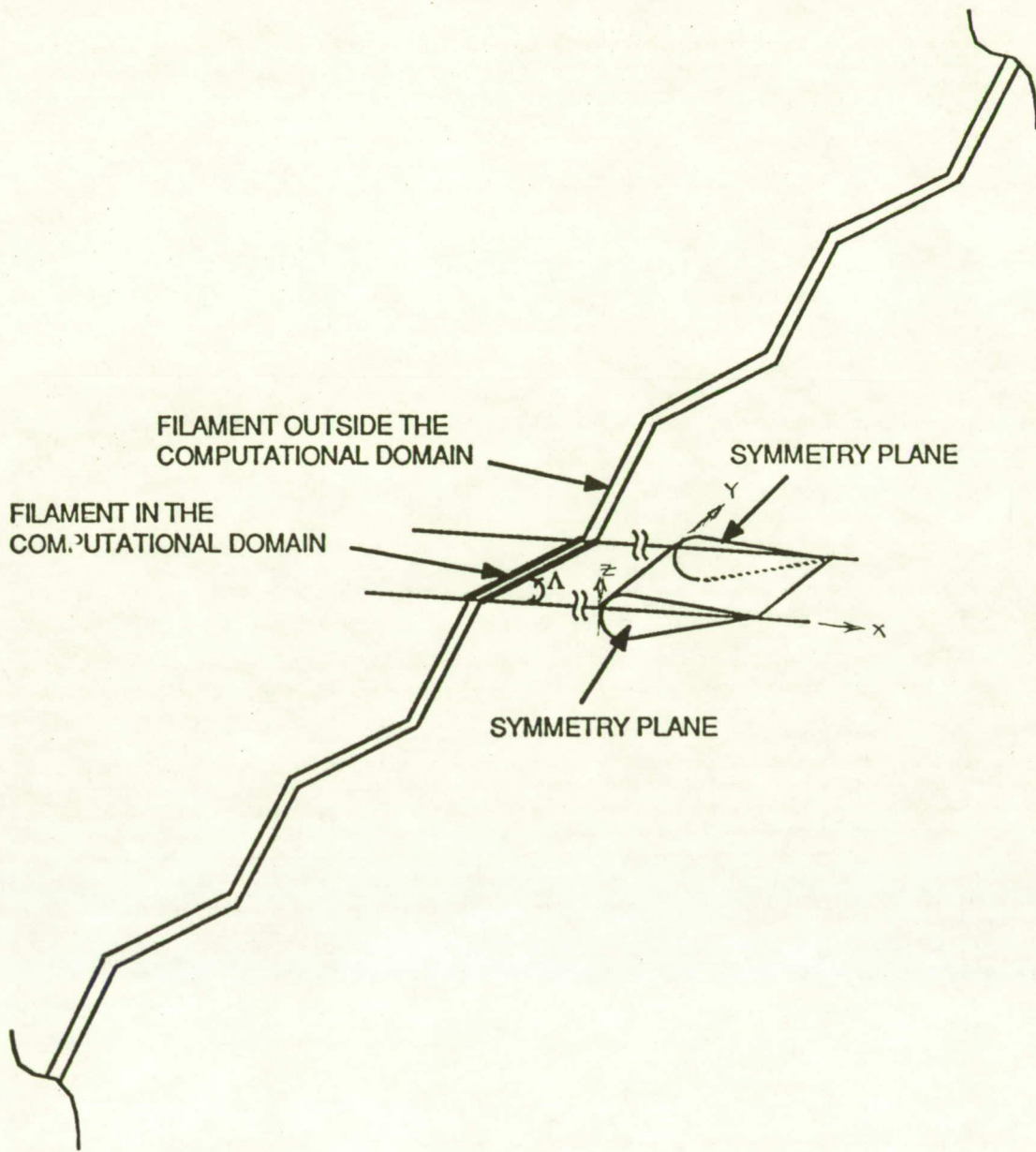
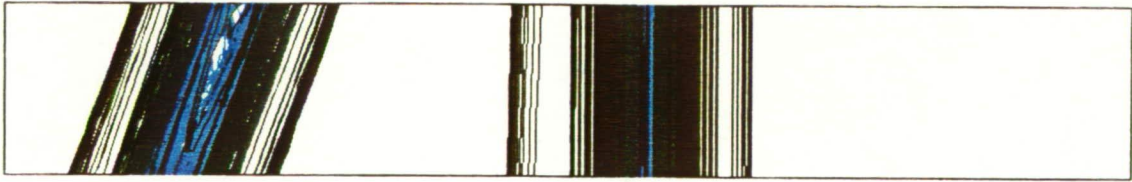


Figure 70 Overall Geometry.



CONTOUR LEVELS

- 0.32500
- 0.35000
- 0.37500
- 0.40000
- 0.42500
- 0.45000
- 0.47500
- 0.50000
- 0.52500
- 0.55000
- 0.57500
- 0.60000
- 0.62500
- 0.65000
- 0.67500
- 0.70000
- 0.72500
- 0.75000
- 0.77500
- 0.80000
- 0.82500
- 0.85000
- 0.87500
- 0.90000
- 0.92500
- 0.95000
- 0.97500
- 1.00000
- 1.02500
- 1.05000
- 1.07500
- 1.10000
- 1.12500

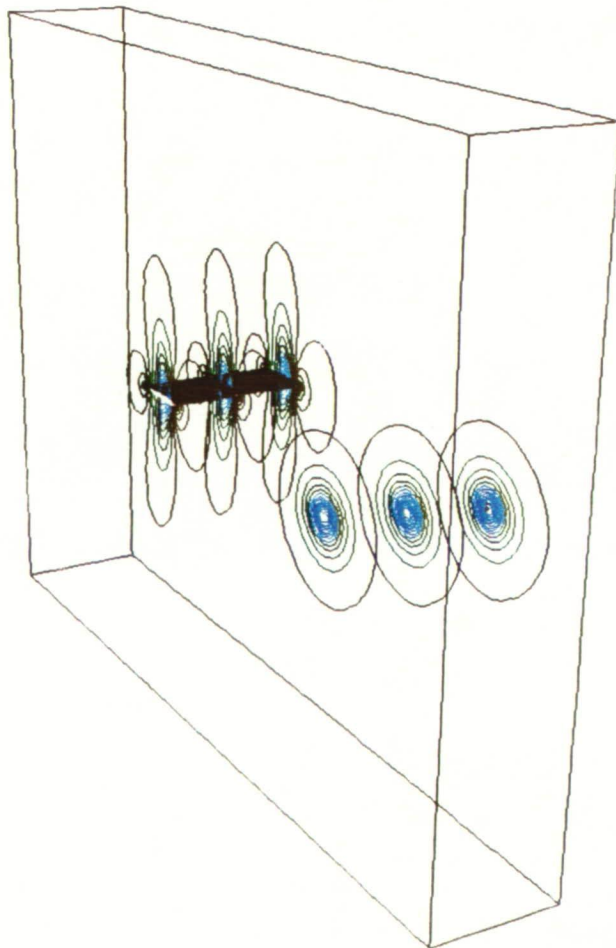


Fig. 71 Initial Pressure Field, $t=0.0$.

ORIGINAL PAGE
COLOR PHOTOGRAPH

CONTOUR LEVELS

- 0.000x10 0
- 0.05000
- 0.10000
- 0.15000
- 0.20000
- 0.25000
- 0.30000
- 0.35000
- 0.40000
- 0.45000
- 0.50000
- 0.55000
- 0.60000
- 0.65000
- 0.70000
- 0.75000
- 0.80000
- 0.85000
- 0.90000
- 0.95000
- 1.00000
- 1.05000
- 1.10000
- 1.15000
- 1.20000
- 1.25000
- 1.30000
- 1.35000
- 1.40000

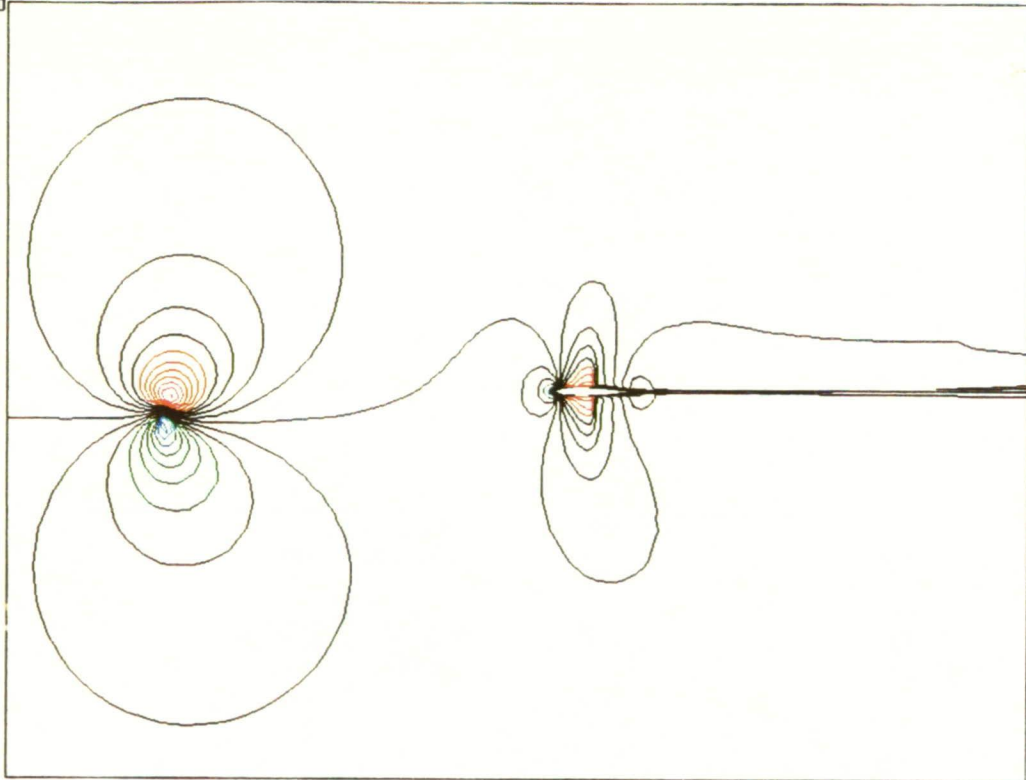


Fig. 72 a Initial Mach Number Field, t=0.0.

CONTOUR LEVELS

- 0.34000
- 0.36000
- 0.38000
- 0.40000
- 0.42000
- 0.44000
- 0.46000
- 0.48000
- 0.50000
- 0.52000
- 0.54000
- 0.56000
- 0.58000
- 0.60000
- 0.62000
- 0.64000
- 0.66000
- 0.68000
- 0.70000
- 0.72000
- 0.74000
- 0.76000
- 0.78000
- 0.80000
- 0.82000
- 0.84000
- 0.86000
- 0.88000
- 0.90000
- 0.92000
- 0.94000
- 0.96000
- 0.98000
- 1.00000
- 1.02000
- 1.04000
- 1.06000
- 1.08000

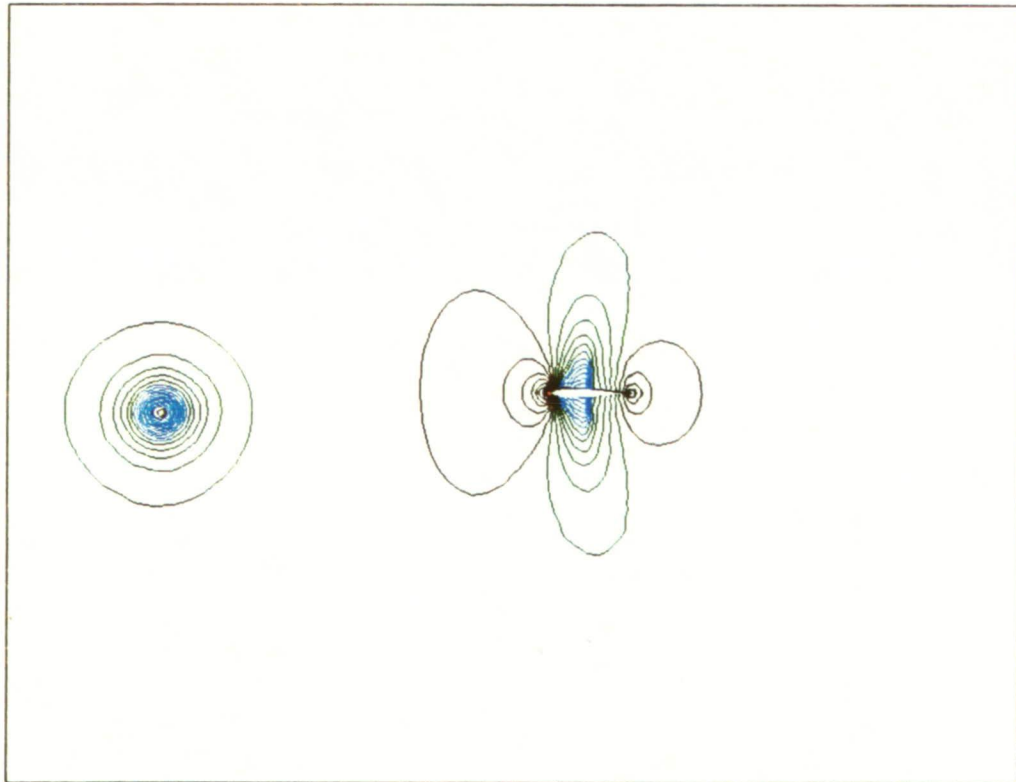


Fig. 72b Initial Pressure Field, t=0.0.

ORIGINAL PAGE
COLOR PHOTOGRAPH

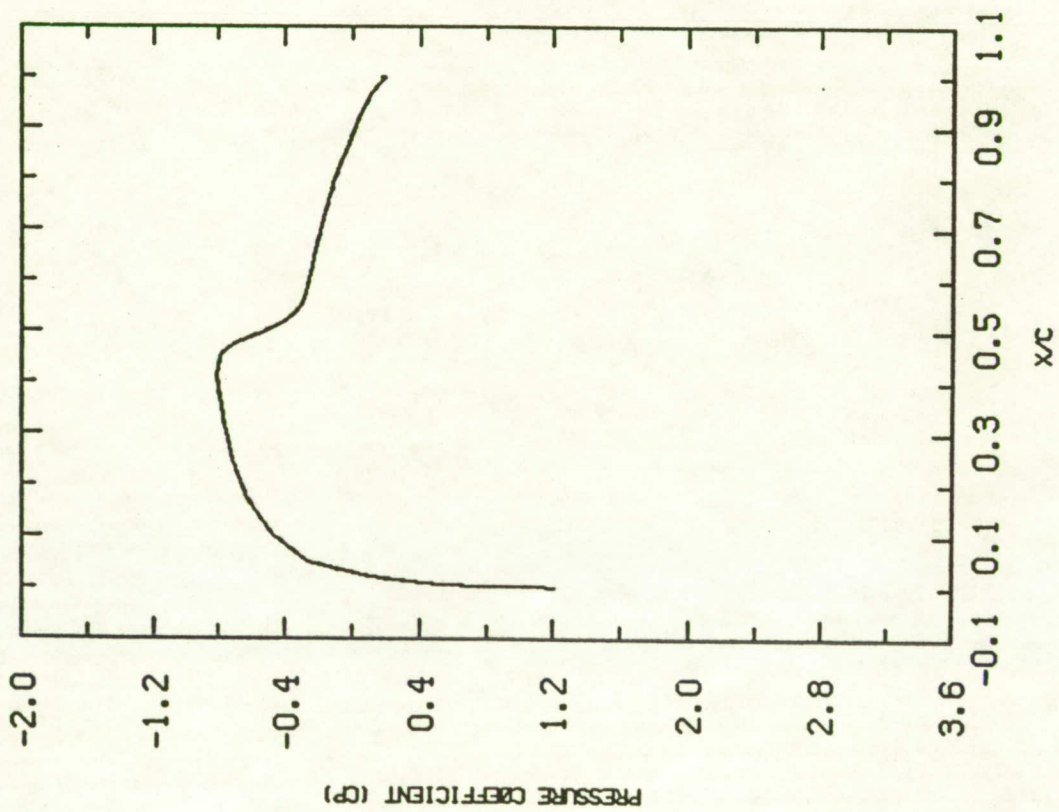
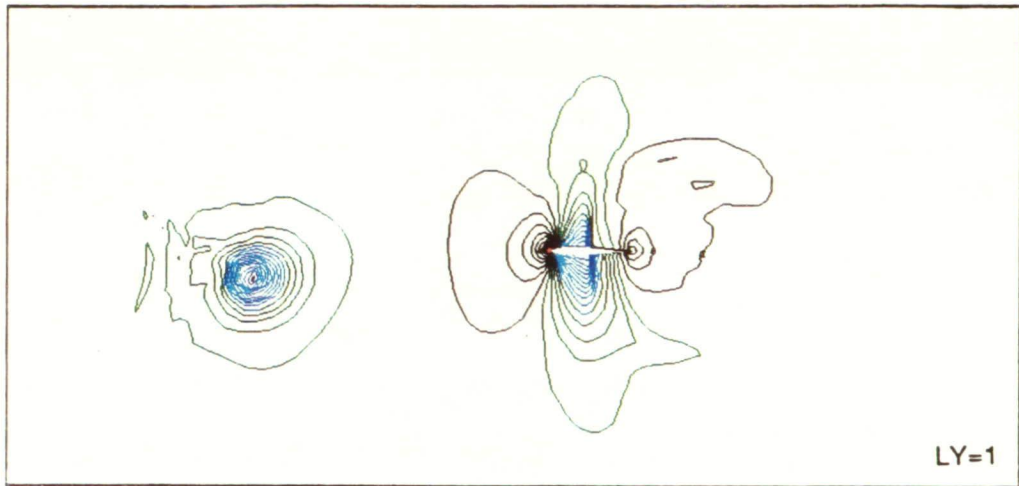


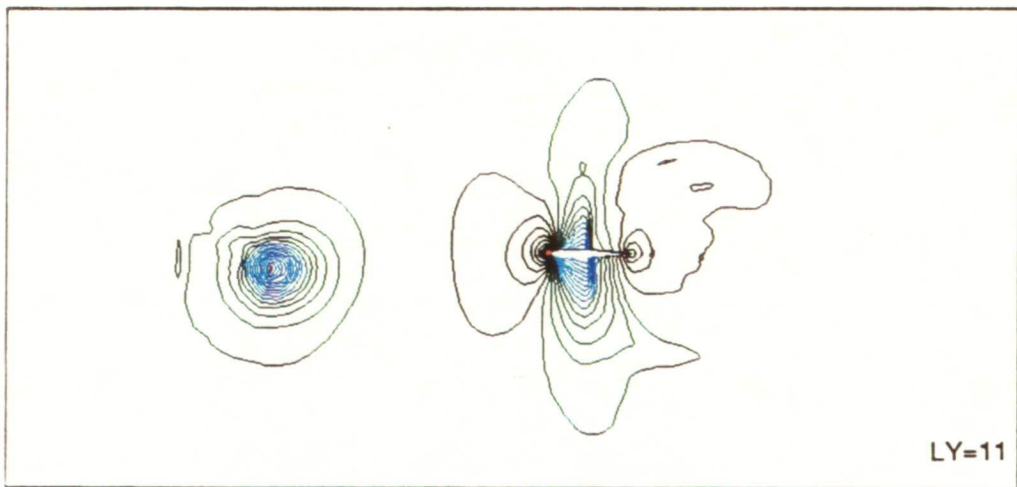
Fig. 73 Surface Pressure, $t=0.0$.



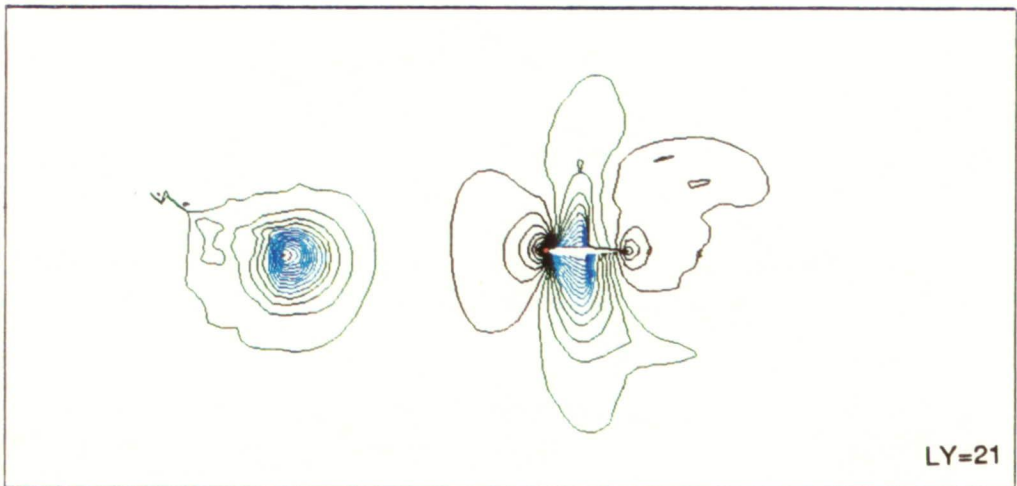
LY=1

CONTOUR LEVELS

- 0.38000
- 0.40000
- 0.42000
- 0.44000
- 0.46000
- 0.48000
- 0.50000
- 0.52000
- 0.54000
- 0.56000
- 0.58000
- 0.60000
- 0.62000
- 0.64000
- 0.66000
- 0.68000
- 0.70000
- 0.72000
- 0.74000
- 0.76000
- 0.78000
- 0.80000
- 0.82000
- 0.84000
- 0.86000
- 0.88000
- 0.90000
- 0.92000
- 0.94000
- 0.96000
- 0.98000
- 1.00000
- 1.02000
- 1.04000
- 1.06000
- 1.08000
- 1.10000



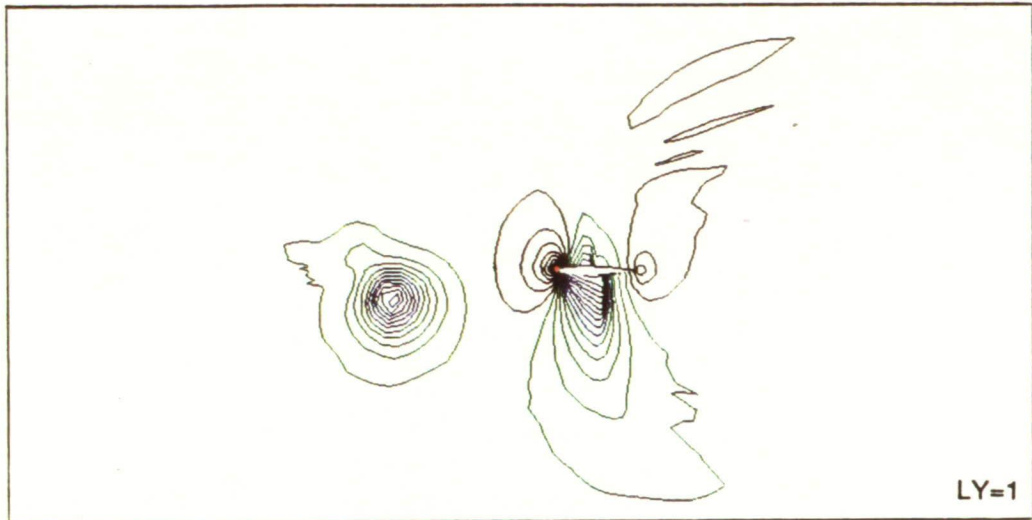
LY=11



LY=21

Fig. 74 Pressure Field, $t=1.23$.

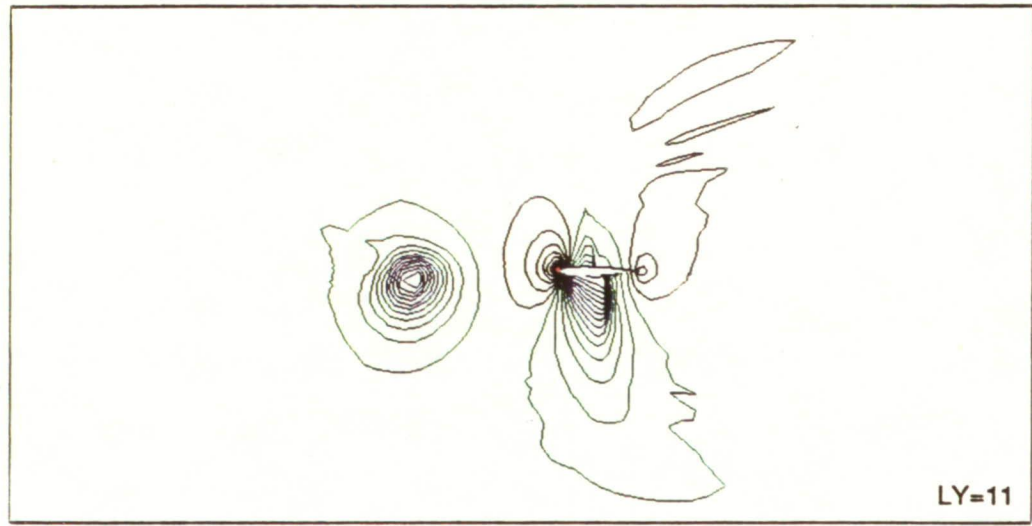
ORIGINAL PAGE
COLOR PHOTOGRAPH



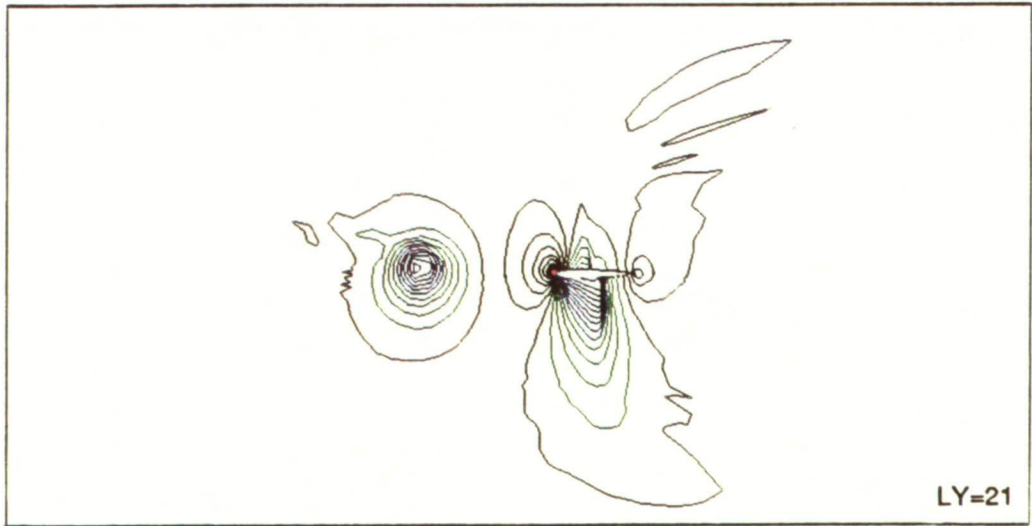
LY=1

CONTOUR LEVELS

- 0.32500
- 0.35000
- 0.37500
- 0.40000
- 0.42500
- 0.45000
- 0.47500
- 0.50000
- 0.52500
- 0.55000
- 0.57500
- 0.60000
- 0.62500
- 0.65000
- 0.67500
- 0.70000
- 0.72500
- 0.75000
- 0.77500
- 0.80000
- 0.82500
- 0.85000
- 0.87500
- 0.90000
- 0.92500
- 0.95000
- 0.97500
- 1.00000
- 1.02500
- 1.05000
- 1.07500
- 1.10000
- 1.12500
- 1.15000

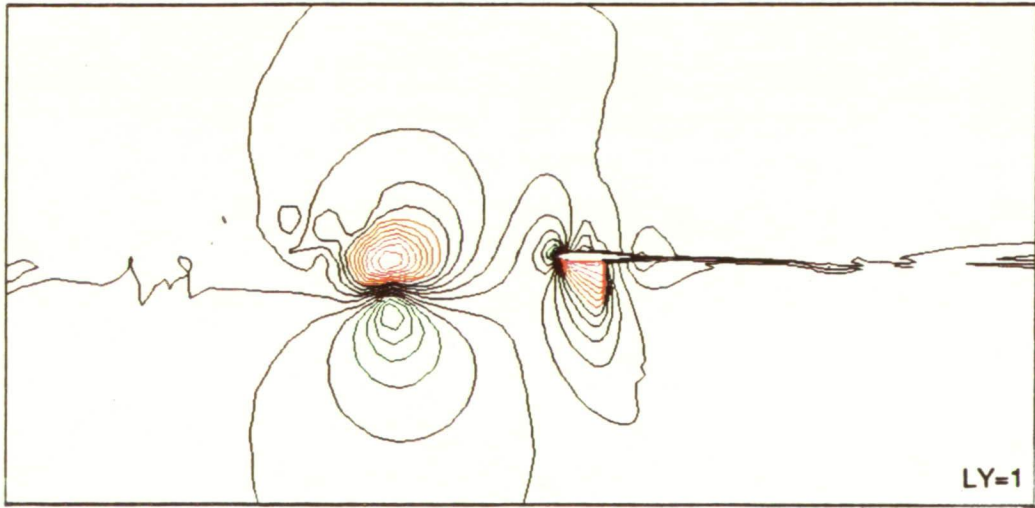


LY=11



LY=21

Fig. 75 Pressure Field, $t=2.838$.



CONTOUR LEVELS

- 0.000x10 0
- 0.05000
- 0.10000
- 0.15000
- 0.20000
- 0.25000
- 0.30000
- 0.35000
- 0.40000
- 0.45000
- 0.50000
- 0.55000
- 0.60000
- 0.65000
- 0.70000
- 0.75000
- 0.80000
- 0.85000
- 0.90000
- 0.95000
- 1.00000
- 1.05000
- 1.10000
- 1.15000
- 1.20000
- 1.25000
- 1.30000
- 1.35000
- 1.40000

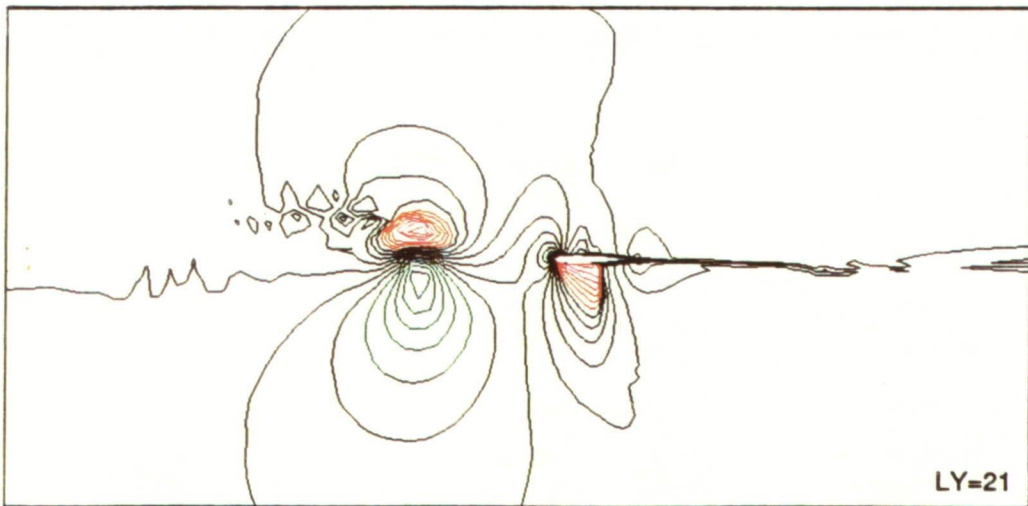
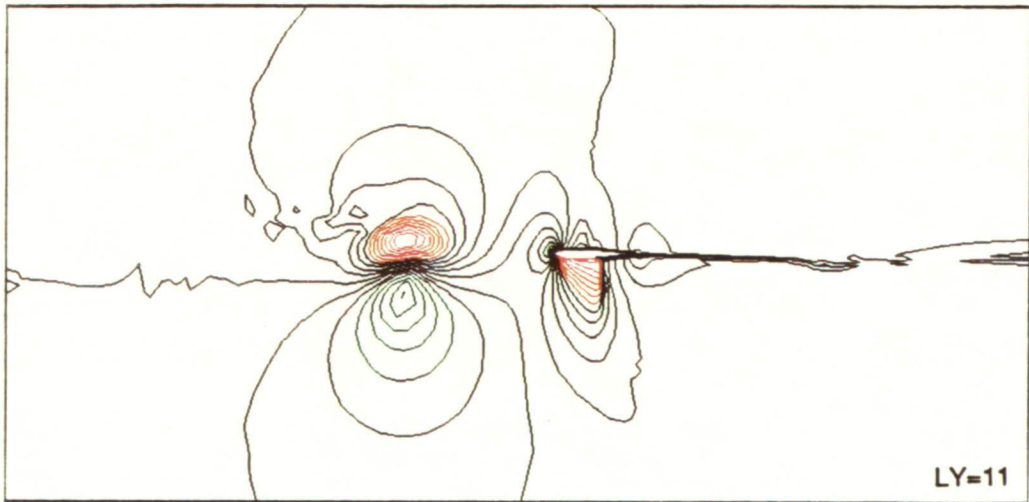


Fig. 76 Mach Number Field, $t=2.838$.

ORIGINAL PAGE
COLOR PHOTOGRAPH

PRECEDING PAGE BLANK NOT FILMED

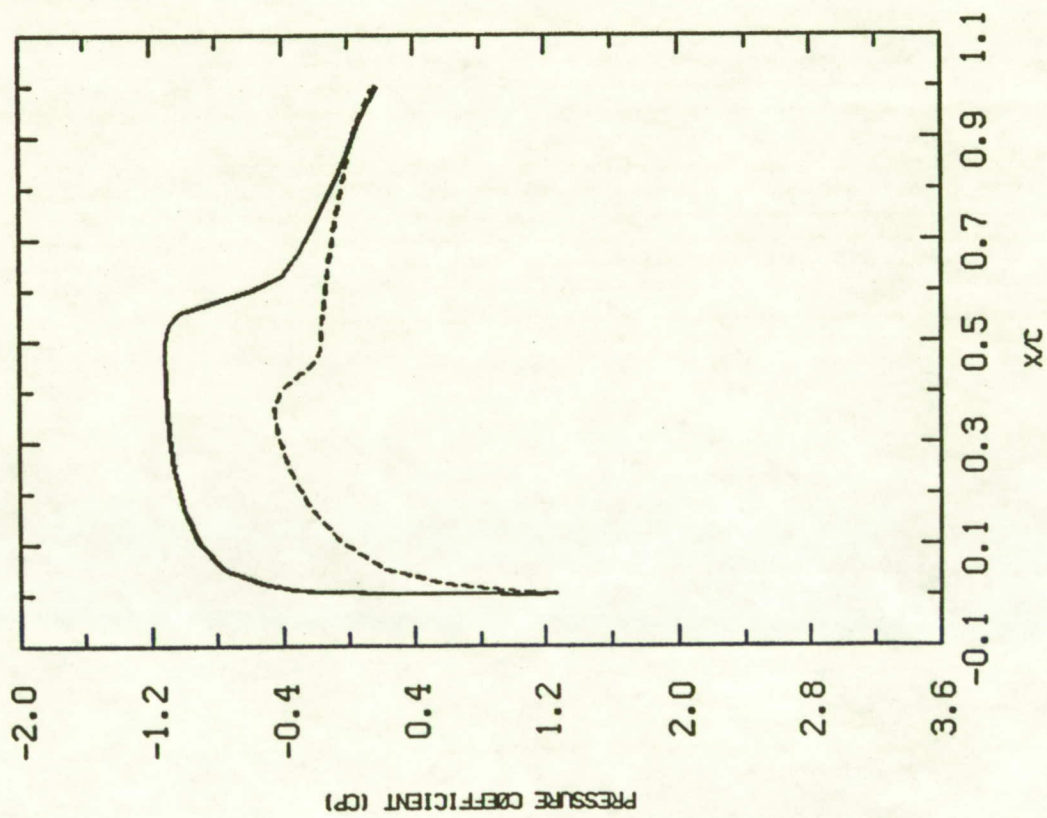


Fig. 77 Composite Surface Pressure, $t=2.838$.

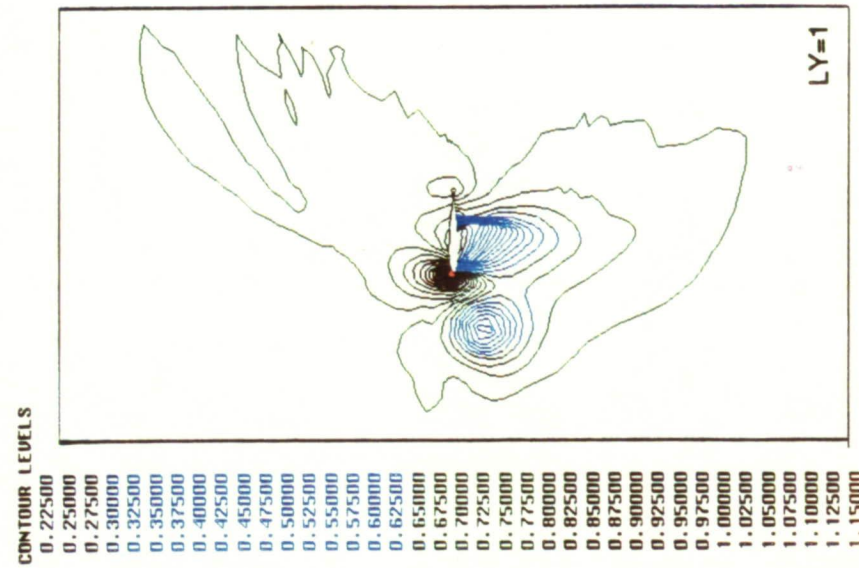
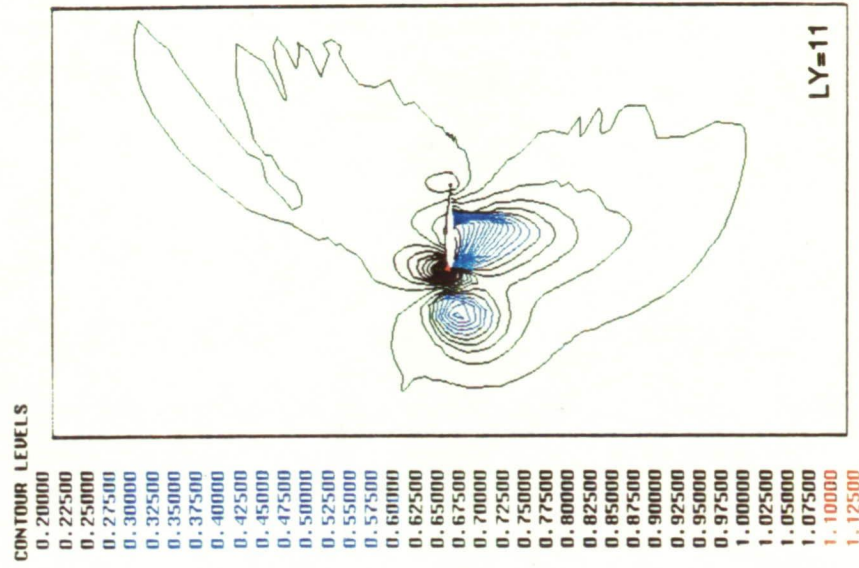
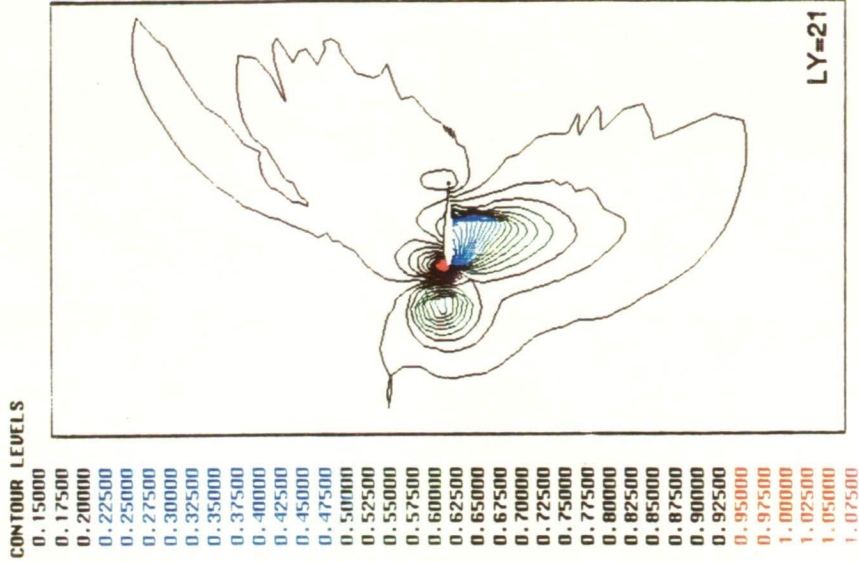
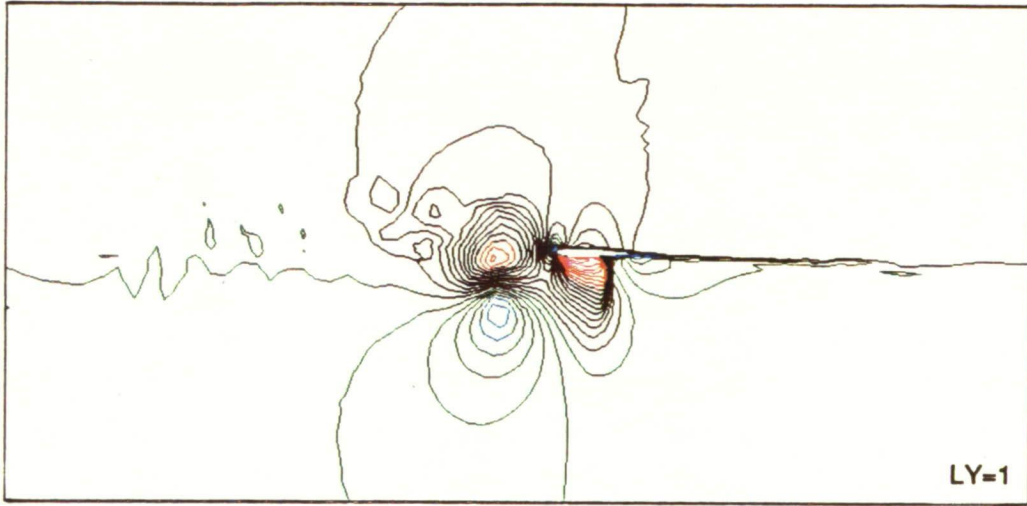


Fig. 78 Pressure Field, $t=4.139$.

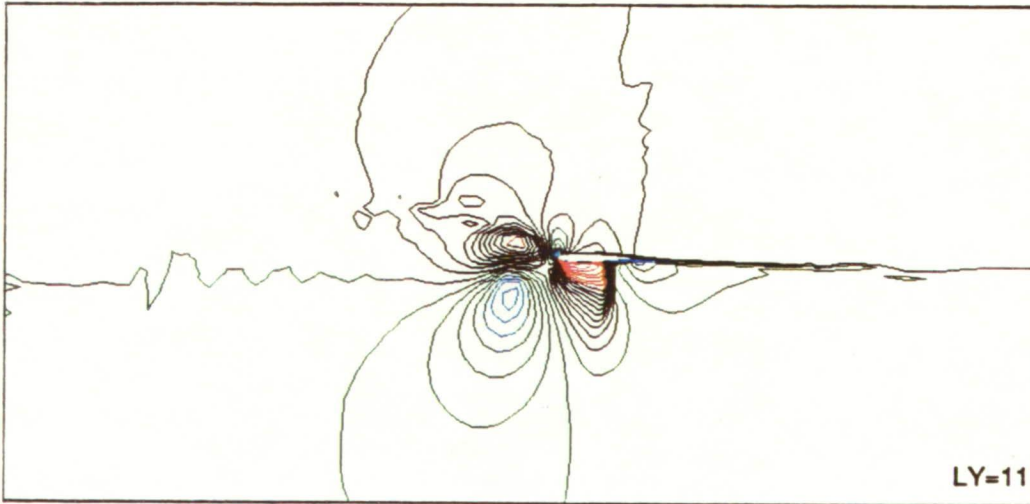
ORIGINAL PAGE
COLOR PHOTOGRAPH



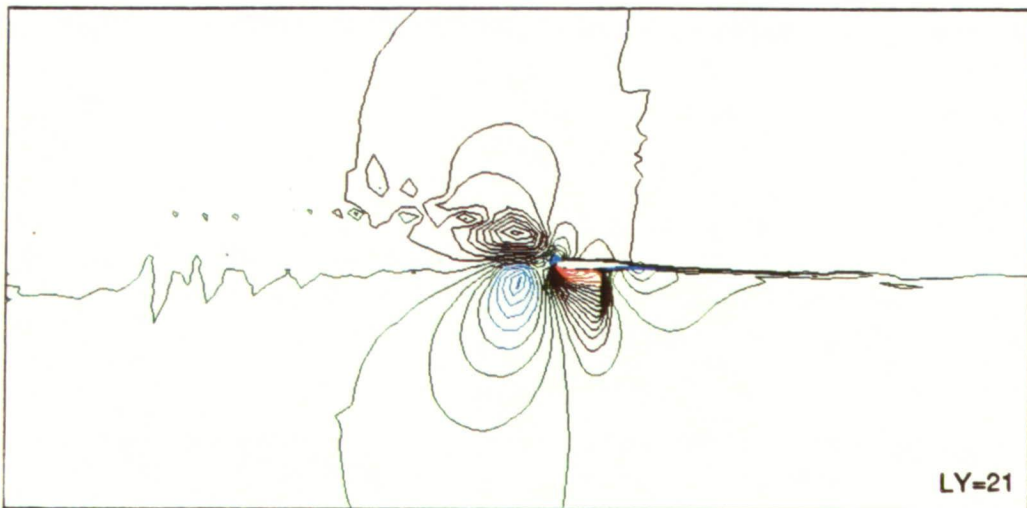
LY=1

CONTOUR LEVELS

- 0.000x10 0
- 0.05000
- 0.10000
- 0.15000
- 0.20000
- 0.25000
- 0.30000
- 0.35000
- 0.40000
- 0.45000
- 0.50000
- 0.55000
- 0.60000
- 0.65000
- 0.70000
- 0.75000
- 0.80000
- 0.85000
- 0.90000
- 0.95000
- 1.00000
- 1.05000
- 1.10000
- 1.15000
- 1.20000
- 1.25000
- 1.30000
- 1.35000
- 1.40000
- 1.45000
- 1.50000
- 1.55000
- 1.60000
- 1.65000
- 1.70000
- 1.75000



LY=11



LY=21

Fig. 79 Mach Number Field, $t=4.138$.

ORIGINAL PAGE
COLOR PHOTOGRAPH

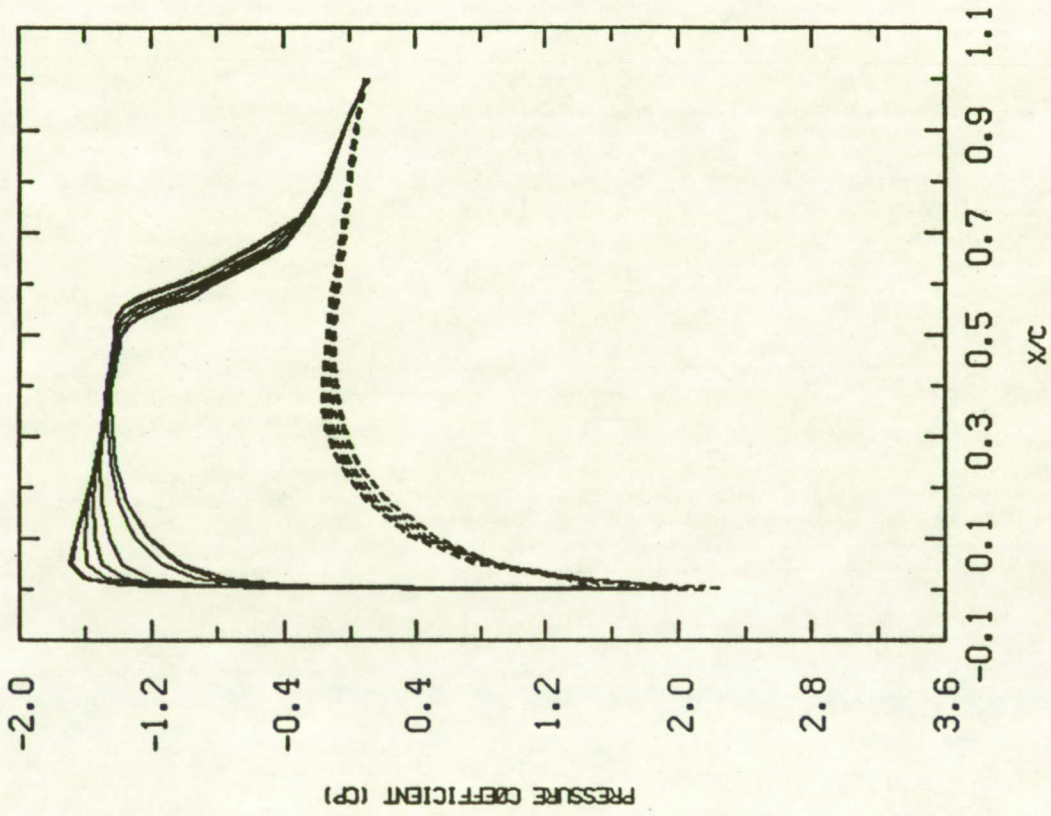


Fig. 80 Composite Surface Pressure, $t=4.138$.

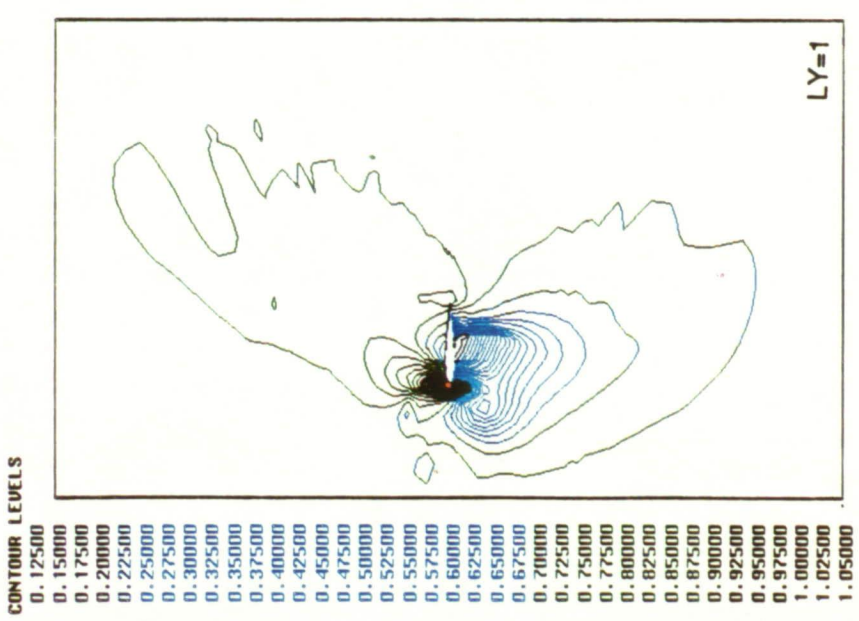
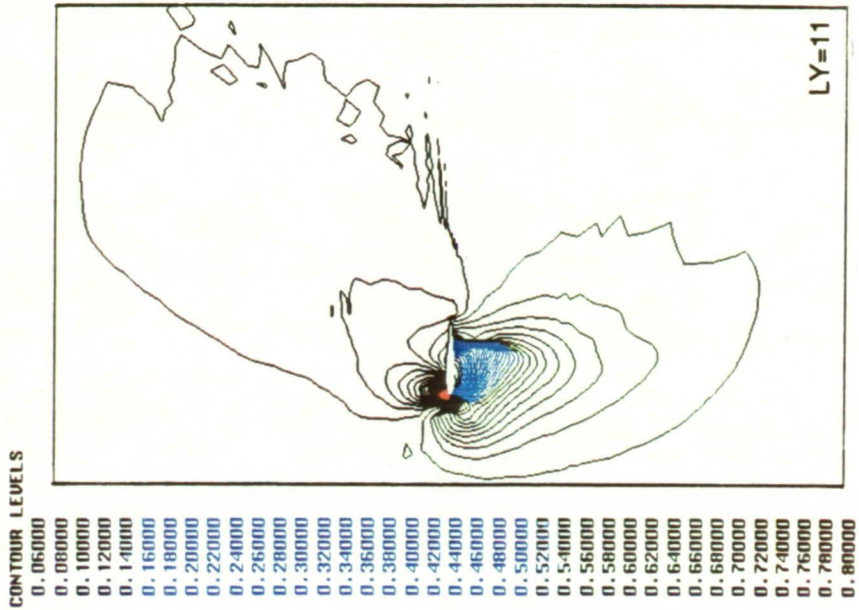
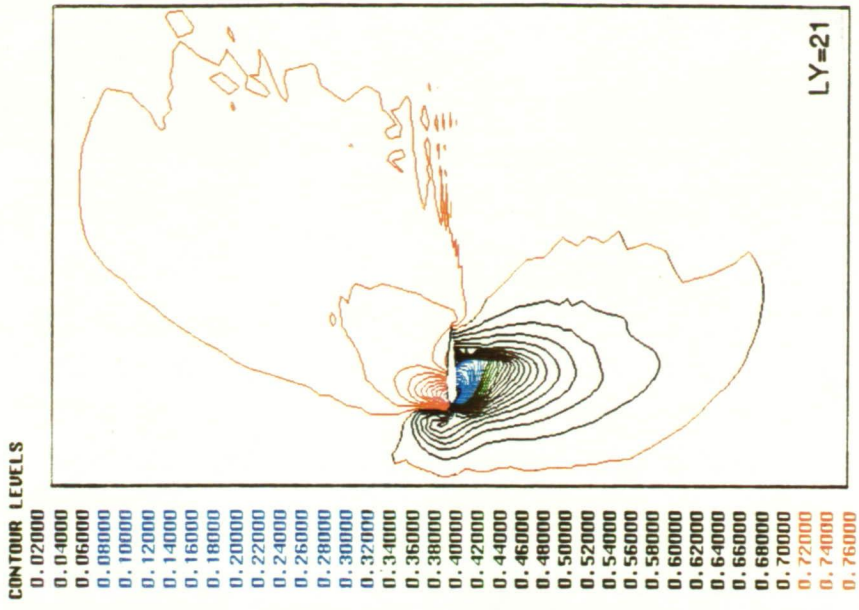


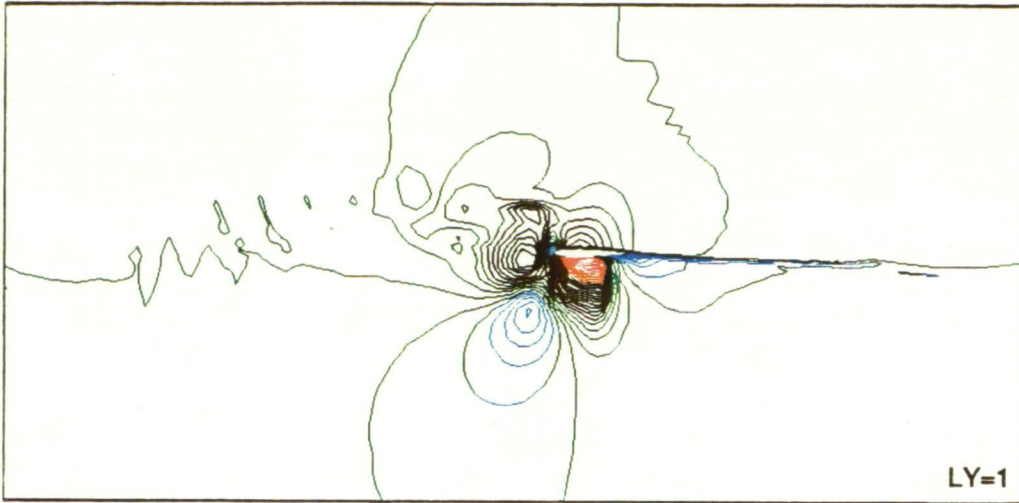
Fig. 81 Pressure Field, $t=4.56$.

ORIGINAL PAGE
COLOR PHOTOGRAPH

166 INTENTIONALLY BLANK

CONTOUR LEVELS

- 0.000x10 0
- 0.05000
- 0.10000
- 0.15000
- 0.20000
- 0.25000
- 0.30000
- 0.35000
- 0.40000
- 0.45000
- 0.50000
- 0.55000
- 0.60000
- 0.65000
- 0.70000
- 0.75000
- 0.80000
- 0.85000
- 0.90000
- 0.95000
- 1.00000
- 1.05000
- 1.10000
- 1.15000
- 1.20000
- 1.25000
- 1.30000
- 1.35000
- 1.40000
- 1.45000
- 1.50000
- 1.55000
- 1.60000
- 1.65000
- 1.70000
- 1.75000
- 1.80000
- 1.85000



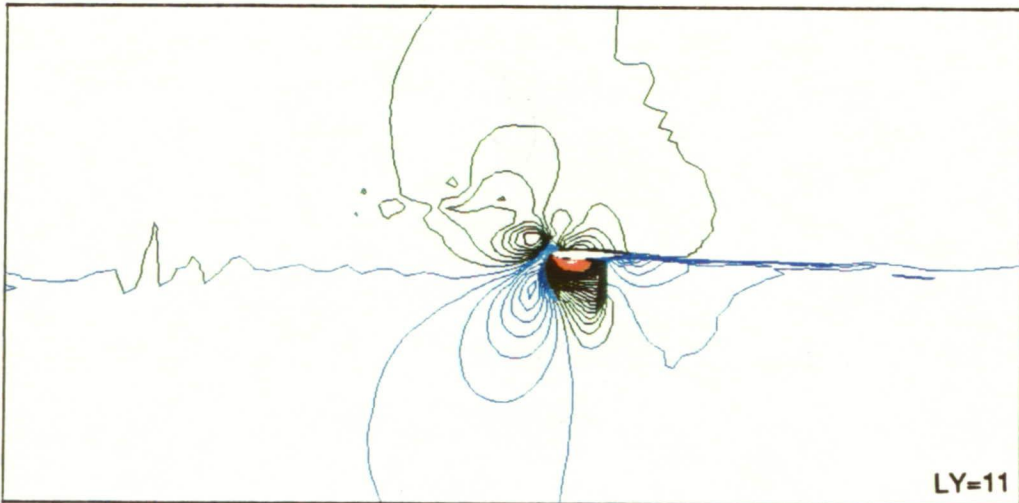
LY=1

CONTOUR LEVELS

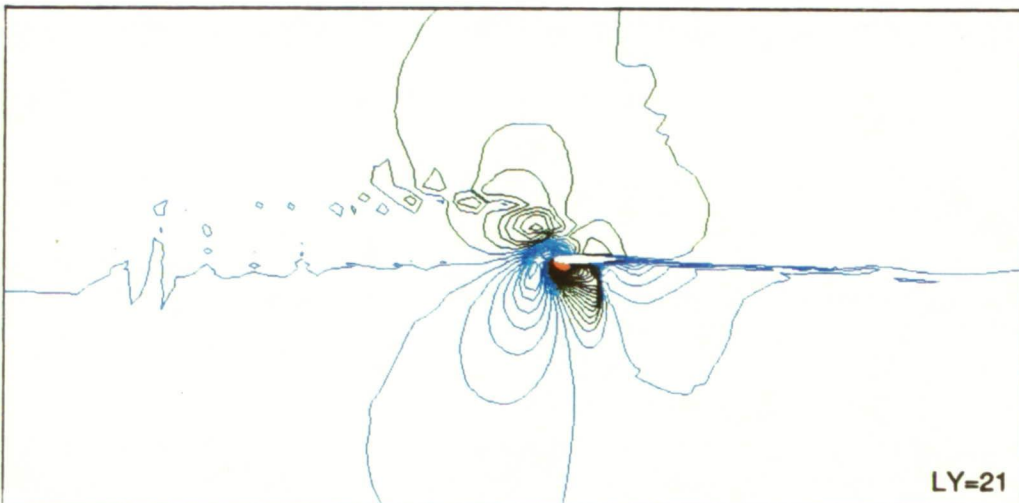
- 0.000x10 0
- 0.05000
- 0.10000
- 0.15000
- 0.20000
- 0.25000
- 0.30000
- 0.35000
- 0.40000
- 0.45000
- 0.50000
- 0.55000
- 0.60000
- 0.65000
- 0.70000
- 0.75000
- 0.80000
- 0.85000
- 0.90000
- 0.95000
- 1.00000
- 1.05000
- 1.10000
- 1.15000
- 1.20000
- 1.25000
- 1.30000
- 1.35000
- 1.40000
- 1.45000
- 1.50000
- 1.55000
- 1.60000
- 1.65000
- 1.70000
- 1.75000
- 1.80000
- 1.85000

CONTOUR LEVELS

- 0.000x10 0
- 0.05000
- 0.10000
- 0.15000
- 0.20000
- 0.25000
- 0.30000
- 0.35000
- 0.40000
- 0.45000
- 0.50000
- 0.55000
- 0.60000
- 0.65000
- 0.70000
- 0.75000
- 0.80000
- 0.85000
- 0.90000
- 0.95000
- 1.00000
- 1.05000
- 1.10000
- 1.15000
- 1.20000
- 1.25000
- 1.30000
- 1.35000
- 1.40000
- 1.45000
- 1.50000
- 1.55000
- 1.60000
- 1.65000
- 1.70000
- 1.75000
- 1.80000
- 1.85000



LY=11



LY=21

Fig. 82 Mach Number Contours, t=4.56.

ORIGINAL PAGE
COLOR PHOTOGRAPH

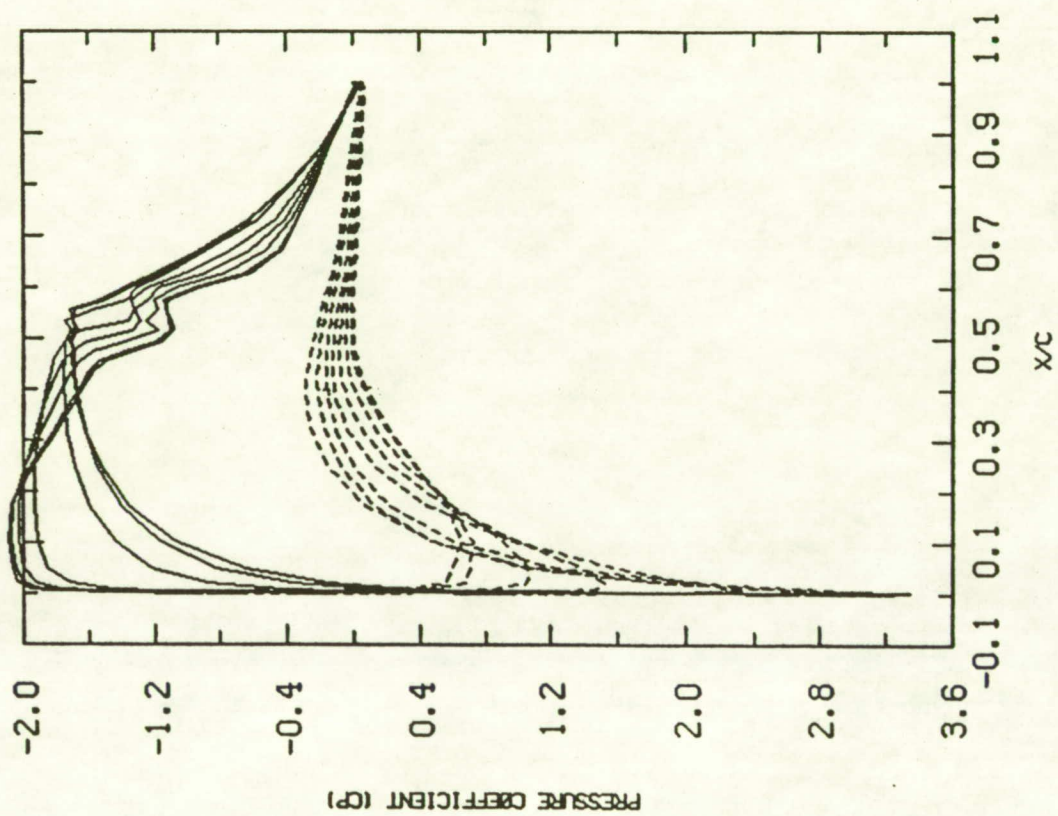


Fig. 83 Composite Surface Pressure, $t=4.56$.

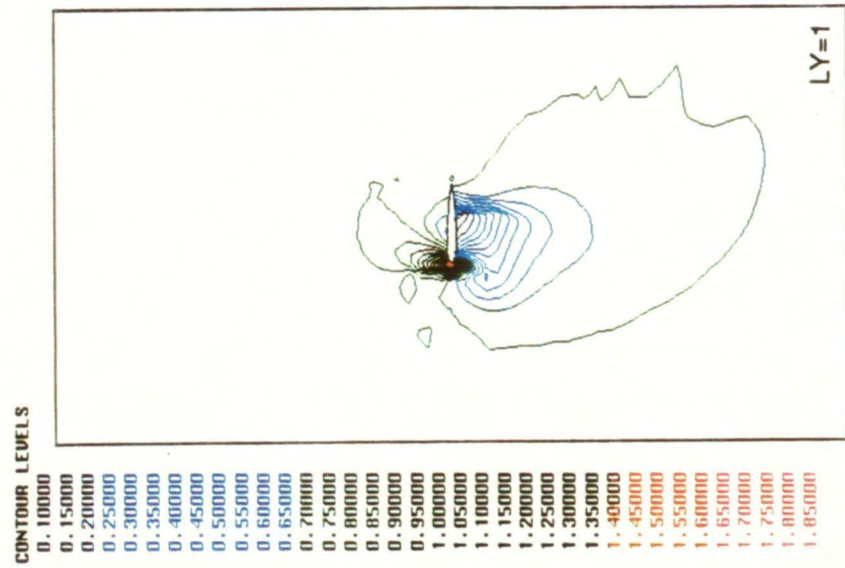
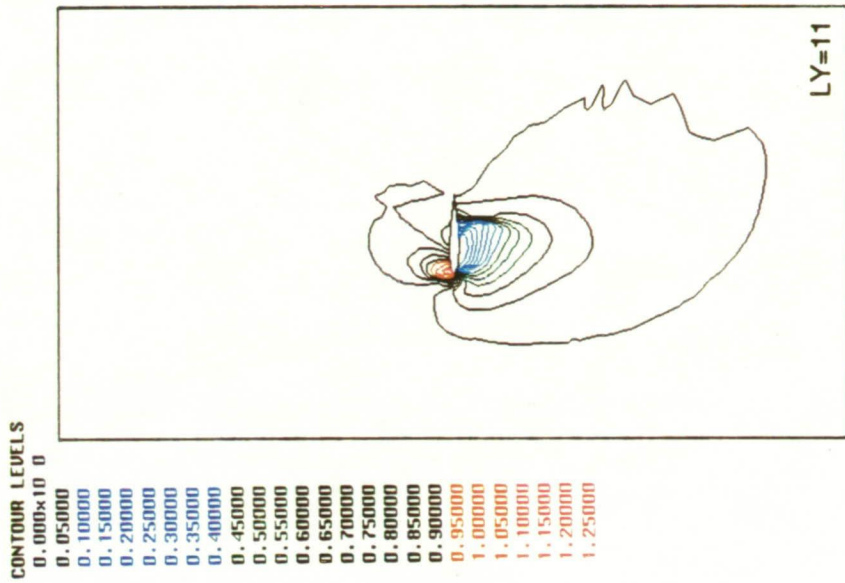
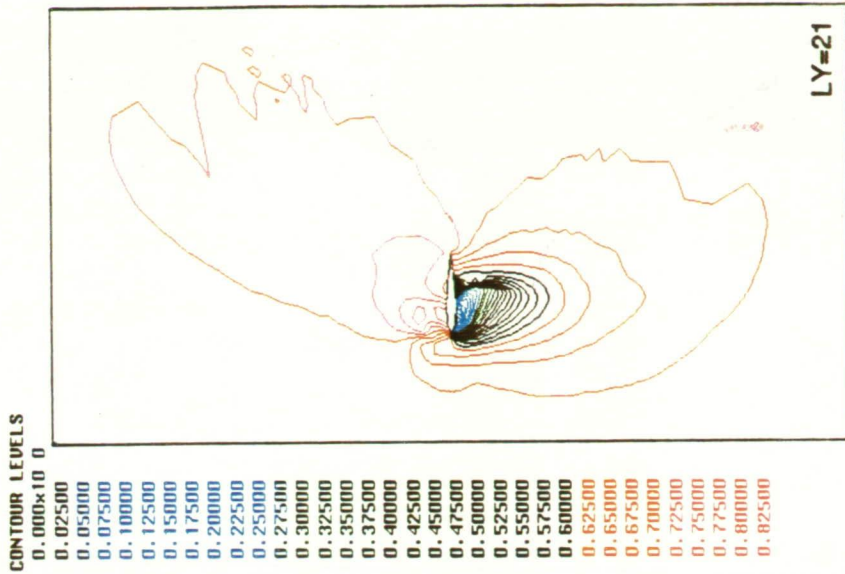
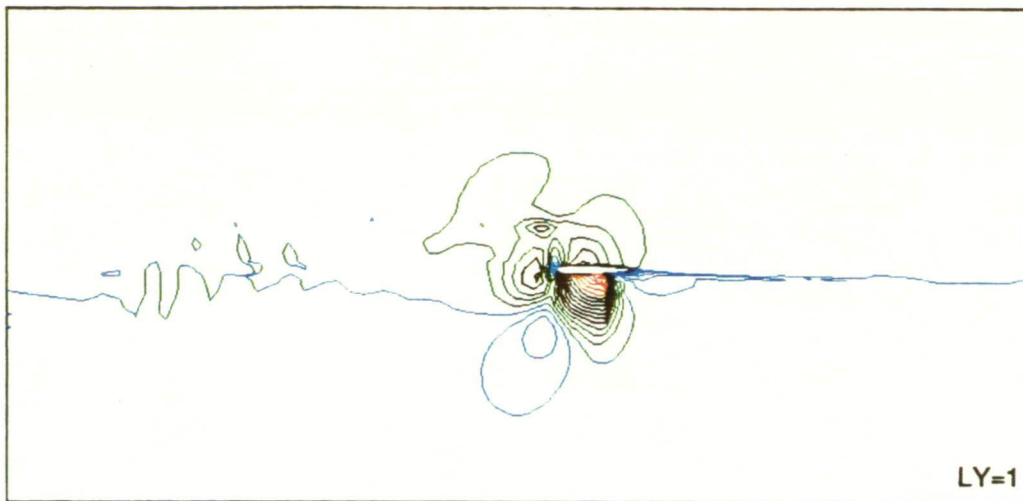


Fig. 84 Pressure Field, $t=4.7$.

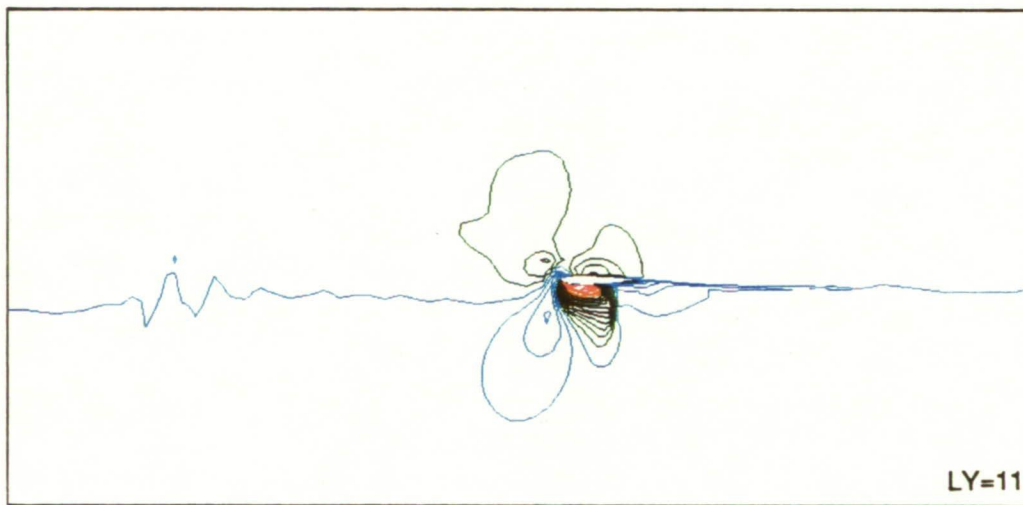
ORIGINAL PAGE
COLOR PHOTOGRAPH



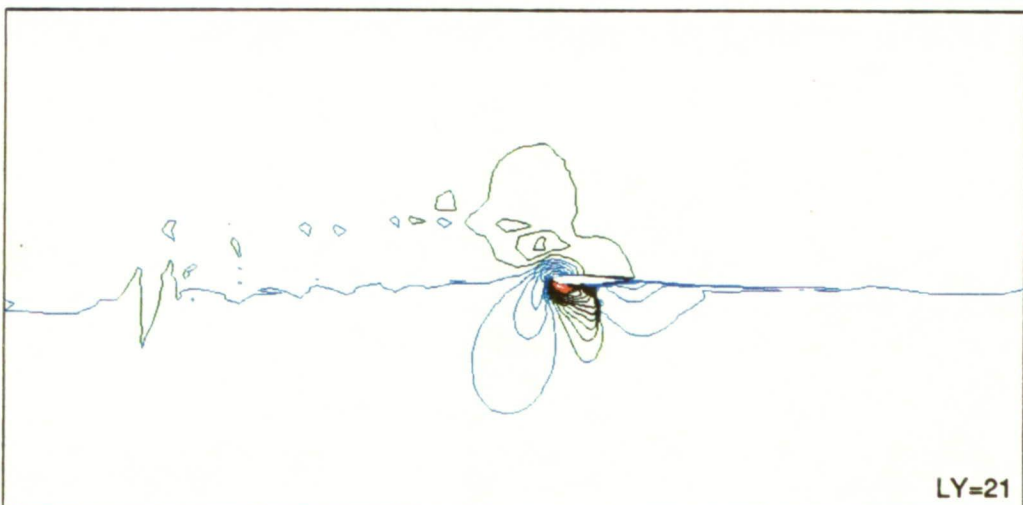
LY=1

CONTOUR LEVELS

- 0.000x10 0
- 0.10000
- 0.20000
- 0.30000
- 0.40000
- 0.50000
- 0.60000
- 0.70000
- 0.80000
- 0.90000
- 1.00000
- 1.10000
- 1.20000
- 1.30000
- 1.40000
- 1.50000
- 1.60000
- 1.70000
- 1.80000
- 1.90000
- 2.00000
- 2.10000
- 2.20000
- 2.30000
- 2.40000
- 2.50000
- 2.60000



LY=11



LY=21

Fig. 85 Mach Number Field, $t=4.7$.

ORIGINAL PAGE
COLOR PHOTOGRAPH

CONTOUR LEVELS

- 0.100000
- 0.120000
- 0.140000
- 0.160000
- 0.180000
- 0.200000
- 0.220000
- 0.240000
- 0.260000
- 0.280000
- 0.300000
- 0.320000
- 0.340000
- 0.360000
- 0.380000
- 0.400000

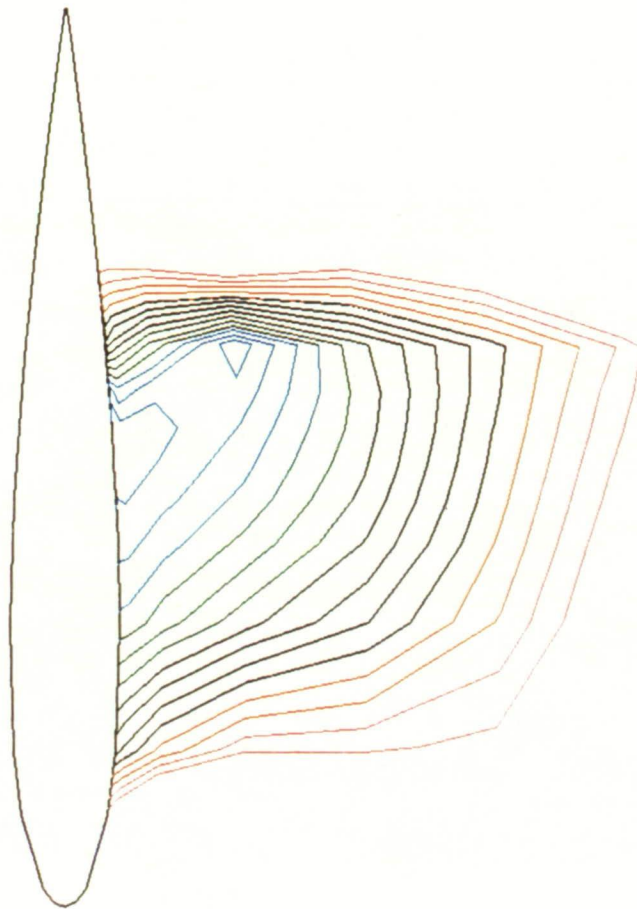


Fig. 86 Details of Suction Side Pressure, LY=1, t=4.7.

ORIGINAL PAGE
COLOR PHOTOGRAPH

CONTOUR LEVELS

- 0.10000
- 0.12000
- 0.14000
- 0.16000
- 0.18000
- 0.20000
- 0.22000
- 0.24000
- 0.26000
- 0.28000
- 0.30000
- 0.32000
- 0.34000
- 0.36000
- 0.38000
- 0.40000

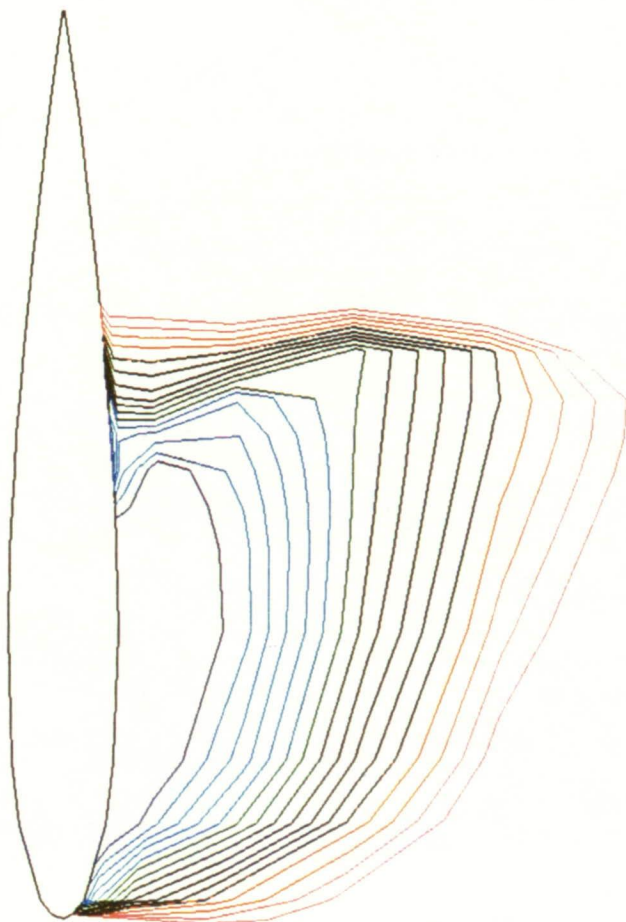


Fig. 87 Details of Suction Side Pressure, LY=11, t=4.7.

ORIGINAL PAGE
COLOR PHOTOGRAPH

CONTOUR LEVELS

- 0.10000
- 0.12000
- 0.14000
- 0.16000
- 0.18000
- 0.20000
- 0.22000
- 0.24000
- 0.26000
- 0.28000
- 0.30000
- 0.32000
- 0.34000
- 0.36000
- 0.38000
- 0.40000

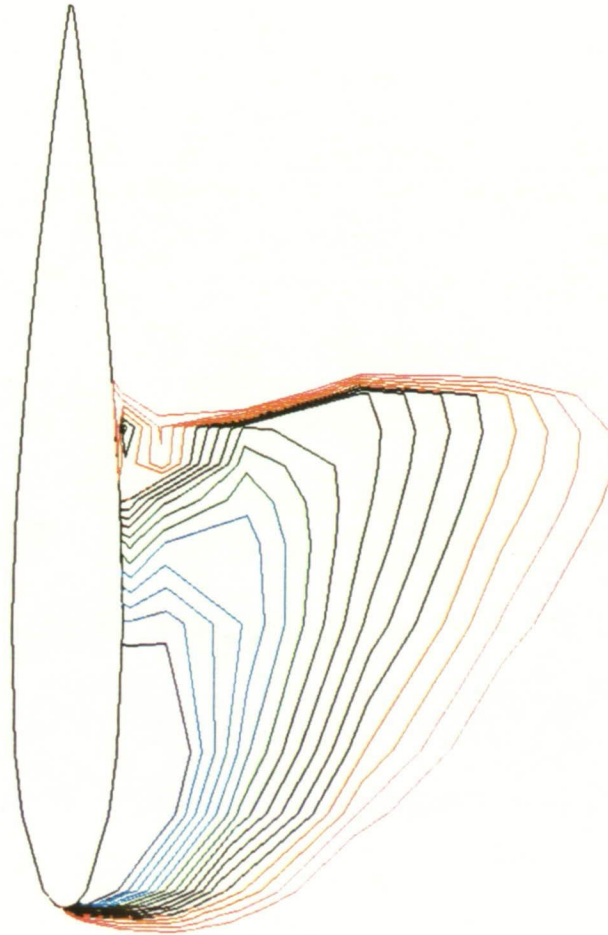


Fig. 88 Details of Suction Side Pressure, LY=21, t=4.7.

ORIGINAL PAGE
COLOR PHOTOGRAPH

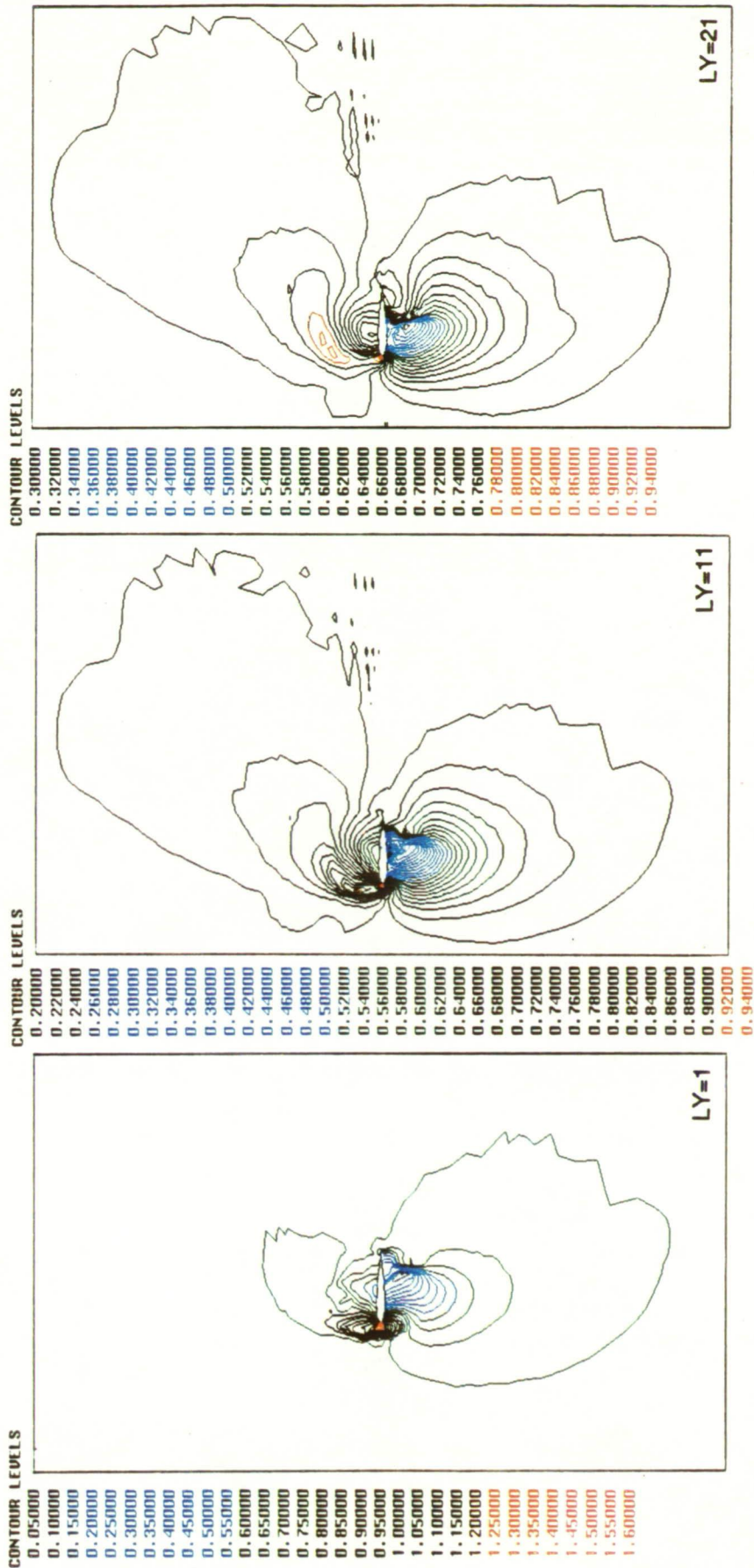
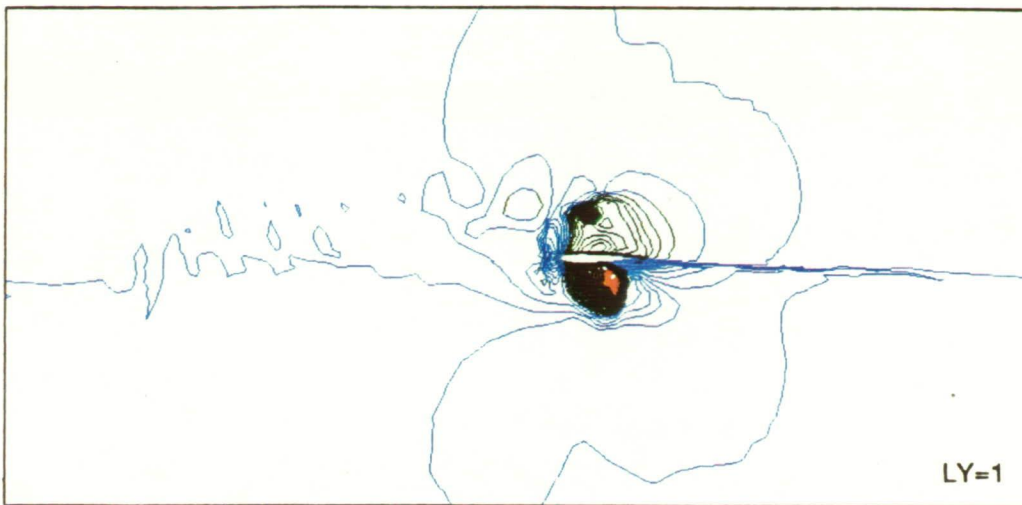


Fig. 89 Pressure Field, $t=5.157$.

ORIGINAL PAGE
COLOR PHOTOGRAPH

CONTOUR LEVELS

- 0.000x10 0
- 0.05000
- 0.10000
- 0.15000
- 0.20000
- 0.25000
- 0.30000
- 0.35000
- 0.40000
- 0.45000
- 0.50000
- 0.55000
- 0.60000
- 0.65000
- 0.70000
- 0.75000
- 0.80000
- 0.85000
- 0.90000
- 0.95000
- 1.00000
- 1.05000
- 1.10000
- 1.15000
- 1.20000
- 1.25000
- 1.30000
- 1.35000
- 1.40000
- 1.45000
- 1.50000
- 1.55000
- 1.60000
- 1.65000
- 1.70000
- 1.75000
- 1.80000
- 1.85000



CONTOUR LEVELS

- 0.000x10 0
- 0.05000
- 0.10000
- 0.15000
- 0.20000
- 0.25000
- 0.30000
- 0.35000
- 0.40000
- 0.45000
- 0.50000
- 0.55000
- 0.60000
- 0.65000
- 0.70000
- 0.75000
- 0.80000
- 0.85000
- 0.90000
- 0.95000
- 1.00000
- 1.05000
- 1.10000
- 1.15000
- 1.20000
- 1.25000
- 1.30000
- 1.35000
- 1.40000
- 1.45000
- 1.50000
- 1.55000
- 1.60000
- 1.65000

CONTOUR LEVELS

- 0.000x10 0
- 0.02500
- 0.05000
- 0.07500
- 0.10000
- 0.12500
- 0.15000
- 0.17500
- 0.20000
- 0.22500
- 0.25000
- 0.27500
- 0.30000
- 0.32500
- 0.35000
- 0.37500
- 0.40000
- 0.42500
- 0.45000
- 0.47500
- 0.50000
- 0.52500
- 0.55000
- 0.57500
- 0.60000
- 0.62500
- 0.65000
- 0.67500
- 0.70000
- 0.72500
- 0.75000
- 0.77500
- 0.80000
- 0.82500
- 0.85000
- 0.87500
- 0.90000
- 0.92500

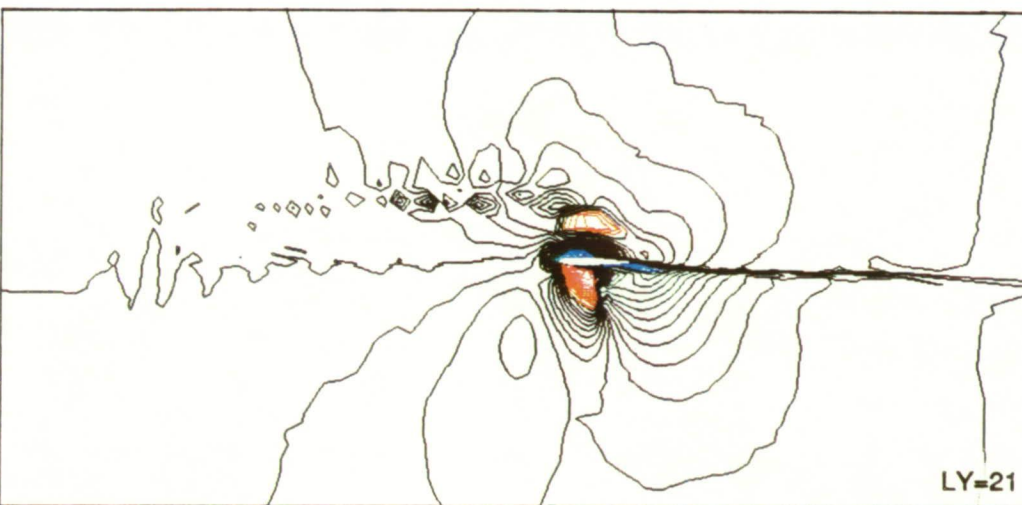
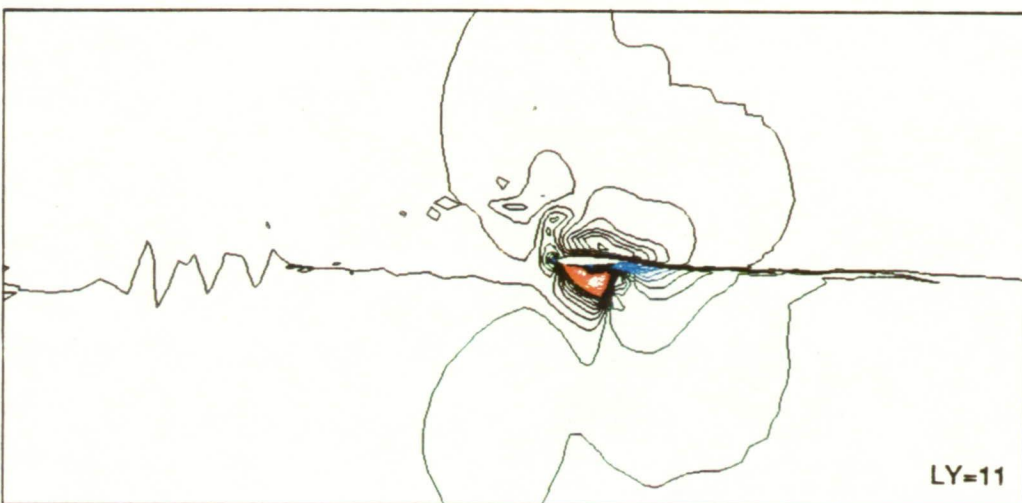


Fig. 90 Mach Number Field, t=5.157.

ORIGINAL PAGE
COLOR PHOTOGRAPH

CONTOUR LEVELS

- 0.10000
- 0.11000
- 0.12000
- 0.13000
- 0.14000
- 0.15000
- 0.16000
- 0.17000
- 0.18000
- 0.19000
- 0.20000
- 0.21000
- 0.22000
- 0.23000
- 0.24000
- 0.25000
- 0.26000
- 0.27000
- 0.28000
- 0.29000
- 0.30000
- 0.31000
- 0.32000
- 0.33000
- 0.34000
- 0.35000
- 0.36000
- 0.37000
- 0.38000
- 0.39000
- 0.40000
- 0.41000
- 0.42000
- 0.43000
- 0.44000
- 0.45000

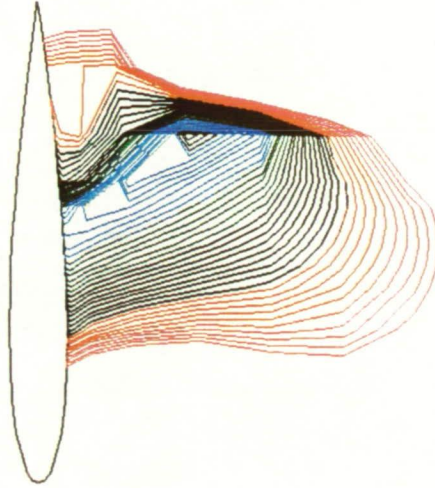


Fig. 91 Details of Suction Side Pressure, LY=1, t=5.157.

ORIGINAL PAGE
COLOR PHOTOGRAPH

CONTOUR LEVELS

- 0.10000
- 0.11000
- 0.12000
- 0.13000
- 0.14000
- 0.15000
- 0.16000
- 0.17000
- 0.18000
- 0.19000
- 0.20000
- 0.21000
- 0.22000
- 0.23000
- 0.24000
- 0.25000
- 0.26000
- 0.27000
- 0.28000
- 0.29000
- 0.30000
- 0.31000
- 0.32000
- 0.33000
- 0.34000
- 0.35000
- 0.36000
- 0.37000
- 0.38000
- 0.39000
- 0.40000
- 0.41000
- 0.42000
- 0.43000
- 0.44000
- 0.45000

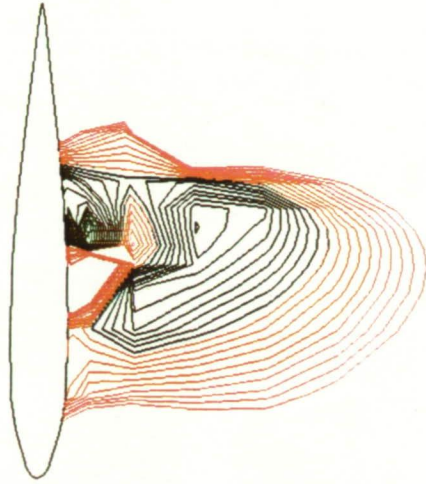


Fig. 92 Details of Suction Side Pressure, LY-11, t=5.157.

ORIGINAL PAGE
COLOR PHOTOGRAPH

CONTOUR LEVELS

0.10000
0.11000
0.12000
0.13000
0.14000
0.15000
0.16000
0.17000
0.18000
0.19000
0.20000
0.21000
0.22000
0.23000
0.24000
0.25000
0.26000
0.27000
0.28000
0.29000
0.30000
0.31000
0.32000
0.33000
0.34000
0.35000
0.36000
0.37000
0.38000
0.39000
0.40000
0.41000
0.42000
0.43000
0.44000
0.45000

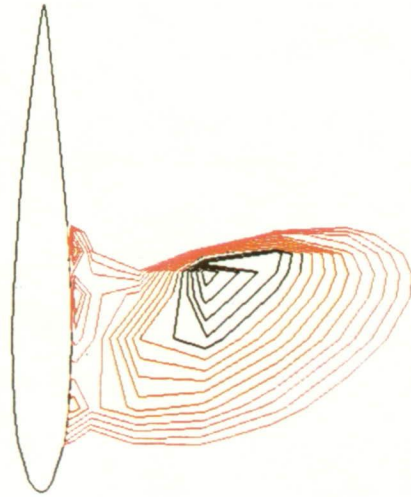


Fig. 93 Details of Suction Side Pressure, $LY=21$, $t=5.157$.

ORIGINAL PAGE
COLOR PHOTOGRAPH

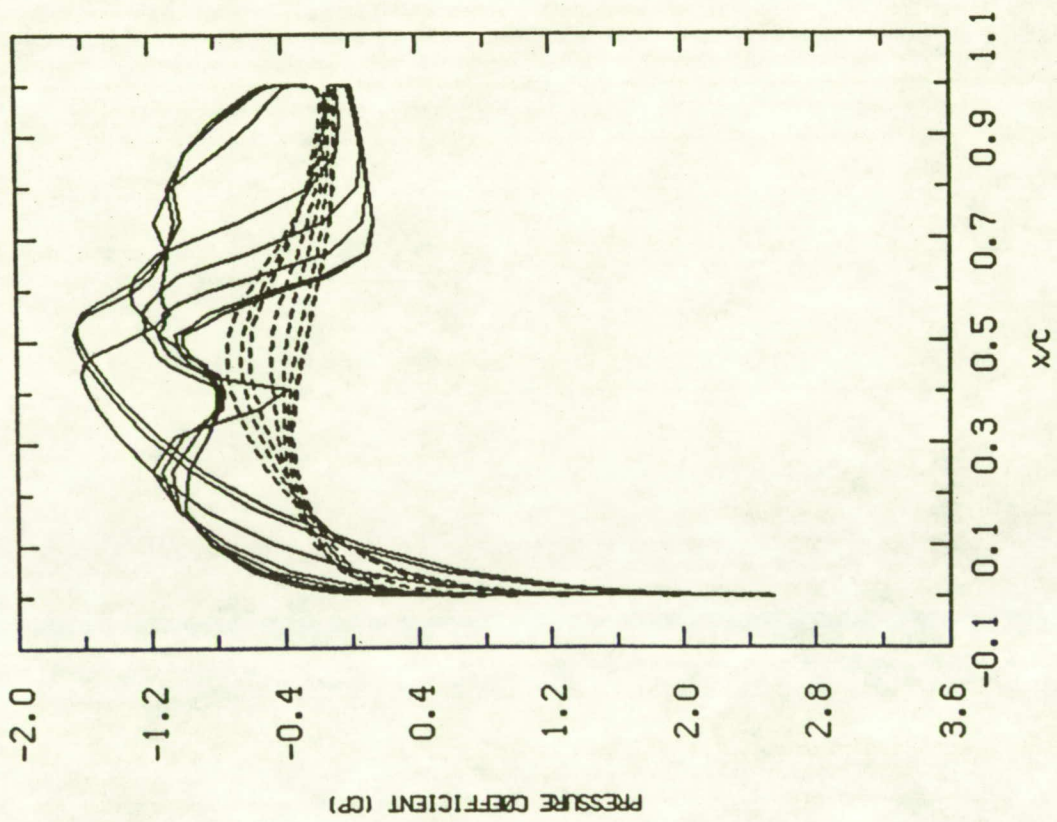


Fig. 94 Composite Surface Pressure, $t=5.157$.

CONTOUR LEVELS

- 0.10000
- 0.11000
- 0.12000
- 0.13000
- 0.14000
- 0.15000
- 0.16000
- 0.17000
- 0.18000
- 0.19000
- 0.20000
- 0.21000
- 0.22000
- 0.23000
- 0.24000
- 0.25000
- 0.26000
- 0.27000
- 0.28000
- 0.29000
- 0.30000
- 0.31000
- 0.32000
- 0.33000
- 0.34000
- 0.35000
- 0.36000
- 0.37000
- 0.38000
- 0.39000
- 0.40000
- 0.41000
- 0.42000
- 0.43000
- 0.44000
- 0.45000

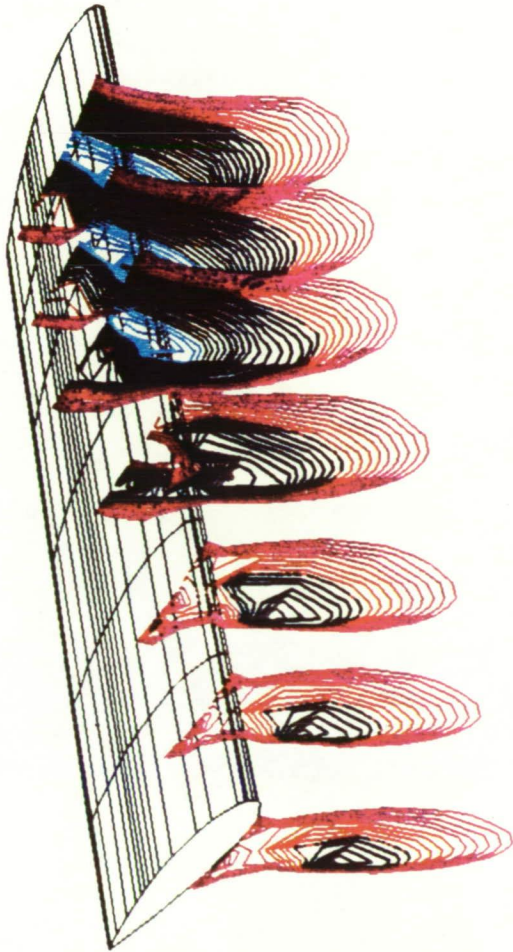


Fig. 95 Pressure Field at $t = 5.157$.

ORIGINAL PAGE
COLOR PHOTOGRAPH

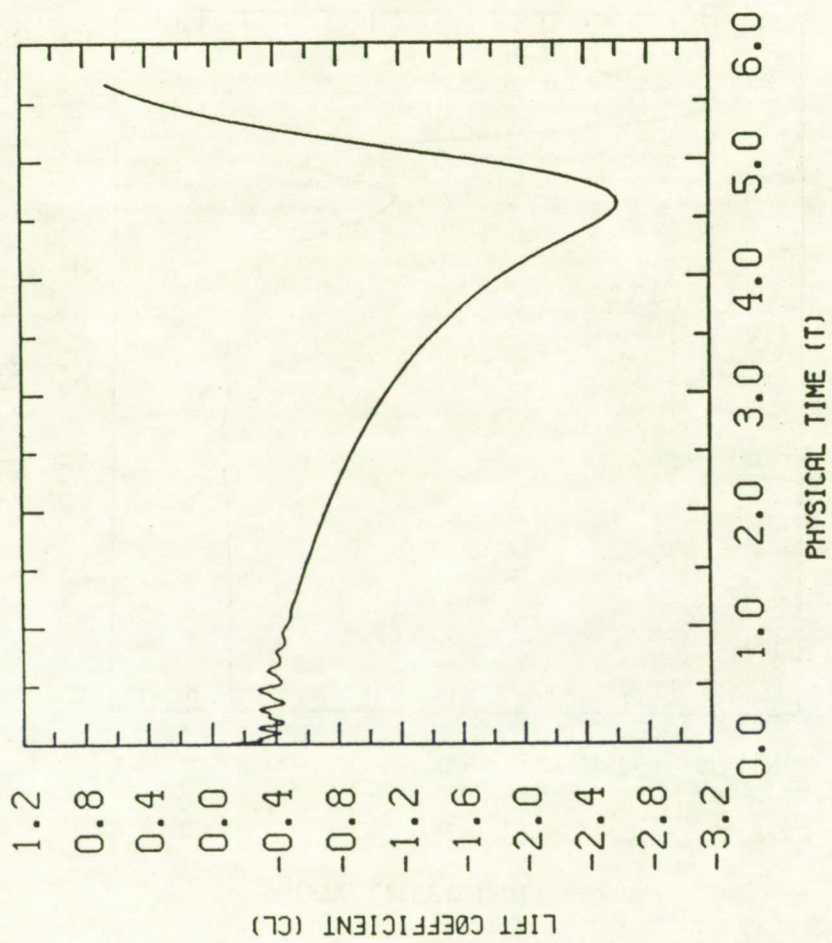


Fig. 96 Blade Lift Coefficient.

ORIGINAL PAGE
COLOR PHOTOGRAPH

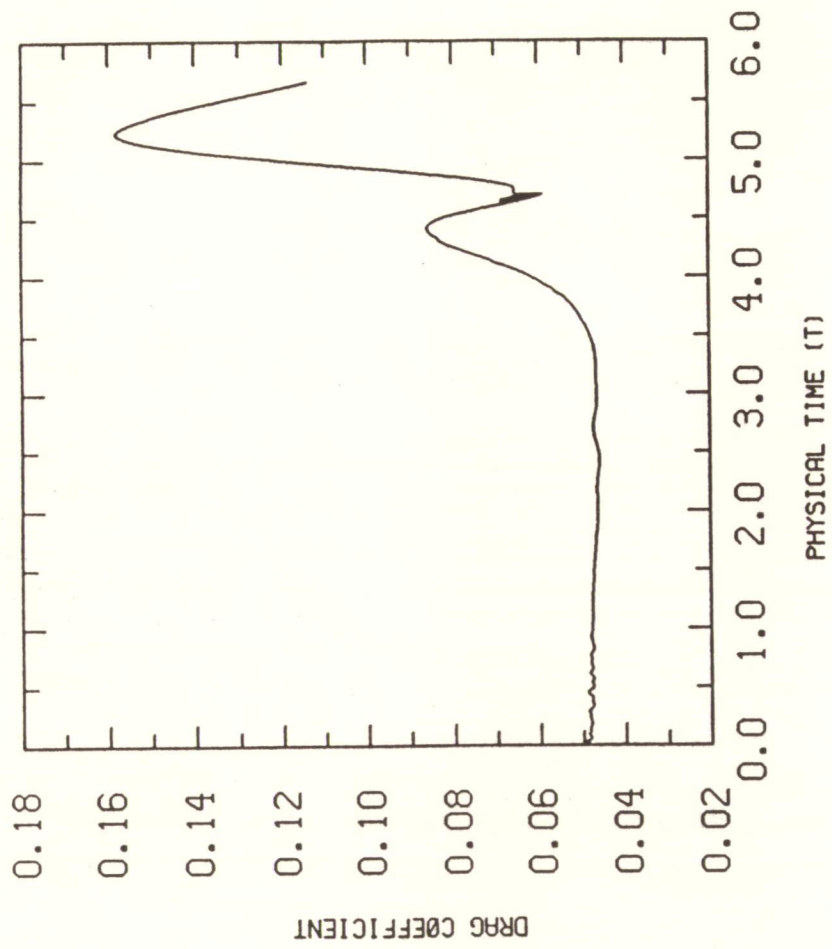


Fig. 97 Blade Drag Coefficient.

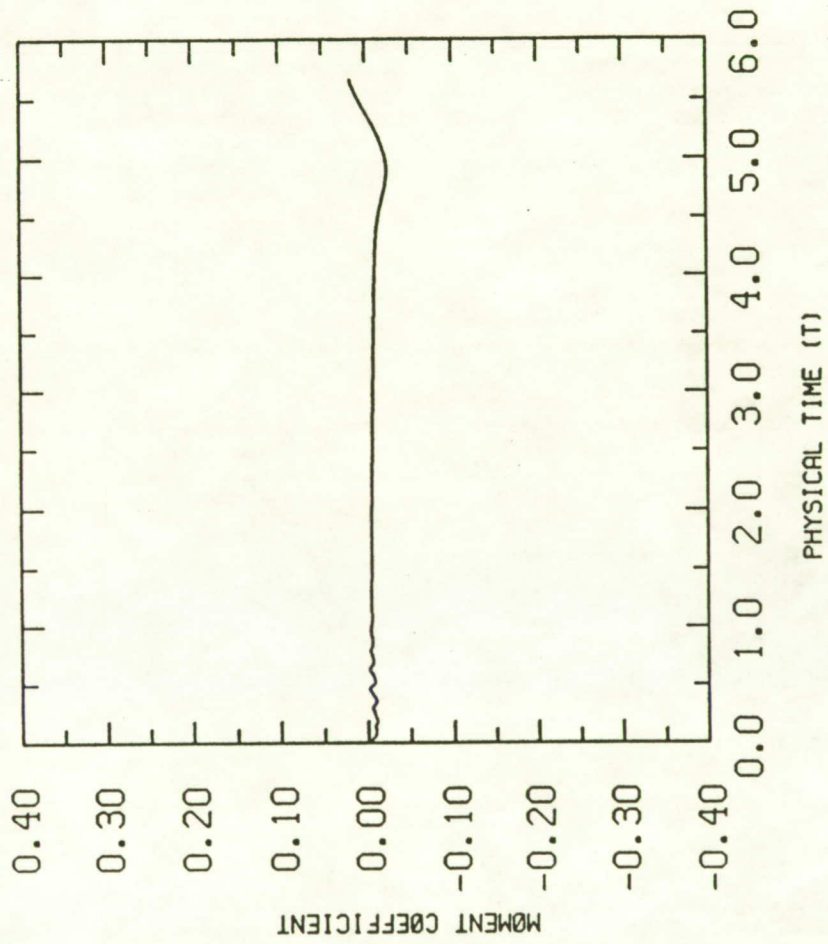


Fig. 98 Blade Moment Coefficient.

CONTOUR LEVELS
 0.45000
 0.46000
 0.47000
 0.48000
 0.49000
 0.50000
 0.51000
 0.52000
 0.53000
 0.54000
 0.55000
 0.56000
 0.57000
 0.58000
 0.59000
 0.60000
 0.61000
 0.62000
 0.63000
 0.64000
 0.65000
 0.66000
 0.67000
 0.68000
 0.69000
 0.70000
 0.71000
 0.72000
 0.73000
 0.74000
 0.75000
 0.76000
 0.77000
 0.78000
 0.79000
 0.80000
 0.81000
 0.82000

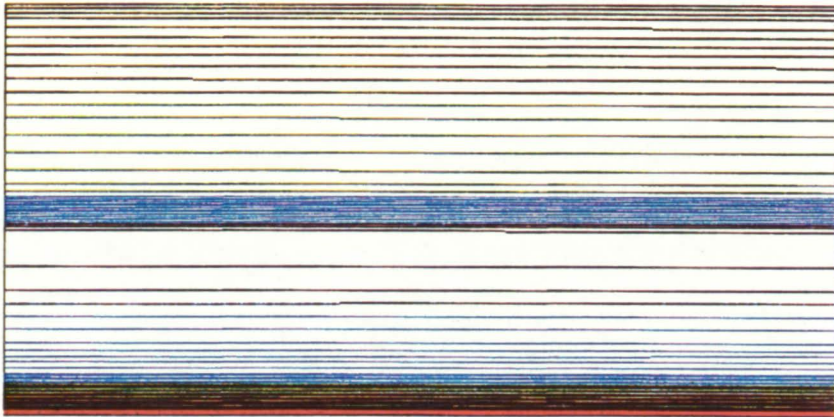
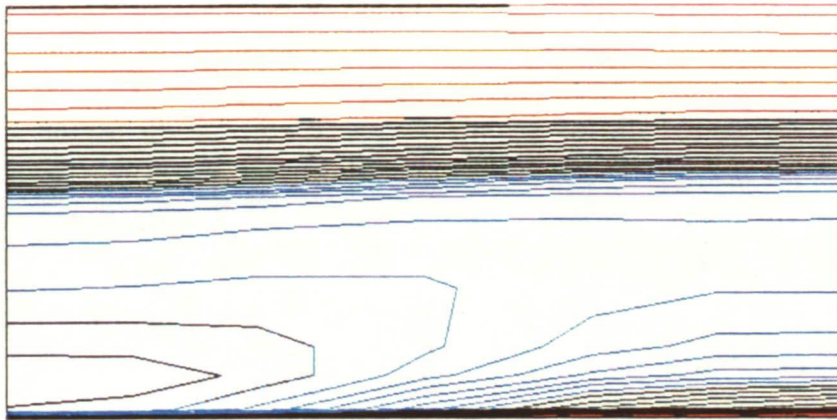


Fig. 99 Surface Pressure Contour at t=0.0.

ORIGINAL PAGE
 COLOR PHOTOGRAPH

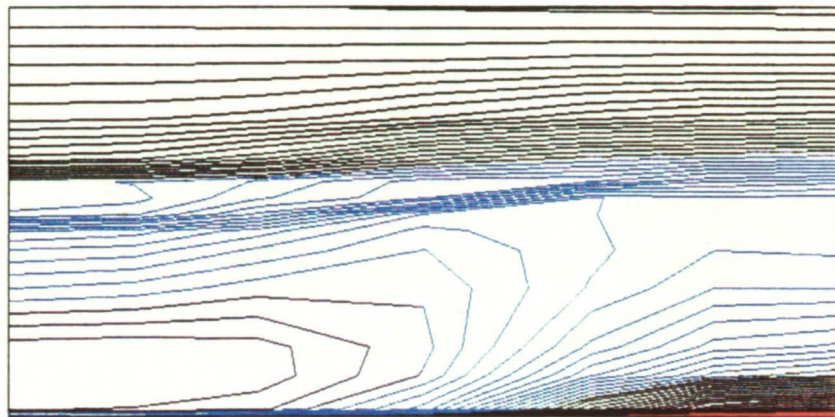


CONTOUR LEVELS

- 0.160000
- 0.180000
- 0.200000
- 0.220000
- 0.240000
- 0.260000
- 0.280000
- 0.300000
- 0.320000
- 0.340000
- 0.360000
- 0.380000
- 0.400000
- 0.420000
- 0.440000
- 0.460000
- 0.480000
- 0.500000
- 0.520000
- 0.540000
- 0.560000
- 0.580000
- 0.600000
- 0.620000
- 0.640000
- 0.660000
- 0.680000
- 0.700000
- 0.720000
- 0.740000
- 0.760000
- 0.780000

Fig. 100 Lower Surface Pressure Contour, t=4.138.

ORIGINAL PAGE
COLOR PHOTOGRAPH

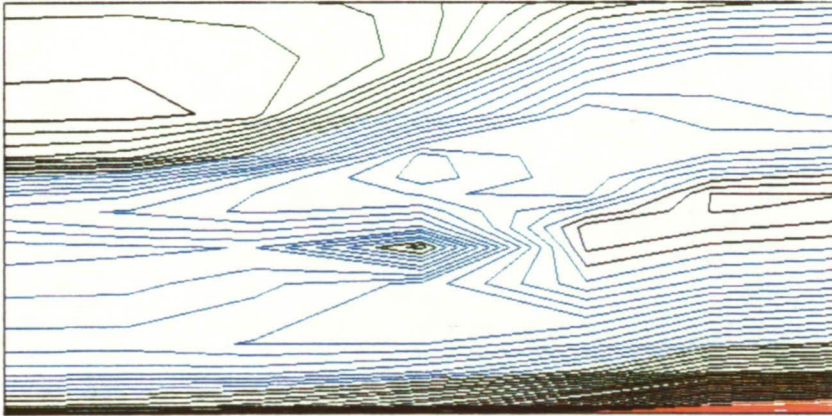


CONTOUR LEVELS

0.02000
 0.04000
 0.06000
 0.08000
 0.10000
 0.12000
 0.14000
 0.16000
 0.18000
 0.20000
 0.22000
 0.24000
 0.26000
 0.28000
 0.30000
 0.32000
 0.34000
 0.36000
 0.38000
 0.40000
 0.42000
 0.44000
 0.46000
 0.48000
 0.50000
 0.52000
 0.54000
 0.56000
 0.58000
 0.60000
 0.62000
 0.64000
 0.66000
 0.68000
 0.70000
 0.72000
 0.74000
 0.76000

Fig. 101 Lower Surface Pressure Contour, $t=4.56$.

ORIGINAL PAGE
 COLOR PHOTOGRAPH

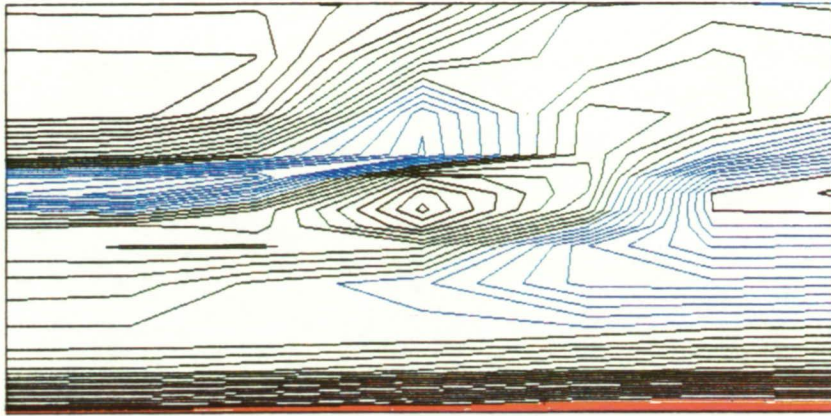


CONTOUR LEVELS

- 0.15000
- 0.17500
- 0.20000
- 0.22500
- 0.25000
- 0.27500
- 0.30000
- 0.32500
- 0.35000
- 0.37500
- 0.40000
- 0.42500
- 0.45000
- 0.47500
- 0.50000
- 0.52500
- 0.55000
- 0.57500
- 0.60000
- 0.62500
- 0.65000
- 0.67500
- 0.70000
- 0.72500
- 0.75000
- 0.77500
- 0.80000
- 0.82500
- 0.85000
- 0.87500
- 0.90000
- 0.92500
- 0.95000
- 0.97500
- 1.00000
- 1.02500
- 1.05000
- 1.07500

Fig. 102 Lower Surface Pressure Contour, t=5.157.

ORIGINAL PAGE
COLOR PHOTOGRAPH

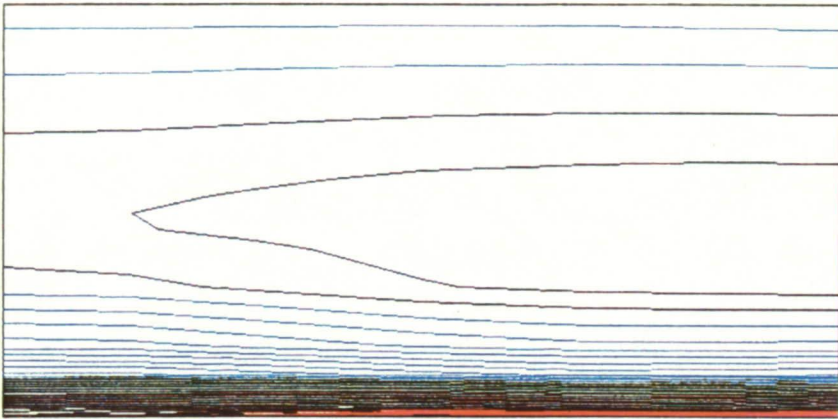


CONTOUR LEVELS

- 0.28000
- 0.30000
- 0.32000
- 0.34000
- 0.36000
- 0.38000
- 0.40000
- 0.42000
- 0.44000
- 0.46000
- 0.48000
- 0.50000
- 0.52000
- 0.54000
- 0.56000
- 0.60000
- 0.62000
- 0.64000
- 0.66000
- 0.68000
- 0.70000
- 0.72000
- 0.74000
- 0.76000
- 0.78000
- 0.80000
- 0.82000
- 0.84000
- 0.86000
- 0.88000
- 0.90000
- 0.92000
- 0.94000
- 0.96000
- 0.98000
- 1.00000
- 1.02000

Fig. 103 Lower Surface Pressure Contour, t=5.498.

ORIGINAL PAGE
COLOR PHOTOGRAPH

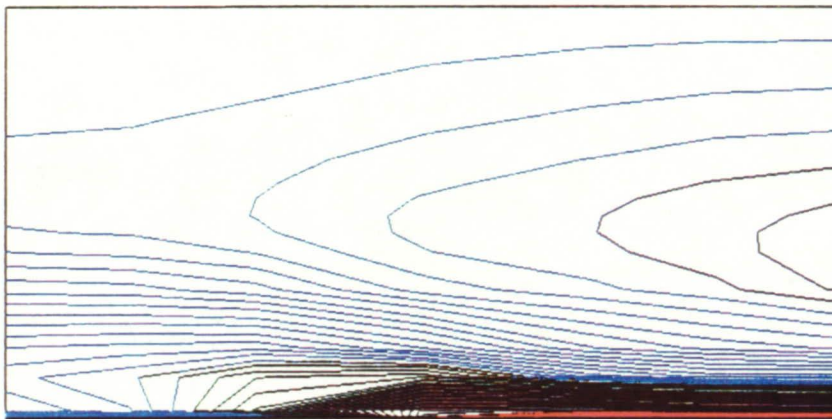


CONTOUR LEVELS

- 0.66000
- 0.68000
- 0.70000
- 0.72000
- 0.74000
- 0.76000
- 0.78000
- 0.80000
- 0.82000
- 0.84000
- 0.86000
- 0.88000
- 0.90000
- 0.92000
- 0.94000
- 0.96000
- 0.98000
- 1.00000
- 1.02000
- 1.04000
- 1.06000
- 1.08000
- 1.10000
- 1.12000
- 1.14000
- 1.16000
- 1.18000
- 1.20000
- 1.22000
- 1.24000
- 1.26000
- 1.28000
- 1.30000
- 1.32000
- 1.34000
- 1.36000
- 1.38000
- 1.40000

Fig. 104 Upper Surface Pressure Contour, t=4.138.

ORIGINAL PAGE
COLOR PHOTOGRAPH

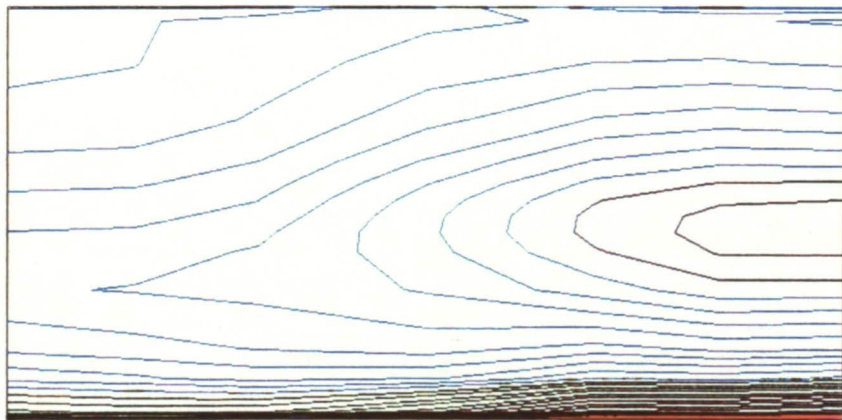


CONTOUR LEVELS

0.60000
 0.62000
 0.64000
 0.66000
 0.68000
 0.70000
 0.72000
 0.74000
 0.76000
 0.78000
 0.80000
 0.82000
 0.84000
 0.86000
 0.88000
 0.90000
 0.92000
 0.94000
 0.96000
 0.98000
 1.00000
 1.02000
 1.04000
 1.06000
 1.08000
 1.10000
 1.12000
 1.14000
 1.16000
 1.18000
 1.20000
 1.22000
 1.24000
 1.26000
 1.28000
 1.30000
 1.32000
 1.34000

Fig. 105 Upper Surface Pressure Contour, $t=4.56$.

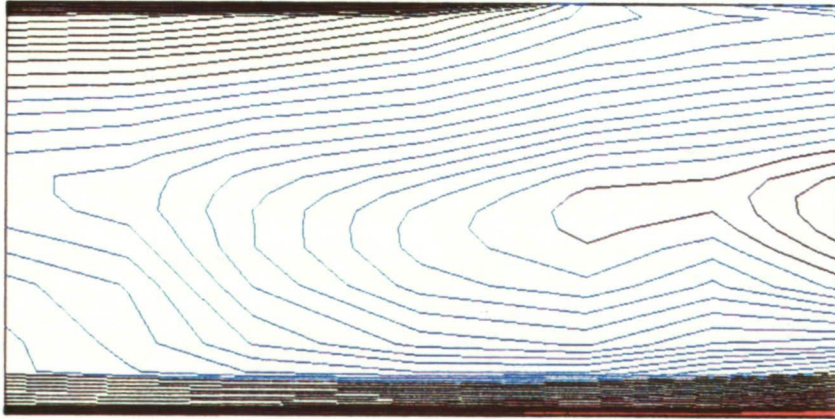
ORIGINAL PAGE
 COLOR PHOTOGRAPH



CONTOUR LEVELS
 0.480000
 0.500000
 0.520000
 0.540000
 0.560000
 0.580000
 0.600000
 0.620000
 0.640000
 0.660000
 0.680000
 0.700000
 0.720000
 0.740000
 0.760000
 0.780000
 0.800000
 0.820000
 0.840000
 0.860000
 0.880000
 0.900000
 0.920000
 0.940000
 0.960000
 0.980000
 1.000000
 1.020000
 1.040000
 1.060000
 1.080000
 1.100000
 1.120000
 1.140000
 1.160000
 1.180000
 1.200000

Fig. 106 Upper Surface Pressure Contour, t=5.157.

ORIGINAL PAGE
 COLOR PHOTOGRAPH



CONTOUR LEVELS
 0.44000
 0.45000
 0.46000
 0.47000
 0.48000
 0.49000
 0.50000
 0.51000
 0.52000
 0.53000
 0.54000
 0.55000
 0.56000
 0.57000
 0.58000
 0.59000
 0.60000
 0.61000
 0.62000
 0.63000
 0.64000
 0.65000
 0.66000
 0.67000
 0.68000
 0.69000
 0.70000
 0.71000
 0.72000
 0.73000
 0.74000
 0.75000
 0.76000
 0.77000
 0.78000
 0.79000
 0.80000
 0.81000

Fig. 107 Upper Surface Pressure Contour, t=5.498.

216 JINCHONKAZEV BLANK

ORIGINAL PAGE
 COLOR PHOTOGRAPH

1. Report No. NASA CR-177567		2. Government Accession No.		3. Recipient's Catalog No.	
4. Title and Subtitle Two- and Three-Dimensional Blade Vortex Interactions				5. Report Date August 1990	
				6. Performing Organization Code	
7. Author(s) F. Davoudzadeh, N. -S Liu, W. R. Briley, R. C. Buggeln, and S. J. Shamroth				8. Performing Organization Report No. A-90275	
				10. Work Unit No.	
9. Performing Organization Name and Address Scientific Research Associates, Inc. 50 Nye Road, P. O. Box 1058 Glastonbury, CT 06033				11. Contract or Grant No. NAS2-12635	
				13. Type of Report and Period Covered Contractor Report	
12. Sponsoring Agency Name and Address National Aeronautics and Space Administration Washington, DC 20546-0001				14. Sponsoring Agency Code	
15. Supplementary Notes Point of Contact: C. Kitaplioglu, Ames Research Center, MS T-042, Moffett Field, CA 94035-1000 (415) 604-6679 or FTS 464-6679					
16. Abstract A three-dimensional time dependent Navier-Stokes analysis was applied to the rotor blade vortex interaction problem. The numerical procedure is an iterative implicit procedure using three point central differences to represent spatial derivatives. A series of calculations were made to determine the time steps, pseudo-time steps, iterations, artificial dissipation level, etc. required to maintain a nondissipative vortex. Results show the chosen method to have excellent non-dissipative properties provided the correct parameters are chosen. This study was used to set parameters for both two- and three-dimensional blade vortex interaction studies. The two-dimensional study considered the interaction between a vortex and a NACA0012 airfoil. The results showed the detailed physics during the interaction including the pressure pulse propagating from the blade. The simulated flow physics was qualitatively similar to that experimentally observed. The 2-D BVI phenomena is the result of the buildup and violent collapse of the shock waves and local supersonic pockets on the blade surfaces. The resulting pressure pulse build-up appears to be centered at the blade leading edge. The three-dimensional interaction study considered the case of a vortex at 20° incidence to the blade leading edge. Although the qualitative results were similar to that of the two-dimensional interaction, details clearly showed the three-dimensional nature of the interaction process.					
17. Key Words (Suggested by Author(s)) Blade-vortex interactions Computational fluid dynamics Navier-Stokes			18. Distribution Statement Unclassified-Unlimited Subject Category-02		
19. Security Classif. (of this report) Unclassified		20. Security Classif. (of this page) Unclassified		21. No. of Pages 224	22. Price A10